

**Geoacoustic investigations
of cold vents and sedimentary processes
at the active continental margin
offshore Nicaragua**

DISSERTATION
ZUR ERLANGUNG DES DOKTORGRADES
DER MATHEMATISCH-NATURWISSENSCHAFTLICHEN FAKULTÄT
DER CHRISTIAN-ALBRECHTS-UNIVERSITÄT
ZU KIEL

vorgelegt von

Dietmar Bürk

Kiel, 2007

Referent:

Korreferent:

Tag der mündlichen Prüfung:

Zum Druck genehmigt:

Prof. Dr. Hans-Jürgen Götze

Prof. Dr. Timothy J. Reston

01.06.2007

01.06.2007

Der Dekan

Abstract

This work investigates cold vents and seeps in the forearc region of the active continental margin offshore Nicaragua with multibeam bathymetry and associated amplitude measurements, high-resolution, 75 kHz deep-towed sidescan sonar, including a 2–10 kHz chirp subbottom profiler, and hull-mounted parametric echosounder. Ground truthing is available from camera system surveys and coring on several of the structures.

The area is characterized by a high number of so-called mound structures visible in the multibeam bathymetry, and various intensity anomalies without a significant topographic expression but showing high backscatter in the sidescan sonar image. The increased backscatter on mounds and intensity anomalies is mainly related to an increased seafloor roughness, and attributed to hardgrounds like authigenic carbonate formations. A significant influence of the seafloor topography on the sidescan sonar signal is ruled out for the IFM-GEOMAR DTS-1 system. This is shown by a new processing algorithm, developed in this work, which applies the specific backscattering vs. incidence angle relation (*shading function*) of the sidescan transducer to the signal, and corrects it for varying incidence angles of the acoustic beam on the true seafloor topography. The topographic influence is only relevant in the nadir area of the system, in the very near-range where the shading function is steep, or when the seafloor gradient in the mid- to far-range is larger than 20°–40°.

Based on their morphology, backscatter signal, and fluid venting activity a classification of the seep sites with three end members is suggested. (1) Mid-sized and dome-shaped mounds have diameters around 700-1000 m and heights of 50-100 m, and show bright backscatter due to authigenic carbonates, with some fluid venting activity and associated vent fauna. (2) Small mounds with very little topographic expression have diameters around 500 m and show irregular outlines. Authigenic carbonates are sometimes covered with sediments, there are no signs of erosion. A wide range of vent biota indicates stronger fluid venting activity. (3) Very large and steep mounds have diameters exceeding 1000 m and heights up to 150–200 m. The plateau areas show widespread, thick authigenic carbonates. Subbottom profiles do not reveal any sediment coverage. Vent fauna is rare indicating little to none fluid venting activity. Calculated ratios of mound volume to base area do not cluster according to the mound types, but are a good measure of how much a mound is exposed above the seafloor.

The shape of the mounds is strongly affected by erosional processes which are active on the slope. Multibeam bathymetry shows very clearly deep incised canyons. Additionally truncation of sediment layers at canyon walls, and moats around mounds are sometimes observed in subbottom profiles. The mounds which consist of a mixture of mud and authigenic carbonates, are more resistant against erosion than the surrounding seafloor, and form topographic highs over time. The geoacoustic data do not indicate any signs of mud volcanism, like mud flows or other deposits of eruptive processes.

However, subbottom profiles do reveal at some locations an upward movement of sediments in the shallow subsurface, which is interpreted as (small-scale) sediment mobiliza-

tion. It is speculated that the sediments are mobilized by the dissociation of gas hydrates, which, in turn, are decomposed by upward travelling warmer fluids from greater depths, preferentially the plate boundary. Deep-tow seismic data image diapiric structures below mounds down to a depth of ~ 400 mbsf, and the sediment mobilization is suggested to occur at the base of the slope sediments [Talukder et al., in press].

The observations are summarized in a modified mound model, which includes the interaction of several processes: Episodic fluid venting and associated authigenic carbonate formation, background sedimentation and subsidence, and erosion.

The dataset covers Momotombo Slide and Masaya Slide, which are probably induced by oversteepening of the middle slope region due to tectonic erosion, or, in the case of Masaya Slide, to a subducting seamount on the lower plate. Both exhibit a translational failure mechanism and some amount of retrogression. Associated extensional fractures serve probably as pathways for upward travelling fluids. Slide volumes are 10.5 km^3 and 7.7 km^3 for Momotombo Slide and Masaya Slide, respectively.

Zusammenfassung

Die vorliegende Arbeit untersucht kalte Fluidaustritte im Forearc des aktiven Kontinentalrandes vor der Küste von Nicaragua mit Hilfe geoakustischer Verfahren. Im Einzelnen sind dies: Fächerecholot Tiefen- und Amplitudenmessungen, tiefgeschlepptes, hochauflösendes 75 kHz Seitensicht Sonar mit eingebautem 2–10 kHz Chirp Sediment-Echolot, sowie ein schiffsbasiertes parametrisches Echolot. Ein Vergleich der Daten mit direkten Meeresbodenbeobachtungen erfolgt durch Videokartierungen und Schwerelot-Kerne an einigen dieser Strukturen.

Das Arbeitsgebiet ist gekennzeichnet durch eine große Anzahl sogenannter Mound-Strukturen, die in den Tiefenmessungen erkennbar sind, sowie durch zahlreiche Rückstreu-Anomalien, die keine oder kaum eine Topographie aufweisen. Die erhöhte Rückstreuung der Mounds und Anomalien wird verursacht durch eine erhöhte Rauigkeit des Meeresbodens, welche wiederum auf Karbonatkrusten zurückgeführt wird. Ein signifikanter Einfluß der Meeresboden-Topographie auf die Höhe der Rückstreuung wird für das IFM-GEOMAR DTS-1 System ausgeschlossen. Ein in dieser Arbeit neu entwickelter Algorithmus bei der Verarbeitung der Daten verwendet die sensorspezifische Beziehung zwischen Rückstreustärke und Einfallswinkel des akustischen Strahles, um das gemessene Signal für die berechneten Einfallswinkel auf der wirklichen Meeresboden-Topographie zu korrigieren. Der Einfluß der Topographie ist lediglich im Nadir oder Nahbereich des Systems relevant, da hier die Funktion eine große Steilheit aufweist, oder, falls im mittleren bis fernen Bereich der Meeresboden Neigungen von mehr als 20° – 40° besitzt.

Aufgrund der Morphologie, der Stärke des Rückstreusignals, sowie der Aktivität der Fluidaustritte wird eine Einteilung der Strukturen in drei Gruppen vorgeschlagen, wobei Übergänge möglich sind. (1) Kuppelförmige Mounds mittlerer Größe besitzen Durchmesser von 700–1000 m sowie Höhen von 50–100 m. Sie sind gekennzeichnet durch eine hohe Rückstreuung, verursacht durch authigene Karbonatbildungen, zeigen eine mäßige Fluidaktivität mit entsprechender chemosynthetischer Fauna. (2) Kleine Mounds mit sehr geringer Morphologie haben Durchmesser von zirka 500 m und stark irreguläre Umrisse. Authigene Karbonatbildungen sind manchmal von Sediment bedeckt, es gibt keine Anzeichen von Erosion. Eine vielfältige Fauna an den Fluidaustritten zeigt eine erhöhte Ausstromrate an. (3) Sehr große und steile Mounds weisen Durchmesser von mehr als 1000 m auf und erreichen Höhen von 150–200 m. Ihre Gipfelplateaus sind häufig bedeckt mit ausgedehnten, mächtigen Karbonatkrusten. In den Sediment-Echolotprofilen ist keine Sedimentbedeckung erkennbar. Faunenvergesellschaftungen sind selten, was eine sehr geringe bis gar keine Fluidaktivität anzeigt. Berechnete Verhältnisse von Mound Volumen zu Grundfläche zeigen keine Gruppierung entsprechend den verschiedenen Mound Typen, sind aber ein gutes Maß, um die Exponiertheit eines Mounds über den umgebenden Meeresboden zu bewerten.

Die Form der Mounds wird stark von erosiven Prozessen geprägt, welche am Kontinentalhang wirken. In der Meeresbodenkarte des Fächerecholotes sind deutlich tief in den Hang eingeschnittene Canyons zu erkennen. Weiterhin sind in den Sediment-Echolotprofilen an

den Canyonwänden gekappte und erodierte Sedimentschichten, sowie ringförmige Gräben um Mound Strukturen zu erkennen. Die Mounds bestehen aus Schlamm und eingelagerten Bänken aus authigenem Karbonat und sind deshalb widerstandsfähiger gegen Erosion als der umgebende weiche Meeresboden. Mit der Zeit bilden sie daher topographische Erhöhungen. Die geoakustischen Daten lassen keine Anzeichen von Schlammvulkanismus erkennen, wie z. B. Schlammströme oder andere Ablagerungen eruptiver Prozesse.

Jedoch zeigen die Sediment-Echolotprofile an manchen Stellen aufdringendes Sediment im flachen Untergrund. Dies wird als (kleinräumige) Sedimentmobilisierung interpretiert. Es wird angenommen, dass die Sedimente durch die Zersetzung von Gashydraten und dabei freiwerdendes Wasser mobilisiert werden. Die Gashydrate ihrerseits werden durch aufsteigendes, wärmeres Fluid aus größerer Tiefe, vornehmlich der Tiefe der Plattengrenze, zersetzt. Tiefgeschleppte Seismik bildet diapirische Strukturen im Untergrund der Mounds bis in eine Tiefe von ~ 400 m unterhalb des Meeresbodens ab, was zu der Annahme führt, dass die Sedimentmobilisierung an der Basis der Sedimente des Kontinentalabhanges erfolgt [Talukder et al., in press].

Die Beobachtungen werden in einem modifizierten Modell der Mound Entstehung zusammengefasst, welches verschiedene, interagierende Prozesse integriert: Episodisch erhöhte Aktivität von Fluidaustritten und damit einhergehende Bildung von authigenen Karbonaten, normale Sedimentationsraten am Kontinentalhang und Subsidenz der Sedimentschichten, sowie Erosion.

Die beiden submarinen Rutschungen, Momotombo beziehungsweise Masaya Rutschung, welche in den aufgenommenen Daten erfasst sind, wurden sehr wahrscheinlich durch eine Übersteilung des mittleren Kontinentalhanges ausgelöst. Diese hatte ihre Ursache in tektonischer Erosion, oder, im Falle der Masaya Rutschung, in einem subduzierten untermeerischen Seeberg auf der abtauchenden Platte. Beide Rutschungen sind charakterisiert durch ein translationales Abgleiten, sowie ein gewisses Maß an Retrogression. Mit den Rutschungen einhergehende Extensionsbrüche dienen sehr wahrscheinlich als Aufstiegswege für Fluide. Das Volumen der Momotombo Rutschung beträgt zirka 10.5 km^3 , das der Masaya Rutschung zirka 7.7 km^3 .

Contents

1	Introduction	1
1.1	Objectives and structural outline of this work	1
1.2	Geologic setting	3
1.2.1	Central America Continental Margin	3
1.2.2	Structure of the forearc	6
1.2.3	Forearc fluid venting	8
1.2.4	Cold seep communities	9
1.2.5	Cold seeps imaged with geoacoustic tools	10
1.2.6	Study area offshore Nicaragua	11
2	Data and Methods	15
2.1	Data acquisition	15
2.1.1	Multibeam Bathymetry	15
2.1.2	IFM-GEOMAR Sidescan Sonar DTS-1	17
2.1.3	Ultra Short Baseline (USBL) Positioning System POSIDONIA	21
2.2	Data processing	22
2.2.1	Processing of EM120 Sounding Measurements with CARAIBES	22
2.2.2	Processing of EM120 Amplitude Measurements with PRISM	23
2.2.3	Processing of Towfish Navigation Data	23
2.2.4	Processing of Sidescan Sonar data	24
2.3	Sediment echosounder data	28
2.3.1	The Parasound System	28
2.3.2	The EdgeTech DTS-1 Chirp Subbottom Profiler	28
2.4	Analysis of seafloor observations	30

3	Mound structures offshore Nicaragua	31
3.1	Introduction	31
3.2	Mound structures in different (tectonic) settings	32
3.2.1	Momotombo Slide Area	36
3.2.2	Central Area upslope Masaya Slide	40
3.2.3	Baula Massive	53
3.2.4	Mound Perezoso & Mound Colibri	57
3.2.5	Mound Ridges	58
3.2.6	Occurrence of gas hydrates and gas flares?	63
3.3	Mound Volume Calculations	65
3.3.1	Methodology	65
3.4	Discussion	69
3.5	Conclusions and outlook	75
4	Influence of topography on sidescan images	77
4.1	Introduction	77
4.2	The backscattering signal	78
4.2.1	Fundamentals	78
4.2.2	Transmission loss	81
4.2.3	Target strength	82
4.2.4	Scattering at an ideal sphere	83
4.2.5	Extended targets	84
4.2.5.1	Surface and volume calculations	84
4.2.6	Models for the reflection and scattering by a rough surface	87
4.2.6.1	Definition of roughness	87
4.2.6.2	Seafloor backscattering	88
4.2.6.3	Lambert's law	90
4.2.6.4	Facet reflection	92
4.2.6.5	Bragg scattering	92
4.2.7	Correcting the backscatter signal for seafloor slope	93
4.3	The DTS-1 angular variation of backscatter	95
4.4	Processing algorithm	101
4.5	The test area	108

4.5.1	Processing the test area	112
4.6	Results and discussion	115
4.7	Conclusions and Outlook	127
5	Canyon system on the continental slope offshore Nicaragua	129
6	Momotombo Slide and Masaya Slide	133
7	Conclusions and Outlook	137
A	Sonar system sediment penetration	139
B	Mound List	141
	Bibliography	149
	List of Figures	157
	List of Tables	161

1

Introduction

1.1 Objectives and structural outline of this work

The amount and mechanisms of volatile and fluid recycling along subduction zones are important parameters for an estimation of their feedback on global climate, and their capability to trigger natural disasters like submarine landslides, earthquakes, and volcanic eruptions. The sites where fluids discharge from the seafloor into the ocean are called *cold vents* or *cold seeps*, due to the fact that their efflux temperature is not significantly different from ocean water, unlike *hot vents* which are based on hydrothermal activity. Cold vents are reported from different tectonic settings since the 1980's [e. g., Suess and Massoth, 1984; Kulm et al., 1986; Sibuet et al., 1988; Jollivet et al., 1990; Paull et al., 1984]. They show various surface expressions and have different driving mechanisms.

The nature of the seep sites offshore Central America is subject of debate. They are often termed mud volcanoes or mud diapirs [Shiple et al., 1990; Moerz et al., 2005; Grevemeyer et al., 2004], but they are also suspected to consist of large amounts of authigenic carbonates [Mörz et al., 2003], which precipitate by the anaerobe oxidation of methane. They can then build chemohierms or form crusts on the seafloor [Kulm et al., 1986]. In backscatter images the carbonates can readily be identified as high backscatter patches, due to their higher surface roughness.

The study within the SFB 574 (*Volatiles and Fluids in Subduction Zones: Climate Feedback and Trigger Mechanisms for Natural Disasters*) investigates an area on the continental slope along the subduction zone offshore Nicaragua with a set of geoaoustic tools. The region is characterized by a high number of so-called mound structures, and is therefore particularly suitable for high-resolution sidescan sonar investigations.

Identification and location of cold vent sites offshore Nicaragua is one goal, to classify them, and to explain their formation and driving mechanisms another. Only a detailed analysis of the geoaoustic dataset allows to understand the link between seep structures and sedimentary processes on the slope, and to understand the role of canyons and slides which are present in the area.

Because the investigated area shows considerable topographic relief, it is important to know, how much of the backscatter signal is due to seafloor slope, and how much is actually due to unusual seafloor roughness, which implies a change in lithology. This information is crucial for a correct interpretation of the data.

The work is therefore structured in the following chapters:

Chapter 1 gives an introduction to the geologic setting of the central american continental margin, and presents an overview of the study area.

Chapter 2 explains data acquisition and data processing.

Chapter 3 summarizes the results of the mound and seep site analysis.

Chapter 4 presents a methodological approach to evaluate the influence of the seafloor topography on the backscatter signal, and applies it to a test area.

Chapter 5 describes briefly the canyon system on the continental slope and shows its contribution to mound formation.

Chapter 6 briefly analyzes two larger slides in the study area, Momotombo Slide and Masaya Slide, respectively, and discusses a possible relationship to seep activity.

Chapter 7 concludes the study and gives an outlook on future work and open questions.

1.2 Geologic setting

1.2.1 Central America Continental Margin

Along the central american pacific margin the *Cocos Plate* subducts at a rate of 85 mm per year under the *Caribbean Plate* (figure 1.1) [DeMets, 2001]. The slightly oblique plate convergence direction relative to the *Middle America Trench* (MAT) results in a dextral strike-slip movement of the forearc region of approximately 14 mm per year to the northwest [DeMets, 2001].

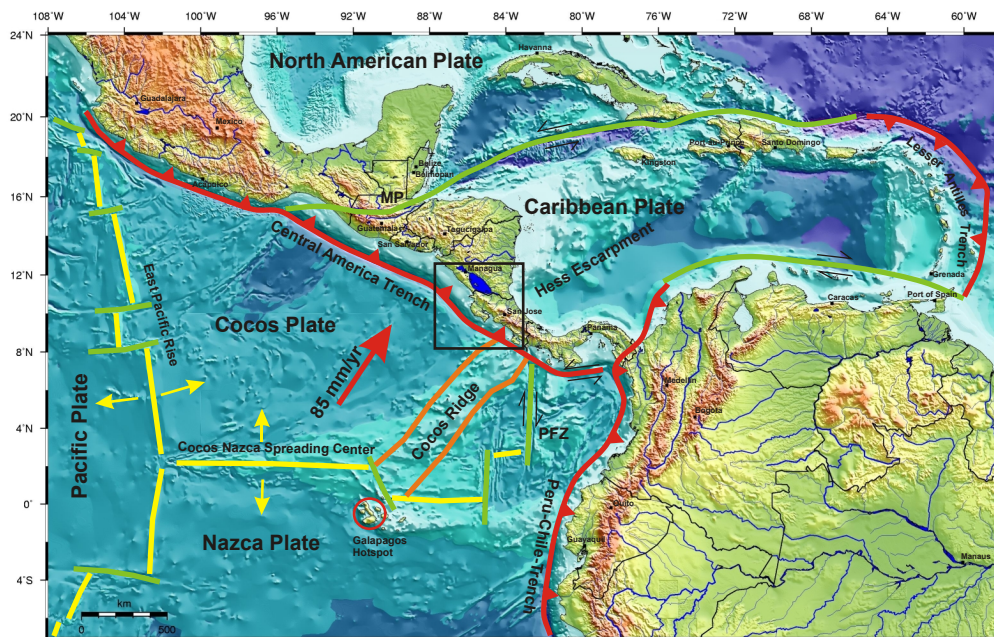


Figure 1.1: General Bathymetric Chart of the Oceans [GEBCO, 2003] with simplified plate tectonic situation of Central America. Thick arrow shows movement of Cocos Plate relative to fixed Caribbean Plate [DeMets, 2001]. Black rectangle marks outline of figure 1.2. PFZ: Panama Fracture Zone; MP: Motagua-Polochic Transform Fault.

The continental Caribbean Plate is made up of several basement blocks. Costa Rica belongs mainly to the *Chorotega Block* and Nicaragua mainly to the *Chortis Block*. The border between these two blocks is assumed to run from the Santa Elena Peninsula in Costa Rica to the Hess Escarpment in the Caribbean [Meschede and Frisch, 1998].

The incoming oceanic Cocos Plate is formed along the east trending *Cocos-Nazca spreading center* (CNS) and the north-south oriented *East Pacific Rise* (EPR). The boundary between these two lithospheric provinces near the continent is called *fracture zone trace* (FZT) and forms a small escarpment entering the trench offshore Nicoya Peninsula [Barckhausen et al., 2001]. The oceanic crust northwest of this boundary is formed at the EPR, to the southeast it is formed at the CNS. The fracture zone itself is thought to be the transform fault along which the former *Farallon Plate* broke down into the Cocos and Nazca Plates approximately 22.7 Ma ago [Barckhausen et al., 2001]. Another im-

1.2. GEOLOGIC SETTING

portant linear feature is a propagator of a transform fault of the (present) CNS which is aligned with the Fisher Ridge and parallels the current convergence vector. Because the spreading rates at the CNS increase eastwards, the Cocos Plate actually rotates counter-clockwise [Barckhausen et al., 2001]. The landward projection of this propagator develops into the *Quesada Sharp Contortion*, a slab tear at a depth of ~ 70 km beneath Central Costa Rica, where the slab dip changes from $\sim 80^\circ$ in the northwest to about $\sim 60^\circ$ in the southeast [Protti et al., 1995]. Above it, the volcanic arc is left-laterally offset across a gap. Another arc volcano offset between Costa Rica and Nicaragua [Carr and Stoiber, 1990] has no counterpart in the Cocos Plate, but seems to reflect major differences in upper plate crustal structure [von Huene et al., 2000]. Based on magnetic anomalies and on morphology, the subducting oceanic crust can be divided into several segments [Barckhausen et al., 2001; von Huene et al., 2000; Ranero et al., 2003, see figure 1.2]:

(1) In the southeast offshore Osa Peninsula approximately 12–20 km thick *Cocos Ridge* crust enters the subduction zone. The ridge is the trace of the *Galapagos hot spot* and forms a morphologic 1.5 km high, broad swell. Due to its thickness and the oceanic fabric inherited from the spreading center running almost perpendicular to the trench, no trench parallel horst and graben structure is observed.

(2) Between Quepos Plateau and Fisher Ridge the *seamount segment* has an approximately 6–7 km thick crust with ages between 15 and 20 Ma. Magnetic anomalies strike oblique to the trench. Faulting parallel to the original fabric from the spreading center occurs within approximately 25 km of the trench axis. Numerous seamounts (approximately 40%) with a Galapagos hot spot geochemical signature, cover the segment.

(3) Northwest of Fisher Ridge up to the fracture zone trace, the seafloor is relatively smooth without any seamounts. This *smooth segment* consists of CNS crust formed during initial breakup of the Farallon Plate, and has ages between 20 and 23 Ma. The smoothness is explained with high spreading rates during an early phase of CNS opening [Barckhausen et al., 2001]. The crust is 5–7 km thick and breaks into few small-offset normal faults trending subparallel to the axis of flexure and essentially perpendicular to the magnetic anomalies.

(4) The EPR crust to the northwest of the FZT and offshore Nicaragua is approximately 5–6 km thick with magnetic anomalies striking parallel to the trench, and ages of 24 Ma at the trench. With bending of the incoming oceanic crust, pervasive normal faulting occurs. The width of the faulted region increases from about ~ 25 km in the southeast to ~ 60 km in the northwest offshore Nicaragua, while individual fault throws increase from ~ 100 m to ~ 500 m, respectively. The number of seamounts on the oceanic plate increases again to the northwest and reaches offshore Nicaragua one of the highest densities worldwide [Berhorst, 2006]. Due to continuous occurrence of mound structures along the middle to upper continental slope, the segment is also referred to as the *mound segment* on the overriding plate [Sahling et al., *subm.*].

The sediment coverage on the oceanic crust generally decreases to the northwest from about 400 m in the area of ODP leg 170 to only 250–300 m offshore Nicaragua [von Huene et al., 2000], and consists of siliceous hemipelagic sediments overlying pelagic calcareous ooze.

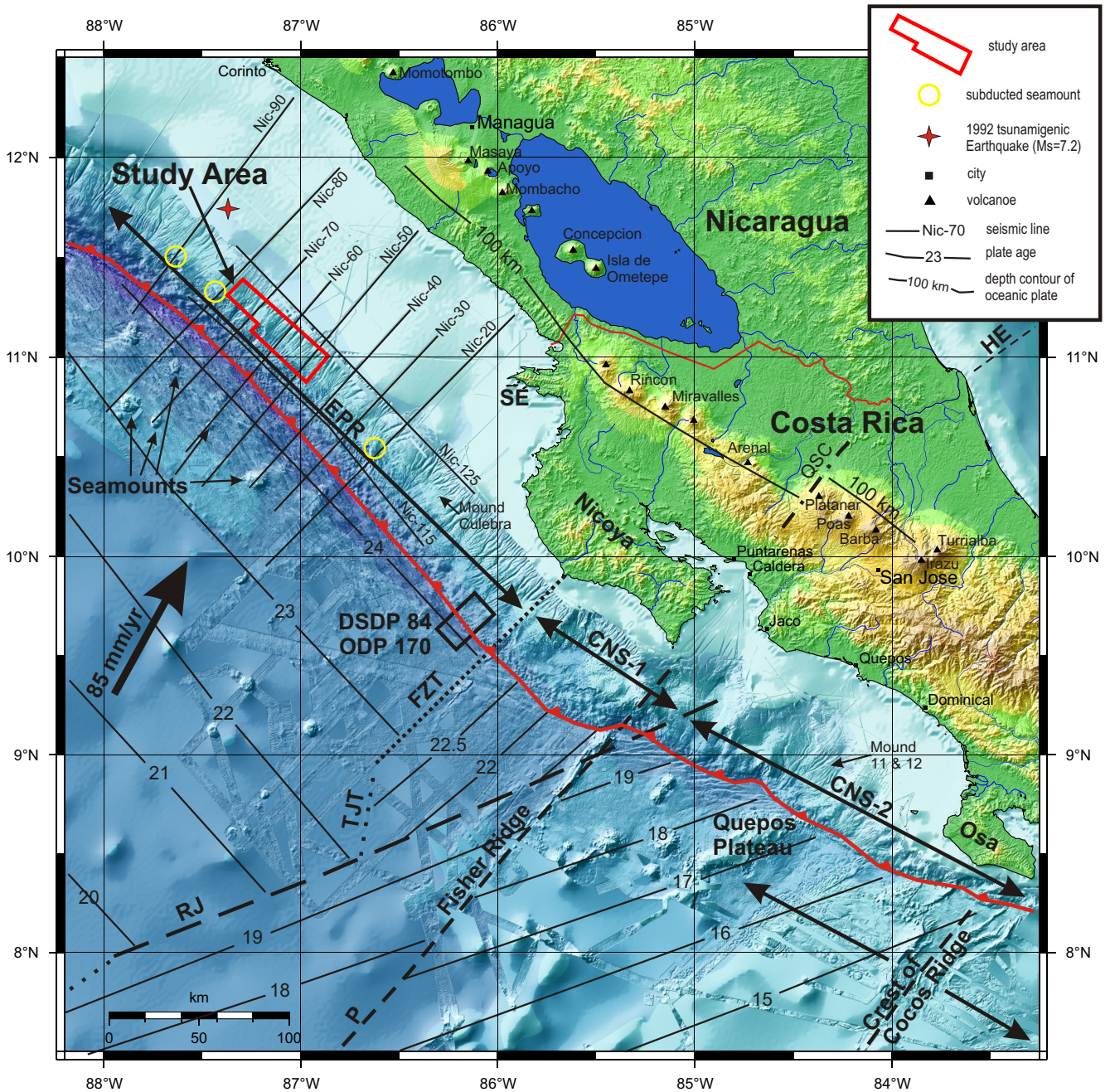


Figure 1.2: High-resolution bathymetry merged with GEBCO data at sea and SRTM-90 data on land along the Central America Pacific Margin with location of study area. Major tectonic elements and Cocos Plate segmentation after von Huene et al. [2000]; Barckhausen et al. [2001], plate ages in million years from Barckhausen et al. [2001]. Convergence vector of Cocos Plate after DeMets [2001]. Seismic lines offshore Nicaragua and location of 1992 tsunami earthquake and subducted seamounts from McIntosh et al. [submitted, 2005]. EPR: East Pacific Rise; CNS-1: initial CNS crust from 22.7–19.5 Ma; CNS-2: CNS crust between 19.5–14.5 Ma; FZT: Fracture Zone Trace; TJT: Triple Junction Trace; RJ: Ridge Jump; P: Propagator; QSC: Quesada Sharp Contortion; DSDP/ODP: Deep Sea Drilling Project/Ocean Drilling Program; HE: Hess Escarpment; SE: Santa Elena Peninsula.

During early research the convergent margin off Costa Rica was considered to be built by accretion of sediment from the oceanic plate against the volcanic arc and forearc [Shipley et al., 1990, 1992; McIntosh et al., 1993]. Drilling during Deep Sea Drilling Project (DSDP) leg 84 instead recovered Mesozoic ophiolitic rocks offshore Guatemala [Auboin and von Huene, 1985], and detailed geophysical studies during RV Sonne cruises SO-76 and SO-81 on the Costa Rica margin supported the interpretation that the margin wedge represents the offshore continuation of the ophiolitic rocks exposed onshore [Flueh et al., 2000]. Interpretation of seismic images of the forearc wedge and further drilling during Ocean Drilling Program (ODP) leg 170 offshore Nicaoya Peninsula led to a tectonic model of subsidence and extension due to tectonic erosion, proposing a landward migration of the Nicoya coastline [Meschede et al., 1999]. Recent seismic cross-sections from Costa Rica to Nicaragua indicate that the process of tectonic erosion is active along most of the Middle America convergent margin [McIntosh et al., submitted, 2005]. Two mechanism of basal erosion are identified: erosion by seamount tunneling, and removal of large rock lenses by bifurcation and an upward jump of the plate boundary [Ranero and von Huene, 2000; Flueh et al., 2000]. The mechanism of the erosion of large rock lenses is modified and explained in more detail with a generic model of subduction erosion [von Huene et al., 2004a]. It proposes that a frontal prism elevates the pore-fluid pressure in the trench sediments, which in turn reduces the décollement friction and allows a complete subduction of the sediments. The overpressured fluids penetrate from the lower plate into extensional fractures on the base of the upper plate. The resulting hydrofracturing separates pieces from the hanging wall and drags them into the subduction channel. As a consequence the plate interface thrust migrates upward, leading to thinning of the upper plate and subsidence of the slope. But not only the pore waters of the subducted sediment, which are partially expelled already at shallow depths along the décollement [Silver et al., 2000], also water released through clay-mineral dehydration at a certain depth- and temperature interval, like the transformation from smectite to illite, contribute to the increase of the pore pressure and the hydrofracturing [Hensen et al., 2004, see figure 1.3].

1.2.2 Structure of the forearc

The structure of the forearc region as revealed through drilling and seismic sections is characterized by a basement margin wedge of ophiolitic material with high seismic velocities [Walther et al., 2000]. Its upper rough surface marks a major unconformity, and forms the *base of the slope sediments* [Flueh et al., 2000]. It is explained by tilted block structures in an extensional domain [Meschede et al., 1999]. Offshore the Nicoya Peninsula in Costa Rica the thickness of the sedimentary slope apron increases from ~ 500 m on the lower slope up to ~ 2000 m on the upper slope [Kimura et al., 1997]. Off Nicaragua the continental slope is ~ 55 km wide and can be divided into a gently dipping upper slope ($\sim 2.5^\circ$) with an approximately 1500 m thick sediment cover, a narrow middle slope, steepening to $\sim 17^\circ$ dip and a sediment cover of less than 1000 m, and a lower slope dipping $\sim 6^\circ$ and a thin sediment cover of ~ 500 m [Ranero et al., 2000a]. At the

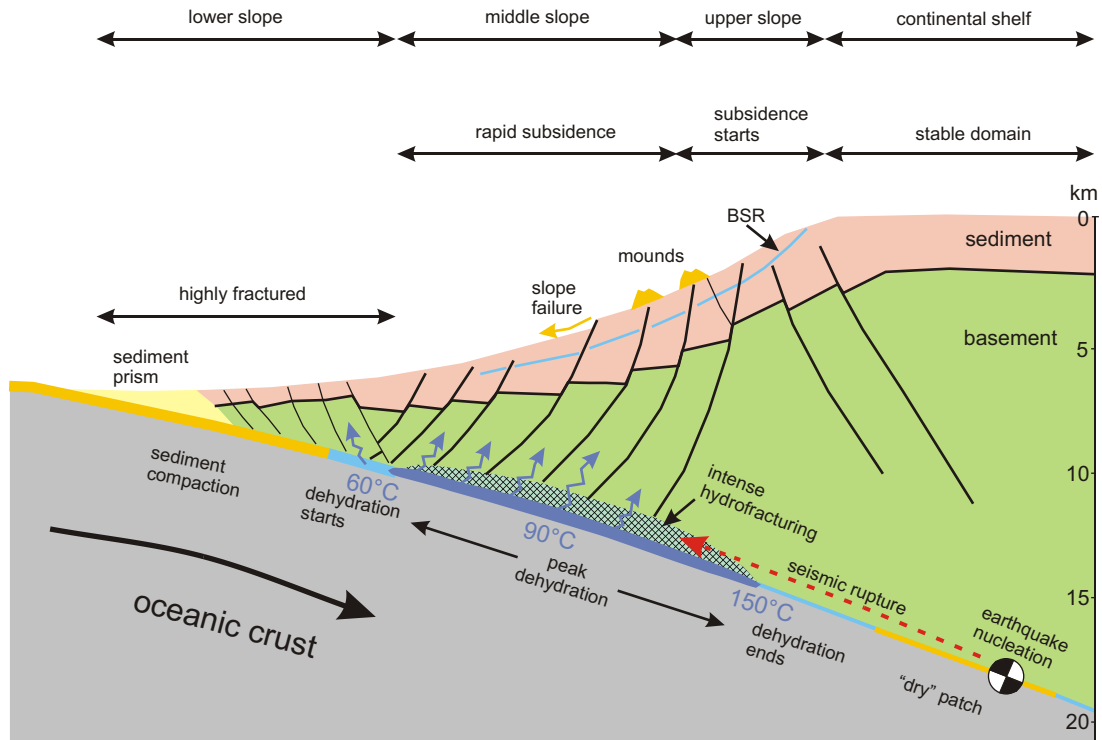


Figure 1.3: Tectonic model of an erosional convergent margin showing the relationship between fluid flow, tectonics and earthquake generation away from subducting seamounts. Sediment in the subduction channel loses pore water rapidly by compaction underneath the lower slope. At around 60°C dehydration reactions start to release water chemically bound in the sediments. Water release continues up to 150°C where all the water has been depleted from the sediment. The released water leads to intense hydrofracturing and tectonic erosion of the upper plate beneath the middle slope where normal faulting and rapid subsidence take place. The fluids can rise from the plate boundary along deep-reaching faults, leading to fluid venting and the formation of mound structures on the middle slope. The subsidence across the middle slope leads also to mass wasting processes. Underneath the continental shelf, where little fluid is present at the plate boundary and the upper plate is competent, ‘dry’ patches may become nucleation asperities of large earthquakes that may rupture into the area of fluid release (redrawn from SFB574 [2003]).

base of the slope a small frontal prism consisting mainly of reworked slope sediments has developed [von Huene et al., 2000]. Here the extensional structures are overprinted in a compressional domain [Meschede et al., 1999]. The backstop of the prism is not a sharp interface but a transition to higher consolidated material with higher seismic velocities. The base is defined by the detachment reflection. Beneath the detachment, thick underthrust sediment sequences of the incoming oceanic plate cut by normal faults are imaged. The prism is probably stable at the present taper ($\sim 10^{\circ}$) and 3–10 km width, only temporarily removed across gaps by subducting relief [von Huene et al., 2000].

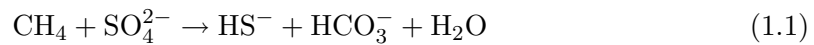
1.2.3 Forearc fluid venting

Forearc fluid venting was first discovered in the 3-D seismic survey area offshore Nicoya Peninsula in structures interpreted as mud volcanoes [Shipley et al., 1990, 1992]. Seafloor observations during *D.S.R.V. Alvin* dives revealed the presence of chemosynthetic communities and authigenic carbonates [Kahn et al., 1996; McAdoo et al., 1996]. Further evidence for widespread fluid expulsion along the Pacific margin off Costa Rica was documented with seafloor observations and water column measurements during RV Sonne cruise SO-144 at landslides, the headwalls of seamount subduction related scars, faults, and mid-slope mud volcanoes [Bohrmann et al., 2002]. Work of the SFB 574 showed that these methane seeps occur not evenly distributed along the slope but as a band at a certain zone (28 ± 8 km) landward from the trench [Sahling et al., *subm.*]. This observation is in agreement with the early descriptions, whereas the most vigorous and focused fluid flow systems are found in the mid-slope region [Kahn et al., 1996; McAdoo et al., 1996; Shipley et al., 1990]. Underthrust sediments of the oceanic plate decrease rapidly in thickness with depth and dewater along bedding parallel permeabilities and the décollement at shallow depths before the deformation front [Silver et al., 2000; Shipley et al., 1990], but leading to a more diffusive flow through the frontal prism sediments [McAdoo et al., 1996]. During further subduction behind the deformation front, dewatering is inhibited through the decreased porosities and permeabilities [Screaton and Saffer, 2005]. Geochemical and isotopic analysis of pore waters expelled at Mound 11, a mound in the mid-slope region, proved that the source of the fluids, depleted in Cl and enriched in B, are clay-mineral dehydration reactions within the subducted sediment at depths of ≥ 12 km in a temperature range between 85 and 130° C [Hensen et al., 2004]. The fluids then migrate upward through deep-seated faults imaged in seismic sections [Hensen et al., 2004; Shipley et al., 1990]. Besides the circulation system consisting of the margin wedge, the décollement, and the underthrust sediment section, another system is proposed in the basement of the incoming plate beneath the oceanic sediments, that could explain the extremely low conductive heat flow values of 14 mW/m² in average as observed on the Cocos Plate off the central Nicoya Peninsula [Silver et al., 2000; Langseth and Silver, 1996]. To the northwest the heat flow on the oceanic plate increases to about 105 mW/m² and correlates roughly with the expected heat flow anomaly of a 24 Ma old plate, probably due to a different structure of the plate and less heat mining through a hydrothermal system [Grevemeyer et al., 2004]. At mid-slope Mound Culebra heat flow measurements showed an increase of 10–20 mW/m² compared with the regional conductive background heat flow of 25–30 mW/m² on the margin wedge, interpreted as a sign of focused fluid flow [Grevemeyer et al., 2004].

1.2.4 Cold seep communities

The presence of authigenic carbonates and dead or living vent fauna, or a methane enrichment in the water column can serve as an indication of past or ongoing cold fluid seepage from the seafloor into the ocean [Kulm et al., 1986]. An early description of cold vent communities in the subduction zone off Oregon where the methane is transported by expelled pore fluids, is given by Suess et al. [1985]. The communities described, consisted of siboglinid tube worms, giant white vesicomyid clams, and solemyid mussels. *Siboglinidae* is a family of annelid worms whose members made up the former phyla *Pogonophora* and *Vestimentifera*, terms which can be read often in earlier literature. Additionally mat-forming bacteria are indicative of strong fluid flux from below [Sahling et al., 2002]. On the Hydrate Ridge offshore Oregon, the different organisms are characteristic species for different benthic communities, which show a zonation pattern around gas hydrate occurrences. The zonation is mainly related to the amount of sulfide flux from sediments underneath with bacterial mats settling on top of the strongest fluxes [Sahling et al., 2002].

Both, the occurrence of chemosynthetic fauna and the precipitation of authigenic carbonates depend largely on a process called *anaerobic oxidation of methane* (AOM). It involves *oxidation* of upward flowing methane and *reduction* of seawater sulfate, in a zone where these two constituents mix, simplified by equation 1.1 [Ritger et al., 1987]:



Due to energetic reasons this reaction must be mediated by a microbial syntrophic consortium of methanotrophic archaea and sulfate-reducing bacteria [Boetius et al., 2000]. The released hydrogen sulfide is then feeding the chemosynthetic communities, either directly like the mats of the filamentous giant sulfide-oxidizing bacteria, or indirectly like the heterotrophic bivalve and tubeworm communities, which harbor sulfide-oxidizing bacteria as endosymbionts in their gills or body [Boetius and Suess, 2004]. At high rates of methane flux the AOM is located directly underneath the sediment surface and the produced sulfide can be used by the surface covering bacterial mats, bridging the close distance between the sulfide enriched sediment and the O_2 - and NO_3^{2-} -rich bottom waters. For the clam and tubeworm communities the high sulfide concentration would probably be toxic. At cold seeps with lower methane fluxes the AOM is located deeper in the bottom sediments and the sulfide concentrations are lower. The symbiotic clams, mussels, and tubeworms have developed distinct physiological adaptations to provide their symbionts with oxygen from the seawater and sulfide from the sediments [Boetius and Suess, 2004]. The clams can take up the sulfide over their foot, whereas the tubeworms settle with their root in the sulfide rich zone and their upper part reaches into the oxic seawater. Besides the anaerobic oxidation, it is also possible that the methane is directly oxidized by oxygen (*aerobe oxidation of methane*). But this process seems to be of minor importance in marine sediments, due to the fact that methane rarely comes into direct contact with oxygen, and because the concentration of oxygen in the seawater is very low compared with sulfate.

A further effect of high rates of AOM is the *precipitation of different carbonate minerals* including calcite, aragonite, and dolomite [Ritger et al., 1987]. Several factors may induce the precipitation: An increase in *alkalinity* resulting from AOM, a decrease in $\sum \text{CO}_2$ solubility resulting from a pressure decrease during fluid escape, and/or an addition of $\text{Ca}^{2+}/\text{Mg}^{2+}$ ions from seawater [Ritger et al., 1987]. The carbonate precipitation occurs below the oxic layer, usually no deeper than several centimetres to a few metres below the seabed [Ritger et al., 1987]. But sometimes the authigenic carbonates can build structures reaching above the seabed which are called then “chimneys” or “chemoherms” [Ritger et al., 1987; Teichert et al., 2005]. Such build-ups seem to grow into the oxic zone of the bottom water, which would be contradictory to the process of carbonate precipitation being strictly anaerobic. An explanation is that the precipitation of the carbonates proceeds in anoxic conditions which exist just below bacterial mats. This shows how microbial life can modify the chemical environment at seep locations [Teichert et al., 2005]. Another example for such local modifications of the environmental conditions by microbes is the occurrence of authigenic carbonates below the *carbonate compensation depth* (CCD) [Greinert et al., 2002a].

1.2.5 Cold seeps imaged with geoaoustic tools

The only appropriate tools for mapping deep-water seeps over large areas are multibeam bathymetry and sidescan sonar systems [Weinrebe and Klaucke, 2005]. Features characterized by an entrainment of solid material by the escaping fluids like mud volcanoes or mud diapirs have a significant morphological expression on the seafloor and hence can be detected with bathymetry measurements. At other sites, however, the fluids just seep through the seabed and do not entrain solid material. Such seeps are often relatively small and usually do not show a morphological relief but are often associated with carbonate precipitates and chemosynthetic communities. For the detection of these features, sidescan sonar systems (surface- or deep-towed), at various frequencies and resolutions, are the perfect tools, because the carbonatic rocks create a stronger backscattering signal due to their higher roughness [Carson et al., 1994; Johnson et al., 2003]. The carbonate precipitates even do not have to outcrop at the seafloor but may be covered with sediment of various thickness depending on the acoustic frequency of the system, because the sonar signal penetrates a certain distance into the sediment [Mitchell, 1993]. Unfortunately authigenic carbonates do not proof current seep activity but may be just archives of past activity. That determination requires either direct seafloor observations, or the acoustic detection of a gas plume (a so-called *flare*) in the water column. Processing these sidescan sonar data allows then a relation of the possible flares to specific seep locations on the seafloor [Klaucke et al., 2005]. A further advantage of bathymetric and sidescan sonar measurements in general is, that the knowledge of the morphology and exact location can be used for a save and precise deployment of lander systems, TV-guided devices and submersibles [Greinert et al., 2002b].

1.2.6 Study area offshore Nicaragua

The study area is located approximately 90 km off the coast of Nicaragua between $10^{\circ} 50' N$ and $11^{\circ} 25' N$ latitude and $86^{\circ} 50' W$ and $87^{\circ} 25' W$ longitude, respectively. The length parallel to the slope is about 60 km and the largest width ~ 20 km, covering an area of approximately 980 km^2 at the middle continental slope in a water depth between 800 m and 2600 m. The area ranges from 20 km to 40 km distance landward from the trench, which is 5200 m deep at this segment of the MAT. The incoming oceanic plate has a rough topography and a 200–300 m thick sediment coverage [Ranero et al., 2000a].

Based on the shaded relief map, the area can be divided into three segments with different morphologies and structures (figure 1.4): (1) An area of slides and large mound structures in the north, (2) an area dominated by slope canyons and mound ridges in the central, and (3) an area showing many normal faults in the south. The north is relatively smooth with several mounds and two prominent, large submarine slides. The headwall of Momotombo Slide is in about 1650 m water depth, that of Masaya Slide in about 1850 m. The width of the slides is 3.5 to 4 km and up to 5 km, respectively. Around the rim of Momotombo Slide, three mound structures have been imaged, two of them are very close to the headwall, which averages 40 to 50 m in height, but reaches up to 90 m in some places. The mounds reach 750 to 950 m in diameter and show a flat upslope and a steep downslope side. The height difference to the surrounding slope is approximately 30 m upslope and up to 120 m downslope. Masaya Slide shows headwalls of about 100 to 150 m height. Upslope of the slide several mounds are visible. In the shallowest part some very large (~ 1100 m diameter, 90–150 m height) and probably old and inactive mounds can be seen. Further down the slope a number of smaller (~ 250 –800 m diameter, 20–80 m height) and probably younger mounds can be identified in both, the bathymetry and the sidescan sonar data (figure 1.6).

The central part of the study area starting just south of Masaya Slide is dominated by deeply incised canyons. Their relief varies between 40 to 60 m and up to 100 m in the southern, larger canyon. The width of the canyon floor varies between 200 and 400 m. They show a dendritic to parallel pattern. Remarkable are some mounds in the south of this segment. They seem to be located on cross-slope trending ridges and oriented linearly, showing diameters of 500 to 600 m and heights between 60 and 70 m.

In the southern segment at the greater depths bathymetry and sidescan image show several normal faults. Their morphological relief is up to 40 m in height.

Very clearly can these structures be identified in a gradient map derived from the *Digital Elevation Model* (DEM) of the seafloor (figure 1.5).

The location of other data relevant for this study, published or still in the focus of research, is shown in figure 1.2. There are especially two intensively investigated mound structures further south, Mound Culebra and the group of Mound 11 & 12, respectively, which can be used for comparison. Mound Culebra is a large mound on the middle slope in approximately 1630 m water depth, facing also incoming EPR oceanic crust like the mounds in the study area offshore Nicaragua. A detailed structural study including

1.2. GEOLOGIC SETTING

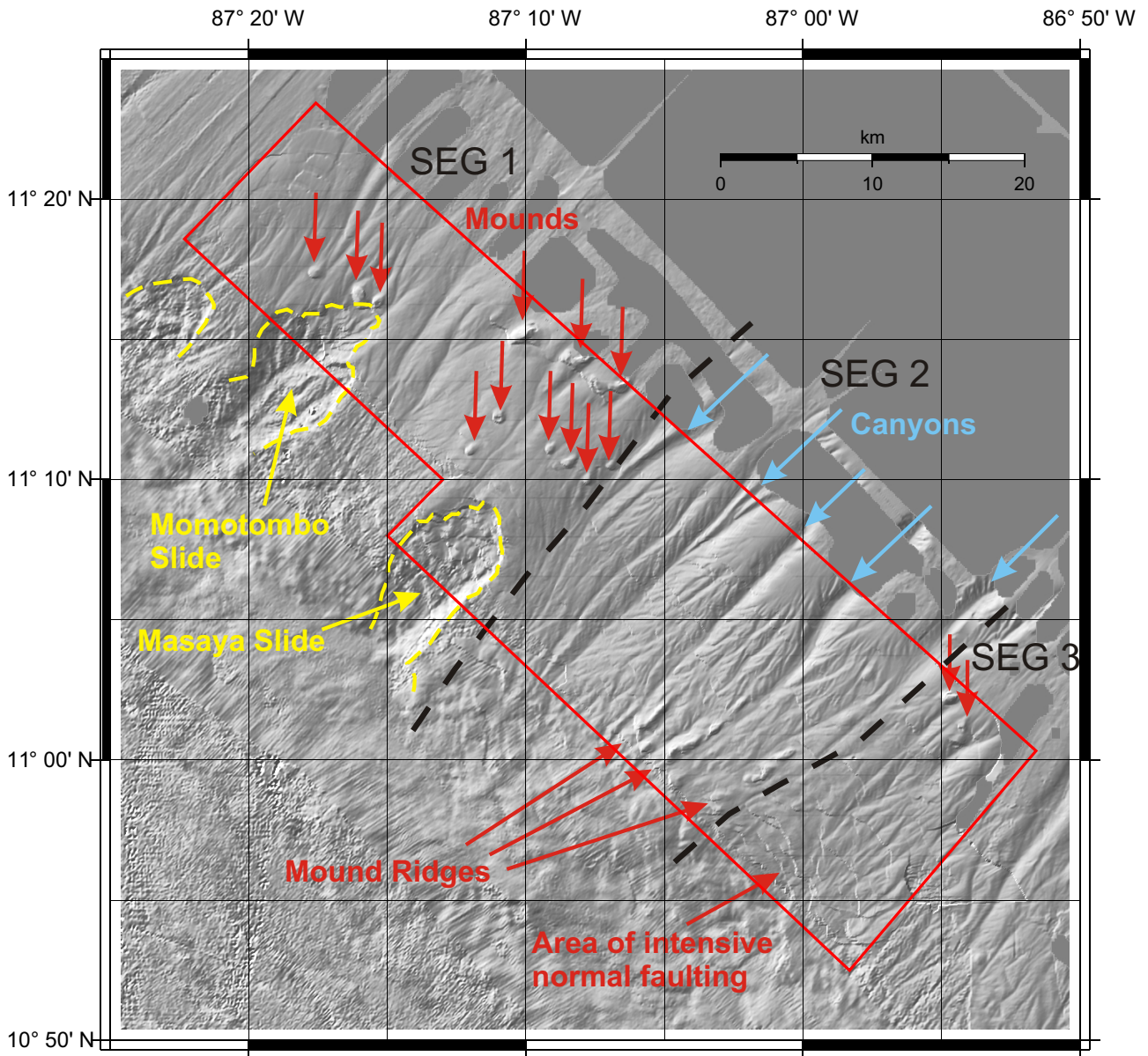


Figure 1.4: Shaded relief map of the study area offshore Nicaragua. The red box marks the area of the high-resolution sidescan sonar survey. Note that bathymetry acquired during this survey is better than outside from earlier cruises. Mound structures have a knoll-like morphological expression, high backscatter patches are not recognizable in the bathymetry. The area can be divided roughly into three segments, separated in the figure by black dashed lines: (1) The northern segment shows a smooth seafloor and is dominated by mound structures and two large slides. (2) In the middle segment the slope is characterized by deeply incised canyons. In their lower part they seem to border three “mound ridges”. (3) In the deeper part of the southern segment many normal faults cut the slope. Only two mounds in the upper corner can be observed.

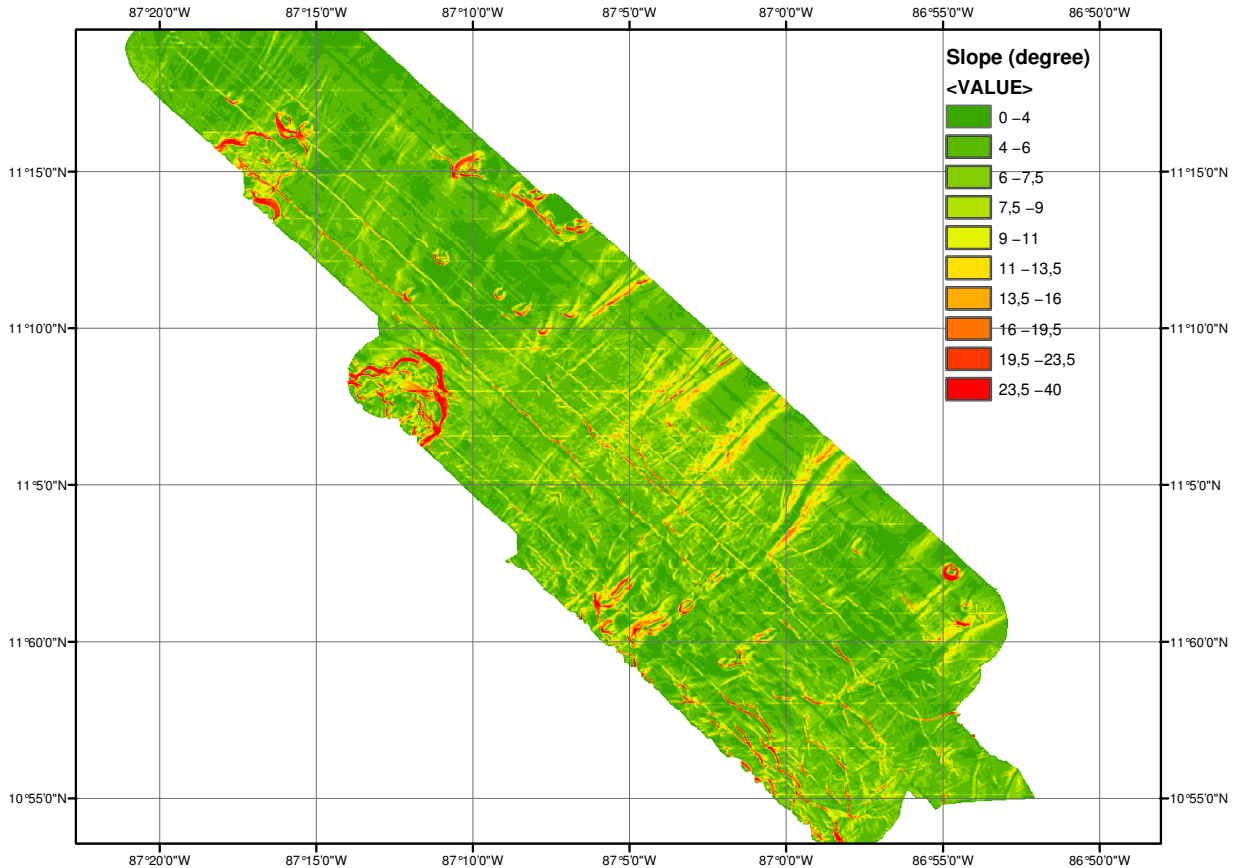


Figure 1.5: Gradient map of the survey area offshore Nicaragua. It delineates the steep downslope flanks of the mound structures, the headwall of the two slides and the side walls of the deep incised canyons. In the southern part many normal faults can be identified.

bathymetric and Multi-Channel Seismic (MCS) data has been performed recently by [Fekete, 2006]. Mounds 11 & 12 are situated offshore central Costa Rica on the continental slope opposite the seamount segment of the incoming CNS-2 oceanic crust. They show much less morphological relief than Mound Culebra but a much higher fluid venting activity and are suspected to be of a different type. New results from high-resolution sidescan sonar data will soon be published by Klaucke et al. [subm.].

The location of seismic reflection profiles offshore Nicaragua from *R/V Maurice Ewing* (EW00-05) cruise, indicated by black lines in figure 1.2, are taken from McIntosh et al. [submitted, 2005]. Unfortunately the profiles Nic-60 and Nic-70 are not yet published. Line Nic-20 is investigated in Berhorst [2006]. The location of the identified subducted seamounts and the 1992 tsunami earthquake are taken from McIntosh et al. [submitted, 2005].

1.2. GEOLOGIC SETTING

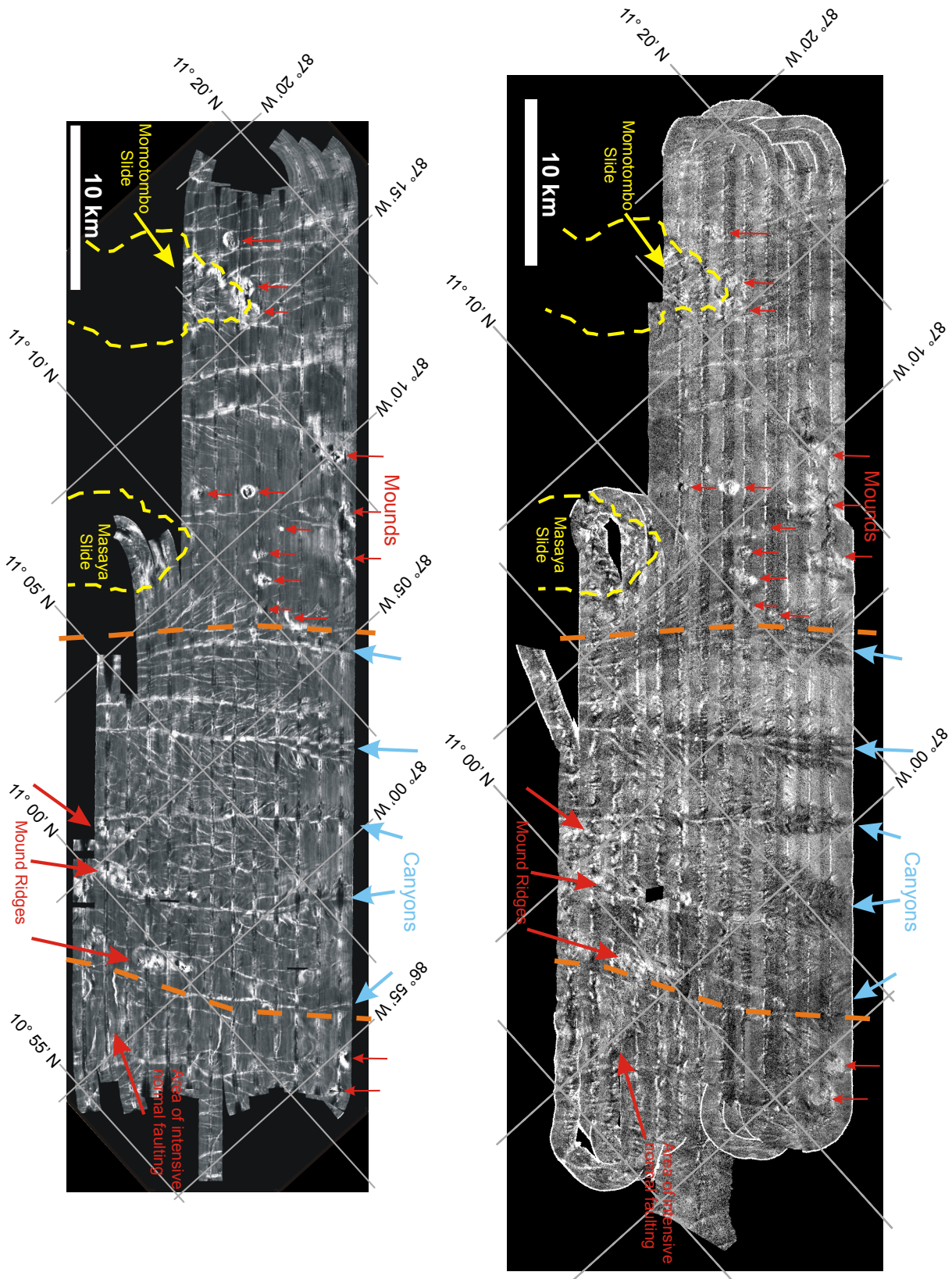


Figure 1.6: Amplitude data of the hull mounted *Simrad EM-120* multibeam system processed for a pixel size of 20 metres (top) and sidescan sonar mosaic acquired with the deep-towed *IFM-GEOMAR DTS-1* processed for a pixel size of 1 metre (bottom).

2

Data and Methods

2.1 Data acquisition

The geoacoustic dataset was acquired between 31. July and 05. August 2003 during *R/V Sonne* cruise SO173 leg 1, on the Pacific continental margin offshore Nicaragua [Flueh et al., 2004]. The cruise was one of a series of cruises to the Central American convergent margin within the framework of the ‘Sonderforschungsbereich 574’, which was established in 2001 as a long-term cooperative research center at the University of Kiel. The objectives of the cruise were to collect a wide range of geophysical data such as standard MCS, high resolution deep-tow seismic and sidescan sonar information to aid further planning and sedimentological, geochemical, and biological sampling [Flueh et al., 2004]. Subject of this study are the bathymetric, deep-towed sidescan sonar and sediment echosounder data from the newly investigated area offshore Nicaragua. For ground truthing seafloor observations with a video sled system and coring acquired during SO173 legs 3 and 4 were used. The data of the deep-tow seismic streamer system which were recorded simultaneously with the sidescan data, are analyzed elsewhere [e. g. Breitzke et al., 2003; Talukder et al., in press].

The survey offshore Nicaragua consists of 13 slope-parallel, high-resolution deep-towed sidescan sonar profiles, acquired with the *IFM-GEOMAR DTS-1* system, and simultaneously recorded multibeam data of the hull-mounted *SIMRAD EM-120* system onboard *R/V Sonne* (see figure 2.1).

2.1.1 Multibeam Bathymetry

The full-range multibeam echosounding system EM120 from Kongsberg/Simrad onboard *R/V Sonne* provides accurate depth and amplitude measurements of 191 beams to a depth of up to 11.000 metres. The system consists of two transducer arrays (transmitter/receiver) fixed on the hull of the ship. The EM120 operates with successive, frequency-coded acoustic signals (chirp) from 11.25–12.60 kHz with a maximum ping rate of 5 Hz. The data acquisition is based on successive emission-reception cycles of this signal. The emission beam covers up to 150° across-track, and 2° along-track. The reception is obtained from 191 overlapping beams, with beam angles of 2° across-track and 20° along-track. The beam spacing can be chosen to be equidistant (default) or equiangular, and the maximum seafloor coverage can be set to be fixed or automatically adjusted. The echoes from the intersection area ($2^\circ \times 2^\circ$) between the transmission and the reception patterns produce a signal from which depth and reflectivity are extracted [Flueh et al., 2004, p. 51].

2.1. DATA ACQUISITION

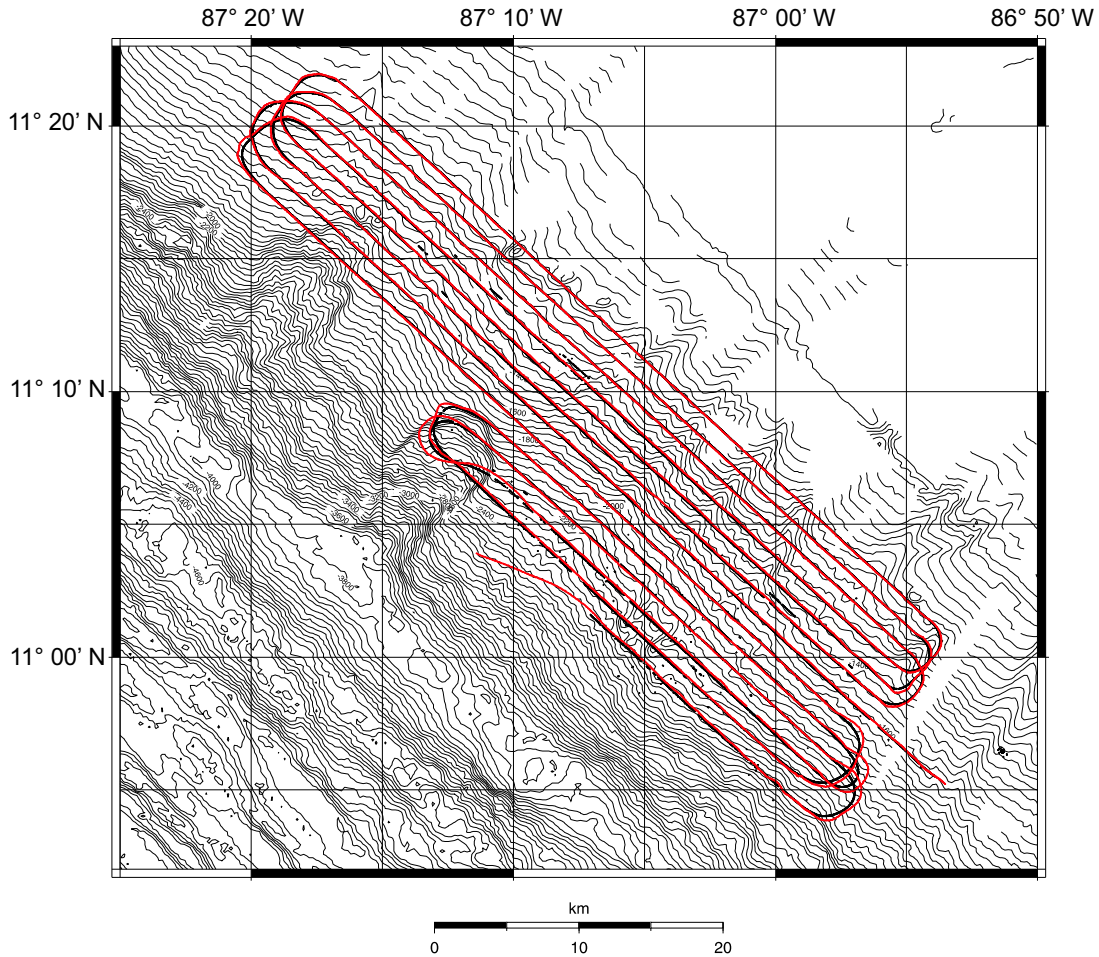


Figure 2.1: Towfish track of deep-towed sidescan sonar survey offshore Nicaragua during R/V Sonne cruise SO173/1. Black line represents POSIDONIA towfish positioning, red line is calculated towfish position with program *wireout* from software package PRISM [Le Bas, 2002]. The program calculates from the ships navigation and the actual cable length the position of the towfish, assuming an inertial behaviour.

Knowing the two-way travel time and the beam angle for each beam, and considering the ray bending due to refraction in the water column by sound speed variations, 191 isolated depth values can be calculated perpendicular to the ships track. The bottom detection is performed using a combination of amplitude (for the central beams) and phase (for the lateral beams), providing a measurement accuracy practically independent of the beam pointing angle [Flueh et al., 2004, p. 51]. Besides the depth measurements the amplitudes of the signal can be used to provide information of the seafloor nature and texture.

For locating the beams geographically on the seafloor the precise position information of the ship (latitude, longitude, altitude with respect to a reference level), which is provided

by the ASHTEC D-GPS system with an accuracy better than 5–10 metres in the area offshore Costa Rica [Flueh et al., 2004, p. 51], and the data from a motion reference unit in the center of the ship are combined.

During the deep-tow survey offshore Nicaragua the opening angle of the EM120 system was reduced to $2 \times 15^\circ$. In combination with the slow ship speed of max. 3 knots this enabled a good data quality [Flueh et al., 2004, p. 97].

2.1.2 IFM-GEOMAR Sidescan Sonar DTS-1

The IFM-GEOMAR DTS-1 deep-towed sidescan sonar system (figure 2.2) is a modified *EdgeTech Full-Spectrum* sonar, deployable to a maximum water depth of 6.000 metres. It operates with a chirp signal of 75 kHz or 410 kHz centre frequencies. The 75 kHz pulse used during this survey has a bandwidth of 7.5 kHz and a duration of 14 ms. The range in this mode was set to 750 metres, with a total swath width of 1500 metres. The line spacing of the survey was ~ 1200 metres, leading to an overlap of 300 metres, which prevents data gaps due to navigational uncertainties. The incoming signal is split into 13.300 samples resulting in a maximum across-track resolution of 5.6 cm. A ping repetition rate of 0.98 Hz (or 1.020 s interval) and a towing speed of 2.5–3.0 knots enable an along-track resolution of 1.3–1.5 metres.

In addition to the sidescan sonar sensors the DTS-1 system is equipped with a chirp subbottom profiler. During the survey it was operated in the 2–10 kHz mode with a pulse length of 20 ms, leading to a nominal vertical resolution of approximately 10 cm. The practical vertical resolution is estimated to be in the order of 40 cm, and the sediment penetration is approximately 30–40 metres below the seafloor. The sidescan sonar and the subbottom profiler are run in the coupled trigger mode, with the sidescan being the master trigger. Connected to the sonar electronics via a serial port is a *Honeywell attitude sensor* providing information on heading, roll and pitch of the towfish.

The towfish contains two titanium pressure vessels, one for the sonar electronics (*FS-DW*) and one for the underwater part of the telemetry system (*SEND DSC-Link*) and the Linux-based Bottom-PC (*SEND*) of the seismic streamer data acquisition system (figure 2.4). Mounted to the towfish are also a releaser, capable to work with the USBL positioning system POSIDONIA (*IXSEA-OCEANO*) with a separate receiver head, and an emergency flash and radio beacon (*NOVATECH*). The optional forward-looking sonar was removed during this cruise for a better balance of the towfish in the water (figure 2.2).

The towing configuration of the deep-towed sidescan sonar and streamer system is shown in figure 2.3. The system is connected to the termination of the deep sea cable via the depressor weight (2 tons) through a 40 m long umbilical cable. The wiring can be coaxial or fibre optic, depending on the available winch cable on the ship. The depressor weight ensures that the system is kept close to the seafloor and the towing ship. The elevation above the seafloor can be regulated by giving out or pulling in the sea cable and varying the ships speed. In the 75 kHz mode the appropriate distance to the seafloor is around 80–110 metres.

2.1. DATA ACQUISITION

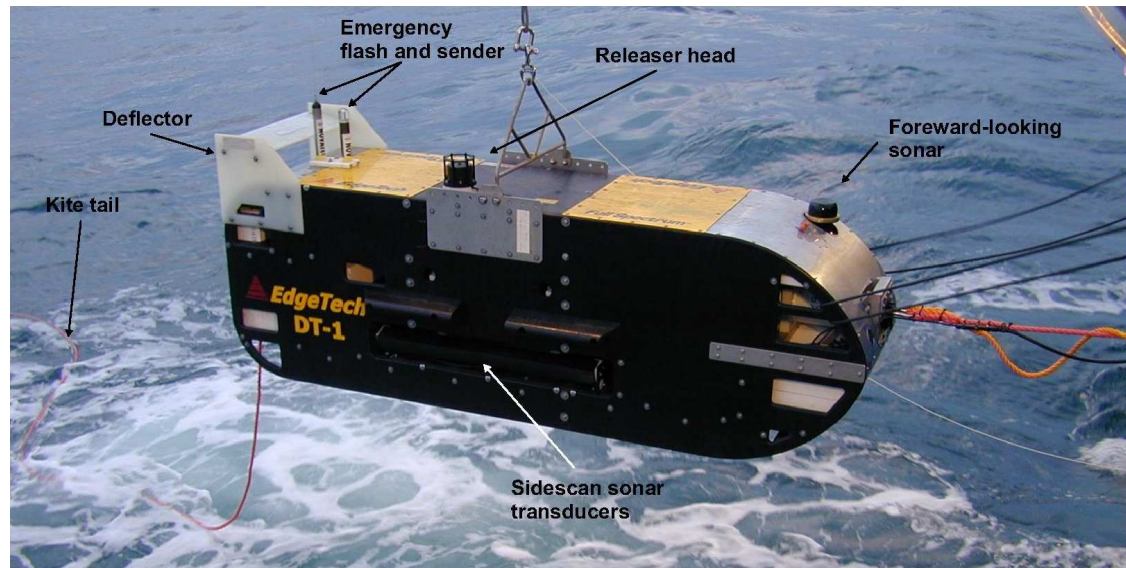


Figure 2.2: IFM-GEOMAR sidescan sonar system DTS-1. The acoustic pulses are transmitted to the port and starboard side by the sidescan sonar transducers. The forward-looking sonar was not mounted during this survey. Size of towfish is $2.8\text{ m} \times 0.8\text{ m} \times 0.9\text{ m}$ (L×W×H). The weight is about 700 kg.

The deep-tow recording and control system consists of components set up in the laboratory of the ship and components housed inside the towfish (figure 2.4). They are connected via the coaxial or fibre optic deep sea cable with the ‘dry’ and ‘wet’ end of the telemetry system (*SEND*), which handles the data transfer and provides all necessary power supplies for the underwater electronics. In the pressure vessel housing the bottom part of the telemetry system there is additionally the Linux-based Bottom-PC having the deep-tow streamer connected to a special streamer network card. A second pressure vessel houses the Full-Spectrum Deep Water (*FS-DW*) part of the sidescan sonar system.

At the top side part the Linux-based Top-PC allows control of the deep-tow seismic streamer and serves as a gateway to the bottom part. An additional PC running the Geometrics StrataVisor NX (*GEOMETRICS*) software is set up for the online recording and quality control of the multichannel seismic data. The sidescan sonar system and the acquisition of the sidescan sonar data are controlled with the dedicated HydroStar PC, running the HydroStar Online (*ELAC*) software. This PC is equipped with two monitors and allows the ‘flying’ the towfish in a save elevation above the seafloor. The software presents in real-time the acquired data from the sidescan sonar and the subbottom profiler sensors, the attitude and, when an USBL system is connected, the navigation data of towfish. It is also possible to set the main parameters of the sonar electronics, and to start and stop the data storage on the local harddisk (in *XSE* format) and on the underwater FS-DW disk (in *JSF* format). The Full Spectrum Interface Unit (*FS-IU*) is the laboratory part of the sidescan sonar electronics. In addition, there are the processing unit of the USBL positioning system POSIDONIA (cf. 2.1.3) and a PC for the online

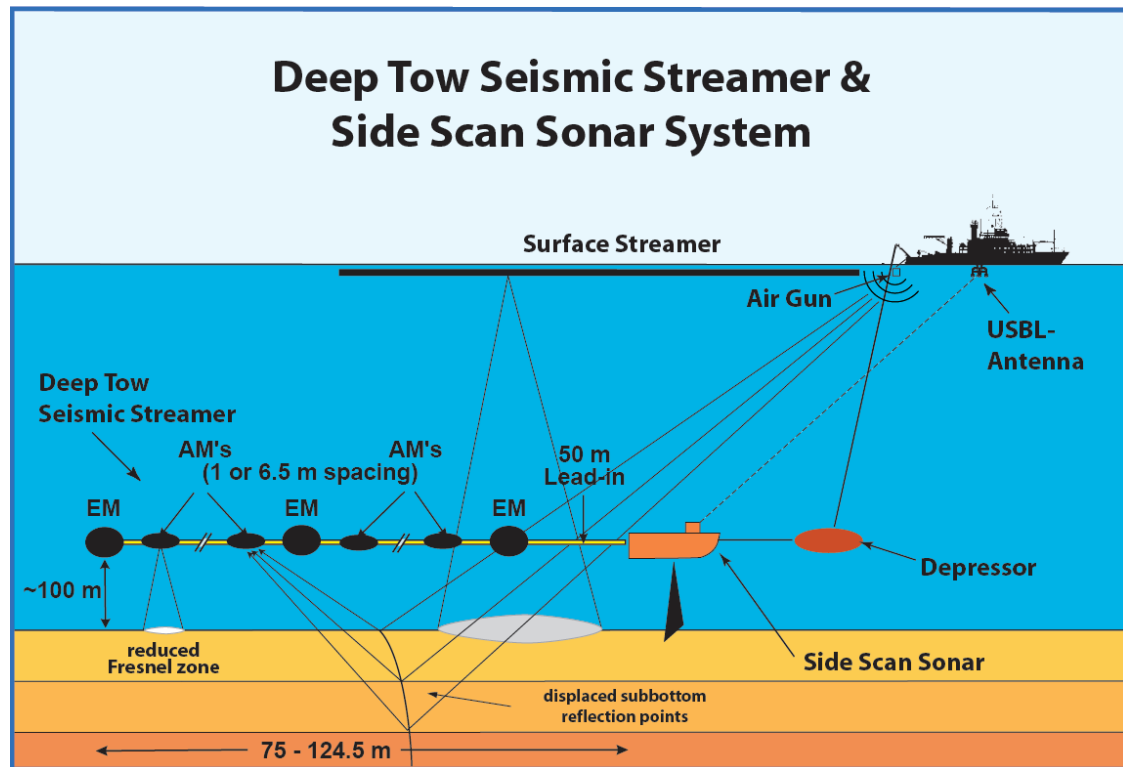


Figure 2.3: Layout of the deep-towed sidescan sonar/streamer system. During some deployments of SO173/1 a shorter lead-in of 6.5 m was used, and the total length of the seismic streamer varied between 37.5 and 74.0 m due to corrosion and contact problems. The sidescan sonar is connected to the sea cable via the depressor weight through a 40 m long umbilical cable (from Breitzke and Bialas [2003]).

recording and display of the measured positions of the towfish. An optional obstacle avoidance sonar was not set up during the survey.

In general it is also possible to run the system without the deep-tow seismic streamer. In this case the Bottom-PC, Top-PC and the Geometrics-PC can be removed. The top-side telemetry routes then the data directly to the FS-IU.

2.1. DATA ACQUISITION

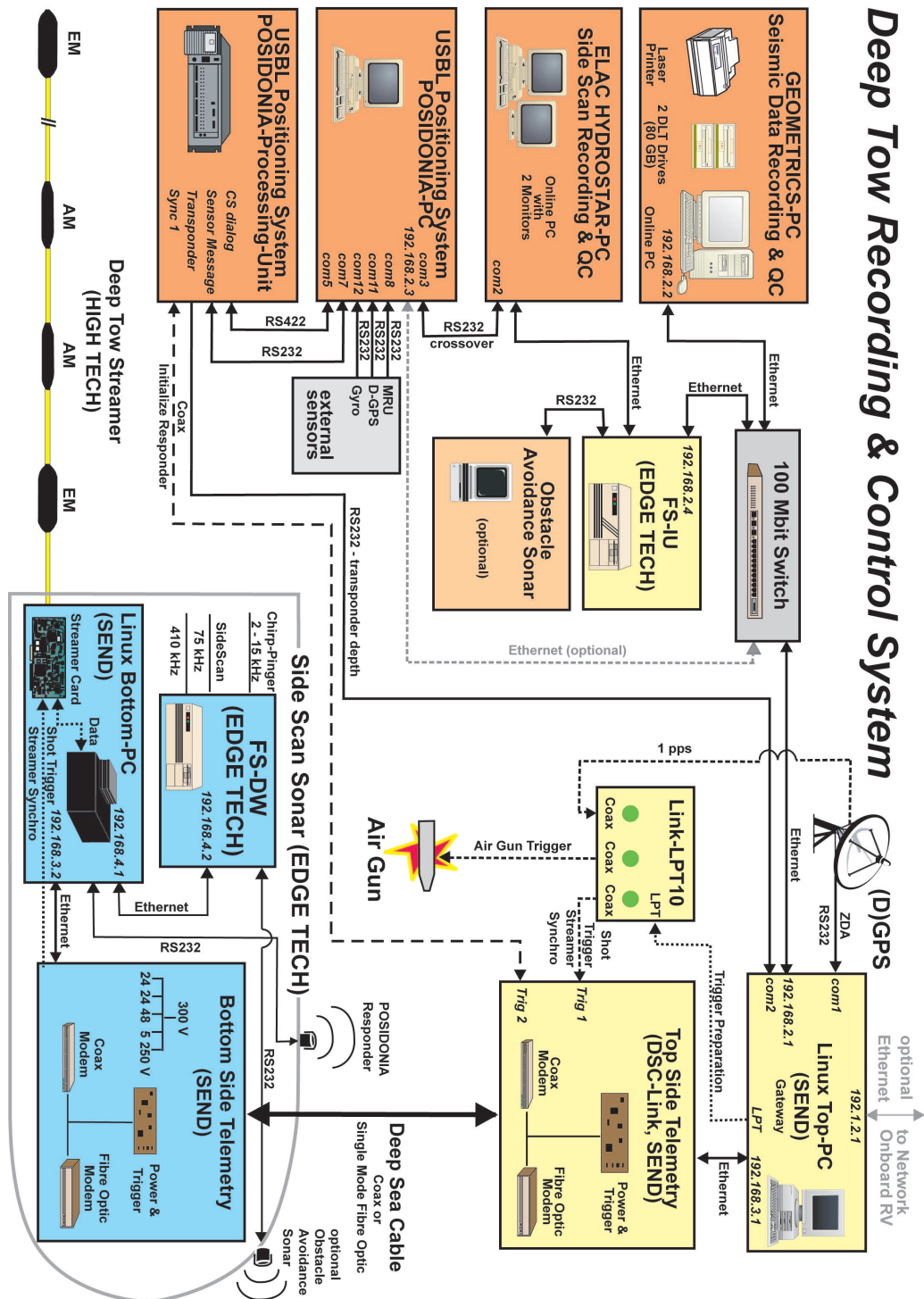


Figure 2.4: Laboratory and underwater components of the recording and control system for the complete deep-tow sidescan sonar and streamer system (from Breitzke and Bialas [2003]).

2.1.3 Ultra Short Baseline (USBL) Positioning System POSIDONIA

Underwater navigation, depth and position measurement of the DTS-1 is done with the ultra-short baseline system POSIDONIA (*IXSEA-OCEANO*, IXSEA-OCEANO [2002]). The system consists of a deployable acoustic array (antenna) installed in the moon-pool of the ship, the transponder mounted in the towfish, housing an additional pressure sensor, and the POSIDONIA processing unit and PC (see figure 2.4). The triggering of the transponder can be via cable link or via acoustic signal. During this survey the transponder was triggered by an acoustic signal via the acoustic array.

The USBL positioning principle is based on the bi-directional exchange of acoustic signals between one (or several) acoustic transponders and the acoustic array which consists of one transmission transducer and two pairs of hydrophones. The transponders are interrogated by an acoustic signal from the transmission transducer on the acoustic array and respond with a characteristic succession of monochromatic pulses of different frequencies ranging from 14.5 to 17.5 kHz. This respond signal is received by the four reception hydrophones on the antenna and transmitted to the processing unit which calculates the relative and geographical position of the transponder from the time between interrogation and reply and the phases of the signals from the four hydrophones.

There are two different tracking modes, free and towed fish mode tracking. In the free mode all four hydrophones are used for the calculation of the transponder, whereas in the towed fish mode only the hydrophones aligned with the towed vehicle are used together with depth information from a built-in pressure sensor. The free mode is applicable when the target is located within a cone of 60° underneath the ship. Beyond this angle the towed fish mode should be used.

As the DTS-1 was towed quite some distance behind the ship (approximately 30 minutes at ~ 3 knots), depending on the water depth, the towed fish mode was used. Assuming a conical angle of $\sim 120^\circ$, the POSIDONIA system allows to calculate the depth and position of the vehicle with an accuracy of 1% of the slant range, taking into account the information from the D-GPS, gyro compass and motion reference unit (MRU). The interrogation interval during this survey was set to 10 seconds, in order to minimize interferences with the sidescan sonar signal.

Prior to using the POSIDONIA system, the antenna has to be calibrated, in order to determine the vertical, longitudinal and transversal offsets of the acoustic array axes relative to the corresponding ship axes, and to take the position of the acoustic array relative to the *common reference point* (CRP) into account. The CRP is usually the position of the D-GPS antenna. The calibration procedure requires that the ship sails a figure of eight around a transponder moored on the seafloor, usually in a water depth of 1000–2000 m, to interrogate the transponder at any angle and from either side of the vessel. The POSIDONIA software (*POSICAL*) calculates then from all measured positions the correction factors for roll, pitch and yaw and gives root mean square (RMS) standard deviations for x, y, and z directions. From the distribution of the data points in the graphical display the precision of the position measurements can be estimated. The cali-

bration prior to the survey offshore Nicaragua resulted in $\text{RMS}_x = 4.8$ m, $\text{RMS}_y = 5.4$ m, and $\text{RMS}_z = 2.5$ m. From the graphical display the general precision of the position measurements was determined to be ± 12 m. This is about $\pm 1\%$ at a transponder depth of 1206 m during the calibration [Flueh et al., 2004, p. 79].

2.2 Data processing

In the following the processing of the acquired data is described. The bathymetry data have to be cleaned from bad soundings, before a grid is calculated. The included amplitude measurements can be plotted as a mosaic to derive lithologic properties of the seafloor. For the processing of the sidescan sonar data it is essential to have a good and reliable navigation of the towfish. Then the individual overlapping profiles can be stencilled and calculated into a mosaic. The subbottom profiler data have to be corrected for the varying elevation of the towfish above the seafloor. The resulting processed data can then be combined to derive new information.

2.2.1 Processing of EM120 Sounding Measurements with CARAIBES

The EM120 sounding measurements have been processed with the software package CARAIBES from *IFREMER*, Brest (France). The raw Simrad data files can be read in and are converted into a xy-file of the soundings and a navigation file. It was not necessary to edit the ships navigation, as the raw data contain already the precise D-GPS positions for each beam. The sound velocity in the water column was taken from a CTD measurement (SO173/3, station 23) at Masaya Slide and imported into CARAIBES. To clean now the soundings from wrong measurements, a statistical approach of iterative gridding was used. The soundings file was gridded repeatedly with a weighted average gridding algorithm and with decreasing cell sizes. After each gridding step the data points were compared to the resulting grid and eliminated if their depth value deviated more than a certain value. The maximum allowed deviation was also decreased with each iteration (table 2.1). The final grid has then a cell size of 50×50 metres (1316×1299 cells). It was interpolated to close some gaps. The maximum depth of the grid is 2578 m, the minimum depth 783 m. In a last step the final grid was exported as a GMT grid and merged with surrounding data from earlier surveys.

	cell size [m]	max. deviation [m]	soundings cancelled	[%]
iteration 1	200	100	246.569	0.96
iteration 2	150	50	561.031	2.19
iteration 3	100	20	3.663.704	14.49
iteration 4	50	10	2.583.869	11.83

Table 2.1: Parameters used during iterative bathymetry gridding with CARAIBES.

2.2.2 Processing of EM120 Amplitude Measurements with PRISM

The EM120 reflectivity values have been processed with the software package PRISM [Le Bas, 2002] from the *National Oceanographic Centre* (Southampton, Great Britain). The processing with CARAIBES did not produce satisfying results with respect to the contrast of the whole mosaic. To process the amplitudes contained in the raw Simrad EM120 data with PRISM, they first have to be converted into the generic *NetCDF* format [Rew and Davis, 1990] with the program *em120cd* which comes with the PRISM package. Then they can be handled the same way as the sidescan sonar data (see 2.2.4), but using a special configuration file (*em12commands.cfg*) for the EM120 sensor. The resulting mosaic with a pixel size of 20 metres shows a good contrast (cf. figure 1.6).

2.2.3 Processing of Towfish Navigation Data

Two ways have been tested to get a good towfish navigation: (1) Processing of the USBL POSIDONIA data (cf. 2.1.3), and (2) a layback method where the towfish navigation is calculated from the ship position and the cable length, assuming an inertial behaviour of the vehicle. In the first case the data from POSIDONIA had to be converted from standard *NMEA* format into a format suitable for import into CARAIBES, where the data had been thinned out, filtered and smoothed. Exporting and converting the processed data into the vehicle navigation format [Le Bas, 2002] made them available for the processing with PRISM. The second way was to use the D-GPS ship navigation and the actual cable length recorded in the ship database (*DVS*), and to apply the program *wire-out* which comes with the PRISM package [Le Bas, 2002]. Figure 2.1 shows a plot of both methods. The vehicle tracks do not differ significantly except during turns. But here the recording was shut off anyways. The figure does not show the along track variation of the vehicle position. Because an important serial connection between the POSIDONIA PC and the HydroStar PC was missing during the survey (*RS232 crossover in figure 2.4*) the position information was not stored with the data, and, which was the bigger problem, the clock settings of the two PC's differed. While the POSIDONIA PC had the correct D-GPS time, the clock of the HydroStar PC had an offset of some minutes. For the positioning of a sidescan ping in geographic coordinates it is necessary to look up the position in the navigation file with the time information of the ping. Therefore it was necessary to shift the ping times to get the correct location. The determination of the actual time shift was done by matching a structure (e. g. canyon, mound) along profiles which were surveyed in opposite direction. Fortunately the time shift turned out to be constant. The integration of the sidescan sonar mosaic with the (D-GPS positioned) bathymetry shows a very good match. But due to these complications it is difficult to give an error estimation.

2.2.4 Processing of Sidescan Sonar data with PRISM and ERDAS Imagine

The onboard processing of some interesting areas of the 75 kHz sidescan sonar survey has been done with the software package CARAIBES (Version 2.5). The raw data format *XSE* (Elac Nautik Exchange Format) can be read directly and is transformed into the CARAIBES *imo* format. The processing of small areas is straightforward and yields fast and satisfying results, presented in an inverse grey-scale (i. e. high backscatter is shown in dark tones, low backscatter is shown in bright tones). But a mosaic of the whole survey area shows a weak and unsatisfying contrast. Therefore the sidescan sonar data presented in this study have been processed with PRISM [Le Bas, 2002], a software package especially designed for the ‘*Processing of Remotely-Sensed Imagery for Seafloor Mapping*’ and the commercial *ERDAS Imagine* package. The processed mosaic in normal grey-scale (i. e. high backscatter is bright, low backscatter is dark) shows a very good contrast. Another advantage of PRISM is the availability of the source code (mainly C or FORTRAN), which allows customizing and extending its functionality. The processing workflow is more complex than in CARAIBES, and is described briefly in the following.

In a first step the *XSE* data as stored by the HydroStar Online acquisition system have to be converted into the *NetCDF* format (Network Common Data Format, [Rew and Davis, 1990]) with an inhouse software called *rawxse2prism* (figure 2.6). The EdgeTech JStar data (*JSF*) stored on the FS-DW harddisk in the towfish (cf. section 2.1.2) serve as a backup but are not further used. During the conversion, the vehicle elevation file, picked manually in CARAIBES, is given as a parameter to *rawxse2prism* and merged into the data. The automated elevation picking applied in PRISM did not work properly. The conversion routine also allows to decimate the number of samples contained in the raw data to provide a similar resolution in the along-track and across-track direction. The *NetCDF* data can then be quality checked with several routines available in the PRISM package [Le Bas, 2002]. Because the processing of all the data would create images which are too big to handle the survey area has to be divided into several mapsheets. PRISM supplies for this the program *mapchoose*, which automatically determines the best mapsheet size and creates coordinate files for all single maps (figure 2.5). Each mapsheet is then processed with the *prism* command requiring a vehicle navigation file, the *NetCDF* data files, and a configuration file (*commands.cfg*). The configuration file describes the processing which is applied to the imagery data. Here the data were processed with the standard options, including navigation merging, slant-range correction, various filtering methods, and a shading correction. As a final result an ERDAS Imagine file *IMG* is created for each mapsheet which can be further processed in the ERDAS Imagine software package (figure 2.7).

If PRISM finds overlapping track areas in a mapsheet, it will produce a multi-band image file. The overlapping track segments can then be viewed in 3 colour bands (red, green, blue) in ERDAS Imagine. To cut the overlap areas, stencil polygons or *Areas of Interest* (AOI) have to be defined in the separate layers. This is an interpretative process done

by the user, as it removes overlapping imagery which covers the same feature from a different illumination direction. These AOIs are then used to trim the layers before they are reduced down into a single layer image. This process is referred to as *stencilling* (figure 2.7). If there are any data at the edges of the mapsheet that have to be removed this can be done in a separate trimming step. When all single mapsheets have been processed this way, a mosaic or one large image can be calculated. To prevent zero value pixels (null data) which represent no backscatter or shadow zones from plotting as white pixels on paper in transparent mode, the routine *background fill* can be applied to the mosaic. It increases the null data pixels by a certain small amount. For map production, viewing, draping of the sidescan mosaic over the bathymetry, and further analysis, the imagery file was imported into the GIS package *ArcGIS* from ESRI. The final sidescan sonar image has been processed for a pixel resolution of $1.0\text{ m} \times 1.0\text{ m}$.

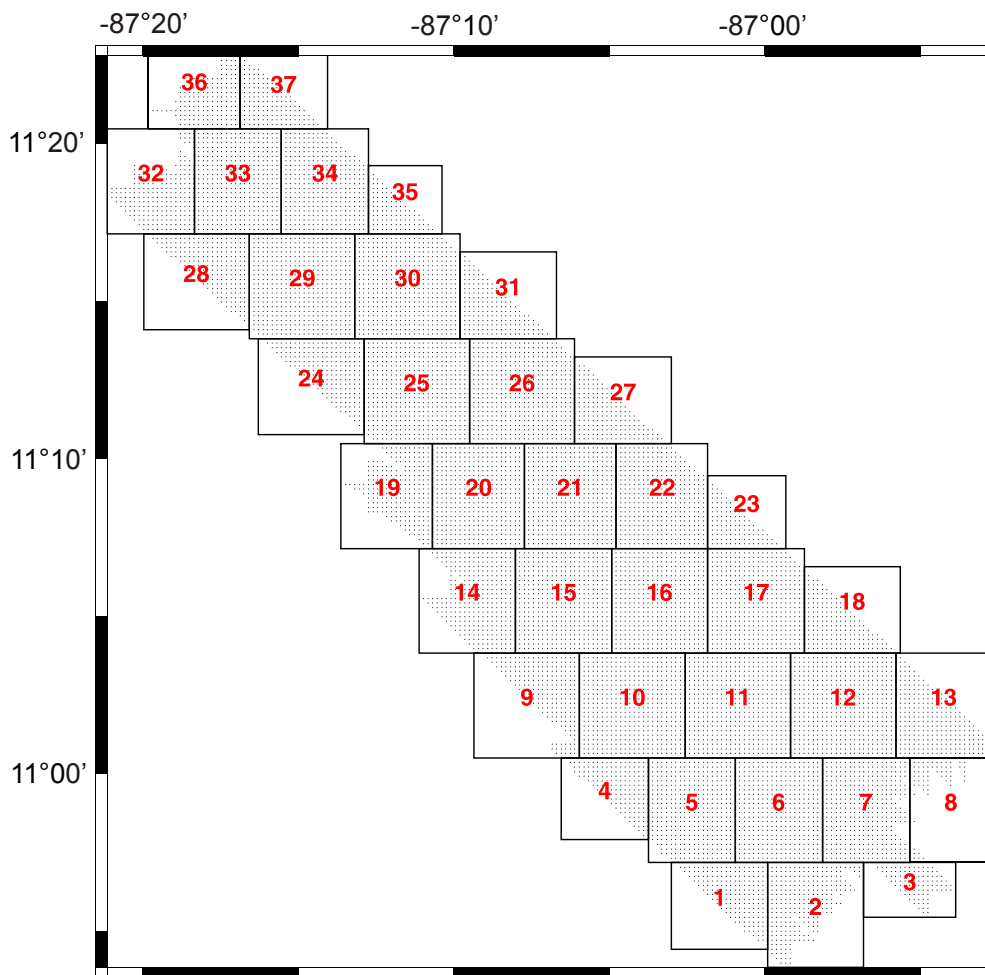


Figure 2.5: Coverage of sidescan sonar profiles offshore Nicaragua with distribution and numbering of mapsheets as created by PRISM program *mapchoose*.

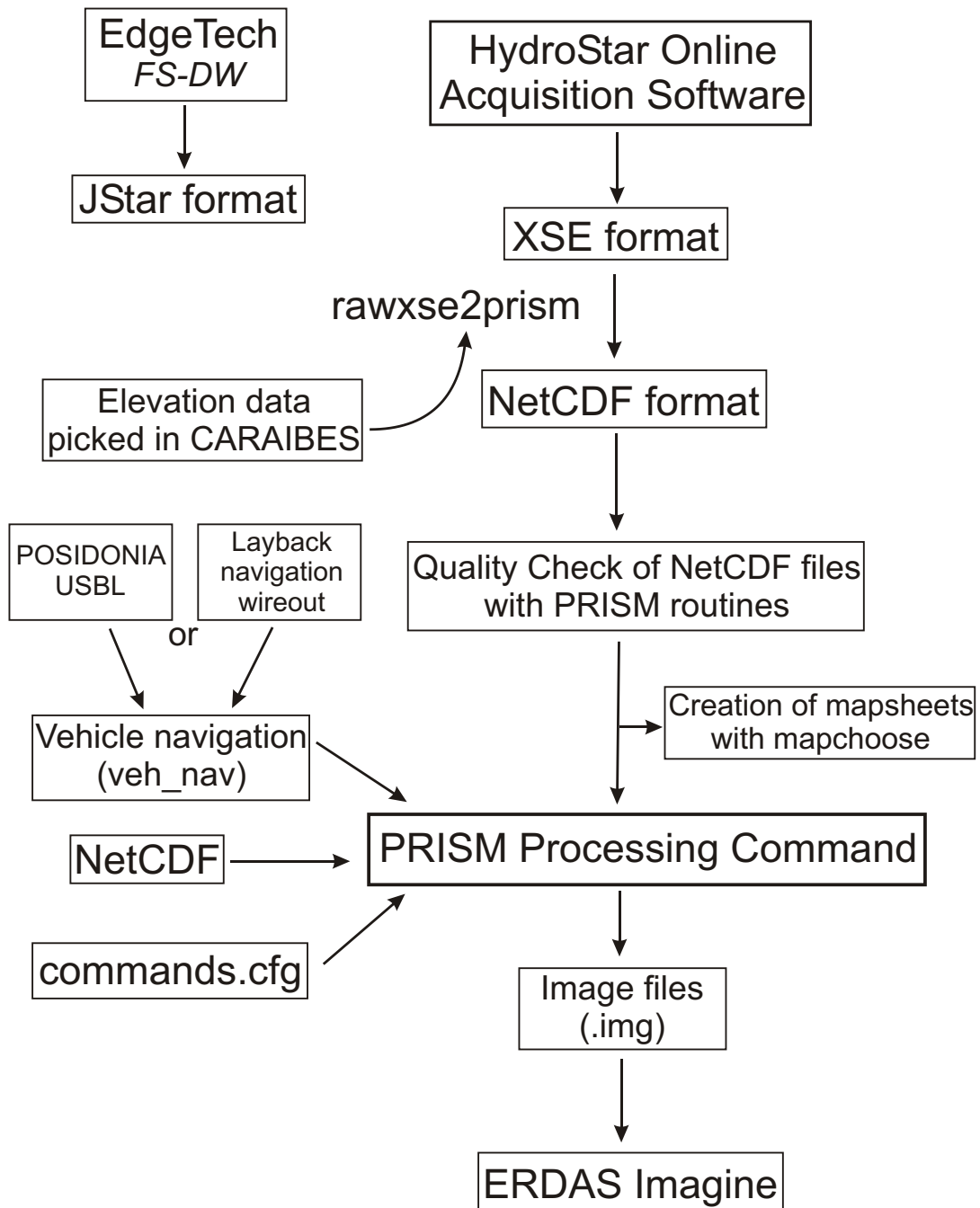


Figure 2.6: Processing workflow with the software package PRISM.

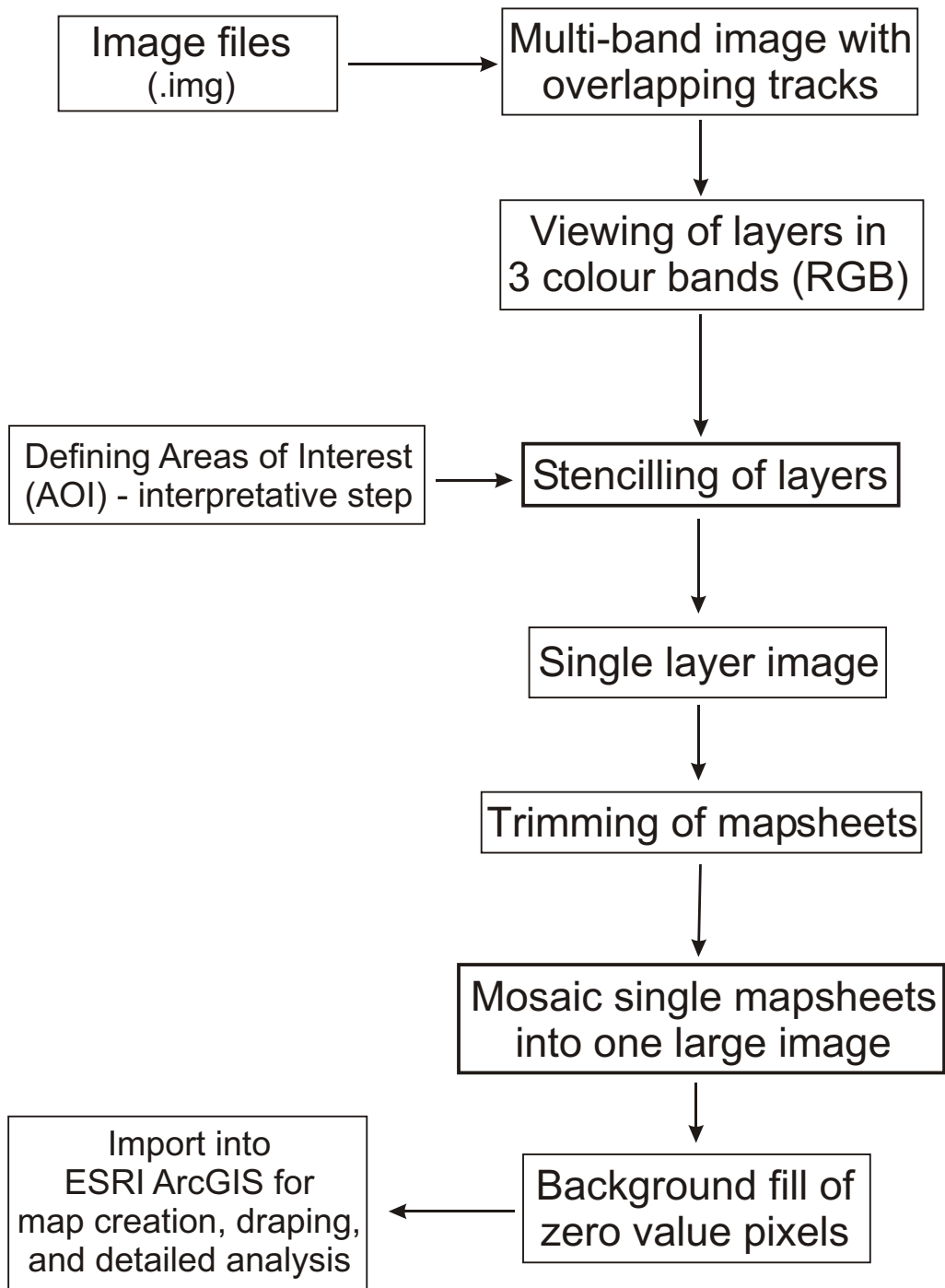


Figure 2.7: Processing workflow in ERDAS Imagine.

2.3 Sediment echosounder data

A cross-section of the uppermost sediment layers is acquired by two echosounding systems, the parametric Parasound System from *ATLAS Hydrographic* mounted on the hull of the ship, and the *EdgeTech* Chirp Subbottom Profiler mounted in the towfish.

2.3.1 The Parasound System

The PARASOUND system [Gerriets et al., 2003] uses the *parametric effect* to generate a low frequency signal travelling within the narrow emission cone of the original high frequency waves. The parametric effect produces a signal of the difference frequency if two sound waves of similar frequencies and sufficient high amplitudes are emitted simultaneously. The installed system uses primary frequencies of 18 and 22 kHz to generate a secondary, band limited, 2–6 kHz sinusoidal wavelet with a dominant frequency of 4 kHz and a duration of 250 μ s total length. The emission cone is limited to an angle of 4°, resulting in an footprint size of only 7% of the water depth which improves both vertical and lateral resolution significantly [Flueh et al., 2004, p. 52]. The seismograms were sampled at a frequency of 40 kHz, with a typical registration length of 266 ms, accounting for a depth window of approximately 200 metres. The data have been stored in digital *ps3* format, a variant of the standard *SEG Y* format, and have been plotted with the software *SeNT* from the University of Bremen (figure 2.8).

2.3.2 The EdgeTech DTS-1 Chirp Subbottom Profiler

Due to the variation of the towfish elevation above the seafloor, the raw subbottom profiler data do not reflect the true topography of the seafloor, but to each ping the traveltime of the variable depth has to be added as a static correction. The towfish depth information is taken from a pressure sensor in the first engineering module of the deep-tow streamer attached to the rear of the DTS-1. From the raw data stored on the HydroStar Online PC in *XSE* format the subbottom profiler data can be extracted with the inhouse software *rawxse2prism* into a standard *SEG Y* file. This can be read in and further processed with the open source software package *seismic unix* [Stockwell Jr., 1999]. The EdgeTech system stores the data in a complex mode, i. e. there exist traces with a *real* and an *imaginary* part. It is possible to remove the phase shift between these traces and to create one trace with the double sample rate. But as the resolution of the profiles was sufficient for a general sedimentological interpretation, only the *envelope* of the different traces was processed and plotted (figure 2.8). Interpretation of the height-corrected profiles, reflecting now true seafloor morphology, with respect to sedimentary processes is then possible.

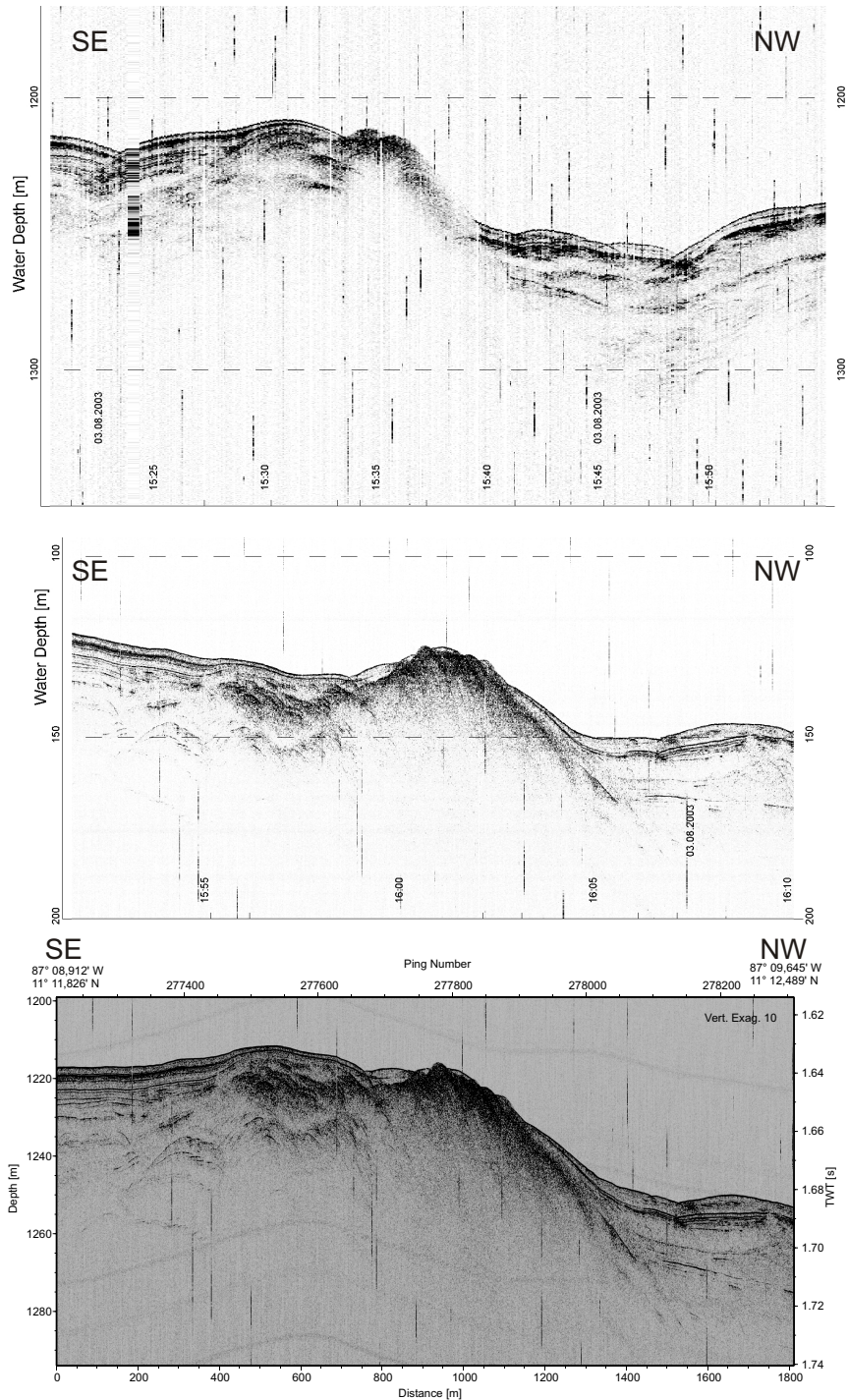


Figure 2.8: Example of Parasound profile, raw- and corrected subbottom profile from Mound Iguana. The Parasound and raw subbottom profile are plotted with the program *SeNT* from the University of Bremen and are based on the recorded ping times. The corrected subbottom profiler data have been processed with Seismic Unix and are merged with the towfish navigation. The distance scale between the endpoints assumes a constant velocity. The towfish depth for the height correction of the seafloor morphology is obtained from a pressure sensor. Note that the final subbottom profiles are oriented from left to right when looking upslope (i.e. these profiles are flipped in the final version).

2.4 Analysis of seafloor observations

During SO173 legs 3 & 4 seven of the fluid venting features offshore Nicaragua, identified by geoacoustic data during the first leg, have been further investigated by direct seafloor observations with a camera system (OFOS, *Ocean Floor Observation System*), gravity cores, TV-guided grab and TV-guided multi-corer. The water column above some of the seep structures was sampled with a CTD/rosette to measure the methane concentration in the water. These observations and preliminary results reported in Flueh et al. [2004] have been included in this study. The video tapes and slides from the still camera system of the OFOS have been analyzed in detail and correlated with the sidescan sonar images as far as possible. The navigation data of the OFOS were taken from the ships database *DVS* and represent the position of the ship or when available the short baseline (*SSBL*) navigation [Flueh et al., 2004, pp. 7 ff, 235].

3

Mound structures on the continental slope offshore Nicaragua - their geology, morphology, and formation

3.1 Introduction

Along the convergent continental margin of Central America features described as mud diapirs, mud domes, or mud volcanoes have been reported already from early seismic and bathymetric surveys [Kimura et al., 1997; Ranero et al., 2000b; Shipley et al., 1992, 1990]. They were interpreted as dewatering structures of accreted, or, to a lesser extent, underthrust sediments [Shipley et al., 1990]. As pathways for the escaping fluids, thrust faults inside the wedge were assumed [Shipley et al., 1990], as well as a substantial dewatering along the décollement towards the trench. The upward movement of the fluid rich sediments was thought to be induced by the high overpressure of the pore fluids. Further investigations showed that fluid expulsion is actually a widespread phenomenon along the margin, and that it is occurring not only in mud volcanoes or diapirs, but also at landslides, along the headwall of seamount subduction related slump scars, and at morphological intersections of faults [Bohrmann et al., 2002]. During the first years of research the margin was considered to be characterized by sediment accretion and a compressional tectonic regime, which supported the model of dewatering of the accreted sediments through mud volcanoes, similar to other accretionary margins [Henry et al., 2002, 1990; Lance et al., 1998; Kopf and Behrmann, 2000; Kopf et al., 2001]. Later, when it became clear that the wedge consists of ophiolitic basement which is covered by a rather thin sedimentary slope apron [Flueh et al., 2000], and that tectonic erosion is active along the margin, resulting in an extensional tectonic setting at the continental slope, this model became questionable. It is therefore the goal to give an interpretation of the nature and mechanisms of the fluid venting structures, using geoaoustic investigations and seafloor observations from an area where they have been observed in earlier reconnaissance surveys in great density. Table B.1 lists the identified 48 mound structures or intensity anomalies in this area with their locations shown in figure 3.1. Ground truthing with a camera system and coring is available at seven of the structures. The activity of fluid venting is indicated by the occurrence of specialized vent-ecosystems [Kulm et al., 1986; Suess et al., 1985], consisting of chemosynthetic organisms such as bacterial mats, vesicomid, solemyid and mytilid bivalves, as well as pogonophoran tubeworms. These organisms host symbiotic sulphide-oxidizing bacteria in their gills. The symbionts use sulphide which results from a process called *anaerobic oxidation of methane* (AOM)

in the sediment below. Here a microbial consortium mediates the anaerobic oxidation of upward migrating methane and reduces the sulphate from the infiltrating seawater [Boetius et al., 2000]. The boundary along which this is occurring is called the *sulphate-methane interface* (SMI) [Han et al., 2004]. The reaction leads finally to the precipitation of authigenic carbonates which can serve as lithological evidence of former or still ongoing venting activity [Ritger et al., 1987].

The term *mound* is used for features which are observed in the multibeam bathymetry data and hence have a morphological expression on the seafloor. The New Oxford American Dictionary (2nd edition) defines a mound as *a rounded mass projecting above a surface, a raised mass of earth, stones, or other compacted material, or a small hill*. Mounds are further characterized by an elevated backscattering signal in sidescan sonar images, differing from normal hemipelagic seafloor. *Intensity anomalies* can only be observed in the backscatter data, but do not show up in the bathymetry. They have none or only very little morphological expression on the seafloor, but are characterized by very high backscattering signals. Mounds are named with characteristic animals of Central America. Intensity anomalies are numbered in each area. Presentation of the backscatter data is in normal mode, i. e. high backscatter values are shown in bright tones, low values are dark.

In the following sections I will first analyse the spatial distribution of the observed venting sites, before I suggest a classification based on size, morphology, backscatter signal, and observed fluid venting activity. Then the most characteristic mounds observed in the study area are presented in spatial order. The high quality of the data and the high density of venting sites in the area allows new insights into the formation mechanisms and structure of the mounds.

3.2 Mound structures in different (tectonic) settings

Spatial Distribution

The mound structures and intensity anomalies identified in the survey area can be spatially grouped into several areas with different characteristic seafloor morphologies and tectonic settings (see figure 3.1):

(1) Three mounds are located around the headwall of the Momotombo Slide Area in about 1400 m water depth (figure 3.2). They show a rounded, dome-shaped morphology and heights between 70 and 100 m with diameters around 1000–1200 m. Mound Carablanca and Mound Congo are right along the headwall of the slide, whereas Mound Tucan is in approximately 1400 m distance from the headwall. All three mounds are bordered by smaller gullies, which they deflect partially.

(2) A larger number of mounds and intensity anomalies is located in the Central Area upslope of the Masaya Slide (figure 3.5). Here the morphology of the relatively smooth seafloor forms a large bulge. The mounds show flat upslope and steeper downslope flanks with diameters around 600–900 m and heights between 40–60 m. The intensity anomalies

are much smaller. They show either a very bright backscatter with an irregular outline (and look very fresh and active) or they are related to canyons where they are located on the canyon floor or flank, or on the a ridge in between. There are almost no faults observed in this area.

(3) Along the upslope border of this Central Area the so called Baula Massive, consisting of a group of similar mounds, is aligned in 800–900 m water depth (figure 3.5). The mounds are generally large with heights between 70–180 m and show an eroded topography. On the downslope side of this group an almost continuous escarpment marks the seafloor morphology.

(4) Mound Perezoso is located in the southeast corner of the survey area in about 800 m water depth and resembles the mounds of the Baula Massive (figure 3.17). It shows a very steep topography with a height of 130 m and a diameter of around 1000 m. Close to Mound Perezoso there is Mound Colibri, a smaller, ridge-like mound with only 30 m height.

(5) In the southern part of the survey area where several large canyons are deeply incised into the continental slope, a number of mounds are aligned on downslope trending ridges, named here Mound Ridge I, II and III respectively (figure 3.18). The ridges are flanked by the canyons and show different lengths. While Mound Ridge I is quite short and consists of only two mounds, the other ridges can be followed further up the slope. Mound Ridge III seems to continue from ~2100 m water depth up to 1200 m depth. But in the upper part above Mound Morpho (water depth 1660 m), the ridge is much more smooth and not that steep and exposed as in the lower part. The mounds which form the ridges are mostly of elongated shape with heights between 60–100 m. Just south of these prominent ridges an area with intensive normal faulting is recognizable in the bathymetry and sidescan data.

Mound Classification

Trying to group the mounds with respect to their size, morphology, backscatter signal and fluid venting activity inferred from seafloor observations it is possible to distinguish three basic mound types (figure 3.5). They represent end members in the range of possible features.

(1) Mounds of type I (e. g. Mound Quetzal) are usually dome- or knoll like mounds with a circular base and steep downslope and flat upslope flanks. The diameters of the mounds are around 700–1000 m and the heights vary between 50 and 100 m. The flat top areas of the mounds show often very bright backscatter caused by authigenic carbonates, which can be up to 1 m thick and fractured. This small-scale topography causes shadows in the sidescan image. Sometimes depressions in the top area are observed. They could be caused by slumping due to instabilities in the mound facies material. In the fractures between the carbonates, preferably on soft sediment, vent fauna is present. The subbottom profiles show partly erosive contacts along the mounds, partly depositional channel sedimentation.

(2) Mounds of type II (e. g. Mound Iguana) are intensity anomalies with a very bright backscattering signal and almost no topographic relief. The shape of the intensity anoma-

lies is irregular with diameters of around 500 m or even less. The very bright backscattering signal is caused by authigenic carbonates. Sometimes ground truthing shows hemipelagic sediments at places where high backscattering signals are originating from. This is probably due to a hard reflector (carbonates) underneath the sediment drape, as the acoustic signal is penetrating some distance into the seafloor. Echosounder profiles show onlapping sedimentary layers without any signs of erosion. Vent fauna is abundant with a wide range of species indicating active fluid or volatile discharge into the ocean. (3) Mounds of type III (e. g. Mound Baula I) are very large and massive mounds with a very steep topography. The mound diameters exceed 1000 m and the heights can reach 150–200 m. The top areas are largely covered with authigenic carbonates up to several meters thick and fractured. Vent fauna is rare, indicating little to none fluid venting activity. Concluding from the amount of authigenic carbonates present, the ages of these mound types are the highest compared to the other types. In the subbottom profiles the large mound bodies appear as unstructured areas showing no sediment deposition or coverage on top or along the flanks.

The different mound types do not show a clear correlation with the spatial distribution pattern.

Description and interpretation of mound settings

In the following the different settings where mounds and intensity anomalies occur are presented in detail. The data used are sidescan sonar drapes over multibeam bathymetry, subbottom profiler cross-sections and, where available, seafloor observations with a camera system.

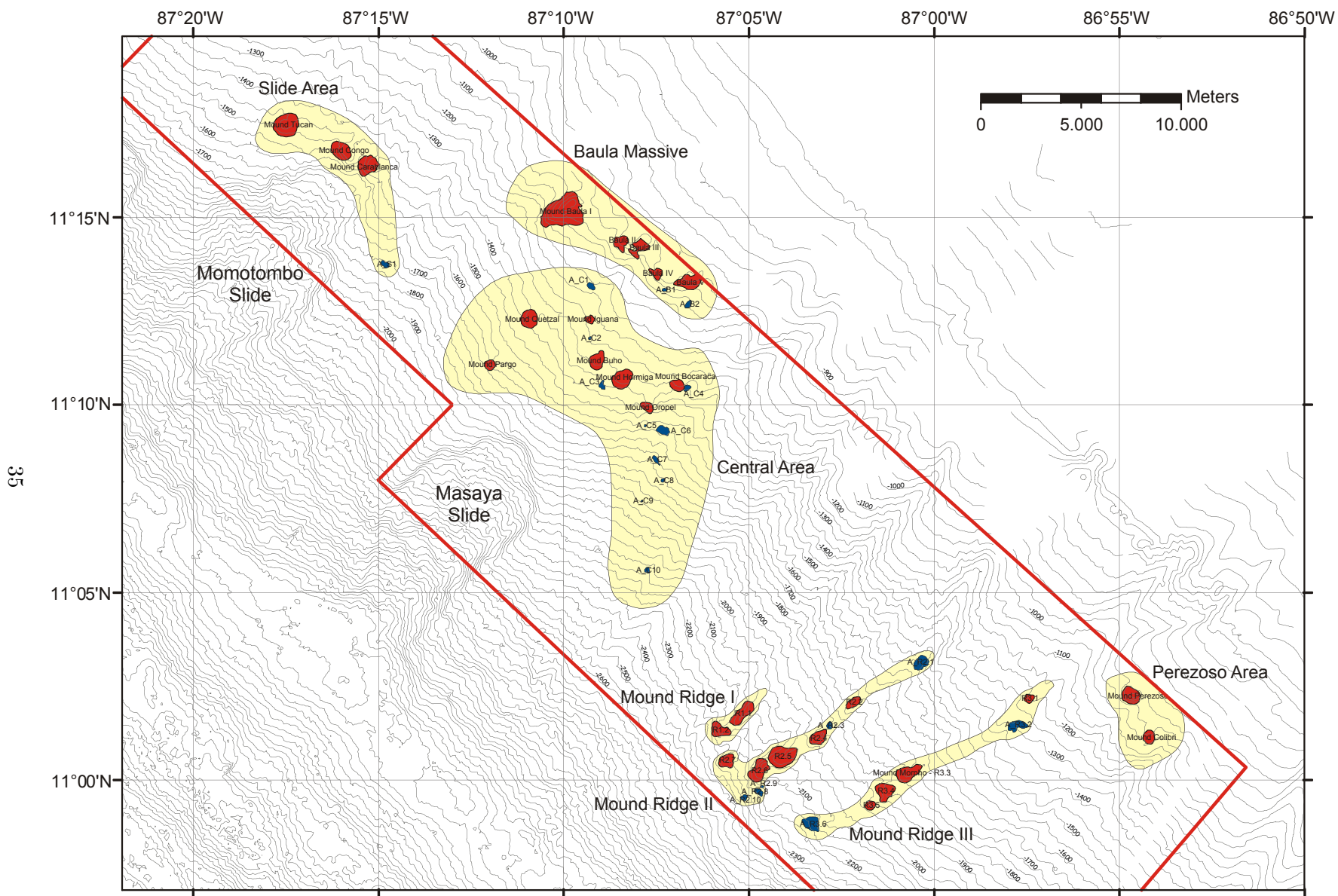


Figure 3.1: Mound structures (red) and backscatter anomalies (blue) observed in the bathymetric and DTS-1 sidescan sonar data offshore Nicaragua. Yellow areas indicate spatial relation to seafloor morphology. Mound names are taken from typical animals of central american fauna. Backscatter anomalies are numbered in each area. See also table B.1.

3.2.1 Momotombo Slide Area

Around the headwall of the Momotombo Slide three mounds are imaged in the multibeam bathymetry and the sidescan sonar data: Mound Tucan, Mound Congo and Mound Carablanca (figure 3.2). They are of about the same size and height and show a dome-shaped morphology with a circular to elongated base (see table B.1). The deep-tow profile lines did not run directly over the top of the mounds but crossed just further up- and downslope. Only for Mound Carablanca direct seafloor observations from a video sled system exist.

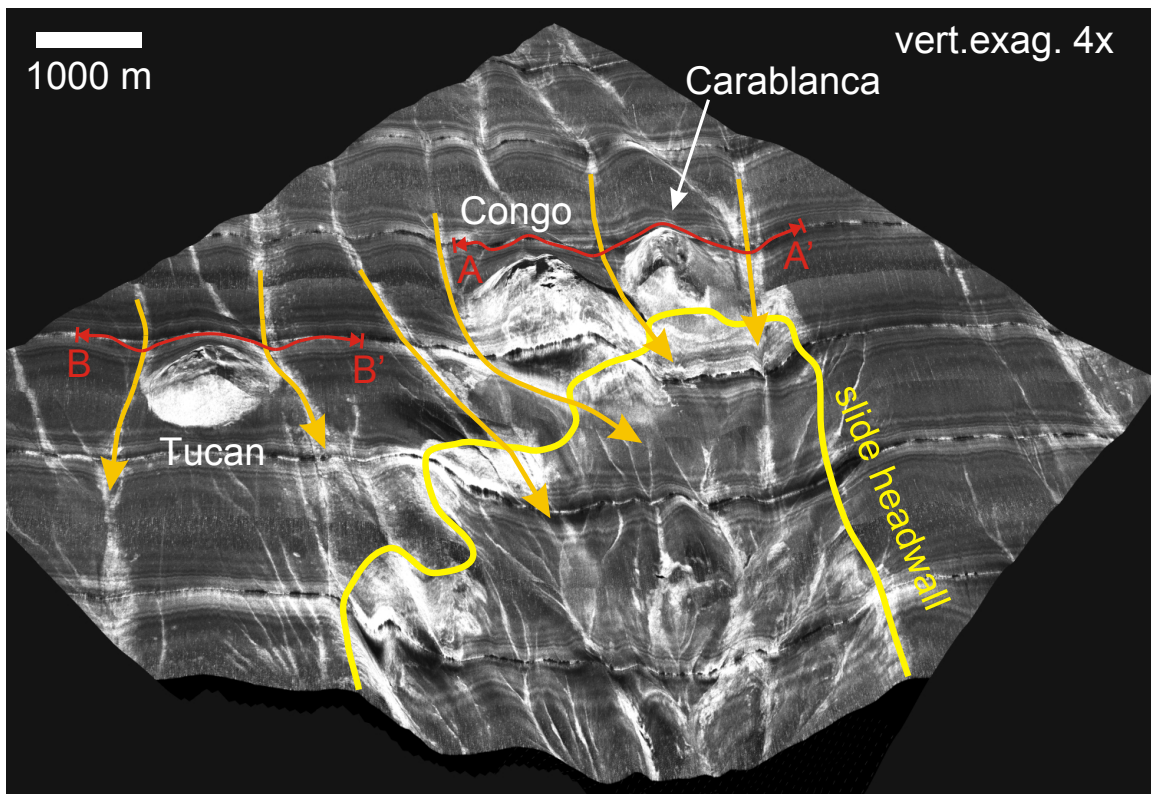


Figure 3.2: Drape of sidescan sonar image over *Digital Elevation Model* (DEM) of the seafloor, showing upper part of Momotombo Slide with three mound structures along or close to the slide headwall (yellow line). Gullies are deflected by mounds (indicated by orange lines), and discharge over the headwall into slide. New erosion pattern has developed on seafloor inside slide, indicating a higher age for this event. Red lines represent location of subbottom profiles (see figure 3.3).

Mound Carablanca Mound Carablanca is located right along the headwall in approximately 1430 m water depth. It shows a slope-parallel height of 70 m and has a size of approximately 915×1060 m. Its SW flank is very steep and borders the slide headwall.

The upslope directed NE side is more flat. The subbottom profile (A–A', figure 3.3, top) shows a deeper incised canyon along the SE flank and a kind of “christmas tree” structure between the mound facies and the canyon overbank deposits. To the NW a smaller gully borders the mound. On the NW mound flank some reflections inside the mound facies are interpreted as sediment slumping, but it is not possible to identify this in the sidescan sonar image. Further to the NW Mound Congo is imaged in the sub-seafloor. The subbottom profile (B–B', figure 3.3, bottom) shows the cross-section of the sedimentary covered upslope flank of Mound Tucan. In the top area of Mound Carablanca seafloor observations show carbonate coverage and 1–2 m sized clusters of very dense vesicomid clams settling on soft sediment ponds (figures 3.4, 3.21, Carablanca B). In the sidescan sonar image the top area is also characterized by smaller shadows caused by the micro-topography. Seafloor observations show at places with increased backscatter sometimes outcropping carbonates, sometimes hemipelagic sediments, but with the impression that this sedimentary coverage could be very thin and a harder seafloor could be underneath. Characteristic in the backscatter signature of the mound are the circular rings of higher and lower intensities. The reason for such a pattern could be a change between thicker soft sediments and hardground or even outcropping carbonate banks. Figure 3.21, Carablanca A, shows such a bank sticking out of the soft sediment. It could be correlated with a band of high backscatter in the sidescan sonar image (figure 3.4). Another feature observed on the seafloor is a circular carbonate structure of about 50 cm in diameter which is interpreted as a fluid conduit or carbonate chimney (figure 3.21, Carablanca C). But this is very speculative.

3.2. MOUND STRUCTURES IN DIFFERENT (TECTONIC) SETTINGS

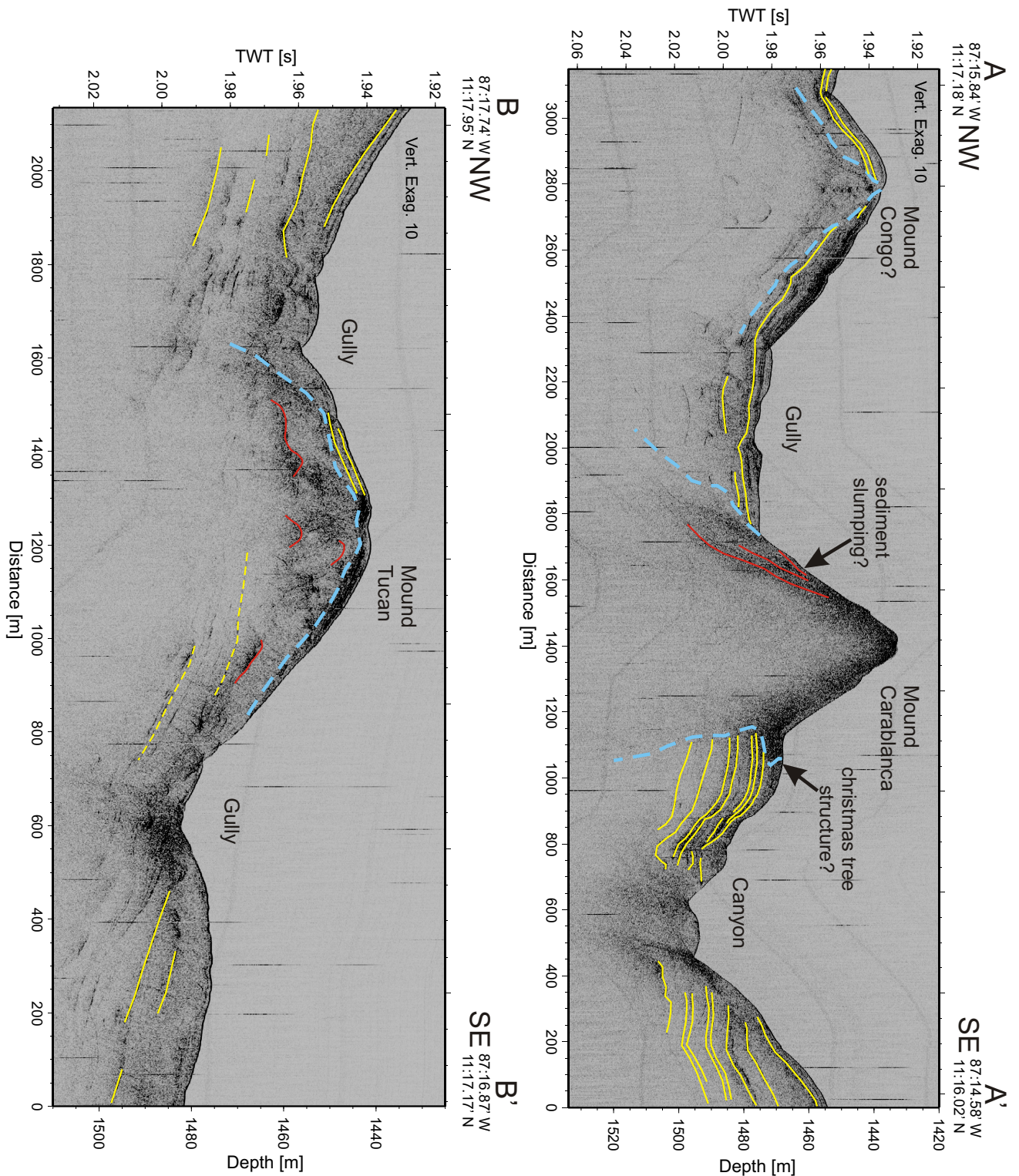


Figure 3.3: Subbottom profiles along Mounds Carablanca and Congo (top) and Mound Tucan (bottom). For location see figure 3.2. Blue: border of mound facies; red: structures inside mound; yellow: hemipelagic sediment layers. The mounds are bordered by smaller gullies or larger canyons.

CHAPTER 3. MOUND STRUCTURES OFFSHORE NICARAGUA

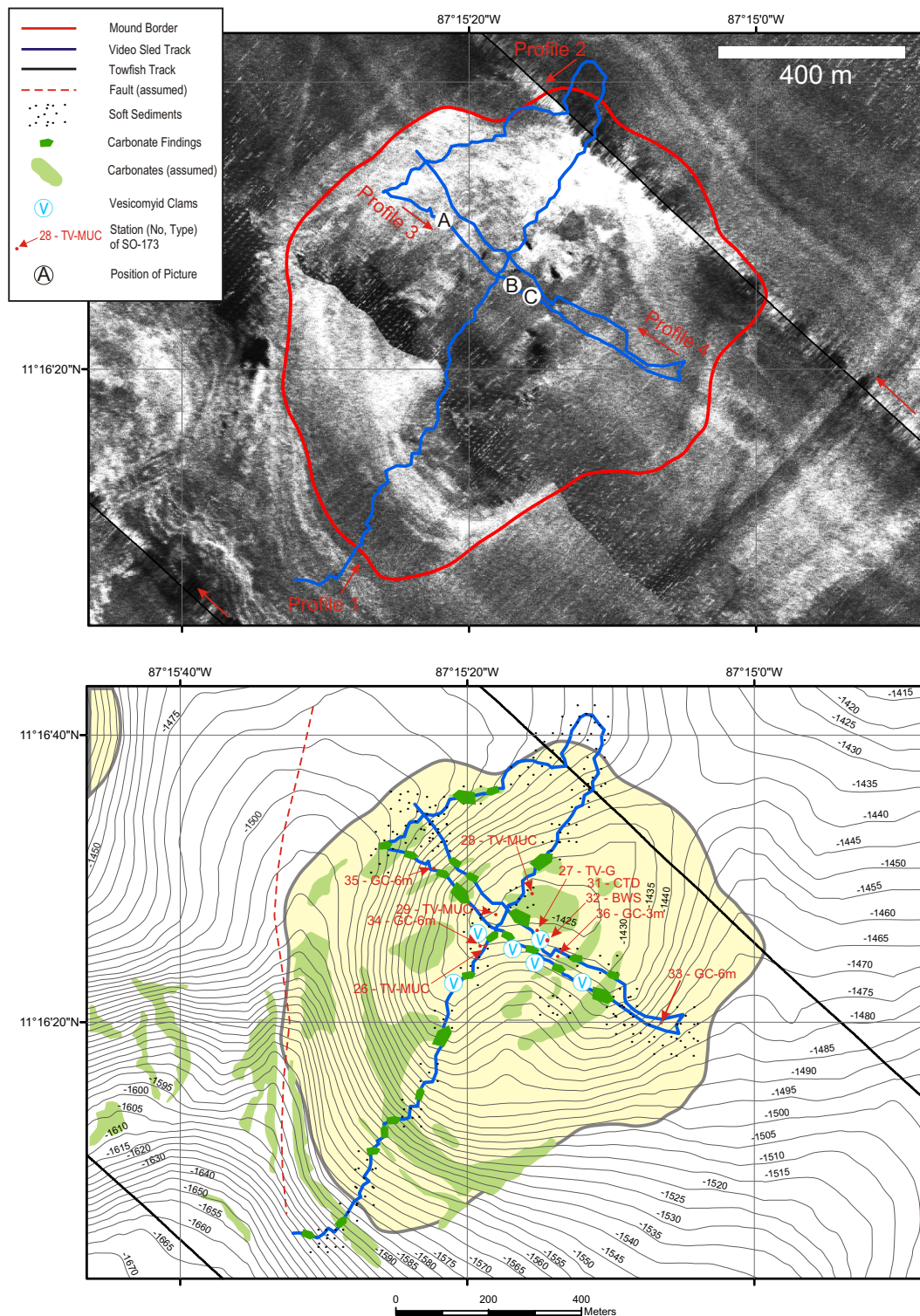


Figure 3.4: Detailed sidescan sonar map with video sled profiles over Mound Carablanca (top), and interpretation of seafloor observations (bottom). Symbols represent direct observations, light green areas are interpreted as authigenic carbonate formations. Note alternation between soft seafloor sediment (dark grey tones in sidescan sonar map) and hardgrounds, which possibly indicates phases of higher and lower seep activity.

3.2.2 Central Area upslope Masaya Slide

On the relatively smooth seafloor upslope of Masaya Slide several characteristic mound structures of different type and intensity anomalies can be observed (figure 3.5, 3.12). Seafloor observations in this area exist from Mounds Quetzal, Buho, Hormiga and Iguana. They are discussed here as well as cross-sections of the subbottom profiler showing interesting sub-seafloor structures.

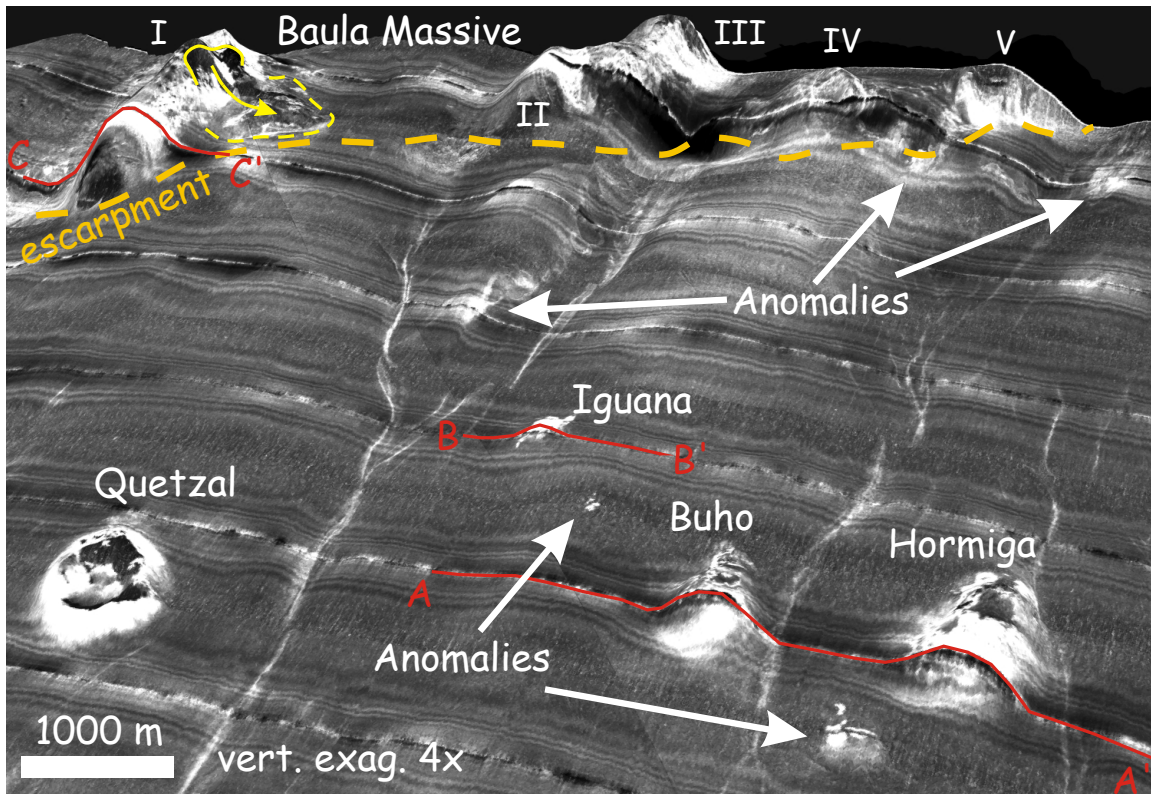


Figure 3.5: Drape of sidescan sonar image over *Digital Elevation Model* (DEM) of the seafloor, showing part of Central Area and Baula Massive. Mid-sized mounds Quetzal, Buho and Hormiga are of similar type with circular to elliptical base and dome-like shape, whereas Mound Iguana shows very little topographic expression, an irregular outline, and represents perhaps a later stage of a Backscatter Anomaly. The Baula Massive consists of several large mounds (numbered I – V) which are all situated upslope of an escarpment (orange dashed line). Red lines represent position of subbottom profiles (figures 3.6, 3.10, 3.15). Slumping on Mound Baula I flank is indicated by yellow lines.

The seafloor in the Central Area forms a large and smooth bulge, bending down towards the Momotombo Slide Area in the NW and towards an area with deeply incised canyons in the SE. It can be speculated that the bulge is related to a (smaller) seamount or obstacle on the incoming Cocos Plate, subducted beneath the continental slope, and perhaps triggering the Masaya Slide. Looking at the spatial orientation of all the mounds and anomalies, they show a semi-circular pattern around the headwall of the slide (figure 3.1). But the backscatter anomalies A.C5–A.C10 are located on the floors and side walls of canyons, and it is doubtful, that they are really fluid venting sites. They could also be related to coarser material or small steps in the gradient of the canyons resulting in higher backscatter echoes. It would then also be possible to see a linear pattern crossing each other in a parallel-slope and perpendicular-slope direction. Mounds Quetzal, Buho, Hormiga and Oropel are oriented in a slope-parallel line, Mounds Oropel and Bocaraca and Mounds Pargo and Quetzal form a downslope trending line. There are hardly any faults observed in the sidescan sonar or subbottom profiler data in the Central Area. This is unusual when compared to other slides or seamount subduction scars offshore Costa Rica [Dominguez et al., 1998; Hühnerbach et al., 2005].

Mounds Buho and Hormiga Mound Buho and Mound Hormiga are located in about 1260 m water depth upslope of the Masaya Slide in a distance of approximately 5000 m from the slide headwall and were imaged along the same track line. They both have a circular to slightly elongated shape with a flat upslope and a steep downslope flank. While Mound Buho is centered on the morphological bulge of the Central Area, Mound Hormiga is located further to the SE where the bulge bends down to Mound Oropel and a larger canyon at greater water depths. The dome-shaped Mound Buho has a size of 890×690 m and a height of approximately 40 m. On the flat top area and the upslope side, the sidescan sonar image shows patches of high backscatter interpreted as outcropping carbonates, and dark areas interpreted as shadows (figure 3.7). The grey intermediate levels correspond to normal hemipelagic sediment. It is remarkable that the steep SW flank of Mound Buho shows an almost uniform high backscatter pattern, even when illuminated downslope from the fish track. The reason for these higher amplitudes are probably carbonate blocks which are scattered and mixed with normal hemipelagic sediments, as imaged along the video sled profile (figure 3.21, Buho A). The subbottom profile over Mound Buho shows a small moat at the NW boundary with a slight decrease in thickness of the neighbouring hemipelagic sediment layers. This indicates some erosion along the base of the mound. In the SE, between Mound Buho and Mound Hormiga, a somehow chaotic structure of the sediments is interpreted as a channel fill. The morphology of Mound Hormiga shows two flat summits separated by a small depression less than 5 m deep (figure 3.12). The size of the mound is 1095×850 m with an approximate height of 60 m. In the sidescan sonar image the central depression shows dark grey values, probably caused by acoustic shadowing. Nevertheless it can be assumed that soft sediments cover the seafloor inside the depression. The surrounding patchy high backscatter pattern is probably caused by blocky carbonates forming a kind of low wall

3.2. MOUND STRUCTURES IN DIFFERENT (TECTONIC) SETTINGS

around the depression (figure 3.21, Hormiga A). In the subbottom profile the contact between the mound facies and the adjacent channel deposits is not clearly imaged. The seafloor observations on both mounds show only very few vesicomid clamshells, mainly not alive and numerous (dead) scattered polychaeta sticks.

A very interesting feature is imaged in the subbottom profiler data just 1200 m to the NW of Mound Buho where the topography forms a small bulge (figure 3.6). The clearly visible upper 25 m of the horizontally layered sediments are thinning out towards a diapir-like structure, about 800 m in length. This structure shows strong reflectivity in the profiler data and rises up to 2.5 m below the seafloor. The overlying sediments are probably hemipelagic drape and the reason why no unusual backscatter signal is observed in the sidescan sonar data (figure 3.5). Identification of the deeper roots of this structure in the deep-tow seismic data reveals no typical zone of ascending fluids like underneath other mound structures, but a sigmoidal sedimentary structure (*Talukder, A., pers. comm.*). How this structure can be explained is not clear yet, but from the subbottom profile it can be inferred that material was or is still moving upward, at least for some tens of meters, leading to the thinning out of the sedimentary units. Similar features can be observed in the profiles upslope and downslope of this line, which is discussed in section 3.2.2.

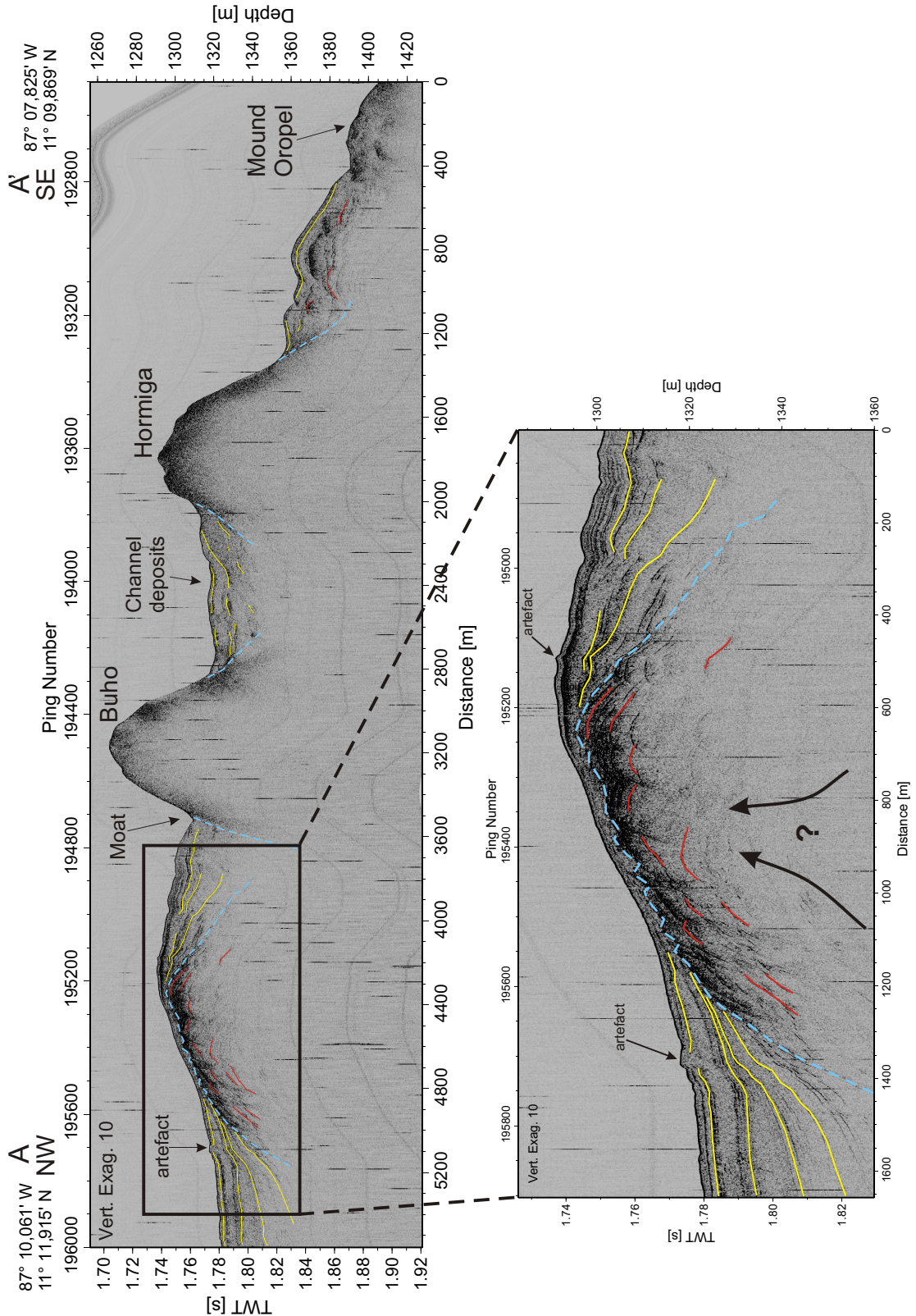


Figure 3.6: Subbottom profile across Mound Buho and Mound Hormiga (top) and enlargement of diapiric structure (bottom). For location of profile see figure 3.5. Blue: border of mound facies; red: structures inside mound; yellow: hemipelagic sediment layers. Mounds are bordered by moats, indicating some amount of erosion, but also by channel sediments, which are indicative of a depositional environment.

3.2. MOUND STRUCTURES IN DIFFERENT (TECTONIC) SETTINGS

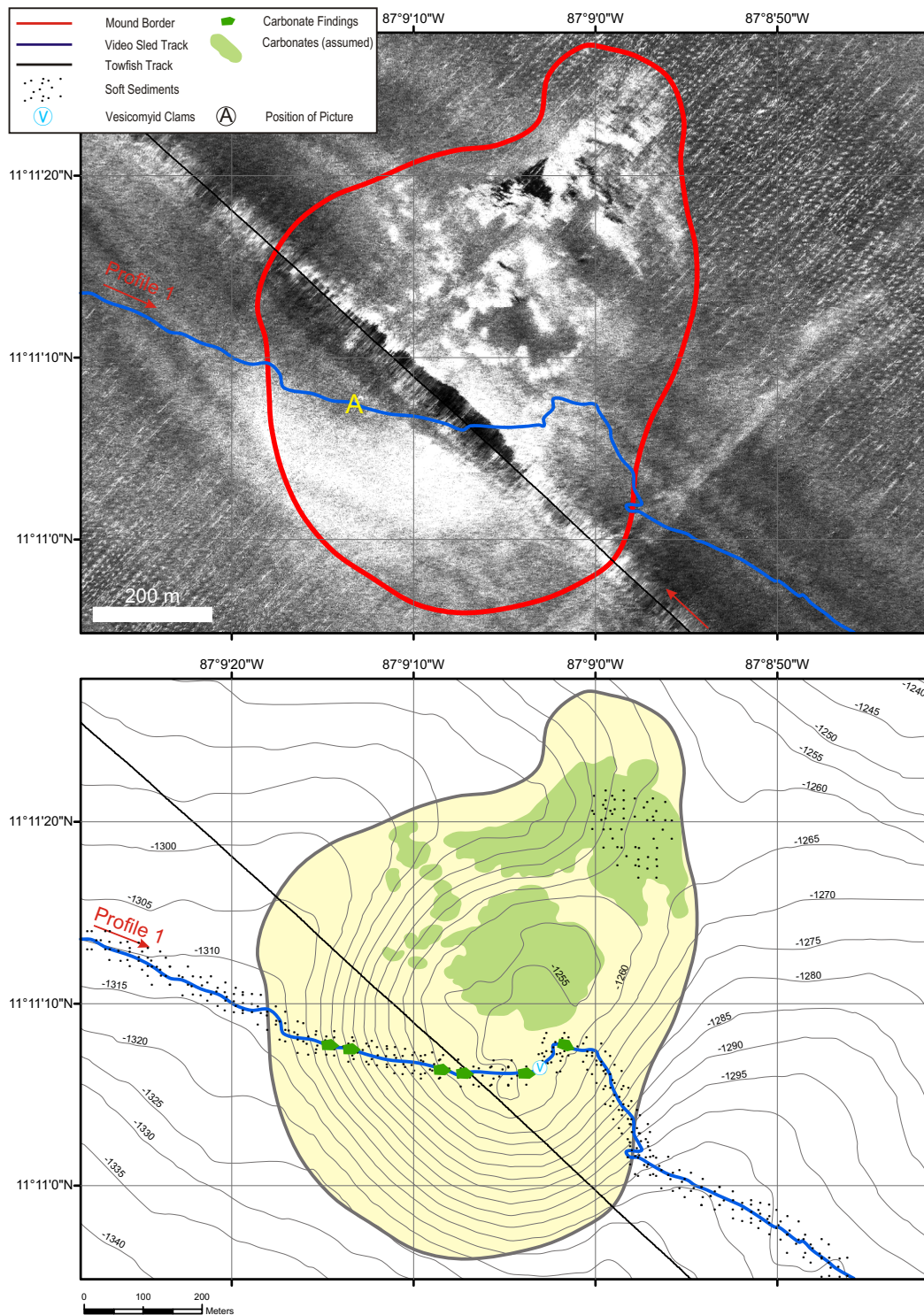


Figure 3.7: Detailed sidescan sonar map with video sled profiles over Mound Buho (top), and interpretation of seafloor observations (bottom). Symbols represent direct observations, light green areas are interpreted as authigenic carbonate formations.

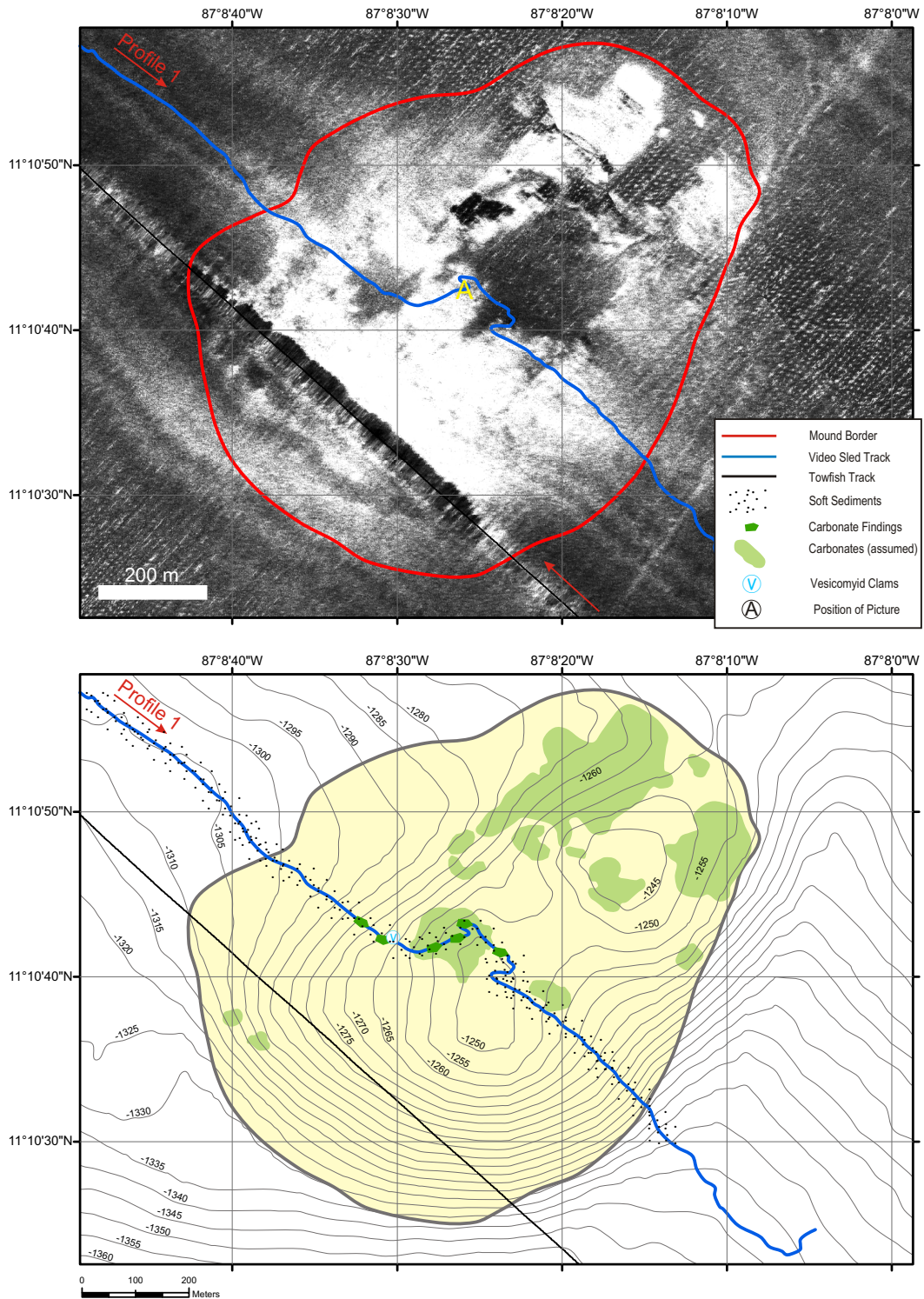


Figure 3.8: Detailed sidescan sonar map with video sled profiles over Mound Hormiga (top), and interpretation of seafloor observations (bottom). Symbols represent direct observations, light green areas are interpreted as authigenic carbonate formations.

Mound Quetzal Mound Quetzal is located about 4500 m to the NW of Mounds Buho and Hormiga at approximately 1310 m water depth. The track line from Mounds Buho and Hormiga does not run directly over the mound, but crosses just upslope (figure 3.12). This subbottom profile and the next one downslope do not image the mound very well. The size of the mound is 920×865 m with a circular base and a slope-parallel height of about 60 m. The morphology of the mound shows a depression in the top area, probably caused by slumping of a part of the top to the SW. The centre of this depression is not in the middle of the mound but is offset to the SW where the sidescan sonar image shows a very dark acoustic shadow (figure 3.9, 3.23). The centre of the mound is therefore surrounded by a rim which makes the interpretation of the sidescan sonar image more difficult due to the strong shadows, and one has always to bear in mind from which direction (i. e. track line) the seafloor was imaged. The seafloor observations along the NE flank (profile 3 in figure 3.9) show that the upslope mound flank is covered by soft sediments even where the sidescan sonar image shows a high backscatter. This may be due to the relatively steep gradient at the mound base, which can cause an increase in backscatter due to a steeper incidence angle (see chapter 4). In the top area the lithological interpretation is based to a large degree on direct seafloor observations, only around the summit the interpretation is possible on the basis of the acoustic backscatter facies. Authigenic carbonates are visible mainly along the flanks and the crest of the rim as smaller detritus or larger blocks of 1.0–1.5 m size (figure 3.21, Quetzal A, B). Some clams, few tubeworms and at one spot possibly a small patch of bacterial mats are observed, but with the overall impression along the video sled profiles, that Mound Quetzal is not very active with respect to present fluid venting.

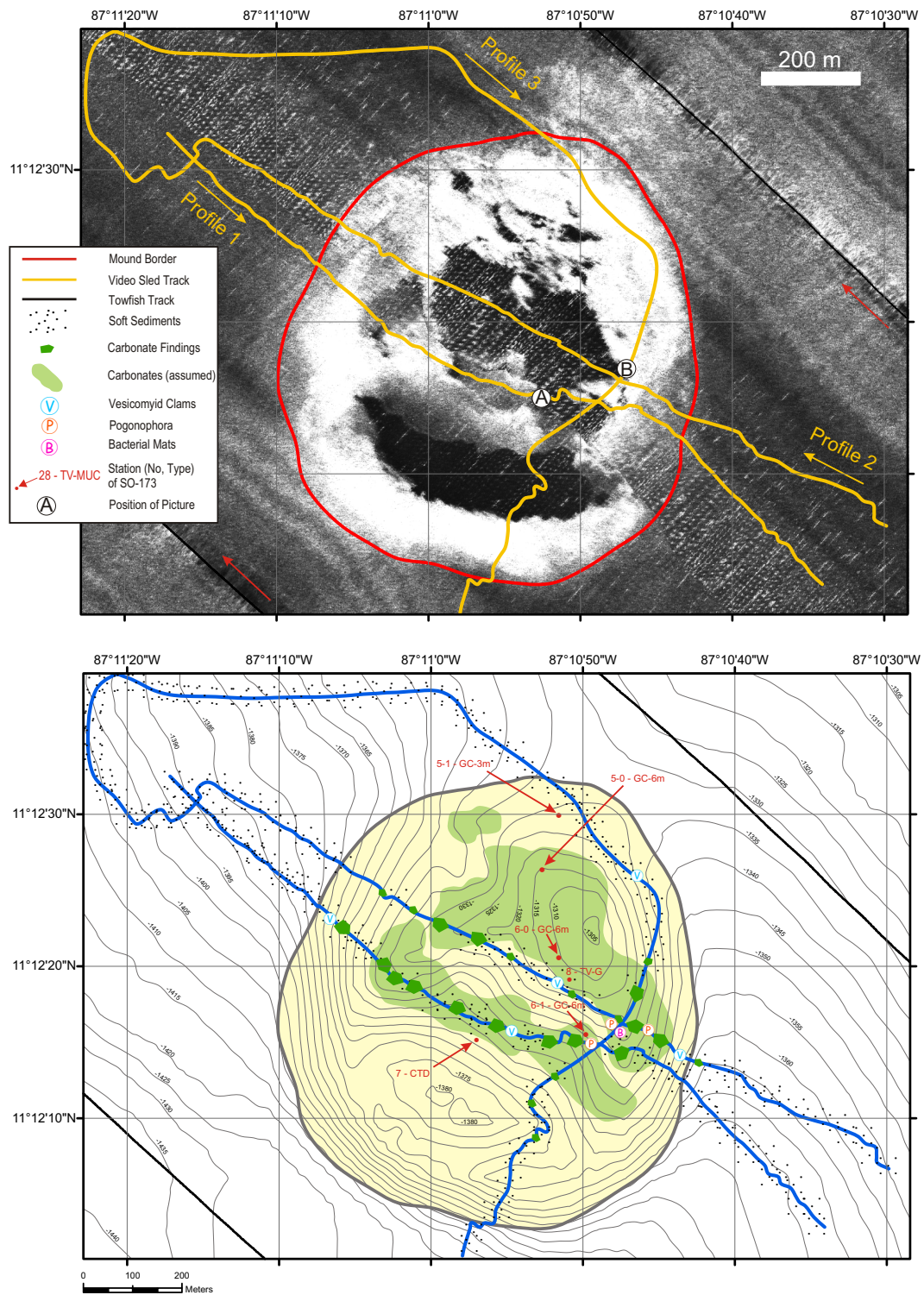


Figure 3.9: Detailed sidescan sonar map with video sled profiles over Mound Quetzal (top), and interpretation of seafloor observations (bottom). Symbols represent direct observations, light green areas are interpreted as authigenic carbonate formations.

Mound Iguana Mound Iguana is located on the shoulder of a canyon in about 1210 m water depth and shows very little topographic relief with an elevation of about 20 m and a size of approximately 380×480 m (figure 3.5, 3.12). In the sidescan sonar data it is imaged with a very bright and uniform backscatter signal which has a very sharp but irregular border to the surrounding normal amplitude values (figure 3.11). The southern and southwestern border of the high amplitude values in the sidescan sonar image correlate with (fractured) authigenic carbonate observations on the seafloor (figure 3.21, Iguana A), whereas in the north and northeast the amplitude values are still very high even when the seafloor observations show hemipelagic sediment coverage and less carbonate detritus, but with indications of venting activity through the presence of vent fauna or even bacterial mats (figure 3.21, Iguana C). The sedimentary coverage seems to increase in thickness towards the landward side of the mound. It can be speculated that beneath the observed soft sediments a hard reflector or scattered carbonate rocks contribute to the backscatter signal. The seafloor observations along the southern border of the mound show several occurrences of vent fauna or hints for seepage along cracks and fractures in the (massive) carbonates, indicating presumably ongoing fluid venting activity (figure 3.21, Iguana B,D). The subbottom profile over the mound shows onlapping sedimentary sequences on both sides and only about 250 m where the mound facies directly outcrops at the seafloor, which correlates quite well with the sidescan sonar image. The mound body with the mound facies seems to be characterized by diapiric structures indicating an upward squeezing of the sediments (figure 3.10). But this could also be a misinterpretation and the observed structures are caused by diffracted reflections.

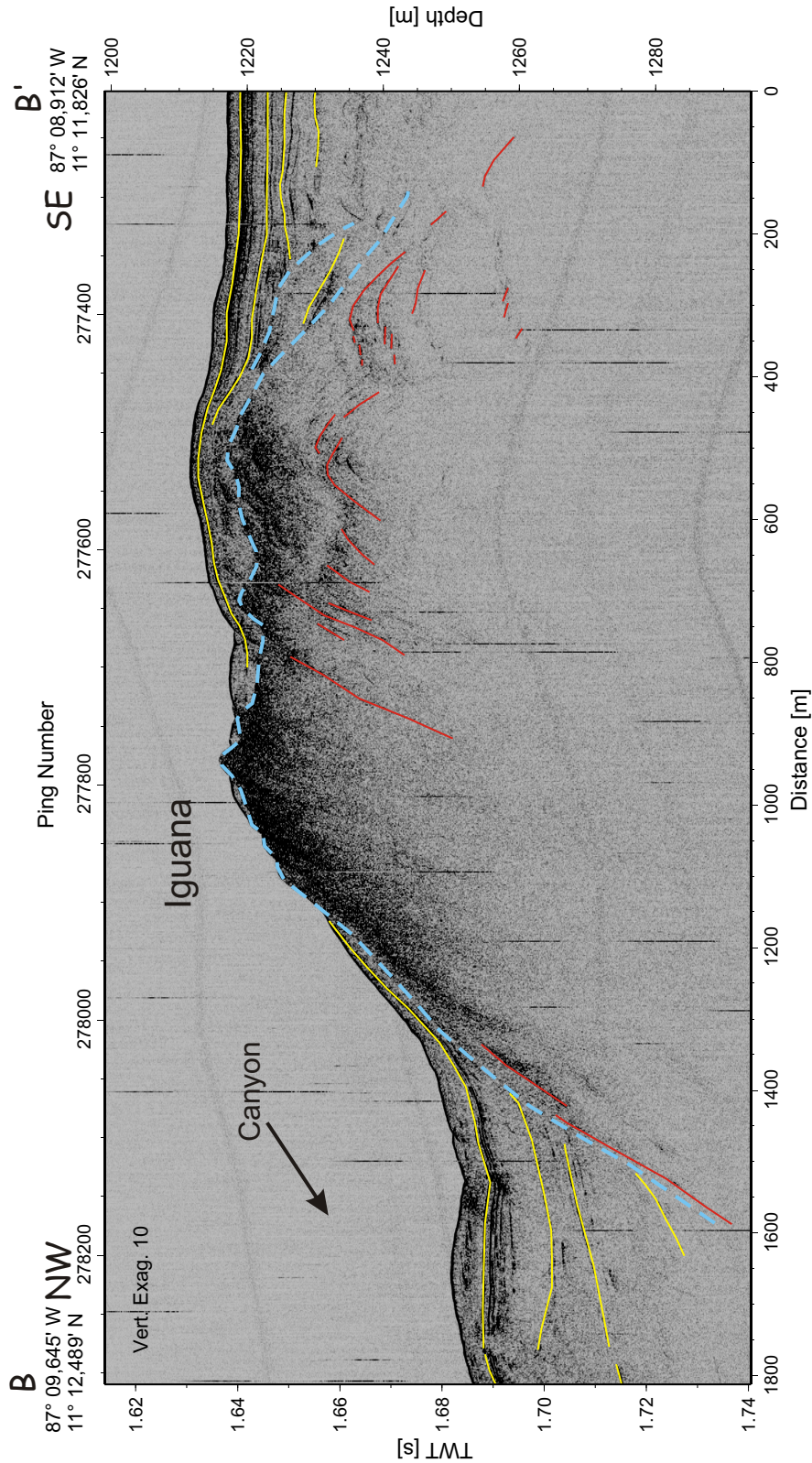


Figure 3.10: Subbottom profile across Mound Iguana. For location of profile see figure 3.5. Blue: border of mound facies; red: structures inside mound; yellow: hemipelagic sediment layers. Mound Iguana is characterized by diapiric structures inside the mound, and onlapping hemipelagic sediment layers. It is situated on the shoulder of a larger canyon.

3.2. MOUND STRUCTURES IN DIFFERENT (TECTONIC) SETTINGS

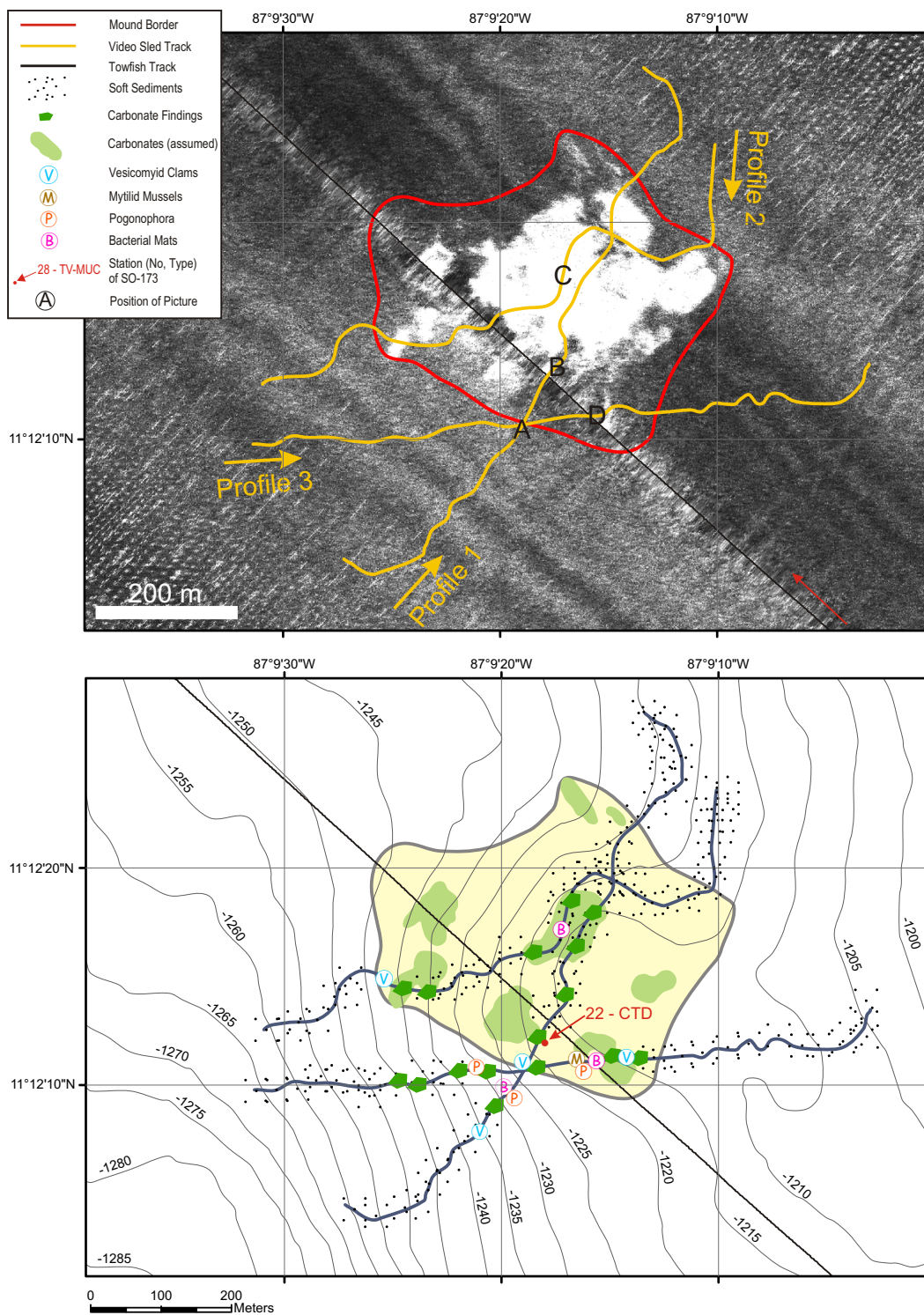


Figure 3.11: Detailed sidescan sonar map with video sled profiles over Mound Iguana (top), and interpretation of seafloor observations (bottom). Symbols represent direct observations, light green areas are interpreted as authigenic carbonate formations.

Sub-seafloor structure – early stage of a mound ridge? In the subbottom profiles across Mound Iguana and its elongation to the SE, the sub-seafloor NW of Mound Buho and the next profile further downslope (i. e. profiles 4, 5, and 6 in figure 3.12), a diapiric structure in the sub-seafloor can be traced across the slope (figure 3.13). It seems to extend over quite a large distance, slightly offset beneath the crest of a little updoming ridge. Its estimated extension is indicated in figure 3.12. At the seafloor surface the sidescan sonar image does not show clear indications for the existence of this structure. Only at Mound Iguana it reaches the seafloor, and also a very small intensity anomaly (A_C2) seems to be related to this feature in the subbottom. Assuming that along this diapiric structure methane-rich fluids are ascending, and interact with infiltrating seawater to form authigenic carbonates, and that in a later stage some denudation and linear erosion shapes the slope, it seems possible that such a sub-seafloor linear feature is evolving into a mound ridge as imaged further south in the survey area (see figure 3.18).

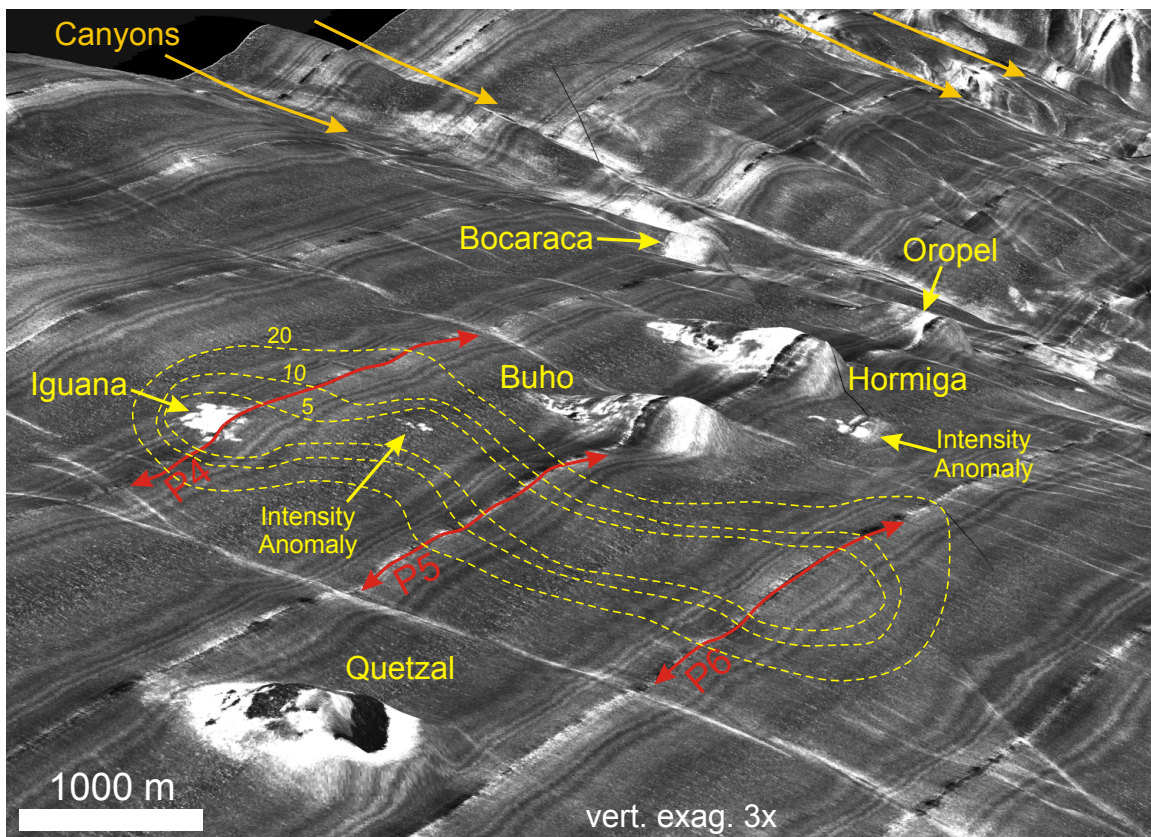


Figure 3.12: Drape of sidescan sonar image over *Digital Elevation Model* (DEM) of the seafloor, showing relatively smooth seafloor of Central Area with several mounds and intensity anomalies, and deeply incised canyons further to the southeast. Subbottom profiles along red lines are shown in figure 3.13. Contour lines denote estimated depth of top of mound facies in metres below seafloor, based on cross-sections.

3.2. MOUND STRUCTURES IN DIFFERENT (TECTONIC) SETTINGS

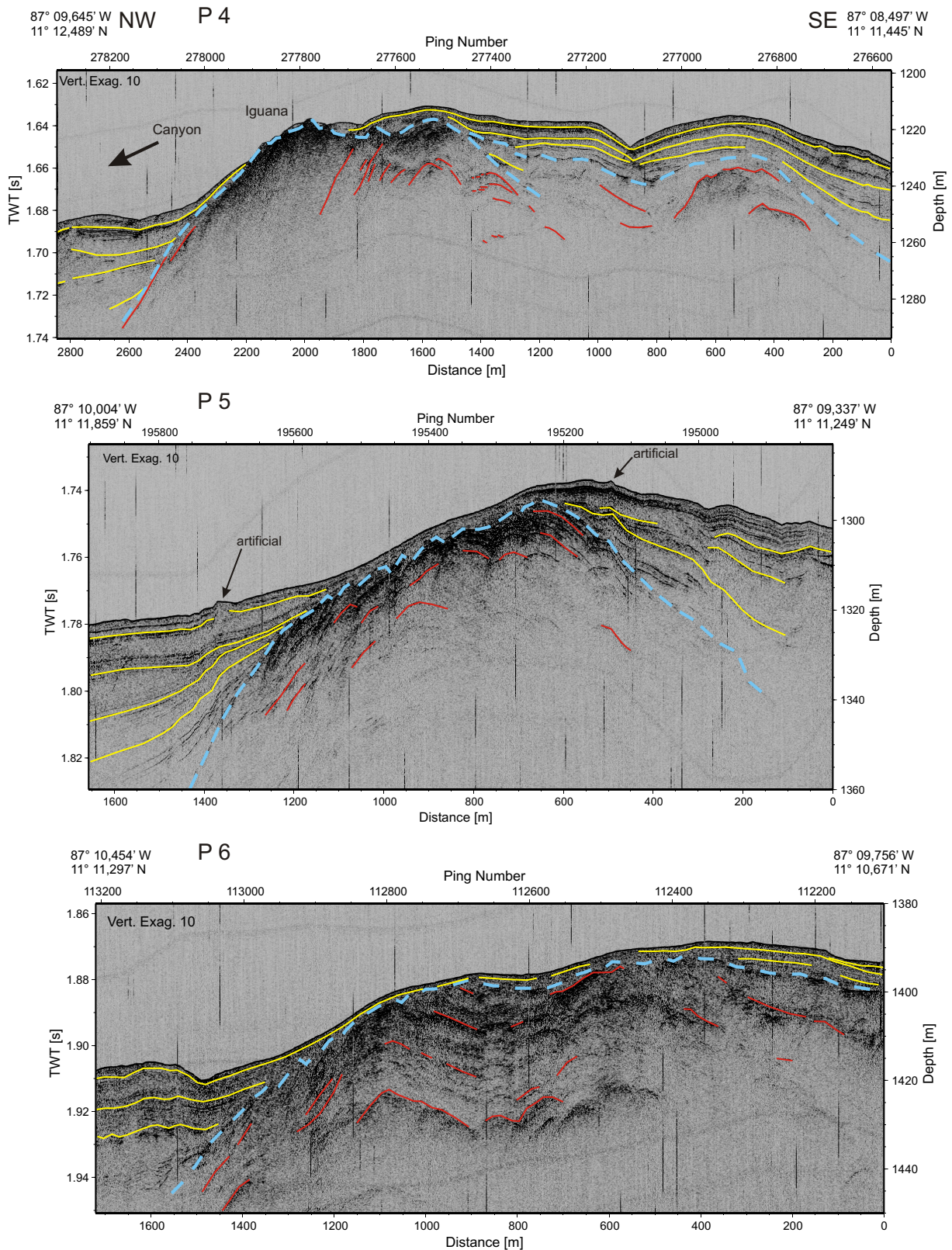


Figure 3.13: Subbottom profiles of sub-seafloor structure of Mound Iguana and two parallel cross-sections further downslope. For location of profiles see figure 3.12. Assuming that denudation and erosion will shape this part of the slope, the sub-seafloor structure could develop into a mound ridge (cf. figure 3.18).

3.2.3 Baula Massive

The Baula Massive is located upslope of the Central Area in about 800–900 m water depth above an escarpment (figure 3.14). It consists of a group of mounds with similar morphologies and backscatter facies. The Mounds Baula II, IV and V are placed right at the escarpment and there are some indications for slumping or sediment creeping observed in the sidescan sonar image. Inferring from seafloor observations on Mound Baula I, it can be assumed that also on the top area plateaus of the other mounds extensive carbonate pavement occurs. The subbottom profiles show almost complete unstructured mound facies without significant layered sediments (figure 3.15). There are no sediment deposits in the bordering canyons, the environment seems to be highly erosive. The escarpment is probably a tectonic lineament, perhaps morphologically shaped by the resistivity difference between carbonate bearing mound facies upslope and softer sediments downslope.

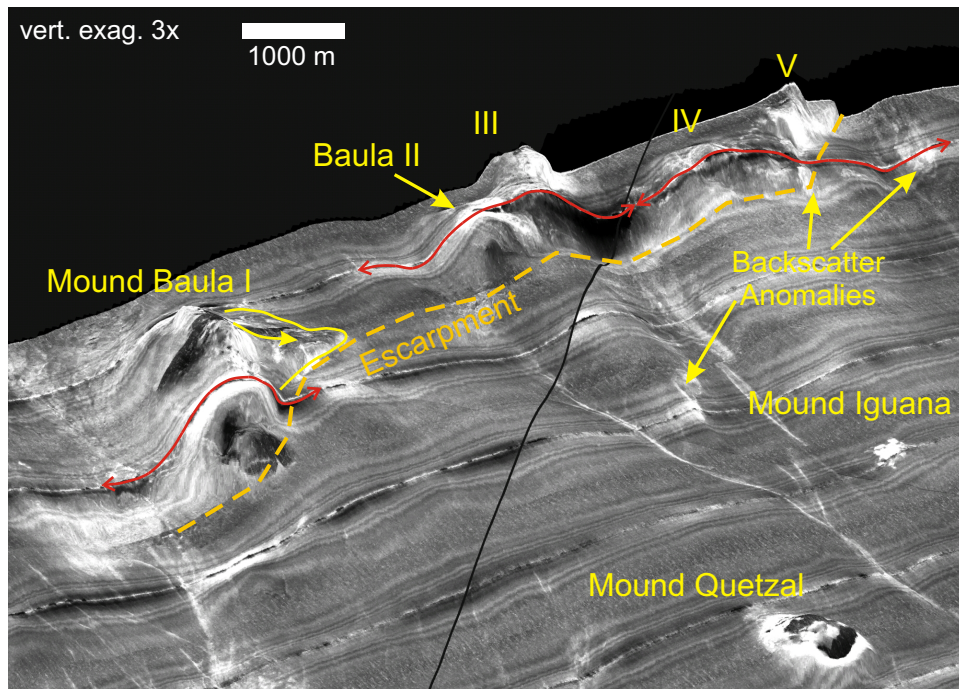


Figure 3.14: Drape of sidescan sonar image over *Digital Elevation Model* (DEM) of the seafloor. The Baula Massive consists of several similar mounds of extraordinary size (numbered I–V), located above an escarpment upslope of the Central Area. Mound Baula I is the largest mound discovered with a base of 2150×1630 m and a height of up to 180 m. Subbottom profiles along red lines are shown in figure 3.15, and reveal unstructured mound facies without any signs of layered sediment coverage.

3.2. MOUND STRUCTURES IN DIFFERENT (TECTONIC) SETTINGS

Mound Baula I Mound Baula I is the largest mound of the Baula Massive and in the survey area. It is located in 870 m water depth. Its elongated shape has a long axis of 2150 m and a short axis of 1630 m. The elevation is approximately 180 m measured slope-parallel and exceeds the heights of all the other mounds in the survey area. The top of the mound consists of two small summits separated by a flat depression, perhaps generated by a slump to the SE (figure 3.16). Seafloor observations show widespread carbonate pavement in the top area, sometimes fractured, forming blocks several meters thick (figure 3.21, Baula A). Vent fauna is not very abundant, some vesicomid clam clusters of approximately 1–2 m size are observed along the NE border of the carbonate pavement to the surrounding soft sediment. Despite the large amount of authigenic carbonates the mound does not make the impression of present high fluid venting activity. Concluding from the abundance of carbonates the mound has either a high age or was very active in the past. Similar to Mound Carablanca at the base of Mound Baula some circular lineaments of higher backscatter are visible in the sidescan sonar image. Again it is possible to correlate such a feature in the sidescan image with an outcropping carbonate ridge of approximately 1 m thickness observed on the seafloor (figure 3.21, Baula B).

CHAPTER 3. MOUND STRUCTURES OFFSHORE NICARAGUA

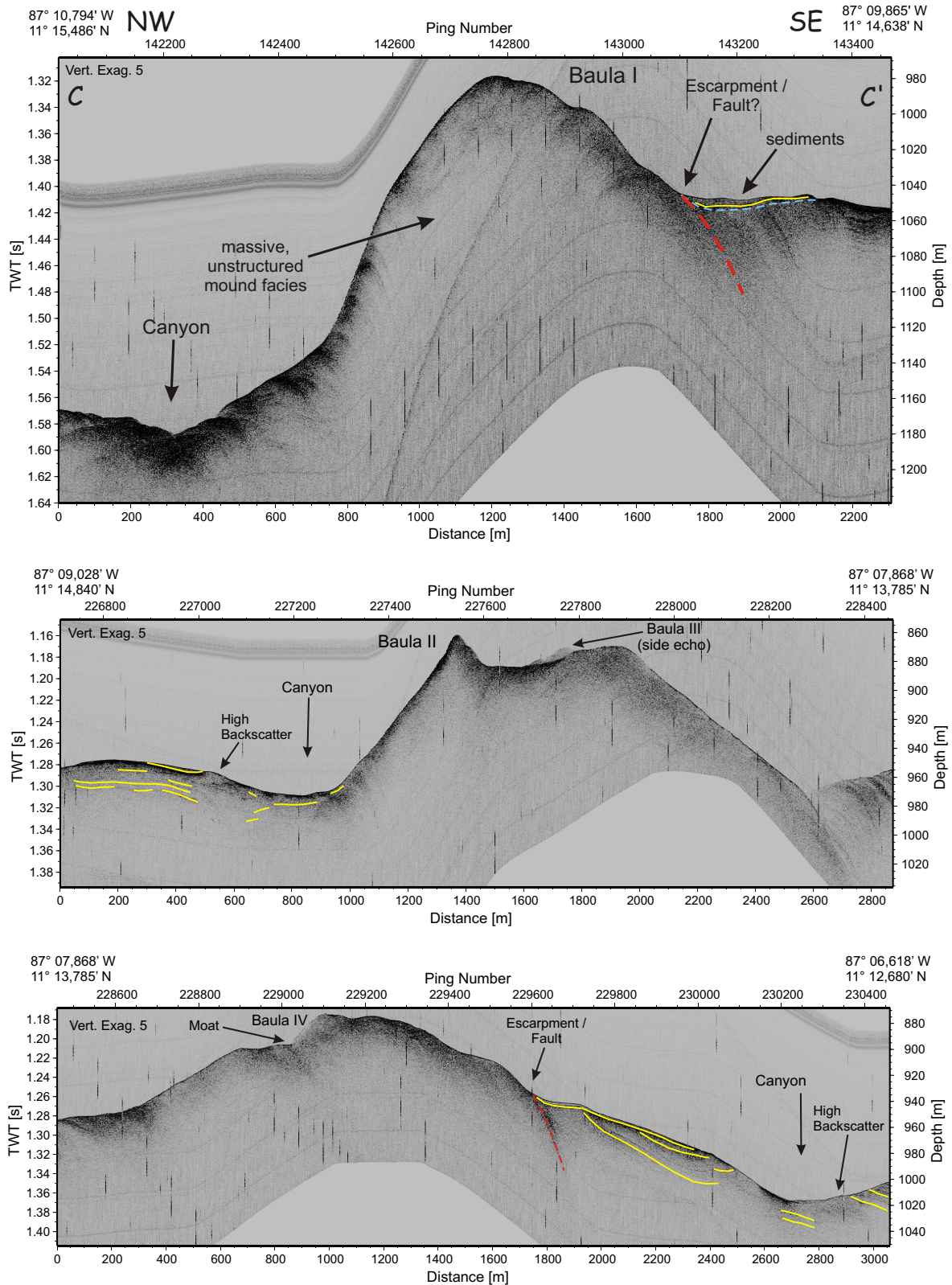


Figure 3.15: Subbottom profiles across Mound Baula I (top), Mound Baula II & III (middle) and Mound Baula IV & V (bottom). For location of profiles see figure 3.14. Blue: border of mound facies; red: faults; yellow: hemipelagic sediment layers. Mounds of Baula Massive show almost complete unstructured mound facies in subbottom profiles.

3.2. MOUND STRUCTURES IN DIFFERENT (TECTONIC) SETTINGS

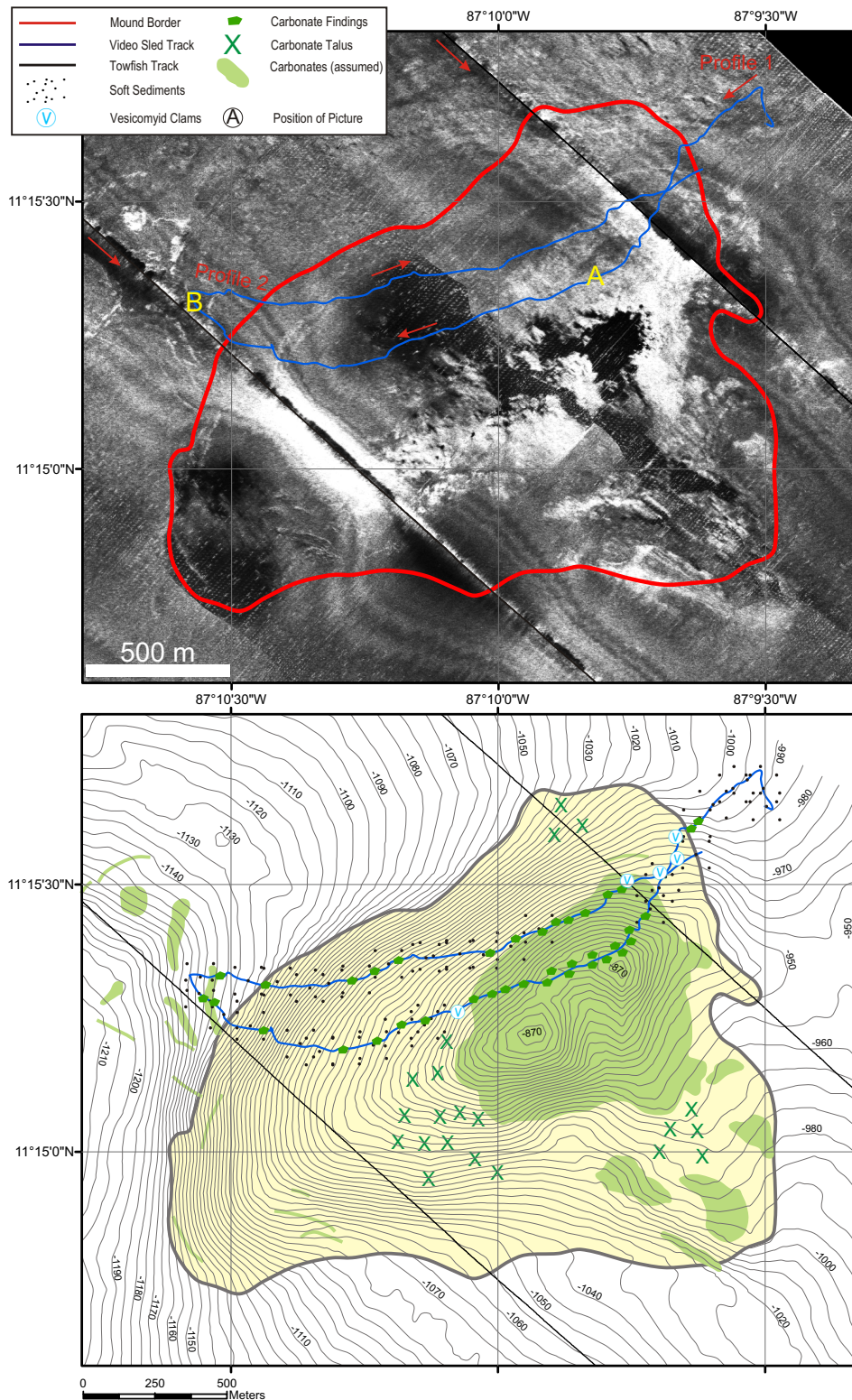


Figure 3.16: Detailed sidescan sonar map with video sled profiles over Mound Baula I (top), and interpretation of seafloor observations (bottom). Symbols represent direct observations, light green areas are interpreted as authigenic carbonate formations.

3.2.4 Mound Perezoso & Mound Colibri

Mound Perezoso and Mound Colibri are located in the southeast corner of the survey area at a similar water depth as the Baula Massive. While Mound Perezoso resembles the Baula Mounds in morphology and backscatter facies, Mound Colibri has more similarities to the mounds of the Mound Ridges (see 3.2.5). Perezoso is characterized by its cone shape with very steep flanks and a very high backscatter signal. It has a height of 130 m with a size of 940×780 m. The top is partly in the acoustic shadow due to a central depression. Mound Colibri is much smaller with a height of only 30 m and a size of 620×580 m. Part of the top area has slumped to the south leading to a small depression.

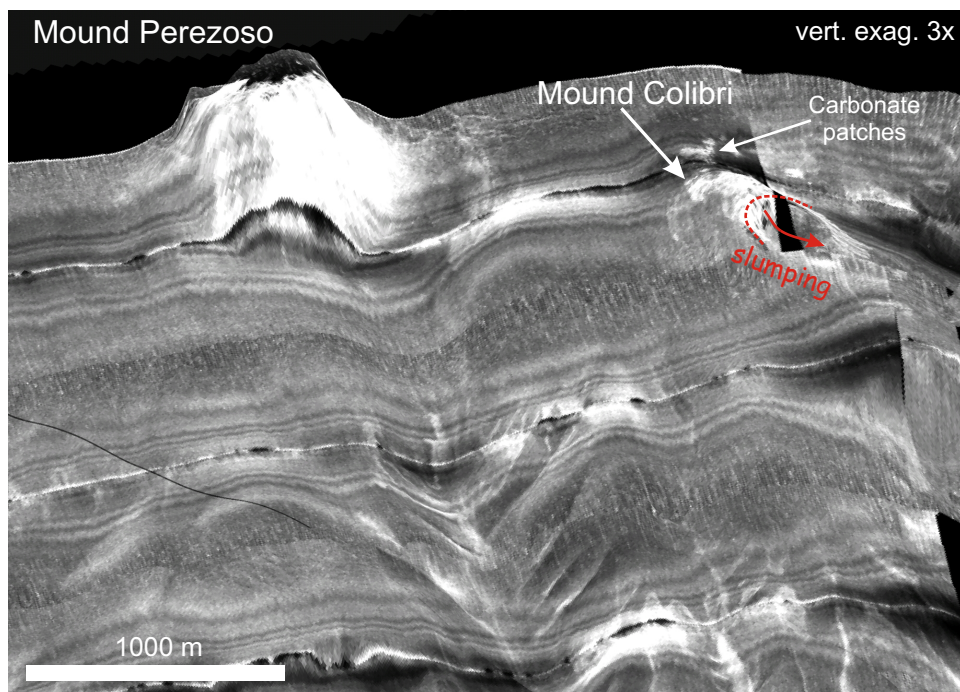


Figure 3.17: Drape of sidescan sonar image over *Digital Elevation Model* (DEM) of the seafloor, showing Mound Perezoso and Colibri. Cone-shaped Mound Perezoso is characterised by very steep flanks with high backscatter and a depression on top, and is of a similar type as mounds of Baula Massive. Both are located in approximately the same water depth. Mound Colibri is a small, hill-shaped mound with patchy high backscatter on top and some slumping to the south.

3.2.5 Mound Ridges

In the southeast part of the survey area where deeply incised canyons cross the slope, several mounds have been observed in a linear orientation on downslope trending ridges (figure 3.18). The canyons show a maximum depth of 150 m and a width of up to 2 km. The canyon floors are usually characterized by higher backscatter, which results probably from the coarser material transported along their thalweg. In the seafloor observations at the beginning of the video sled profile over Mound Morpho instead, it was not possible to recognize an increased coarseness of the sediments, when the small channel along the SE flank of the mound was crossed. But this could be different in the large canyons. In the upslope region the morphology of the smooth seafloor shows large plateau-like areas which separate the canyons. Further downslope small gullies originate on this plateaus and contribute to the main canyons. The distinct mound ridges developed in the lowermost part between 1650 m and 2100 m water depth. While Mound Ridge I is very short and consists of only two mounds, five mounds and several intensity anomalies form Mound Ridge II. At first glance Mound Ridge III has about the same length as Mound Ridge II, but following the smoothly curved ridge upslope, another small mound or intensity anomaly with very little topographic relief shines through the hemipelagic seafloor coverage at about 1190 m water depth. One can speculate whether erosion of the soft sediments on the topographic ridge between these mounds would reveal other occurrences of mound structures. The analysis of several subbottom profiles crossing the mound ridges gives clear evidence of erosion of sedimentary layers along the flanks of the canyons or gullies and shows sometimes the deposition of overbank sediments on the shoulders of the canyons or in some higher parts on the mounds itself.

Mound Morpho on Mound Ridge III Mound Morpho is located on Mound Ridge III in a water depth of 1660 m. It has an elongated shape with a size of 1360×730 m and a height of 70 m. The top area is characterized by a rough small-scale topography which causes dark shadow areas in the bright backscatter (figure 3.20). The rugged morphology on top can also be seen in the subbottom profile over the mound (figure 3.19). The steep flanks of the mound are not covered with thicker sediment layers. To the northwest a larger canyon borders the mound, in the smaller gully to the southeast some dewatering structures are visible. Seafloor observations from the mound show a large number of alive vesicomid clam fields, approximately 1 m in size, settling in the soft sediment ponds besides the carbonate patches (figure 3.21, Morpho A). The authigenic carbonates are exposed on the topographic elevations, whereas the depressions are covered with thicker sediments. A carbonate ridge observed at the seafloor almost at the end of the video sled profile probably correlates with a high backscatter lineament in the sidescan sonar image (figure 3.21, Morpho B). The misfit between the recorded time in the video tape and the video sled navigation on the seafloor is in the range of normal navigation errors.

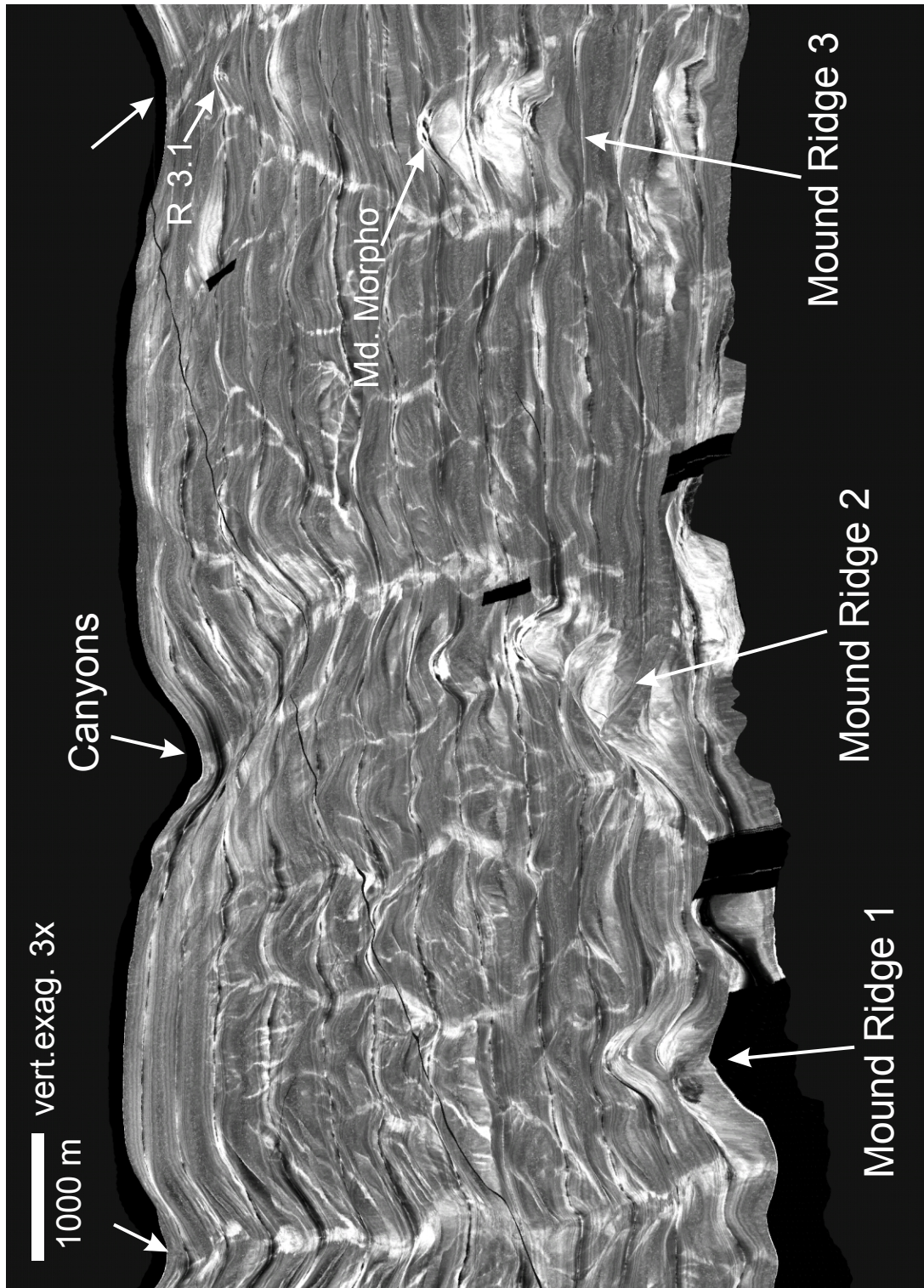


Figure 3.18: Drape of sidescan sonar image over *Digital Elevation Model* (DEM) of the seafloor, showing canyons and mound ridges in the southern part of the survey area. The mound ridges can be followed upslope to different water depths and consist of different numbers of mounds.

3.2. MOUND STRUCTURES IN DIFFERENT (TECTONIC) SETTINGS

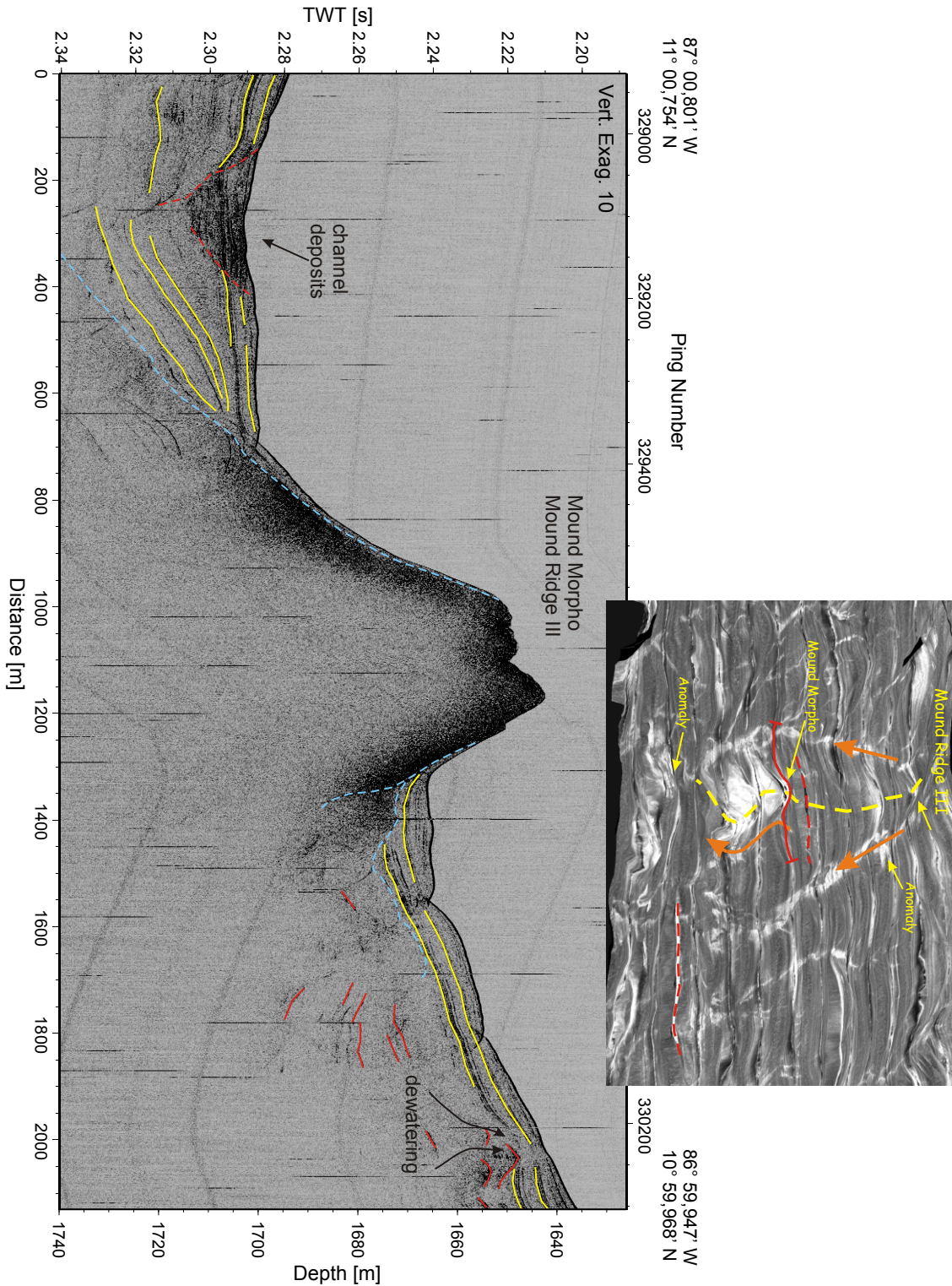


Figure 3.19: Subbottom profile across Mound Morpho on Mound Ridge III. Small inset shows location of profile. Note channel deposits in larger canyon NW of ridge and possible dewatering structure in gully SE of ridge. Top of mound shows rugged topography leading to shadows in sidescan sonar image (see figure 3.20). Blue: border of mound facies; red: structures inside mound; yellow: hemipelagic sediment layers; red dashed: faults.

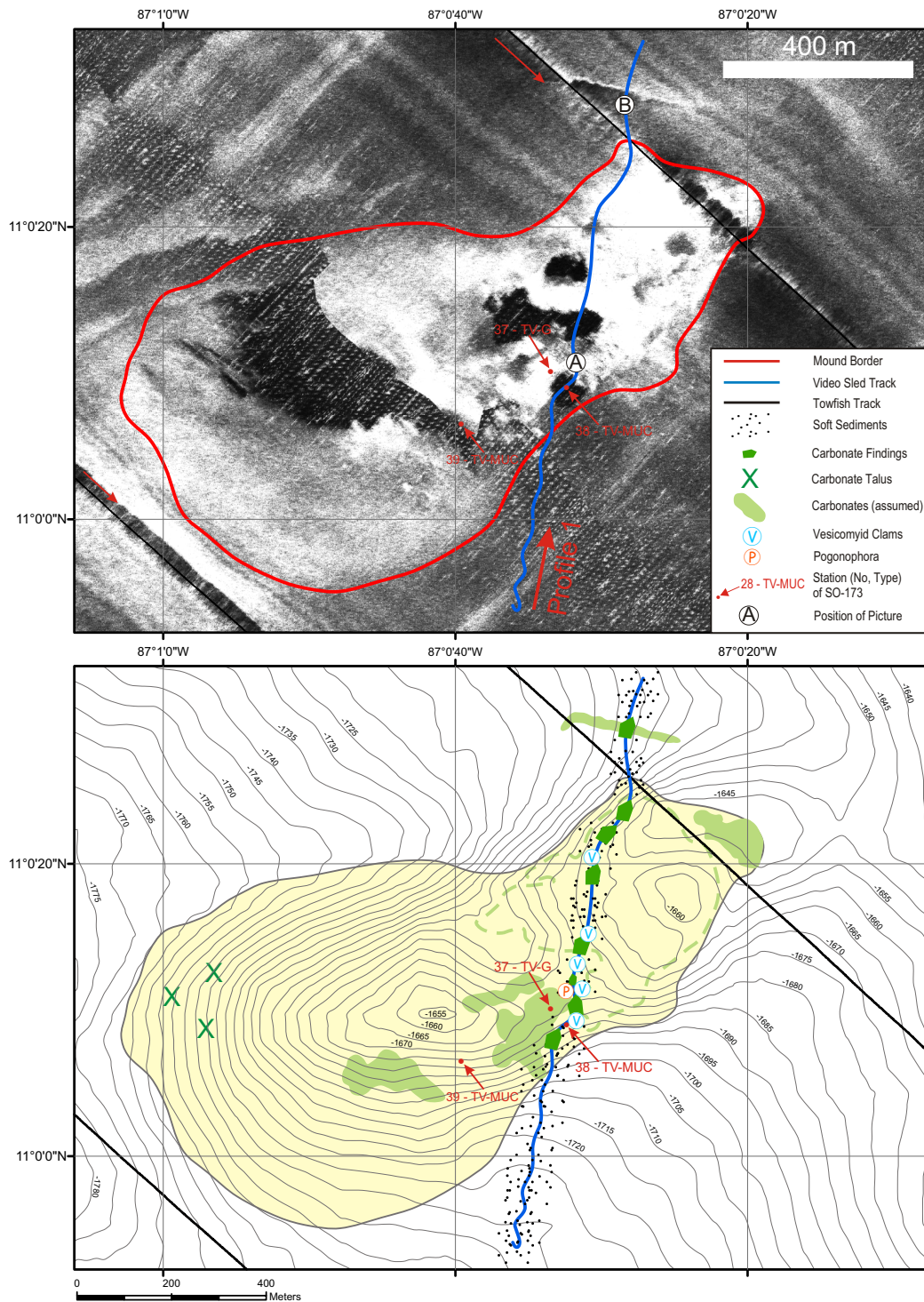


Figure 3.20: Detailed sidescan sonar map with video sled profiles over Mound Morpho (top), and interpretation of seafloor observations (bottom). Symbols represent direct observations, light green areas are interpreted as authigenic carbonate formations.

3.2. MOUND STRUCTURES IN DIFFERENT (TECTONIC) SETTINGS

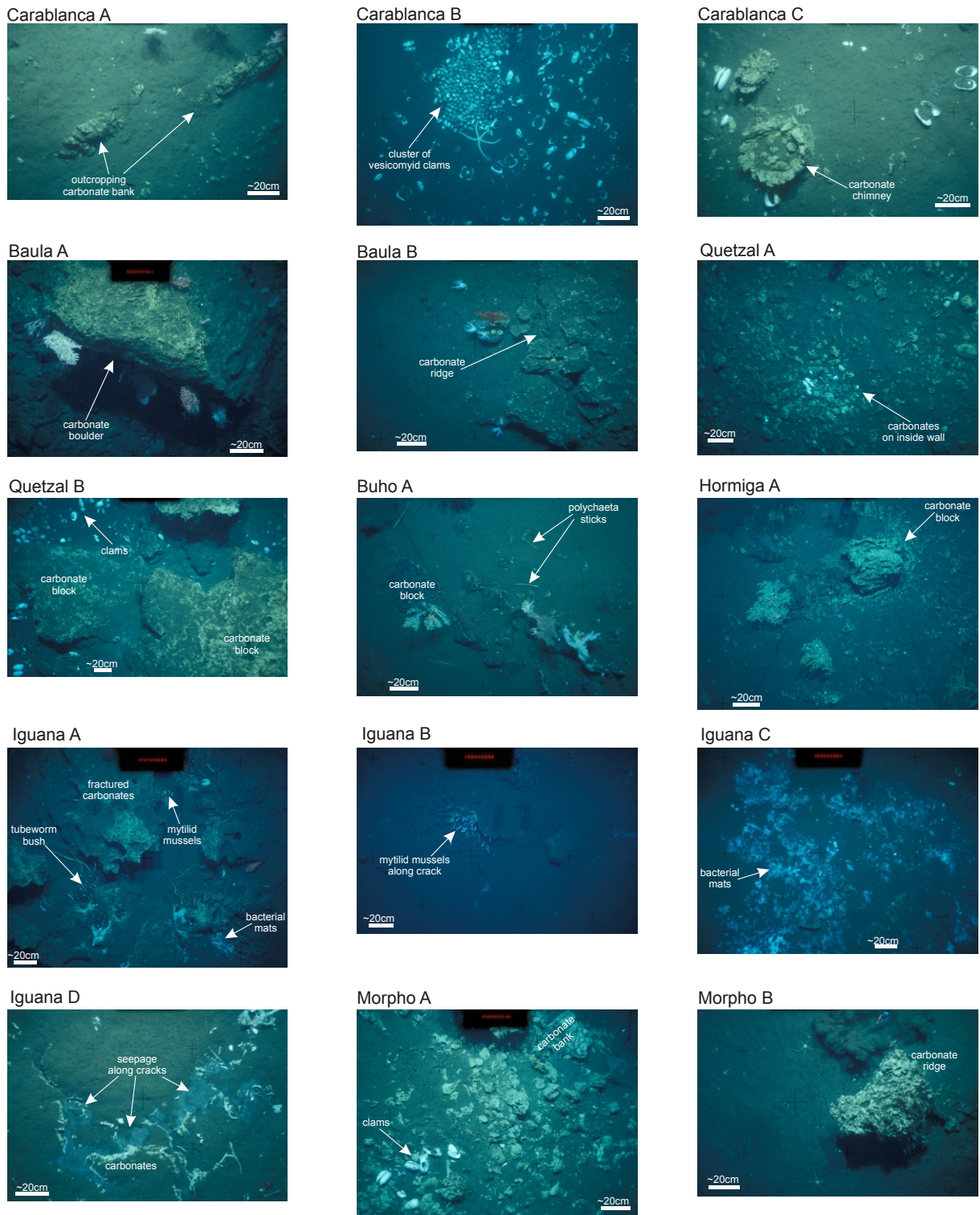


Figure 3.21: Pictures taken with seafloor observation system during surveys on several mounds. The capital letters (A,B,C,D) refer to locations shown in detailed mound maps (figures 3.4, 3.7, 3.8, 3.9, 3.11, 3.16, 3.20). Scale is taken from distance between red laser points, or length of bottom weight.

3.2.6 Gas Hydrates in shallow subsurface and associated gas flares in water column?

In the uppermost profile of the survey area upslope of the Momotombo Slide at a water depth of approximately 1090 m a diffuse bright spot of about 350 m in diameter can be observed in the sidescan sonar map (figure 3.22). It is located on a small and short ridge between two gullies. The backscatter anomaly has a circular shape with varying intensities. The associated subbottom profile shows in this region a very unique structure, which could not be observed in other parts of the survey. Underneath a drape of clearly layered hemipelagic sediments of varying thickness, the profiles reveal an unstructured and uniform facies. The contact to the overlying sediments is very sharp but undulating. Sometimes it shows troughs filled with sediments, sometimes the unstructured facies is outcropping at the seafloor. Often the sediment packages seem to be offset along faults. One of the larger spots where the structureless facies comes directly up to the seafloor can be correlated with a bright backscatter spot in the sidescan sonar data. Because the contact between the unstructured facies and the sediments resemble a gas front with blanking of the signals from the deeper seafloor, the idea is, that the sharp border could be caused by dissociating gas hydrates in the sediment. This would imply a high heatflow to stimulate the generation of free gas, which is contradictory to the calculated heat flow values from the depth of the bottom simulating reflector (BSR) in the deep-tow seismic data. According to Talukder, A. (*pers. comm.*) the heat flow values in this particular region are quite low with values between 20 and 30 mW/m^2 . On the other hand observations of very small, circular to elongated patches (~10–50 m in diameter) could be interpreted as gas flares in the water column [cf. Klaucke et al., 2005]. Unfortunately there is no evidence for flares in the raw data recorded in the time interval between the pulse and the first reflection from the seafloor to proof this hypothesis.

A very different interpretation of the unstructured facies in the subbottom profile would be to assume that it represents a former erosional surface with an older and higher compacted lithology underneath a drape of fresh hemipelagic sediments. Especially on the left hand side of the subbottom profile (NW end of the profile in the map) a larger canyon seems to erode the seafloor and the structureless facies crops out along the whole flank of the canyon (figure 3.22). But in the sidescan map this flank shows no unusual backscatter. Following this interpretation, the hemipelagic sediments would have been deposited discordantly on the unstructured facies and there would be a hiatus in between.

Which of the two interpretations is the correct one can only be proofed by e.g. direct observations of gas flares in the water column or by drilling into the seafloor at the locations where the structureless facies is close enough to the surface. Due to the general appearance of the seafloor morphology in this region upslope of the Momotombo Slide where canyons are incised into the seafloor, I favour the erosional hypothesis. Perhaps the higher erosion rates were related to the event of the Momotombo Slide itself, which led to a steeper gradient and thus faster downslope transport mechanisms. In this case the discordance can be helpful for the determination of the age of the Momotombo Slide.

3.2. MOUND STRUCTURES IN DIFFERENT (TECTONIC) SETTINGS

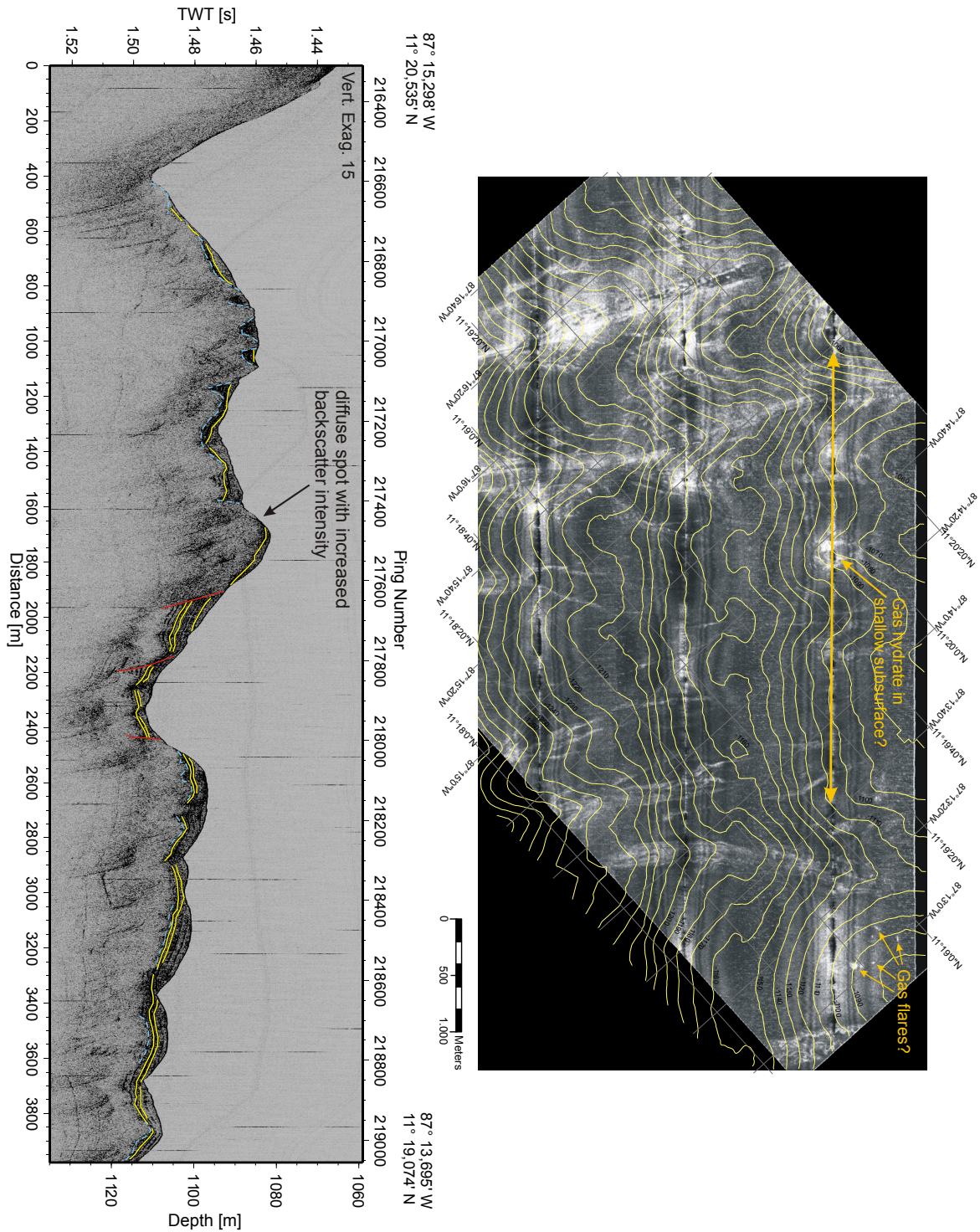


Figure 3.22: Sidescan sonar image and subbottom profile of possible gas hydrate occurrences in the northern, upslope part of survey area. Diffuse, high backscatter spots in sidescan image correlate with outcropping of unstructured subbottom profile facies in cross-section. Additionally some small, circular bright spots could be interpreted as gas flares in the water column which could result from the dissociation of gas hydrate. See discussion in text.

3.3 Mound Volume Calculations

Because of the different types of mound morphologies, the question is, whether these different types do have an expression in a morphometric number. Therefore volume and associated base area were calculated for each mound. The ratio (mound volume/base area) is a characteristic index or classification number which can be compared.

3.3.1 Methodology

To calculate a mound volume, the bathymetry grid, clipped along the base area of the mound, is converted into a *Triangular Irregular Network* (TIN). The base of a mound is determined by the change in the gradient (bend or kink in morphology). The mound- or base area is the area enclosed by several tangents along the mound base. The volume of a mound is then by definition the volume between the horizontal base plane in the lowermost point of the mound base and the triangular irregular network. Figure 3.23 visualizes some mound TINs with horizontal base planes and calculated volumes in between. There are several geological reasons why it should be allowed to assume a horizontal base plane, and not a slope parallel one: A mound in my understanding does not only have a feeder channel with a small diameter, where material erupts and forms a large surface structure, like it is the case for a mud volcano, but a mound is a seep structure, where upward travelling fluids alter the sub-surface sediments in a large area, and precipitation of authigenic carbonates occurs. The mound is therefore only the peak, and seepage affected material will be probably found below the whole area of the mound. Then it is reasonable to include the volume down to the deepest level where mound material has been found, into the calculations. The volume depends then strongly on the erosion level.

In table 3.1 28 mound structures with their morphometric numbers are listed, in increasing order of the volume/base area index. Additionally Mound 11 and 12 and Mound Culebra from offshore Costa Rica have been added for comparison. For Mound Culebra two calculations are given, one with values for base area and mound volume from Moerz et al. [2005], and one calculated with the methodology as described above. While the numbers for the base area are almost identical, the volumes differ by a factor of 3, and hence the volume/base area index numbers do. This is due to a different methodology. The cited Mound Culebra volume was calculated assuming not a horizontal base plane, but a slope parallel one (*Moerz, T., pers. comm.*).

The values for the volume/base area index show a large range, roughly between 20 and 180. According to the mound classification in section 3.2, the (small) mounds of type II (e.g. Mound Iguana) have numbers between 20 and 40, the (middle-sized) mounds of type I (e.g. Mound Quetzal) are in a range between 40 and 60 and the (large) mounds of type III (e.g. Mounds of Baula Massive) have numbers larger than 60, up to 180. These numbers can be seen as an expression of how much a mound structure is elevated above the surrounding seafloor surface. The Mounds 11 and 12 are at the very lowermost part of the spectrum, and seem to resemble pure fluid venting sites without major topographic

3.3. MOUND VOLUME CALCULATIONS

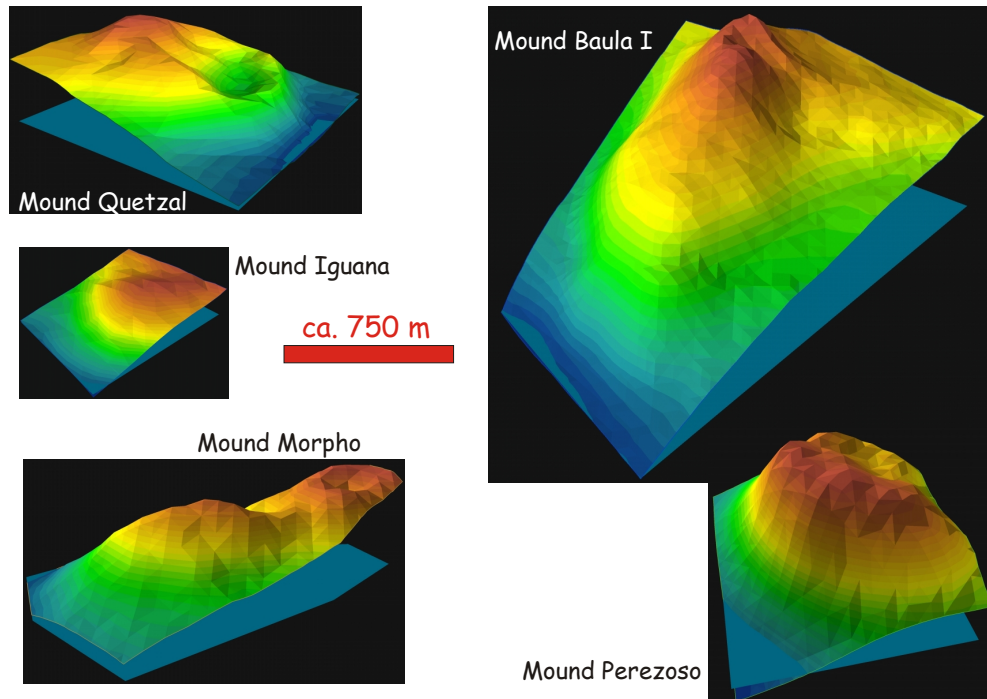


Figure 3.23: Triangular Irregular Networks (TINs) demonstrate the variety in morphology and size of mounds. TINs are generated from multibeam bathymetry. Volume of mounds is calculated between horizontal base area (blue plane) and mound surface represented by TIN meshes. Geological reasoning allows to use horizontal instead of slope parallel plane.

expression, or they consist of a very liquid material (mud!?) which tends to spread out very easily [cf. Klaucke et al., subm.]. Mound Culebra however has a quite large index number (104,0) and is well exposed above the seafloor surface.

An analysis of these index numbers does not show a clustering, but shows more or less a continuous trend between 20 and 100, with few outliers larger than 100. Also a plot of the calculated mound volumes against their base areas does not reveal a clustering with respect to their sizes (see figure 3.24). Note that a mound volume/base area index is the gradient of the line from the origin to the point in the diagram. The index number is not necessarily related to the size of a mound, even when the correlation seems to be that larger mounds tend to have higher index numbers than smaller ones. In the diagram the trend line through all plotted mounds is drawn. Mounds with higher volume/base area index numbers plot above this line, mounds with smaller index numbers plot below the line.

The comparison of the actual mound (TIN) surface (3D-Area) with the base plane area (2D-Area), is a measure of how much the plane area is stretched to fit the real (3D) mound morphology. The general trend is that the ratio of 3D-/2D-Area is increasing with increasing volume/base area index (see table 3.1).

Mound	Base [m]	3D-Area [m ²]	2D-Area [m ²]	Volume [m ³]	Cube [m]	3D/2D -Area	Vol./ 2D-A.
Mound 11	-1.047	218.550	217.439	3.670.815	154,3	1,0051	16,9
Mound 12	-1.018	257.613	256.035	4.778.238	168,4	1,0062	18,7
Iguana	-1.250	273.982	272.814	6.558.594	187,2	1,0043	24,0
R3.1	-1.230	204.241	202.731	5.579.885	177,4	1,0074	27,5
Colibri	-1.000	399.372	392.448	13.579.792	238,6	1,0176	34,6
R3.5	-1.940	233.057	228.523	9.331.511	210,5	1,0198	40,8
R2.2	-1.740	338.530	330.648	14.014.342	241,1	1,0238	42,4
Buho	-1.330	735.964	727.209	32.287.835	318,4	1,0120	44,4
Hormiga	-1.340	964.276	949.409	54.188.781	378,4	1,0157	57,1
Quetzal	-1.420	962.902	944.267	55.318.497	381,0	1,0197	58,6
R2.7	-2.270	548.684	531.693	32.131.770	317,9	1,0320	60,4
Tucan	-1.530	1.523.301	1.507.871	91.425.334	450,5	1,0102	60,6
Baula II	-960	577.384	565.507	34.367.002	325,1	1,0210	60,8
Bocaraca	-1.360	416.582	407.058	25.008.424	292,4	1,0234	61,4
Baula IV	-960	361.720	353.670	22.270.487	281,3	1,0228	63,0
R2.4	-1.950	594.021	574.361	36.905.855	332,9	1,0342	64,3
Pargo	-1.640	306.483	295.479	19.324.054	268,4	1,0372	65,4
Morpho	-1.770	929.967	911.473	61.352.948	394,4	1,0203	67,3
R3.4	-1.880	769.579	754.721	52.765.914	375,1	1,0197	69,9
Oropel	-1.450	342.267	333.231	23.922.226	288,1	1,0271	71,8
R1.1	-2.140	879.813	842.952	66.071.094	404,3	1,0437	78,4
Congo	-1.540	914.280	889.927	71.749.446	415,5	1,0274	80,6
Baula V	-950	906.654	856.461	69.496.434	411,1	1,0586	81,1
R2.6	-2.160	1.016.987	980.846	86.993.553	443,1	1,0368	88,7
R2.5	-2.090	1.408.425	1.371.923	128.605.434	504,8	1,0266	93,7
Carablanca	-1.580	923.490	898.565	87.925.798	444,7	1,0277	97,9
R1.2	-2.270	604.416	576.632	57.442.140	385,8	1,0482	99,6
Perezoso	-950	938.813	881.693	88.802.282	446,1	1,0648	100,7
Culebra [calc.]	-1.689	2.147.228	2.085.620	216.918.546	600,9	1,0295	104,0
Culebra [Lit.]	-1.623		2.080.000	73.000.000			35,1
Baula III	-1.010	676.589	644.479	85.879.859	441,2	1,0498	133,3
Baula I	-1.190	3.624.362	3.520.686	620.276.965	852,8	1,0294	176,2

Table 3.1: Morphometric numbers and volumes of mounds offshore Nicaragua. Columns are mound name, depth of base plane, area of mound surface, area of base plane, mound volume, size of cube with same volume, area of mound surface divided by area of base plane, and mound volume divided by area of base plane. This last column gives a measure for how much a mound is raised above the seafloor surface (see text for discussion). Numbers for Mound Culebra [Lit.] are taken from Moerz et al. [2005].

3.3. MOUND VOLUME CALCULATIONS

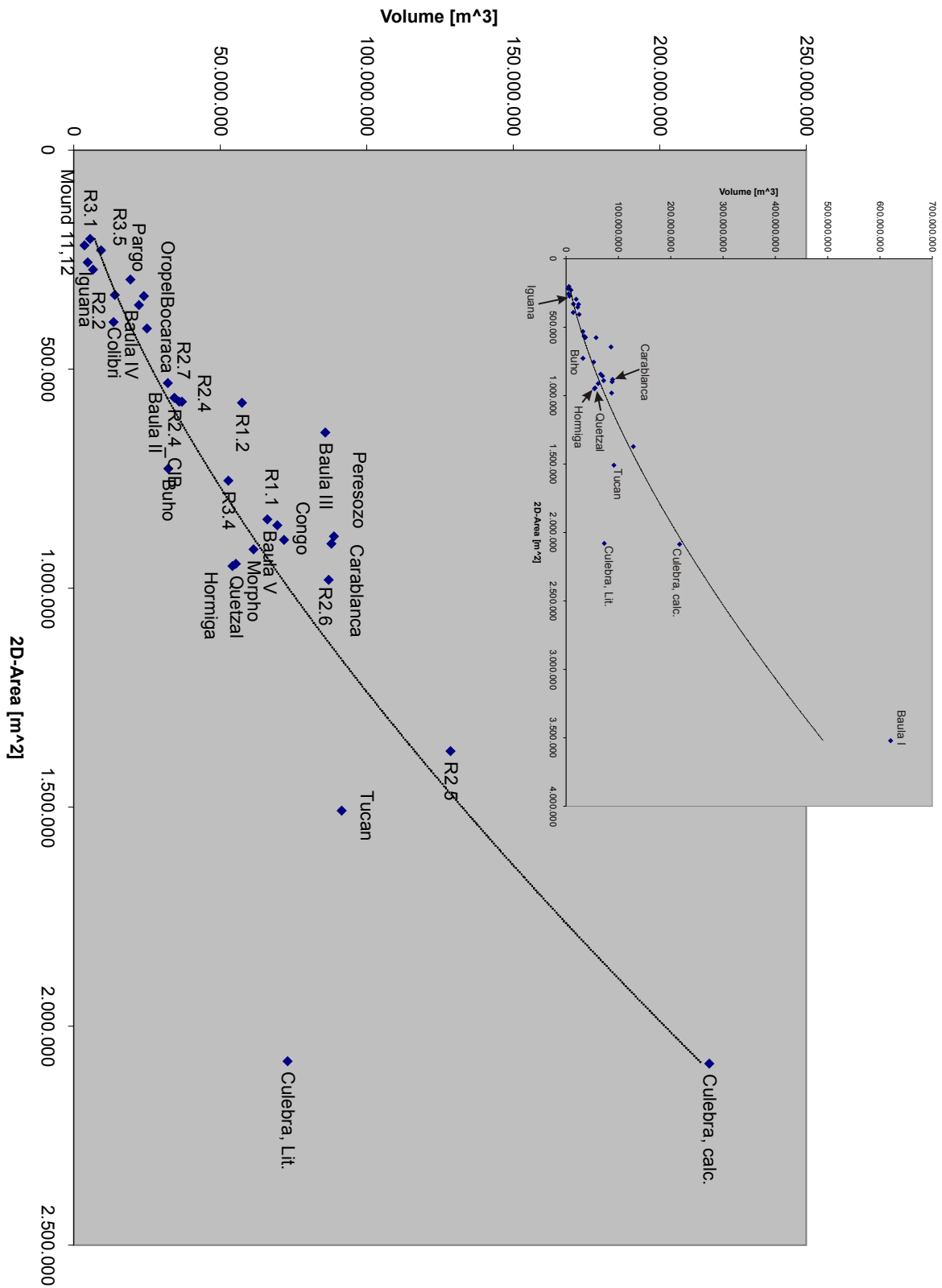


Figure 3.24: Calculated mound volumes plotted against base area. Small inset shows location of exceptionally large Mound Baula I (volume/base area index of 176,2) in diagram.

3.4 Discussion

A large number of so called mound structures or mounds has been identified on the central american margin [Sahling et al., *subm.*]. While the first discoveries were described as mud volcanoes [Shipley et al., 1992; Kimura et al., 1997; Bohrmann et al., 2002], matching the interpretation of the central american subduction zone as an accretionary margin, the nature of these structures became unclear with the evidence that the margin wedge consists of ophiolitic basement. It was questioned whether the observed sediment thicknesses of 500 m at the lower slope to a maximum of 2000 m at the upper slope [Ranero et al., 2000a] are sufficient for real mud diapirism and volcanism. They are very much below thicknesses reported from other diapiric provinces (e. g. Alboran Sea in the Western Mediterranean with 7–9 km sediment thickness, Talukder et al. [2003]). The actual sediment thicknesses below the survey area range from <1 km in the deeper part to about 1.5 km in the upper, shallow part. The *bottom simulating reflector* (BSR) is roughly 450 m below the seafloor. These values are taken from seismic section Nic-220, published by Ranero et al. [2000a], which is basically co-located with profile Nic-80 from McIntosh et al. [submitted, 2005] along the northern border of the survey area (figure 1.2). The sediments below the upper and middle slope can be seismostratigraphically correlated to drillholes in the Sandino Basin and consist of the Units 1, 5, and 6 according to Ranero et al. [2000a]. They range from Late Cretaceous to Middle Eocene and from Middle Miocene to Holocene time, respectively.

In literature it is basically distinguished between *mud volcanoes* and *mud-* or *shale diapirs*. A mud volcano is described as a topographically expressed seafloor edifice, from which mud and fluids flow or erupt. Main morphological elements are one or several craters, peripheral mud flows with a hummocky surface, and gryphons [Milkov, 2000]. The complete and scenic range of features can well be studied on land, and is to a large part applicable to the submarine environment [Planke et al., 2003]. The term *diapir* means “pierce-through” (from greek $\delta\iota\alpha\pi\epsilon\iota\rho\omega$ = *diapairo*), and is defined as a structure that has risen from deep subsurface into shallow sediments or even to the seafloor (*seafloor-piercing diapir*, Milkov [2000]). Characteristic for diapirs is further a density contrast between rising and host material which causes a buoyancy force (i. e. gravitation). This is the main driving mechanism. And finally it is necessary that the material has sufficient plasticity to move [Bahlburg and Breikreuz, 2004, p. 236]. The material uprise is mainly triggered by tectonic processes, e. g. discontinuities along tectonic faults, or tectonic compression or extension. In contrast to mud diapirs with buoyancy as driving force, Brown [1990] introduces the term *diatrema* for upwelling structures which contain sediments, fluidized during rapid fluid advection, and which are directly driven by the hydrogeologic system (i. e. they follow the hydraulic pressure head). A mud volcano as a surface feature can hence develop on top of a seafloor-piercing diapir, or above a diatrema. Important for its development is sufficient fluid migration and sediment fluidization [Milkov, 2000].

In the following I want to discuss the various aspects and arguments favouring or opposing the different possibilities. Fact is, that besides the topographically elevated mounds a

large number of backscatter anomalies, and fluid venting activity is observed. In the sub-bottom, upwelling sedimentary structures have been imaged, and seafloor observations reveal massive findings of authigenic carbonates.

The analysis of the geoaoustic data precludes the interpretation of the mound structures as mud volcanoes. The imaged features offshore Nicaragua do not seem to be typical mud volcanoes as reported from many other sidescan sonar surveys [e. g. Krastel et al., 2003; Vogt et al., 1999; Limonov et al., 1998; Ivanov et al., 1996]. There are no indications of mud flows, which typically show a characteristic “flow banding” pattern in sidescan sonar images. Such a pattern results from topographic irregularities on top of higher viscous mud expulsions [Limonov et al., 1998]. Concentric ring structures as described and imaged from mud volcanoes in the Gulf of Cadiz, originating from periodically fluctuating, near-circular mud expulsions [Murton and Biggs, 2003], are also not observed. The concentric variations in backscatter strength, imaged on Mound Carablanca cannot be related to the undulating surface of a mud flow, as direct investigations with a camera system showed. Instead a high backscatter rim could be correlated with an outcropping carbonate bank (see figure 3.4, 3.21, Carablanca A).

I even speculate that an observed change in the consistency of the sediment, when the distance weight beneath the video sled touched the seafloor along the track over Mound Carablanca, and which roughly paralleled the backscatter variations, results from a bedding of soft sediments and horizons with larger content of carbonate precipitates. It has to be mentioned that the 75 kHz signal penetrates at least a few centimetres into the sediment, so that also a massive carbonate bank, covered with a thin drape of sediment and invisible with a camera system, would result in a high backscatter return.

The change in carbonate concentration in the sediment would originate then from a variation in fluid venting activity and associated carbonate precipitation. Numerical modeling of carbonate precipitation and dissolution in a 2 m long sediment column, located under a bacterial mat at Hydrate Ridge, Cascadia Margin, showed actually strong oscillations in the precipitation and dissolution rates. They were evoked by changes in permeability and fluid flow over a time span of 7000 years [Luff et al., 2005]. The simulation predicted cycles of carbonate crust formation and dissolution with a duration of 2000–2700 years, and resulted in several distinct carbonate layers. It is important to note that the system itself is able to produce the oscillations, it does not need an external forcing. Nevertheless, I think it is more appropriate to assume changes in the fluid flow from depth than a self-oscillating system, because the suspected layering in the sidescan sonar image of Mound Carablanca is larger than in the modeled sediment section. Such external oscillations could be triggered by e. g. earthquakes [Mau et al., submitted; Brown et al., 2005].

Another argument which contradicts the interpretation of the mound structures as mud volcanoes is that the morphologies of the mounds are generally steeper, with smaller base areas than reported from mud volcanoes. Concluding from the morphology, the material the features consist of, cannot be mud with high liquid content, because then they would form flat-topped mud pies. Also the central depressions, I think, are more likely slumping

and sliding structures than eruption craters. They are often not really circular and not centered, but offset to the downslope side, uncovering a larger slide plane.

It is well known that mud volcanism occurs usually in areas with high sedimentation rates and lateral tectonic compression [e.g. Milkov, 2000]. The tectonic stress acts then as a trigger to its formation. In an extensional regime, mud volcanism can occur only in combination with an excessively thick sedimentary overload on top of the potential source layer [Ivanov et al., 1996]. The upper slope offshore Nicaragua is in an extensional tectonic regime resulting from subduction erosion [Meschede et al., 1999], but sedimentation rates inferred from tephra stratigraphy are low with $\sim 17\text{--}20$ cm/1000 a (*Kutterolf, S., pers. comm.*). Also sediment thickness is low, as stated at the beginning. This would prevent the formation of mud volcanoes. On the other hand suggests a calculation of the (potential) mud source depth of Mound Culebra offshore Costa Rica, following an isostatic model of Murton and Biggs [2003], that the sediment thickness of the slope apron offshore Nicaragua would be sufficient for the phenomenon of mud extrusions. The mud source of Mound Culebra was determined to be in 600–800 m depth below the seafloor [Moerz et al., 2005]. But the critical variables in this model of isostatic compensation are the unknown densities of the “extruding” material and of the sediment column on the slope.

The assumption that the mounds are seafloor-piercing diapirs consisting of viscous mud with a low fluid content would count for the observed morphologies and the absence of liquid mud flows. As it can be excluded that a diapir would rise through the ophiolitic margin wedge, the question is then, how likely a buoyancy-driven shale- or mud diapirism would be inside the sediments of the middle and upper continental slope. What would be the possible source sediments of such a diapirism? According to Meschede et al. [1999] the sediments directly overlaying the base-of-slope-sediments (BOSS) reflector are formed under shallow water conditions in coastal waters. Due to the subduction erosion and subsidence of the forearc they have been transported into successively deeper water and are covered with hemipelagic sediments. Because shallow water sediments are less prone to form a source for diapirs, and the subsidence itself is a long-lasting process, the remaining hemipelagic sediment section is probably less than 1 km thick. Usually large sediment thicknesses in combination with high sedimentation rates favour the formation of diapirs. Rapid burial of low permeable sediments are most favourable for disequilibrium compaction, resulting in overpressured, underconsolidated layers [Osborne and Swarbrick, 1997]. As long as the pore pressure stays below the lithostatic pressure, the sediment package will behave in a weak, ductile manner and follow the critical state deformation [Maltman and Bolton, 2003]. If the plastic mud is less dense than the overlying layers, it can be triggered to uprise by a buoyant force and form a diapir. The mud and pore fluid upwell then en masse and fluid migration is a subsidiary process [Brown, 1990]. But when the pore pressure is exceeding the lithostatic pressure due to an increasing sediment load under complete sealing, or an injection of fluids from a deeper source, the overpressured sediments may become liquefied or fluidized and follow the hydraulic gradient. If the fluid supply is sufficient and the overpressure of the pore fluids can be

sustained in the mobilized sediment, then a diatrema can form, but this requires enormous quantities of fluid [Maltman and Bolton, 2003; Brown, 1990]. As the sediments in the case of mobilization through liquefaction or fluidization are also usually less dense than the overlying layers, a buoyancy effect is added, so that both processes (gravitational force and hydraulic force) interact [Maltman and Bolton, 2003]. By remote geophysical means, it is very difficult to distinguish between the two processes [Brown, 1990].

That the observed mound structures are surface expressions of diatremes is not very likely, because diatremes require a vigorous fluid circulation system and a large amount of fluids [Brown, 1990]. The sediment thicknesses on the incoming oceanic lithosphere reported from seismic sections are only around 200–300 m [Ranero et al., 2000a]. A large portion of the pore fluids of these sediment packages is expelled right beneath the frontal prism and dewatered along the décollement or bedding-parallel backflow. Geochemical analysis of the fluids sampled at mound locations showed that mineral dehydration processes in the subducted oceanic sediments are their source [Hensen et al., 2004]. But quantitative considerations revealed that an advective flow of approximately 300 cm/yr through a mound could dewater a large catchment area [Hensen et al., 2004]. As cited in Brown [1990] the minimum fluid velocities for the entrainment of unconsolidated clays and grain sizes up to fine sands (0.5 mm or less) are around 0.07 cm/s, which is more than 7000 times faster than the observed ones.

Further arguments which favour a diapiric origin of the mound structures are the occurrence of basaltic clasts, mud clasts and deformed clays with scaly fabric within the suspected overcompacted mud breccia [Moerz et al., 2005]. Also hints for hydrofracturing are found in some gravity cores. But the basaltic clasts are reported to be very sparse and do not exceed a diameter of 1 cm [Moerz et al., 2005], and could possibly be explained by reworked material from the shelf. A mud breccia or silty clays containing mud clasts, interpreted as typical deposits of a mud diapir, resemble the deposits generated by debris flows, which are likely to occur at the relatively steep continental slope. The strongest argument for diapiric origin are the deformed clays showing a scaly fabric, because such fabrics develop during deformation and compaction of mud matrix, and are taken as an indicator of a deep origin. Even when [Brown, 1990] stresses that the development of scaly fabrics in diapiric muds is bound to a trajectory path experiencing increasing effective stresses, and that such a path is in general scale-independent, which means, that it can occur either at shallow or at very large depths, these observations can probably not be explained satisfactorily with sediment mobilizations in the uppermost 100–200 m of the slope sediments.

But excluding the findings of scaly clays, most arguments presented so far favour a modified model for the formation of the mound structures. Compaction of subducted oceanic sediments, as well as clay dehydration reactions like the transformation of smectite to illite, release fluids along the plate boundary [Hensen et al., 2004]. They travel upwards through the ophiolitic margin wedge along deep-seated faults, which form conduits and pathways for the rising fluids [Ranero and von Huene, 2000]. When reaching the slope apron sediments, the fluids may contribute to an increase in pore pressure at some level,

when encountering a less permeable layer. In my understanding this does not have to occur necessarily at the base of the slope sediments, as these sediments have probably been deposited in a shallow marine environment. They tend to have larger permeabilities therefore. If the pore pressure is increased in a layer inside the slope apron, this can lead to the formation of a less dense mass of mud, which can form a diapiric upwelling driven by a buoyant force, or, if the pore pressure is raised above the lithostatic pressure, the sediments can be liquefied and follow the hydraulic gradient. When approaching the seafloor, the escape of the fluids decreases the pore pressure, and the sediment becomes plastic again. This is why liquid mud flows are not observed. But as there is no thick sedimentary sequence on the slope, and no vigorous fluid circulation system, either of which would be necessary to drive sediment mobilization over large distances, I propose that these processes occur in the upper few hundred metres of the sediment section. Maybe the sediment mobilization is additionally triggered by gas hydrate dissociation, even when that is not a dominant source of freshwater addition [Hensen et al., 2004]. But already a small amount of enclosed gas bubbles could enhance the local shearing, and thus contribute to get the sediment mobilized [Van Rensbergen et al., 2003]. It is also possible that the uprising fluids are not hindered by impermeable layers, and just continue on their way up, and finally seep out of the seafloor or react with the infiltrating seawater to form authigenic carbonates. In figure 3.25 another very important and often neglected process is described. Seafloor erosion is much more common than heretofore realized [Bouma et al., 1990].

Erosion is not only evidenced in some of the presented subbottom profiles, but also from correlated marine tephra layers (*Kutterolf, S., pers. comm.*). In several gravity cores taken on or in the near surrounding of some mounds, white to grey ash layers of centimetre to decimetre thickness have been found. These ashes can be stratigraphically correlated to onshore tephra layers with known ages, and theoretical sedimentation rates can be calculated (*Kutterolf, S., pers. comm.*). Assuming normal sedimentation rates of 17–20 cm/1000 a at the continental slope offshore Nicaragua, the dominating process (sedimentation or erosion) can be concluded by comparison with the calculated ones (*Kutterolf, S., pers. comm.*). For example around Mound Iguana sedimentation rates are in the order of 20 cm/1000 a, indicating little to none erosion. A core on the flank of Mound Perezoso reveals a sedimentation rate of only 6 cm/1000 a, and indicates therefore a clearly erosional environment. This supports the conclusions drawn from the geoaoustic data, that Mound Perezoso is a mound of type III. Two cores on the flanks of Mound Carablanca reveal sedimentation rates of 15–18 cm/ka, and therefore only little erosion. A correlation of the tephra layers in the cores, with high-reflectivity horizons in the high-resolution subbottom profiles, like demonstrated by Bowles et al. [1973], will offer a much more complete picture of the erosion processes offshore Nicaragua.

According to the presented model, the surface expression of the fluid venting sites can show a wide variety: Mud domes of mobilized sediment can develop by interaction of upwelling mud and erosion on the slope. They can pierce through the seafloor, or still be covered with hemipelagic sediments. Through interaction of seeping fluids with seawater,

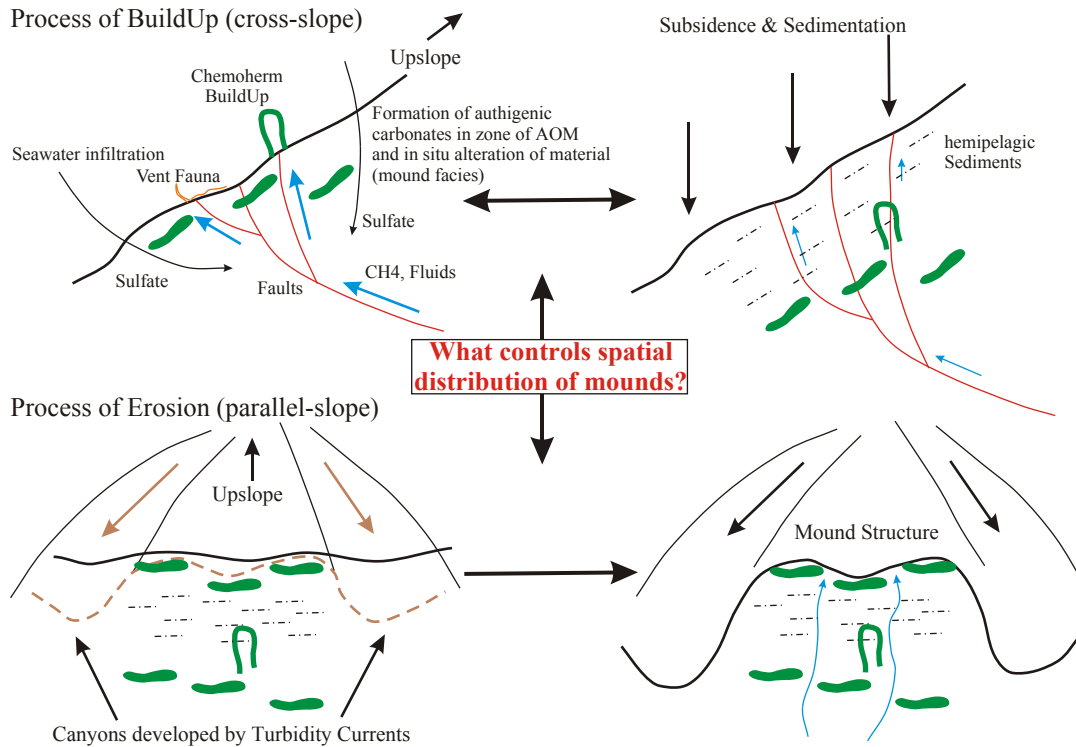


Figure 3.25: Generic model of mound structure formation, including several interacting processes like fluid venting and associated precipitation of authigenic carbonates, hemipelagic background sedimentation, subsidence, and erosion by turbidity currents or debris flows along submarine canyons. During phases of buildup, sub-seafloor precipitation of authigenic carbonates or above-seafloor formation of carbonate chemoherms occurs where fluids or volatiles from larger depths react with sulfate from infiltrating seawater. Phases of lower venting activity result in the deposition of hemipelagic sediments and subsidence. Processes like denudation and focused transport in turbidity currents shape the slope surface according to its resistivity.

often carbonate crusts develop on their top areas. Where the fluids seep to the seafloor without sediment mobilization, carbonate patches without morphological expression, or even carbonate chemoherms rising above the seafloor, may result. The prominent mound ridges (figure 3.18) show the considerable influence of erosion to the shaping of the mounds, whereas for other mounds like Mound Quetzal or Mounds Buho and Hormiga, which are surrounded by relatively flat seafloor, an active upward movement is likely.

3.5 Conclusions and outlook

- Depending on size, morphology, backscatter and subbottom profile facies, and fluid venting activity, three different mound types as end members are distinguished offshore Nicaragua. They are closely linked to sedimentary processes on the continental slope.
- Mound volume calculations do not reveal any clustering, but the mounds can be grouped according to their volume/base area index. Mounds with low topographic relief have numbers between 20–40, mid-sized mounds have numbers from 40–60, and the large and exposed mounds have numbers larger than 60. The exceptional large Mound Baula I has an index of almost 180.
- The observed mound structures are no mud volcanoes. They do not reveal any morphological characteristics of erupted mud flows in the geoaoustic data.
- The formation of the mound structures is mainly due to the interaction of several processes. Fluid venting is the primary process, sometimes inducing sediment mobilization, possibly through liquefaction or buoyancy-driven diapirism. An important factor is erosion and denudation acting on the slope, and shaping the slope surface according to its resistivity.
- The source depth of the sediment mobilization is unknown, but it could be very shallow, perhaps triggered by gas hydrate dissociation.

Future research to proof the suggested model, should focus on following topics:

- Correlation of tephra layers with high-reflective horizons in subbottom profiles to get a spatial distribution of erosional processes on the slope.
- High-resolution seismic imaging of the slope apron sediments (down to 2–4 km), to determine source depth of possible diapirism.
- Drilling of mound down to 50–100 metres (or more) to determine distribution of authigenic carbonate formations with depth.
- Age determination of mound structures, to reveal history of fluid venting activity (cf. Hammerich, T., *PhD thesis*).
- Comparison of mound volume calculations and volume/base area indices with mud diapirs or mud volcanoes from other continental margins.
- Modelling of mound volume to base area indices for different shapes (cone, half-sphere, tetraeder), to get an understanding of mound shapes.

4

The influence of topography on sidescan sonar images

4.1 Introduction

The backscattering signal on sidescan sonar images is mainly dependent on

- (1) the angle of incidence of the acoustic beam onto the seafloor,
- (2) the (micro-scale) roughness of the seafloor,
- (3) the intrinsic properties (lithology, composition, density) of the seafloor and
- (4) the sonar frequency and pulse characteristics

in decreasing order of magnitude [Blondel and Murton, 1997]. As sidescan sonar systems are often used to identify unusual seafloor lithologies or to support the sedimentological interpretation of the seafloor at higher resolution compared to multibeam systems, the difference in backscattering strength caused by varying incidence angles hinders these goals. An experienced interpreter of sidescan sonar images automatically takes the sensor specifications, the geometry and acquisition parameters, and the seafloor morphology into account. But to highlight the lithologically most interesting parts in a sidescan sonar image, it would be necessary to reduce or even remove the influence of the morphology on the magnitude of the backscattering signal.

Two reasons exist why such a reduction of the topographic influence on deep-towed sidescan sonar images has not been tried yet:

- Most sidescan sonar systems do not measure backscattering strengths calibrated to a pressure level ($p_{ref} = 1\mu Pa$, given at dezibel scale), but unreferenced amplitudes. Therefore it is not possible to apply theoretical seafloor backscattering models.
- Deep-towed sidescan sonars insonify the seafloor by more side-looking acoustic pulses than shallow-towed systems. This is due to the low elevation above the seafloor, compared to the more vertical insonification in the case of multibeam amplitude measurements or shallow-towed sidescan sonars. The oblique insonification results in the formation of shadow zones behind obstacles, which is sometimes desirable, as it helps imaging e.g. sedimentary structures [Hammerstad, 2000], but makes it difficult to correct the signal for the topographic influence.

The cases where quantitative seabed backscatter measurements have been performed or a topographic reduction of the amplitude values has been applied, are consequently dealing with multibeam acoustic imagery [Augustin et al., 1996] or with sidescan sonars towed at shallow depths [Carson et al., 1994; Mitchell and Somers, 1989].

Going even further and attempting a (computer-based) classification of a sidescan sonar mosaic with classification techniques already developed in the field of satellite remote sensing, would make it necessary to first adapt these techniques to the acoustic processes which created such a picture [Blondel, 2002]. This would also require a topographic reduction of the backscatter values.

A good comprehensive overview of various classification techniques for many types of sensors is given in Blondel [2002]. In contrast to classifying a sonar image solely based on the tonal information it is realized that much of the information about the type of seabed is conveyed in the texture of the image. The texture itself corresponds to the spatial organisation of the grey levels within a certain neighbourhood which can be quantified with stochastic methods, such as *Grey-Level Co-occurrence Matrices (GLCM's)* [Blondel, 2002]. Furthermore by calibrating surveying sidescan sonars properly and expressing the final backscatter images in decibels [dB] and not in relative grey levels, a great progress in the performance of any classification technique could be achieved [Blondel, 2002].

An example of manual interpretation and classification of authigenic carbonates along the Hydrate Ridge region is given in Johnson et al. [2003].

In the area offshore Nicaragua a large number of mound structures show considerable topographic relief, and the seafloor has a rugged morphology where canyons incise the middle continental slope. Therefore an approach is made to evaluate and perhaps to reduce the effect of morphology on the backscatter signal, for pointing out the lithologically most interesting and unusual places with respect to fluid venting.

4.2 The backscattering signal

4.2.1 Fundamentals

Acoustic waves originate from the propagation of pressure changes through an elastic medium with a velocity $c = \lambda \cdot f$, where λ is the wavelength and f is the frequency of the acoustic wave. They can be characterised by the amplitude, the single particle velocity, and the resulting acoustic pressure [Lurton, 2002]. The propagation velocity is linked to the propagation medium by the density ρ and the elasticity modulus E with $c = \sqrt{\frac{E}{\rho}}$. In sea water the velocity of an acoustic wave is approximately 1500 m/s, depending on pressure, salinity and temperature. The density is around 1030 kg/m³.

The propagation of acoustic waves in fluids (gases, liquids) can be described by the *Helmholtz equation*:

$$\Delta p = \frac{\partial^2 p}{\partial x^2} + \frac{\partial^2 p}{\partial y^2} + \frac{\partial^2 p}{\partial z^2} = \frac{1}{c^2(x, y, z)} \frac{\partial^2 p}{\partial t^2}, \quad (4.1)$$

- p = pressure of wave propagating in (x, y, z) [Pa]
- $c(x, y, z)$ = local propagation velocity [m/s]
- Δ = Laplace operator

In a medium where the propagation velocity is constant, $c(x, y, z) = c$, and the propagation is restricted to a single direction x , the wave fronts or surfaces of constant phases of a sinusoidal wave of frequency f_0 and constant amplitude will form planes. This type of wave is therefore called a *plane wave* and can be described with:

$$p(t) = p_0 \exp\left(2j\pi f_0 \left(t - \frac{x}{c}\right)\right) \quad (4.2)$$

In the case that there is a point source in the center of the coordinate system and the propagation velocity is constant $c(x, y, z) = c$, the solution to equation 4.1 will be a *spherical wave*, with distance $R = \sqrt{x^2 + y^2 + z^2}$ to the source, and the imaginary unit $j = \sqrt{-1}$. The amplitude of the wave decreases from its value p_0 considered 1 metre away from the source with $1/R$. This type of wave can be described with:

$$p(t) = \frac{p_0}{R} \exp\left(2j\pi f_0 \left(t - \frac{R}{c}\right)\right) \quad (4.3)$$

Local processes which are far enough away from the sound source so that the amplitude is almost constant and the wave fronts show a negligible curvature can be best modeled by plane waves. They are used e. g. to describe the interaction of acoustic waves with the seabed. Spherical waves are used to model an acoustic wave field around a well-localized source where the decrease in amplitude has to be considered [Lurton, 2002].

The *acoustic impedance* of a propagation medium relates the acoustic pressure level to the corresponding particle velocity and amplitude. It can be calculated with:

$$Z_a = \rho \cdot c \quad (4.4)$$

$$\begin{aligned} \rho &= \text{density of propagation medium [kg/m}^3\text{]} \\ c &= \text{propagation velocity of acoustic wave in medium [m/s]} \end{aligned}$$

The unit for acoustic impedance is the Rayleigh (rayl). In a high-impedance medium, a particle movement with a given amplitude will yield a higher acoustic pressure level than in a low-impedance medium.

The emission and propagation of a sound wave is associated with an acoustic energy. As a measure for the mean energy flux by a plane wave on a surface A in the time t the *acoustic intensity* is given in $[W/m^2]$ with:

$$I = \frac{P}{A} = \frac{E}{t \cdot A} = \frac{p_0^2}{2 \cdot \rho \cdot c} \quad (4.5)$$

$$\begin{aligned} P &= \text{acoustic power [W]} \\ A &= \text{area [m}^2\text{]} \\ E &= \text{energy [J]} \\ t &= \text{time [s]} \\ p_0 &= \text{pressure (amplitude) of wave [Pa]} \\ \rho &= \text{density of propagation medium [kg/m}^3\text{]} \\ c &= \text{propagation velocity of acoustic wave in medium [m/s]} \end{aligned}$$

Equation 4.1 and its solutions describe the propagation of a sound wave in a medium without considering the properties of the source/receiver, the medium, and the target. To calculate the echo level of a signal backscattered from a target the general sonar equation can be applied [Lurton, 2002]:

$$EL = SL - 2 \cdot TL + TS \quad (4.6)$$

$$\begin{aligned} EL &= \text{echo level [dB]} \\ SL &= \text{source level [dB]} \\ 2 \cdot TL &= \text{two-way transmission loss [dB]} \\ TS &= \text{target strength [dB]} \end{aligned}$$

Because acoustic parameters like pressure or energy have a large dynamic range, they are quantified on a logarithmic scale, and noted in *decibels* [dB]. The decibel is defined as ten times the base-10 logarithm of the ratio of two powers. As the power P_i (or energy, intensity) is proportional to the square of pressure p_i^2 (cf. equation 4.5), the same ratio can be expressed as:

$$10 \log \left(\frac{P_1}{P_2} \right) = 10 \log \left(\frac{p_1^2}{p_2^2} \right) = 20 \log \left(\frac{p_1}{p_2} \right) \quad (4.7)$$

To give not only a ratio but an absolute level of an acoustic value in decibel, a reference level must be used. In underwater acoustics the absolute acoustic pressure is expressed in dB relative to $1\mu Pa$, noted $dB/1\mu Pa$ or $dB \text{ re } 1\mu Pa$, in contrast to the reference in air, $20\mu Pa$, which is the average human hearing threshold at 1 kHz.

$$p_{dB} = 20 \log \left(\frac{p}{p_{ref}} \right) \quad (4.8)$$

The relation between a signal pressure (in $dB \text{ re } 1\mu Pa$) and the corresponding intensity (in $dB \text{ re } 1W/m^2$) for a plane wave with $I = p^2/2\rho c$ (cf. equation 4.5), and $\rho = 1030kg/m^3$ and $c = 1500m/s$ is:

$$\begin{aligned} 10 \log \left(\frac{I}{1W/m^2} \right) &= 20 \log \left(\frac{p}{1Pa} \right) + 10 \log \left(\frac{1}{2\rho c} \right) \\ &\approx 20 \log \left(\frac{p}{1\mu Pa} \right) + 20 \log \left(\frac{1\mu Pa}{1Pa} \right) - 64.9 \\ &\approx 20 \log \left(\frac{p}{1\mu Pa} \right) - 184.9 \end{aligned}$$

In the following sections theoretical aspects of the transmission loss (section 4.2.2) and the target strength (section 4.2.3) are summarized, and models for the reflection and scattering at a rough surface are given (section 4.2.6). Finally the methodology for the correction of the backscattering signal for the seafloor topography is explained (section 4.2.7). A more detailed discussion is given in Lurton [2002] and Augustin et al. [1996].

4.2.2 Transmission loss

Transmission loss is the loss of intensity of an acoustic wave propagating through a medium, due to geometrical spreading of the acoustic wave (divergence effect) and the absorption of acoustic energy by the propagation medium.

Geometrical spreading When an acoustic wave propagates from a sound source it will spread the acoustic energy on an increasingly larger surface. As a consequence the intensity decreases in inverse proportion to the surface. In the most simple and ideal case the propagation medium is homogeneous, isotropic, and infinite, and a small-dimensioned point source is radiating in all directions. The energy is then spread over spheres with increasing radii and the intensity decreases with $1/R^2$. The transmission loss due to spherical spreading at the reference unit distance $R_{1m} = 1m$ can then be expressed in decibels [dB]:

$$TL = 20 \log \left(\frac{R}{R_{1m}} \right) \quad \text{or} \quad TL = 20 \log R \quad (4.9)$$

Absorption An acoustic medium dissipates part of the energy of the transmitted acoustic wave through its viscosity or chemical reactions. The attenuation depends strongly on the propagation medium and the frequency of the transmitted signal. In sea water, attenuation comes from:

- the viscosity of pure water
- the relaxation of magnesium sulphate ($MgSO_4$) molecules above 100 kHz
- the relaxation of boric acid ($B(OH)_3$) molecules above 1 kHz

Molecular relaxation is the dissociation of some ionic compounds in solution through local pressure variations created by the acoustic wave. When the period of the local pressure variation is longer than the *relaxation time* of the molecule, this process is reproduced continuously and dissipates energy.

This attenuation is proportional to the distance R with α as the *attenuation coefficient*, expressed in decibels per metre [dB/m]. α is a function of signal frequency, salinity, depth and temperature, and can be calculated using various models.

In a first approximation the transmission loss due to spherical spreading and absorption can be described as:

$$TL = 20 \log \left(\frac{R}{R_{1m}} \right) + \alpha R \quad \text{or} \quad TL = 20 \log R + \alpha R \quad (4.10)$$

$$\begin{aligned} TL &= \text{transmission loss [dB]} \\ R &= \text{range [m]} \\ \alpha &= \text{absorption coefficient [dB/m]} \end{aligned}$$

4.2.3 Target strength

The target strength TS is defined as the ratio (expressed in dB) of the intensities of the backscattered (I_{bs}) and incident (I_i) waves.

$$TS = 10 \log \left(\frac{I_{bs}}{I_i} \right) \quad (4.11)$$

It depends on the physical nature of the target, the external and internal structure of the target, as well as the signal characteristics, like incident angle and frequency. The incident wave with its intensity I_i is assumed as a locally plane wave (which is valid, if the source and the target are far enough from each other), the scattered wave is assumed spherical (Fig. 4.1). The backscattered intensity I_{bs} is measured at a distance of 1 m from the center of the target.

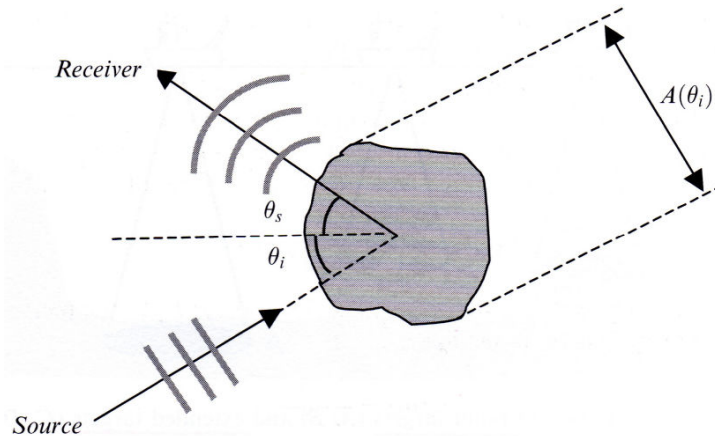


Figure 4.1: Geometry of target scattering. The incident wave is assumed to be locally plane, and the scattered wave is assumed spherical. All processes should be considered in full 3-D space, even when only described for the 2-D case (from Lurton [2002]).

The actual acoustic power intercepted by the target is the product of the *apparent cross-section* $A(\theta_i)$ with the intensity of the incident wave I_i (Fig. 4.1).

$$P_i(\theta_i) = A(\theta_i) \cdot I_i \quad (4.12)$$

The spatial distribution of the retransmitted energy, radiated from the target into the neighbouring space is described by the *scattering function* $G(\theta_i, \theta_s)$. The intensity scattered in a certain direction θ_s can then be calculated at the unit distance R_{1m} , with:

$$I_s(\theta_s, R_{1m}) = \frac{P_i(\theta_i)}{R_{1m}^2} \cdot G(\theta_i, \theta_s) \quad (4.13)$$

The *effective scattering cross-section* is the apparent cross-section $A(\theta_i)$ multiplied with the scattering function $G(\theta_i, \theta_s)$:

$$\sigma_s(\theta_i, \theta_s) = \frac{I_s(\theta_s) R_{1m}^2}{I_i(\theta_i)} = A(\theta_i) \cdot G(\theta_i, \theta_s) \quad (4.14)$$

It has therefore the dimension of a surface [m^2]. The *effective backscattering cross-section* is the scattering back towards the source in the direction θ_i . Its expression in decibels [dB] relative to one reference unit section [$A_1 = 1 m^2$] is called the *target strength TS*.

$$TS = 10 \log \left[\frac{\sigma_{bs}(\theta_i)}{A_1} \right] \quad (4.15)$$

There are various variables used in this section with the dimension of an area [m^2]. R_{1m}^2 expresses that the values are measured in a distance of 1 m, while the unit section A_1 means that the value is measured over an area of $1m^2$, and $A(\theta_i)$ is the cross-section of the target.

4.2.4 Scattering at an ideal sphere

In the case of an ideal rigid sphere with radius r and an apparent cross-section of $A = \pi r^2, \forall \theta_i$, which is retransmitting the received energy entirely and isotropically into the entire space, the scattering function is everywhere:

$$G(\theta_i, \theta_s) = \frac{1}{4\pi}, \quad \forall(\theta_i, \theta_s)$$

The effective scattering or backscattering cross-section is then simply:

$$\sigma_{bs} = \sigma_s = \frac{\pi r^2}{4\pi} = \frac{r^2}{4} \quad (4.16)$$

When calculating the target strength of spheres with different radii, one has to consider whether wave effects have to be taken into account or not. Depending on the relative size of the target with respect to the acoustic wavelength, three different scattering regimes can be distinguished (Fig. 4.2):

- *Rayleigh regime* - acoustic wavelength is much larger than the target
- *interferential regime* - target circumference is a few wavelengths, leading to interference effects of the reflected and refracted waves on the spheres surface
- *geometric regime* - acoustic wavelength is small relative to the target

In the case of seafloor backscattering with an insonification frequency of about 75 kHz the scattering regime is geometric at an acoustic wavelength of approximately $\lambda = 2$ cm, assuming a sound velocity of 1500 m/s. Rayleigh scattering or the interferential regime are important for scattering processes at gas bubbles, planctonic organisms, or fish.

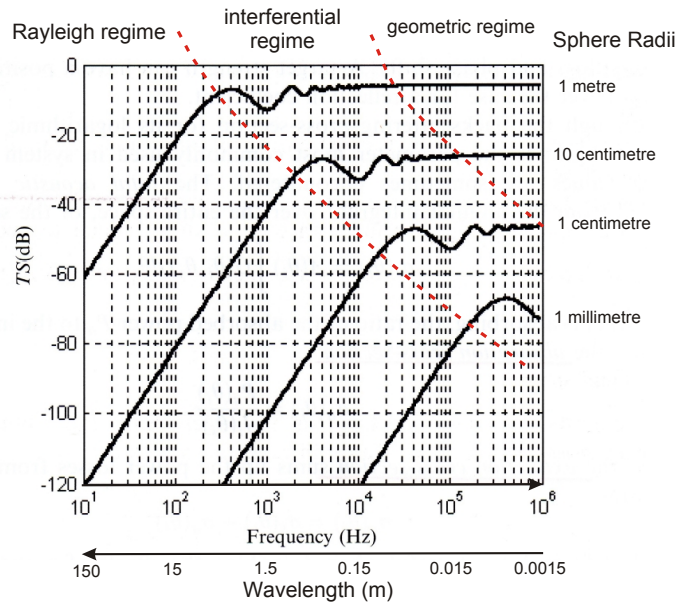


Figure 4.2: Target strengths for perfect rigid spheres of different radii as a function of frequency. The target strength is strongest in the geometric regime, where the acoustic wavelength is small relative to the target size (modified from Lurton [2002]).

4.2.5 Extended targets

Extended targets are targets which are too large to be completely insonified at once by the same beam. They are delimited by the sonar characteristics (beam width, signal length) rather than by their own dimensions. Their target strength is then composed of two contributors:

- (1) The size of the target surface or volume insonified $A_{s,v}$, and
- (2) the corresponding target or backscattering strength $BS_{s,v}$ (cf. equation 4.15).

To emphasize that in the case of an extended target the backscattering strength $BS_{s,v}$ is normalized to a unit section or unit volume, it is noted in $[dB \text{ re } 1m^2]$ or $[dB \text{ re } 1m^3]$. The sonar equation (eq. 4.6) can then be written as:

$$EL = SL - 2TL + TS = SL - 2TL + 10 \log \left(\frac{A_{s,v}}{A_1} \right) + BS_{s,v} \quad (4.17)$$

4.2.5.1 Surface and volume calculations

To calculate the insonified surface or volume in equation 4.17 the sensor specifications have to be considered. Figure 4.3 shows the parameters for the calculation of the insonified area at grazing incidence. Knowing the along-track beam aperture ϕ and the pulse length T of the sensor, the insonified area on the seafloor can be calculated with:

$$A_s = \phi R \frac{cT}{2 \sin \theta} \quad (4.18)$$

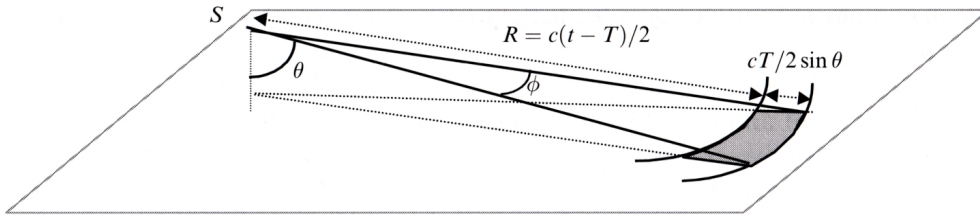


Figure 4.3: Calculation of insonified surface at grazing incidence (from Lurton [2002]).

- R = range [m]
- ϕ = along-track beam aperture
- θ = beam angle or incident angle
- c = sound velocity [m/s]
- T = pulse length [s]

Multibeam systems illuminate the seafloor at smaller (steeper) incidence angles than sidescan sonar systems. Their beam geometry is shown in figure 4.4, and the insonified area can be calculated with:

$$A_s = \frac{\theta_T \theta_R R^2}{\cos \theta} \quad (4.19)$$

- R = range [m]
- θ_T = along-track transmission beam angle
- θ_R = across-track reception beam angle
- θ = beam angle or incident angle

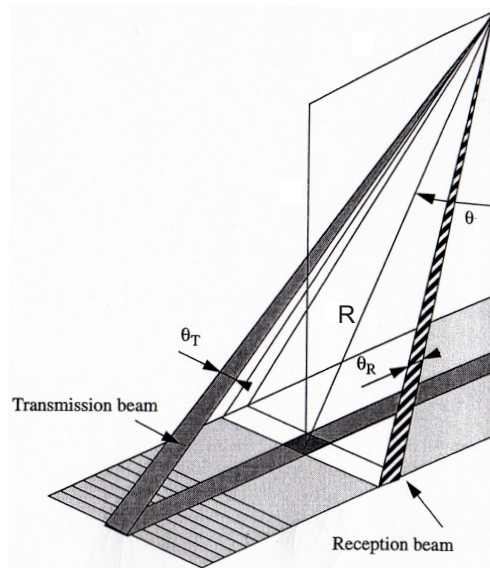


Figure 4.4: Beam geometry of multibeam acquisition system (modified from Augustin et al. [1996]).

4.2. THE BACKSCATTERING SIGNAL

The scattering volume insonified by a signal with pulse length T and an aperture of the directivity cone ψ is included between two spheres with radii $c(t-T)/2$ and $ct/2$ (Fig. 4.5). For $T \ll t$ the portion of the cone can be approximated by a cylinder and the scattering volume becomes:

$$A_v = \psi R^2 \frac{cT}{2}, \quad (T \ll t) \quad (4.20)$$

- R = range [m]
- ψ = aperture of the directivity cone [steradians]
- c = sound velocity [m/s]
- T = pulse length [s]

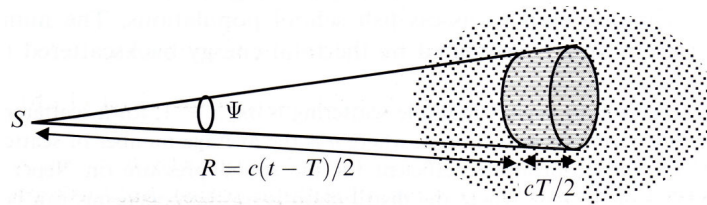


Figure 4.5: Geometrical model of volume backscattering (from Lurton [2002]).

Before explaining some models for the calculation of the backscattering strength BS_s in equation 4.17 at rough surfaces, a simple approach is given for the volume backscattering strength BS_v . The more sophisticated *small-perturbation model* is described in Brekhovskikh and Lysanov [2003].

BS_v can be seen as the incoherent sum of the individual backscattering cross-sections of each target present in an average cubic metre of volume. If N is the average number of targets in a unit volume, the average backscatter cross-section per unit volume can be approximated by $N \cdot \bar{\sigma}$, where $\bar{\sigma}$ is the average individual backscattering cross-section. With the assumption that all targets are identical, the backscattering strength equals the individual backscattering strength TS , corrected by the number of targets in a unit volume. In logarithmic notation BS_v can be calculated with:

$$BS_v = TS + 10 \log N \quad (4.21)$$

Multiple scattering between individual targets as well as masking of scatterers by each other are neglected in this model.

When describing the interaction of an acoustic wave with the seafloor it has to be considered that often a part of the incident acoustic energy is penetrating into the sediment and is scattered at volume heterogeneities inside this sediment (e.g. sediment grains, organisms, shells, gas bubbles). The part scattered back to the transmitter is called volume backscattering and is depending not only on the backscattering strength of the

heterogeneities itself, but also on the characteristics of the water–sediment interface, and the absorption inside the sediment.

Volume backscattering is an important process in soft sediments at oblique incidences, it decreases with increasing grain size due to higher absorption. Lower frequencies result in stronger volume backscattering, as they are less absorbed. A simple model for the calculation of penetration depths of a sonar signal into the sediment is given in appendix A.

4.2.6 Models for the reflection and scattering by a rough surface

4.2.6.1 Definition of roughness

As the seafloor is far from being an ideal plane surface, the question is, how *roughness* can be defined, and how it influences the backscatter signal. First it can be distinguish between *large-scale roughness*, where the elements of the seafloor may be considered as locally plane but with varying inclination against the horizontal, and *microscale roughness*, which is significant, if its characteristic dimensions are in the range of the acoustic wavelength. *Surface roughness* is then the ratio between the characteristic amplitude of the relief and the wavelength of the acoustic signal. Small relief amplitudes with respect to the acoustic wavelength (low interface roughness) increase the component of coherent, specular reflection at the interface, while larger relief amplitudes (high interface roughness) increase the scattering in all directions (Fig. 4.6). A rough surface

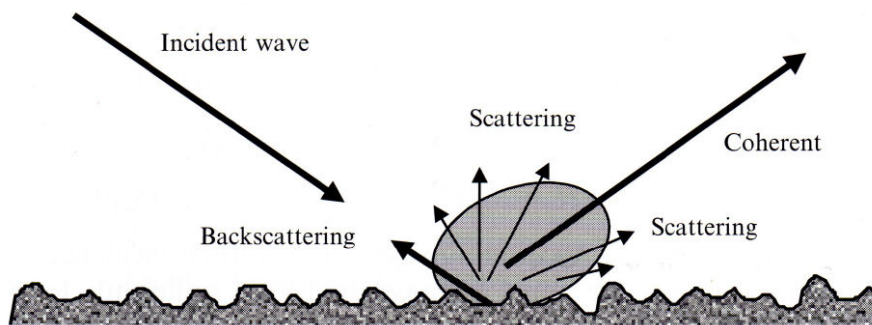


Figure 4.6: Coherent reflection and scattering of an incident wave by a rough surface (from Lurton [2002]).

consists of several, superimposed irregularities of different amplitudes and wavelengths (e. g. seafloor morphology, carbonate blocks, sand ripples, pebbles, different grain sizes). They can be separated and quantified in a *spatial spectrum* of the surface (Fig. 4.7). A relief where structures are strongly organised along preferential directions is characterized by anisotropy of its spatial spectrum.

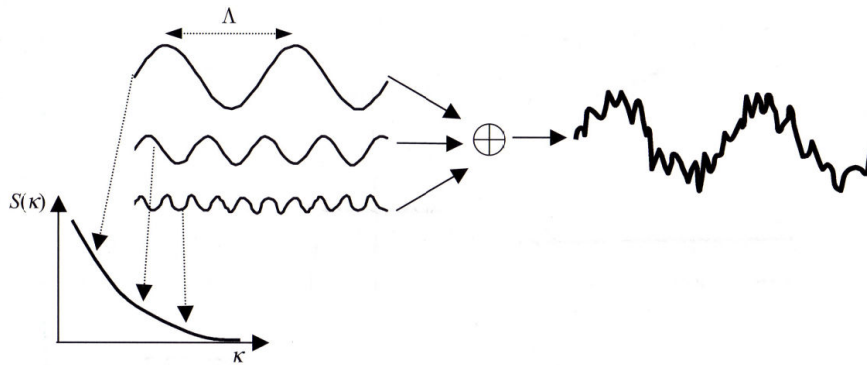


Figure 4.7: Decomposition of the amplitude of a random rough surface into its spatial spectral components. Each component is defined by a *wave number* $\kappa = 2\pi/\Lambda$, with Λ being the *spatial wavelength*. Because larger amplitudes are associated with longer wavelengths, the power spectrum $S(\kappa)$ decreases with the wave number [from Lurton, 2002].

4.2.6.2 Seafloor backscattering

The backscattering strength BS_s (cf. equation 4.17) of the seafloor is a complicated function of the nature of the seafloor (e. g. impedance contrast), its structure (e. g. roughness), the incidence angle of the acoustic signal (θ), as well as the frequency of the signal. At *near vertical* incidence ($\theta \leq 20^\circ$) the backscattering strength essentially depends on large scale roughness, where a large number of *facets* are oriented in such a way that a specular echo is reflected. This corresponds to the maximum backscattered energy (Fig. 4.8, top). This facet reflection is also called the *tangent plane model* [Augustin et al., 1996]. At *oblique* incidence ($\theta \geq 20^\circ$) mechanisms like *Bragg scattering* and scattering at volume inhomogeneities in the subsurface become more dominant (Fig. 4.8, top). Bragg scattering is the constructive interference of scattered waves coming from a continuum of sources along a rough interface. The scatter points are a function of the observation angle and the microscale roughness. It is important to note that a smooth seafloor increases the contribution from facet reflection, whereas a rough seafloor shows an increase of backscattered levels in the Bragg domain [Lurton, 2002]. However the intensity of the decrease in backscattering strength with increasing incidence angles is more important for seabed characterization (Fig. 4.8, bottom).

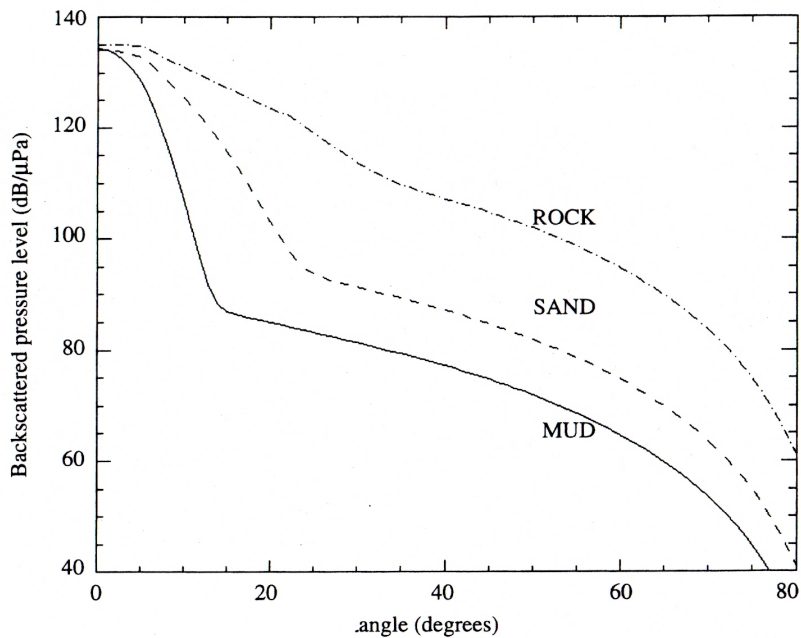
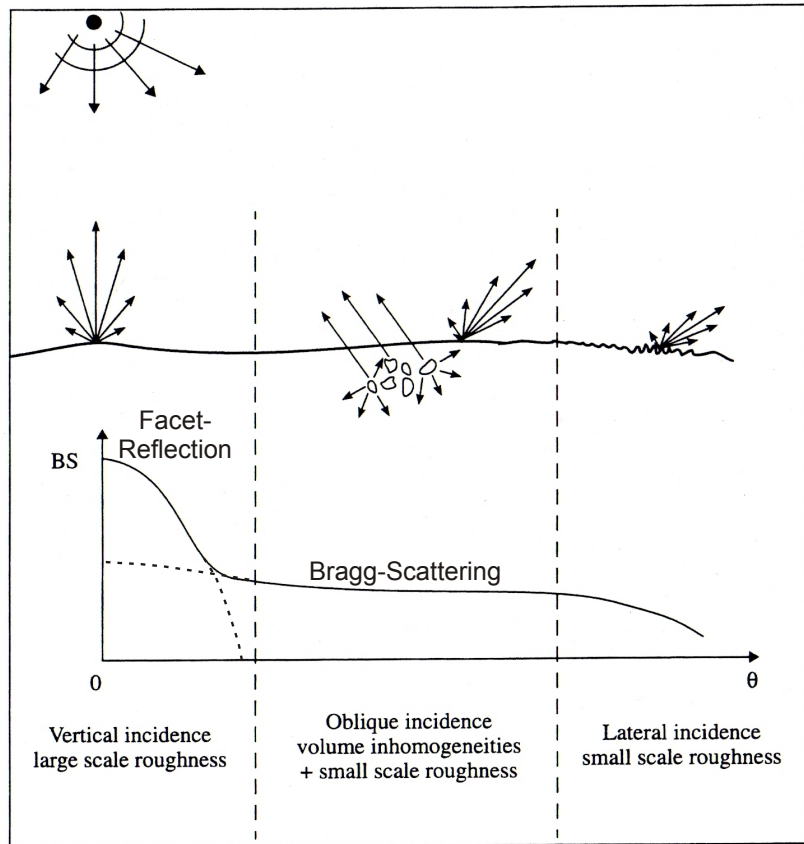


Figure 4.8: General relation of backscattering strength vs. incidence angle with contributing mechanisms (top) and dependence on seafloor type (bottom). With increasing roughness, the level of the Bragg regime increases and the level of the specular component decreases (modified from Augustin et al. [1996]).

4.2.6.3 Lambert's law

A first approximation assumes that the rough surface is a perfect scatterer following *Lambert's law*. In figure 4.9 sound of intensity I_i incidents at angle θ_i on the surface area dA . The power intercepted by the area is $I_i \cos \theta_i dA$. Lambert's law assumes, that

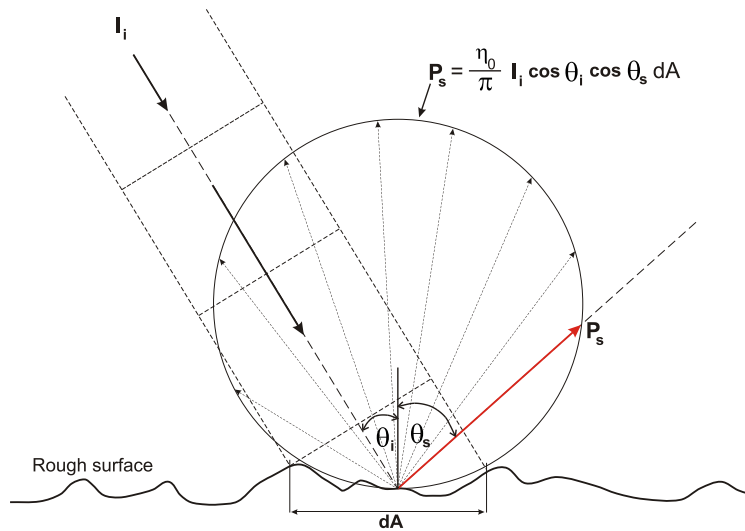


Figure 4.9: Diffuse scattering at a Lambert scatterer. The intercepted power $I_i \cos \theta_i dA$ is scattered following the cosine of θ_s . The scattered intensity which is the power per unit area, is constant at unit distance in all directions, and is dependent on the incident intensity I_i and the portion η of the acoustic energy being redistributed into the upper medium. This is why a Lambert scatterer sounds with the same 'loudness' in all directions (redrawn and modified from Urick [1983]).

the scattering and redistribution of this power into the upper medium is directed, and is proportional to the cosine of the angle of scattering θ_s . With $\eta = \text{const.}$ being the portion of the intercepted power actually scattered and not transmitted by the interface, it is:

$$\begin{aligned}
 P_s &= \frac{\eta}{\pi} I_i \cos \theta_i \cos \theta_s dA & /A_1 (= 1m^2) \\
 \frac{P_s}{A_1} &= \frac{\eta}{\pi} I_i \cos \theta_i \cos \theta_s \frac{dA}{A_1} & I = \frac{P}{A} \quad (\text{cf. equation 4.5}) \\
 I_s &= \frac{\eta}{\pi} I_i \cos \theta_i \cos \theta_s \frac{dA}{A_1} \\
 \frac{I_s}{I_i} &= \frac{\eta}{\pi} \cos \theta_i \cos \theta_s \frac{dA}{A_1}
 \end{aligned}$$

When considering a unit area ($dA = A_1 = 1m^2$) and taking 10 times the logarithm, it is:

$$10 \log \left(\frac{I_s}{I_i} \right) = 10 \log \left(\frac{\eta}{\pi} \right) + 10 \log (\cos \theta_i \cos \theta_s)$$

In the backscattering direction with $\theta_i = \theta_s$, this result is known as the Lambert law, expressed in decibels [Lurton, 2002]:

$$BS(\theta_i) = BS_0 + 10 \log(\cos^2 \theta_i) = BS_0 + 20 \log(\cos \theta_i) \quad (4.22)$$

Figure 4.10 shows a plot of Lambert's law for a value of -20 dB for BS_0 . The gradient of the curve is steepest in the far range ($\theta \geq 80^\circ$), which will be important for the evaluation of the influence of the seafloor slope on the backscatter strength. A theoretical upper limit of BS_0 can be determined when assuming that all the acoustic energy incident on the interface is scattered and nothing is transmitted into the lower medium, so that $\eta = 1$ and $BS_0 = 10 \log(1/\pi)$, i. e., around -5 dB re 1 m^2 . Measured seafloor values for BS_0 range between -10 dB and -40 dB re 1 m^2 [Lurton, 2002].

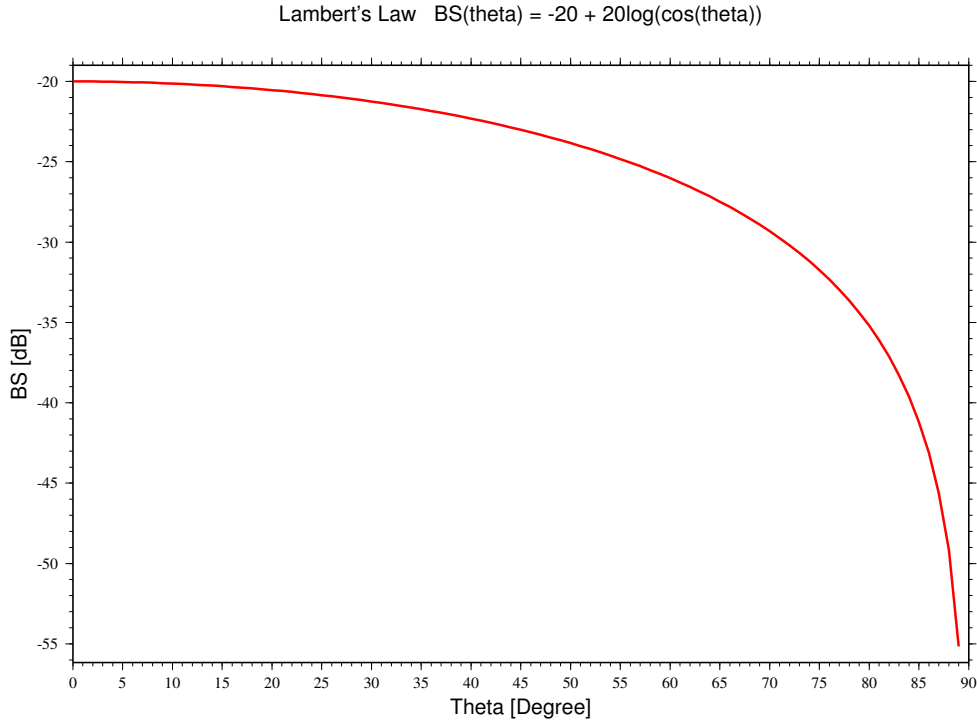


Figure 4.10: Backscatter strength BS over incidence angle θ for *Lambert's law* ($BS(\theta) = BS_0 + 20 \log(\cos \theta)$) with $BS_0 = -20 \text{ dB}$. The gradient of the curve, which determines the change in backscatter for a certain change in incidence angle, is steepest in the far range.

4.2.6.4 Facet reflection

The facet reflection or tangent plane model is based on the assumption that the roughness is sufficiently smooth (large), that sound reflection at a point takes place in the same way as reflection at an infinite plane tangent to a rough surface at the point considered [Brekhovskikh and Lysanov, 2003]. It sums up the contributions from the local reflecting planes whose distribution is given by the roughness slope spectrum [Augustin et al., 1996]. Lurton [2002] describes it as the mainly specular reflections from a mosaic of facets with random tilt angles, distributed around the average surface plane. As most facets are oriented around the horizontal, the backscattering strength will be maximum around vertical incidence. With increasing incidence angle, fewer and fewer facets are oriented to contribute to the specular reflection (Fig. 4.11). The backscatter strength decreases therefore drastically. This approach is commonly used for modeling backscatter close to the vertical.

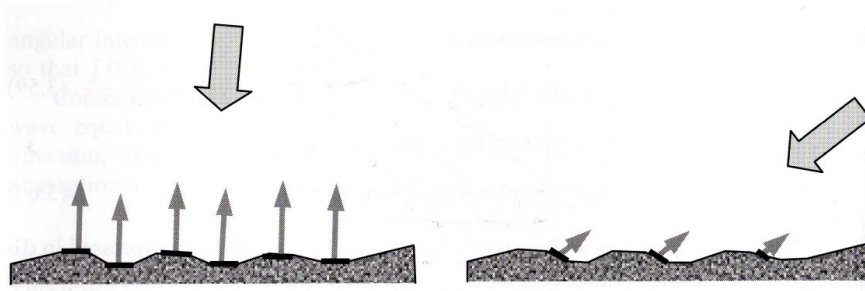


Figure 4.11: Facet backscattering: Larger number of facets with specular orientation at incidence angles close to the vertical (left) than at grazing angles (right) (from Lurton [2002]).

4.2.6.5 Bragg scattering

When microscale roughness is small relative to the acoustic wavelength λ , the backscattered field is made of a continuum of contributions from points along the interface. At oblique observation angles θ , the signal is dominated by scattered waves which are in phase, i. e., which interfere in a constructive mode. The scatter points from which these waves originate, are then distributed at distances d from each other, so that (Fig. 4.12):

$$2d \sin \theta = \lambda \quad (4.23)$$

The main contributor to scattering along this angle of observation is then the roughness spectrum component with the spatial wavelength Λ being equal to the distance d and defined by the wave number κ (cf. 4.2.6.1, figure 4.7):

$$\kappa = \frac{2\pi}{d} = \frac{4\pi \sin \theta}{\lambda} \quad (4.24)$$

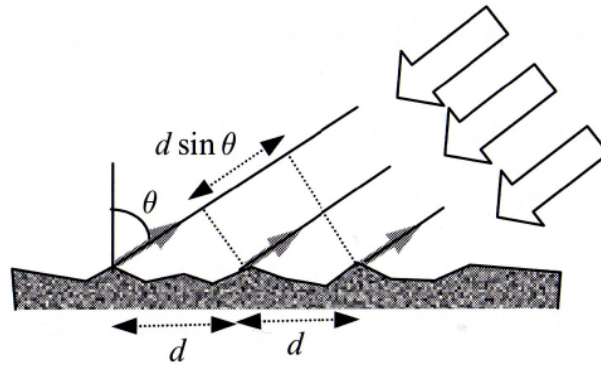


Figure 4.12: Bragg backscattering: Constructive interference of backscatter from scatterers with spacing d , when $\lambda = 2d \sin \theta$ (from Lurton [2002]).

4.2.7 Correcting the backscatter signal for seafloor slope

As the variation of the backscatter strength BS with incidence angle θ can lead to misinterpretations in areas with topographic relief (e.g. highly reflective areas due to the general slope of the seafloor are interpreted as local hard structures), it is one goal to eliminate the influence of the seafloor slope on the backscatter signal. Here the methodology applied is described.

During processing of backscatter data a so-called *shading* is applied to the measured (raw) amplitude values. This means that the sensor-specific backscatter strength–incidence angle relationship (*shading function*), ideally determined on a horizontal, smooth and uniform seafloor, is used to normalize the values, so that a seafloor with identical physical properties has exactly the same backscatter level in the resulting sonar image, independent of range or incident angle. Usually a horizontal seafloor is assumed for this correction. With the exact seafloor morphology the (additional) change in the incidence angle by the gradient of the seafloor in the direction of the sensor can be considered. Then a different backscatter value has to be applied to normalize the amplitude value. This is shown in figure 4.13.

As the incidence angle is the angle between the acoustic beam and the local normal to the seafloor, two cases must be distinguished:

- (1) the seafloor is inclined *towards* the sensor, or
- (2) the seafloor is inclined *away* from the sensor.

In the first case the incidence angle will be reduced by the amount of seafloor slope, in the second case it will be increased by this amount. Because the general trend of the shading function is a decrease in backscatter strength with increasing incidence angles, the backscatter values will be larger in the first case, and smaller in the second. Such a correction is easily achieved for amplitude measurements of multibeam echosounders because the corresponding depths are acquired at the same time and in the same resolution, and the sensor position is known very precisely from onboard GPS logging.

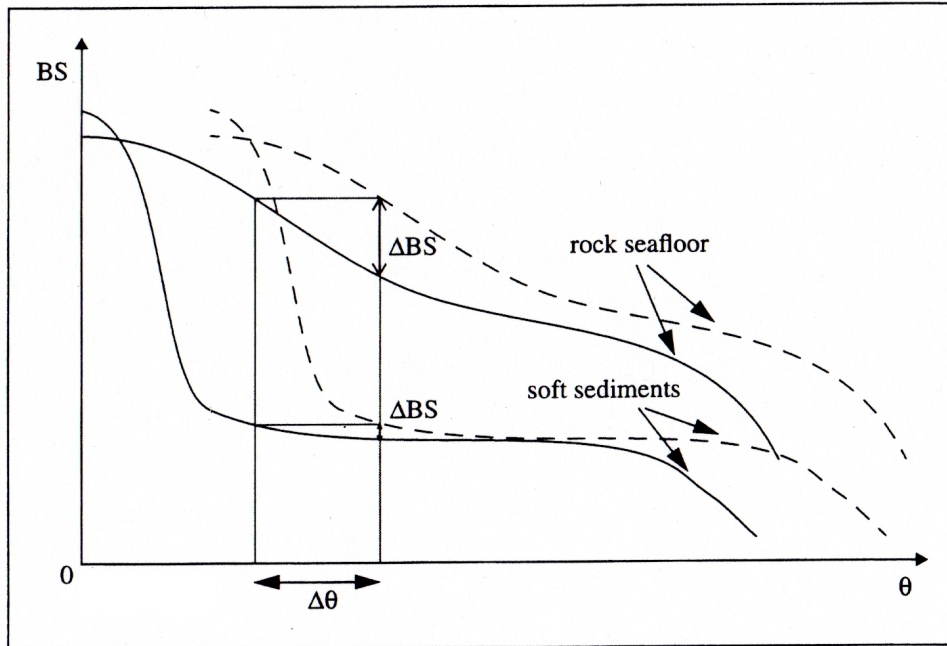


Figure 4.13: Backscatter strength on a horizontal and an inclined seafloor. The change in incidence angle due to slope is $\Delta\theta$. The corresponding backscatter strength for the new incidence angle can be read by shifting the curve or adding/subtracting $\Delta\theta$ to/from the incidence angle on the horizontal seafloor. The change in backscatter strength depends on seafloor lithology (from Augustin et al. [1996]).

Applying these corrections to deep-towed sidescan sonar data is more difficult because of:

- imprecise positioning of the towfish,
- varying elevation of the towfish above the seafloor,
- shadow areas behind obstacles due to the low position of the towfish relative to the insonified seafloor,
- resolution discrepancy between sidescan mosaic pixels and available bathymetry grid, and
- the lack of calibrated and quantitative amplitude measurements excluding the application of theoretical models.

Despite these problems, I wrote a software program in order to calculate from the towfish position and the bathymetry grid (as well as the derived gradient and azimuth grids) the incidence angle of the acoustic beam from the transducers on each seafloor grid cell. Depending on these incidence angles θ the measured sidescan sonar backscatter amplitude values are tentatively corrected.

4.3 The DTS-1 angular variation of backscatter

As the sensor of the IFM-GEOMAR DTS-1 sidescan sonar does not measure calibrated backscatter strengths, but raw amplitude values, the theoretical models described in section 4.2.6 are not applied to reduce the topographic effect in the backscatter signal. Instead, it is more promising to derive the sensor- and survey-specific relationship between backscatter strength and incidence angle from the acquired sidescan data directly. Because such a relationship is also used during ‘conventional’ processing to perform the *shading* of backscatter values, it is referred to as shading function.

In the ideal case the function is determined on a profile section where the seafloor is horizontal and smooth, and shows a uniform backscatter. Additionally the vehicle elevation above the seafloor should be constant over the length of the section, because the incidence angle varies with towfish height. A function derived under these circumstances can then be used for shading of raw data from other parts of the survey. Applying at the same time the method described in section 4.2.7 will reduce the effect of a seafloor slope in the backscatter signal. When the seafloor consists of different lithologies with differing backscatter strength vs. incidence angle relationships, a complete elimination of the topographic effect will only be achieved when a change in incidence angle induces for both lithologies the same change in backscatter strength (see figure 4.13 for explanation). In this case the residual variation in backscatter strength will be solely due to a difference in lithology or roughness.

The individual values of the shading function (the *shading coefficients* $BS(\theta)$) are calculated by adding up all the amplitude values in the same distance from the nadir (in a range bin, parallel to the track) from successive pings along the profile section, and forming their average. Because the shading function is not identical for the starboard and port side transducers, this must be done for each side separately. Figure 4.14 illustrates the calculation principle and points out, that the water column samples, included in the raw data, have to be neglected, to actually add up samples along the same distance (on the seafloor) from the trackline. To investigate the characteristics of the transducers and the seafloor, the shading function has been calculated and plotted as graph for several areas (figure 4.15). First, the backscatter strength–incidence angle relationship was derived over the whole length of the test area. This area was chosen to demonstrate and investigate in detail the influence of topography on sidescan sonar images, as explained in the following sections.

The resulting shading function shows a strong asymmetry of maxima between the port and starboard transducers (figure 4.16). It can be plotted as shading coefficient over sample number (as ordered in the raw data), over distance from nadir, or over incidence angle θ . For the presentation shading coefficient over incidence angle θ the average vehicle elevation of the considered profile section is used to convert nadir distances into incidence angles with $distance = elevation \cdot \tan \theta$. Note that the two extreme maxima on starboard and port side are within a distance of less than 100 m from the nadir. The gradient of the curve decreases then around 200 m, and the curve turns almost horizontal between 300 m

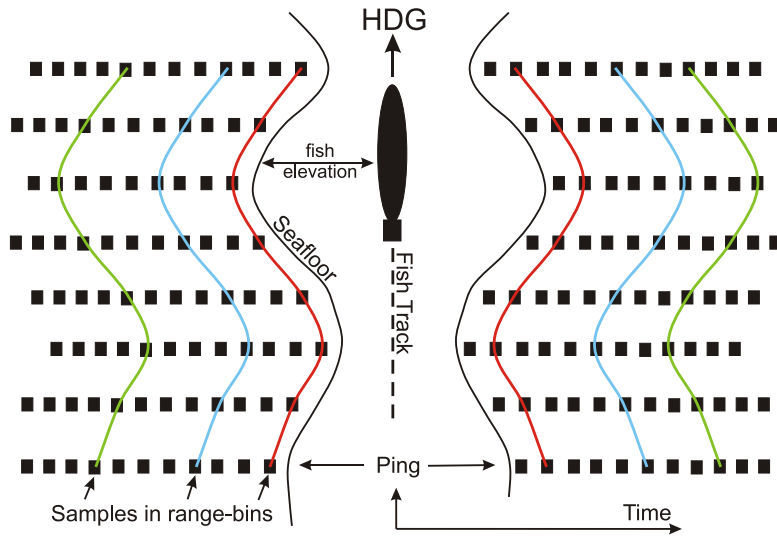


Figure 4.14: Calculation principle of shading coefficients illustrated in a sketch of a raw sidescan sonar image. The center represents the water column until the first return from the seafloor. Each value of the shading function is calculated by adding up and averaging the amplitude values parallel to the towfish track. Because this is done on the raw data, the water column samples must be removed first. The coloured lines represent range-bins, amplitude values measured in the same distance parallel to the towfish track.

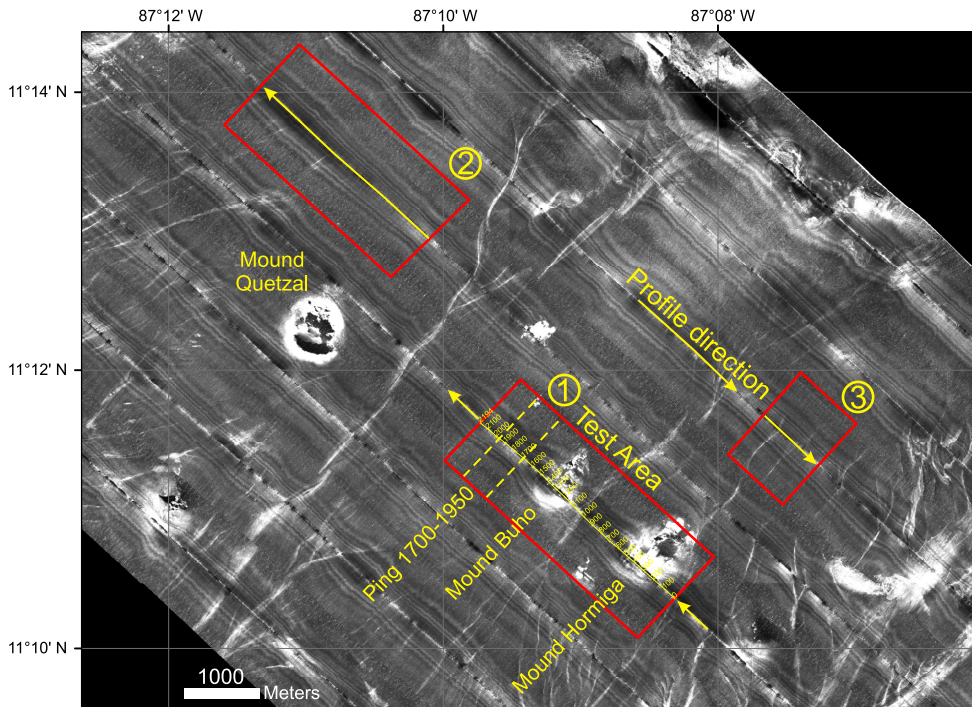


Figure 4.15: Profile sections for calculation of DTS-1 shading function. Note survey direction relative to the general direction of seafloor slope which is to the SW.

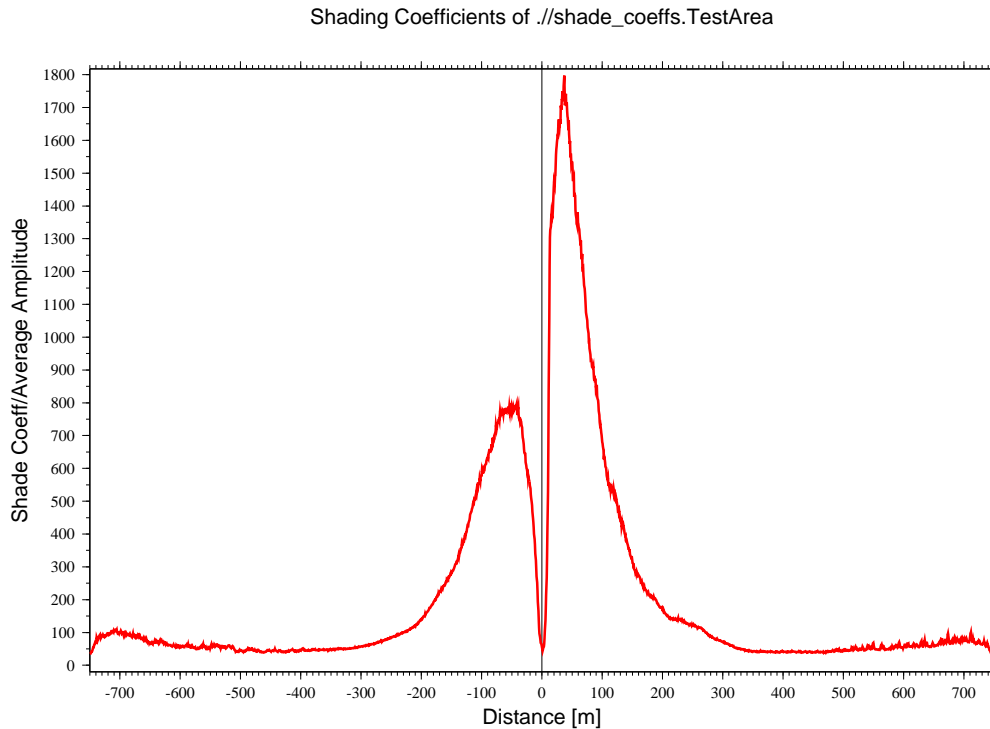


Figure 4.16: Shading coefficients over whole length of test area, plotted over nadir distance. The average vehicle elevation above seafloor is 137 m, resulting in a ground range of 737 m, when slant range is set to 750 m, and a horizontal seafloor is assumed. Water column samples have been removed.

and 400 m. Between 400 m and 500 m distance the shading coefficients start to increase slightly with increasing range. This is due to the strong amplification of the incoming signal by a *time-varying gain*. Lacking a clear backscatter echo, it amplifies the *ambient noise*. It is remarkable that this happens already in mid-range and not, as expected, only in the very far-range around 700 m.

Because a first suspicion was that the asymmetry of the maxima results from the two mound structures present in the test area, another area of the seafloor without any irregularities was chosen for a further calculation of a shading function (area number 2 in figure 4.15). Again the maximum on the starboard side exceeds the maximum on the port side. But this time the (averaged) amplitudes are much lower in general and do not exceed a value of 600. This is attributed to the fact that the high backscatter values from the mounds are missing.

To proof that the difference in the maxima of the amplitude values between port and starboard side is actually due to the general slope of the seafloor the shading curve was calculated for an area where the sidescan sonar was towed in the opposite direction (area number 3 in figure 4.15). Now the port side transducer shows the higher peak. Additionally this result was verified with data from a portion of the seafloor in the Black

4.3. THE DTS-1 ANGULAR VARIATION OF BACKSCATTER

Sea, where the seafloor is known to be uniform, plain and horizontal. Here the shading function turns out to be symmetric. The possibility that transmission loss along differing travel paths of the acoustic signal through the water column at an inclined seafloor is responsible for the asymmetries, can be ruled out, because then the asymmetry should be strongest in the far range and not in the nadir area, where the difference in travel path is minimal.

To explain the difference in the amplitude peaks between port and starboard transducers, it helps to look at the geometrical situation of an inclined seafloor and an incident acoustic beam (figure 4.17). Downslope, the beam has never vertical incidence on the seafloor, the smallest possible incidence angle is reached in the nadir where it is equal to the seafloor slope. Upslope, the beam ‘crosses’ vertical incidence, which is not directly underneath the towfish, but some distance upslope. It is important to note that the minimum in amplitude values in the nadir is due to the fact that sidescan sonar systems emit much less energy vertically down. If a system would have a completely circular directivity pattern, the minimum would disappear, and the resulting curve would consist of one peak, offset in upslope direction on an inclined seafloor.

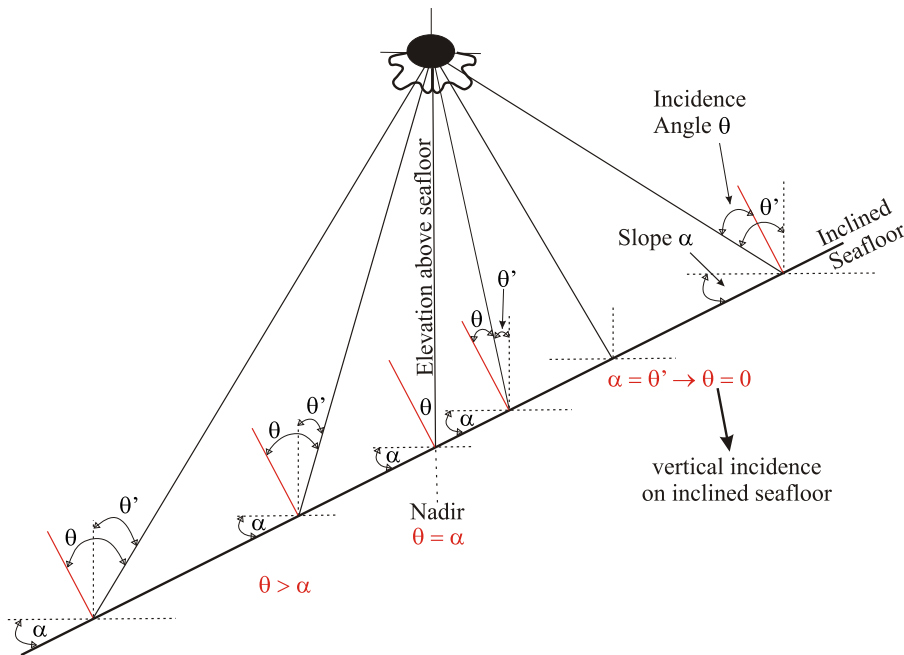


Figure 4.17: Seafloor slope causing differing port and starboard amplitude peaks. θ' is the angle of incidence on a horizontal grid cell. Due to slope α the local normal to the seafloor rotates by α , so that the real incidence angle becomes θ .

In order to derive an as far as possible symmetric shading function, a section in the test area where the seafloor in the near range is almost horizontal, was investigated. Figure 4.18 shows a plot of the seafloor morphology, the vehicle depth, and the calculated vehicle elevation in the along-track direction over the whole length of the test area. Between ping numbers 1700 and 1950 the vehicle elevation is reasonably constant, the seafloor slope in across-track direction is small and almost horizontal to about 30° (~ 75 m), and the seafloor is uniform and smooth enough (figure 4.15). The section between ping numbers 780 and 980 was investigated as well, but did not deliver a symmetric curve.

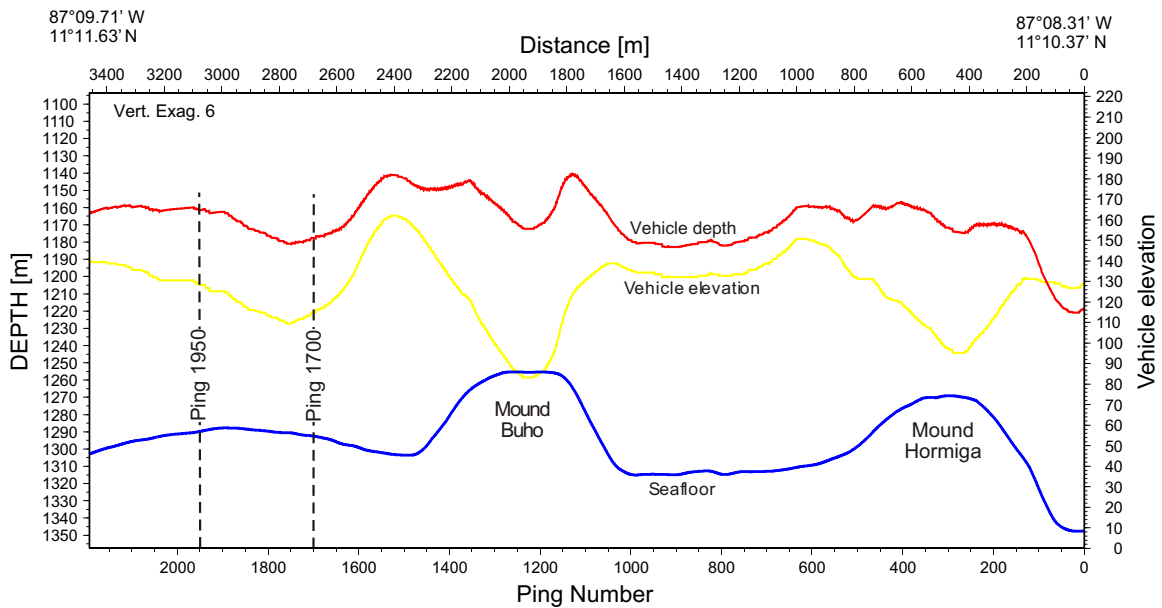


Figure 4.18: Along-track seafloor morphology (blue), vehicle depth (red), and calculated vehicle elevation (yellow) in test area. From the averaged amplitude values between ping numbers 1700 and 1950 the (final) shading function is derived. The average towfish elevation along this section is 128.65 m.

Figure 4.19 shows the symmetric shading function derived between ping numbers 1700 and 1950 of the test area, plotted as shading coefficient over incidence angle θ . The presentation over the angle stretches the near range and reduces the far range very strongly, and it is always important to consider the actual ground distances! But the shading function is implemented and applied in this way in the following approach. To have a simple relationship between the shading coefficient and the incidence angle, the curve is linearly approximated. Around 80° the curve is bended to smaller shading coefficient values, because the increase in the averaged amplitude values is due to an amplification of ambient noise by the time varying gain. The minimum in the nadir is due to the fact that a sidescan sonar with transducers mounted to the port and starboard side cannot emit high acoustic energies vertically down. Therefore it would be correct to bridge the minimum and interpolate between the two amplitude peaks. But as the

4.3. THE DTS-1 ANGULAR VARIATION OF BACKSCATTER

maxima occur at around 20° , which corresponds, at a vehicle elevation of 128 m, to a distance of roughly 45 m to either side of the track, this weakness is neglected. It is important to remember, that the correction of a backscatter signal for the topography does not work correctly, when shading coefficients from the centre of the curve are applied.

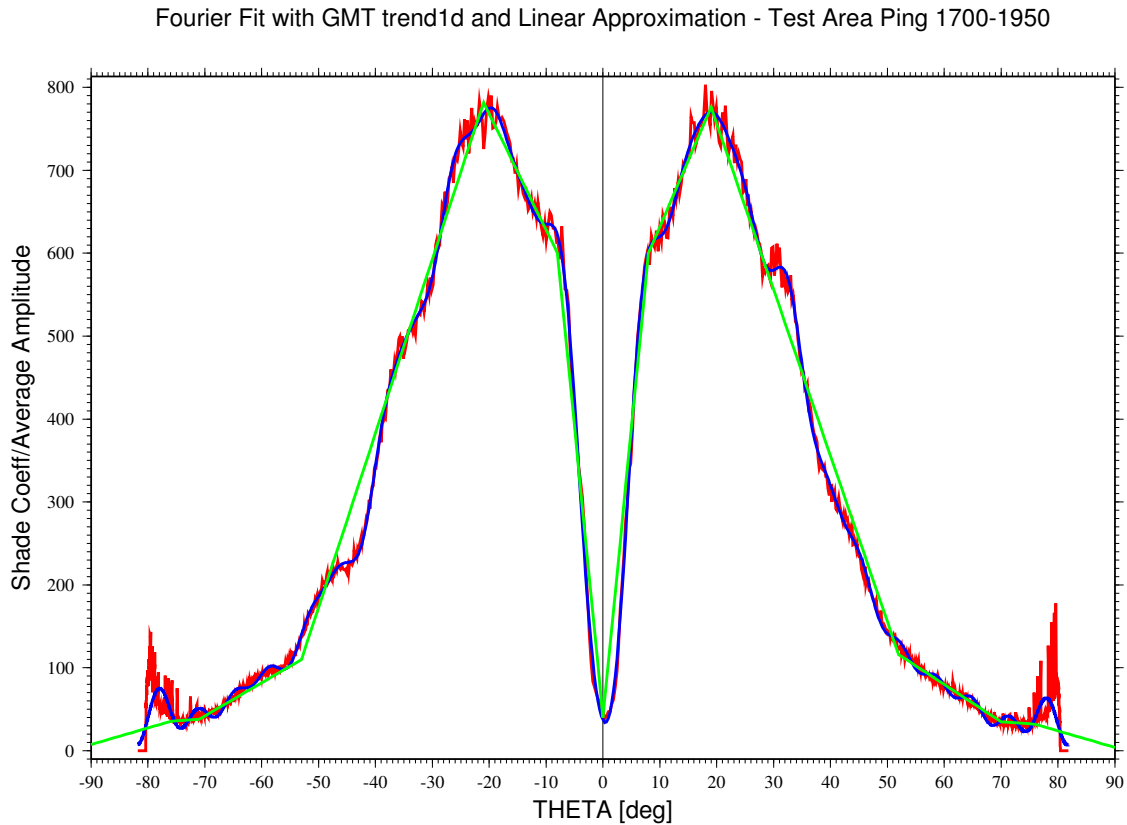


Figure 4.19: Linear approximation of symmetric shading function from ping numbers 1700 to 1950 in test area. Plotted are the averaged amplitude values (red), a Fourier fit (blue), and the approximation with line segments (green). The linear functions are used by the algorithm to correct the backscatter signal for topographic influence.

4.4 Processing algorithm

Important for the calculation of the incidence angle θ , discussed in section 4.2, is on one hand the geometric relationship between the sidescan sonar towfish (i. e. the transducers) and the observed seafloor grid cell, and on the other hand the orientation of this seafloor grid cell in space, i. e. slope and azimuth of slope. In this section the algorithm for the calculation of the incidence angle of an acoustic beam on a seafloor grid cell, and the methodology applied to reduce the measured backscatter value according to this incidence angle are described. The various steps are implemented in a software program, and are illustrated in a flowchart (see figure 4.21). But first some general assumptions are given.

General assumptions

The sound velocity in seawater is assumed to be constant with 1500 m/s. The slant range of the sonar (to port and starboard side) was set to 750 m during the survey. The ping time interval (defined through the range setting) is then 1.020 seconds, with an actual recording time on each transducer of 1.0 seconds. The recorded signal is sampled by an A/D converter with 13300 Hz and stored in a digital format. The two-way-travel time (TWT) per sample results then from the division of the recording time through the number of stored samples at each transducer. Actually the number of stored samples can vary slightly which has its reason in the transformation of the raw xse data into the generic netCDF data format with the software routine *rawxse2prism* (see figure 4.21). Figure 4.20 shows the generation of a sidescan sonar image from successive acoustic pulses (pings). The signal is sent out at each ping time interval by the transducers at the port and starboard side of the towfish in a direction perpendicular to the heading. The sound wave then spreads out spherically and insonifies the seafloor at increasing distances from the nadir. It is important to note that the transducers have a characteristic directivity pattern, which shows an angle dependent energy distribution of the signal. After travelling through the water column the signal hits the seafloor first at the shortest distance, which is in case of a horizontal seafloor in the nadir of the vehicle. It is assumed that the incoming signal over time is directly related to points on the seafloor of increasing distances from the nadir. In other words, the incoming signal is digitized into a sequence of samples containing the measured amplitude values.

The description of the processing algorithm follows the structure of the software program *topored*, which was developed for this study. The flowchart (figure 4.21) shows that preceding *topored*, the data have to be converted from the raw acquisition data format xse into the generic format netCDF. During this conversion the vehicle elevation information from a textfile is integrated into the data file. The netCDF (*network Common Data Format*) is an interface for array-oriented data storage and access, and a library that provides an implementation of that interface (<http://www.unidata.ucar.edu/software/netcdf/index.html>).

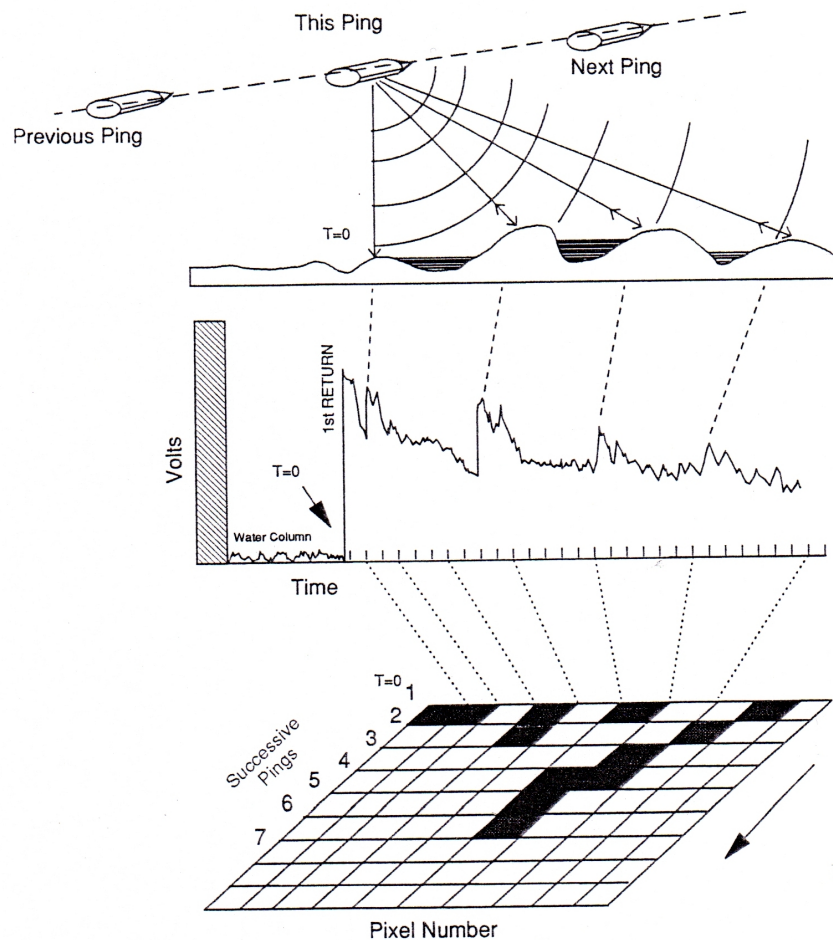


Figure 4.20: Generation of image pixels from an outgoing acoustic pulse. The sound wave is reflected back from the seafloor leading to peaks and valleys in the transducer voltage (shown as the rapidly varying line in the middle diagram). These peaks and valleys in voltage are then integrated and translated into pixel values ('samples'), which are displayed as dark and light 'greyscale' regions in the sidescan image. As the raw data contain the samples from the two-way travel time through the water column, these have to be removed to get a map representation of the seafloor (from Johnson and Helferty [1990]).

Class *CDF_Data*

The class *CDF_Data* opens and reads the netCDF data file, using the defined netCDF interface. The data contain the recorded image or backscatter information, arranged in a two-dimensional array with ping and sample as the dimensions. For each ping the vehicle attitude information from a motion sensor, like heading, pitch, roll and yaw, and the vehicle elevation above seafloor are available. Additionally the class reads the vehicle navigation information from a pre-processed external navigation file. These are vehicle position and water depth at each ping. The class also contains the implementation

of the linear approximation of the DTS-1 shading function (cf. 4.19), which is used in class *Sample* (`CDF_Data.BS_THETA()`). The main loop over all pings starts then the processing.

The data file used for this study contains 2195 SSL (sidescan 75 kHz) pings, with each ping consisting of 2606 pixels or samples. The number of samples is actually decimated from 26076 to 2606 during the conversion to netCDF format, to achieve a similar along-track and across-track resolution.

Calculations on class *Ping*

The class *Ping* performs the following calculations:

- First a ping is initialised with the necessary information for the calculations, i. e. ping number, vehicle latitude and longitude, water depth at vehicle position, vehicle elevation above the seafloor and the vehicle attitude values from the built-in motion sensor (heading, pitch, roll, yaw).
- It calculates then the positions of all samples contained in the ping on the seafloor. Therefore it is necessary to know the number of water column samples from the vehicle elevation. The (across-track) size of one sample on the seafloor is then the ground range (calculated for a horizontal seafloor) divided by the number of seafloor samples. Knowing the size and number of seafloor samples, the position of each sample on the seafloor can be calculated, starting from the nadir and assuming a horizontal seafloor.
- The sample positions (latitude, longitude) are then stored in a file.
- At the sample positions in the file, the seafloor depth, gradient, and azimuth can be retrieved from corresponding *GMT* grids [Wessel and Smith, 1991], and are added to the file.
- A loop over the file containing now all seafloor samples with the relevant information processes then each seafloor sample. A new backscatter value is returned from the *Sample* class, and is set in the netCDF array at the location [*ping_number*, *sample_number*].
- Finally all ping parameters are logged to a file.

Calculations on class *Sample*

The class *Sample* performs the actual calculation of the new backscatter value. It calculates from the specific geometric situation between the transducer and the sample on the seafloor the elevation angle, converts it to the incidence angle on a horizontal plane, and adds or subtracts the portion of slope of the sample grid cell (figure 4.22). For

4.4. PROCESSING ALGORITHM

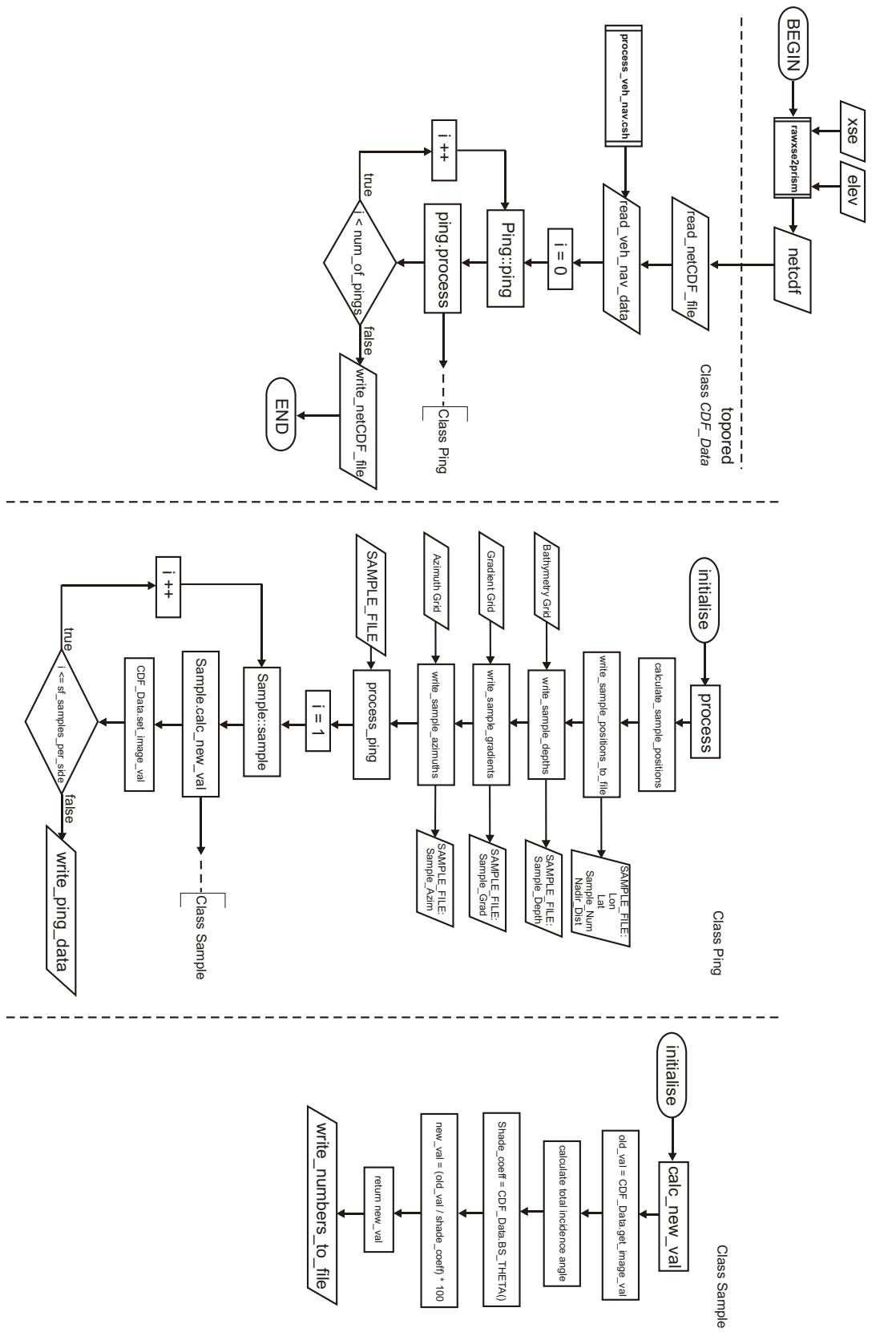


Figure 4.21: Flowchart of program *TopoRed*; see explanation in the text.

this incidence angle relative to the local normal it retrieves the shading coefficient from the *CDF_Data* class and scales the amplitude value appropriately. Finally it writes all parameters and results of the calculations to a log-file.

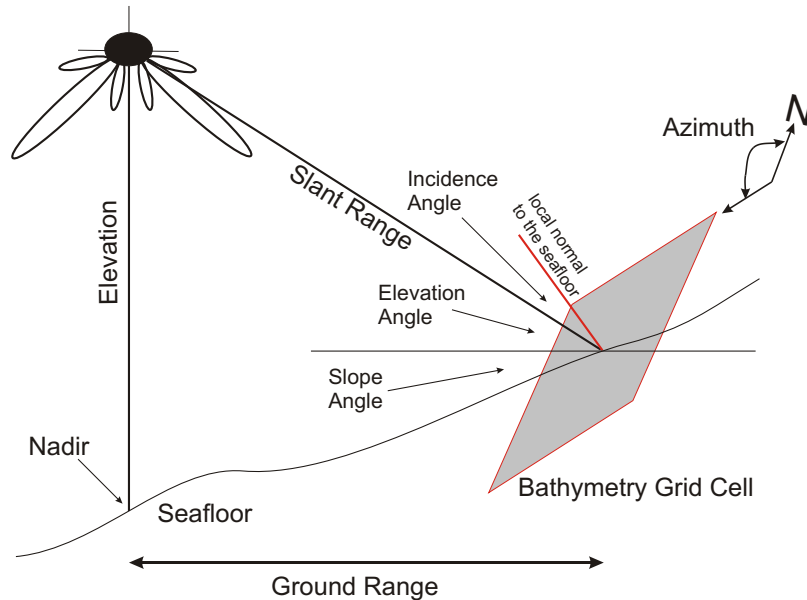


Figure 4.22: Geometry between sidescan transducer and bathymetry grid cell.

A more detailed description of the steps is given here:

- From the ping number and sample number the original amplitude value is retrieved from the netCDF data array.
- From the geometric situation, i. e. the relative height of the towfish above (or below) the sample grid cell, and the distance of the sample grid cell from the nadir, the *elevation angle* is calculated (figure 4.22). In case the towfish is below the sample grid cell, the elevation angle is negative. The elevation angle is then converted into the *incidence angle* relative to a horizontal seafloor with (90° - elevation angle).
- Additionally the seafloor slope and the direction of the slope at the sample location have to be considered. The gradient is known from the sampling of the gradient grid (see class *Ping*). But this is the maximum slope in the direction of the azimuth of the sample grid cell, and it has to be scaled according to its portion along the direction of the acoustic beam. Therefore the angle between the acoustic beam heading and the azimuth of the sample grid cell is calculated, and a cosine law applied. So, if the azimuth of the slope is perpendicular to the acoustic beam, the slope component in the direction to the transducer would be zero. Vice versa, if the azimuth is parallel to the acoustic beam, the slope component would be maximum.

- In this calculation of the slope component along the direction of the acoustic beam, it is also important to account for the cases, where the sample grid cell can not be illuminated by the beam but is in the acoustic shadow. Figure 4.23 examines possible spatial relations between the position of the transducer and a seafloor sample grid cell. It is important to note that solely the geometric situation between transducer and grid cell is observed, and any obstacles along the acoustic path are not considered. If a grid cell is claimed to be in the shadow, the slope is set to zero, intending that the original amplitude value (which is very low due to the shadow) is not changed.
- With the (relevant) slope component of the sample grid cell the incidence angle relative to the local normal can be calculated. For this it is necessary to know, whether the inclination of the sample grid cell is *towards* the transducer or *away* from it. When the grid cell is inclined towards the towfish, the amount of the slope has to be subtracted from the incidence angle on a horizontal plane. Is it inclined away from the towfish, it has to be increased, respectively. To distinguish the two cases the heading of the acoustic beam and the azimuth of the sample grid cell are compared. The borderline where the direction of inclination swaps is basically the vehicle track.
- To retrieve the appropriate shading coefficient from the shading function implemented on class *CDF_Data* the incidence angles on port side are turned negative, the starbord ones stay positive.
- The original amplitude value is scaled with:

$$new\ value = \frac{original\ value}{shading\ coefficient} \cdot 100 \quad (4.25)$$

... and converted into an integer number. The multiplication with 100 is applied, because a smooth, uniform and horizontal seafloor would have amplitude values around 1.0 after division of the original value through the shading coefficient, which makes the integer conversion problematic.

- The new backscatter value is returned.
- Finally, all parameter values and calculation results are logged to a file. Gridding with *GMT* produces their map representation. The columns in the file are in particular:
 - ping number
 - sample number
 - sample location (starbord or port side, s or p)
 - sample longitude
 - sample latitude
 - distance from nadir

- water depth at sample location
- gradient of sample grid cell
- azimuth of sample grid cell
- grid cell inclined towards transducer? (bool 1 or 0)
- towfish above sample grid cell? (bool 1 or 0)
- is the sample grid cell claimed as shadow? (bool 1 or 0)
- elevation of towfish above sample grid cell
- elevation angle
- incidence angle relative to horizontal plane (90° - elevation angle)
- slope of sample grid cell in degrees
- azimuth factor applied to slope ($\cos \angle$ (beam heading, sample azimuth))
- effective slope (result of slope \cdot azimuth factor)
- incidence angle relative to local normal (incidence angle \pm effective slope)
- original amplitude value
- re-calculated, new amplitude value
- difference between new value and original value
- change in percentage [$((\text{new value} - \text{original value}) / \text{original value}) \cdot 100.0$]
- applied shading coefficient from built-in shading function

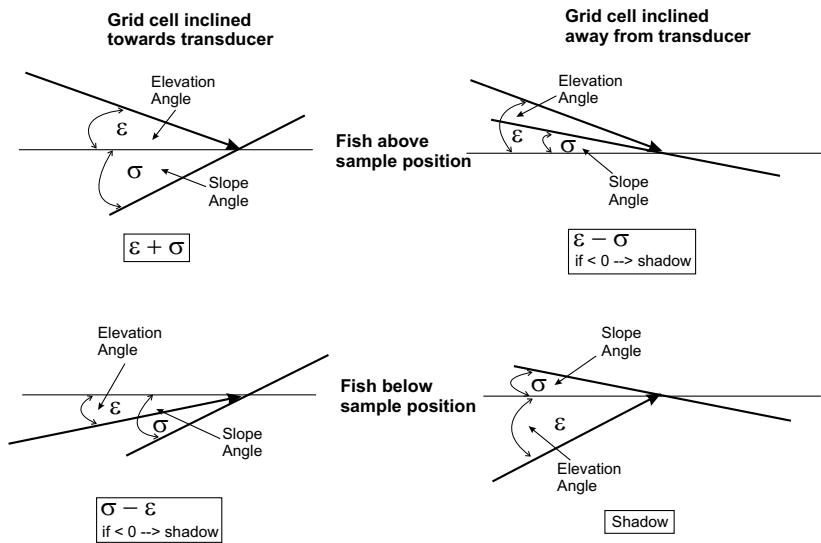


Figure 4.23: Possible spatial relations between an incident acoustic beam (large arrow) and a bathymetry grid cell. The elevation angle ε is the angle of the beam against a horizontal seafloor. The slope angle σ is the inclination of the seafloor against the horizontal. The sidescan sonar vehicle can be above or below the seafloor grid cell, which can be inclined towards or away from the transducer. In the small rectangle below each figure, the calculation of the total incidence angle relevant for the appropriate shading is given, or, if the seafloor grid cell is not illuminated by the acoustic beam, it is marked as shadow.

4.5 The test area

To demonstrate the influence of seafloor topography on a sidescan sonar image, a profile section over Mound Buho and Mound Hormiga is processed with the software program *topored*, described in section 4.4. As a reference figure 4.24 shows the sidescan image processed with the *PRISM* software package, and marks the main features. The image has a pixel resolution of 1 m. The actual resolution of the data is even better (around 60 cm). Both mounds are almost completely inside the swath width of 1500 metres. Additionally to the large mound structures, two distinct backscatter anomalies are visible in the far range. At the southeastern border of Mound Buho, the profile crosses a small gully with slightly increased backscatter intensities. Both mounds show a patchy backscatter signature on top, probably due to larger carbonate blocks and associated shadows. Central depressions in the top areas are not directly illuminated by the acoustic beam, and are presented as shadow areas.

The bathymetry and gradient grid (figures 4.25, 4.26) for the test area have a cell size of approximately 50 m. The seafloor slopes in general to the southwest with a dip of approximately 4° . The steep mound flanks of Mound Buho and Mound Hormiga show a gradient of up to 20° , both, parallel track and across track. The top areas of the mounds are more or less horizontal, any carbonate blocks are not resolved. Only the depression between the two summits of Mound Hormiga is indicated by the gradient arrows. The intensity anomaly north of Mound Buho is not observed in the multibeam data, but the one west of Mound Hormiga seems to cause an increase in dip further downslope. The vehicle track crosses Mound Hormiga along its southwest flank, Mound Buho is crossed almost right over the top.

Several questions can be raised:

- What influence does a general seafloor slope have on the backscatter signal?
- How much of the backscatter signal from the mound flanks is due to topography, and how much can be attributed to lithology?
- How are the top areas of the mounds with patchy backscatter and shadow areas changed?
- Is the backscatter signal from the intensity anomalies increased or decreased, when considering the topographic influence?

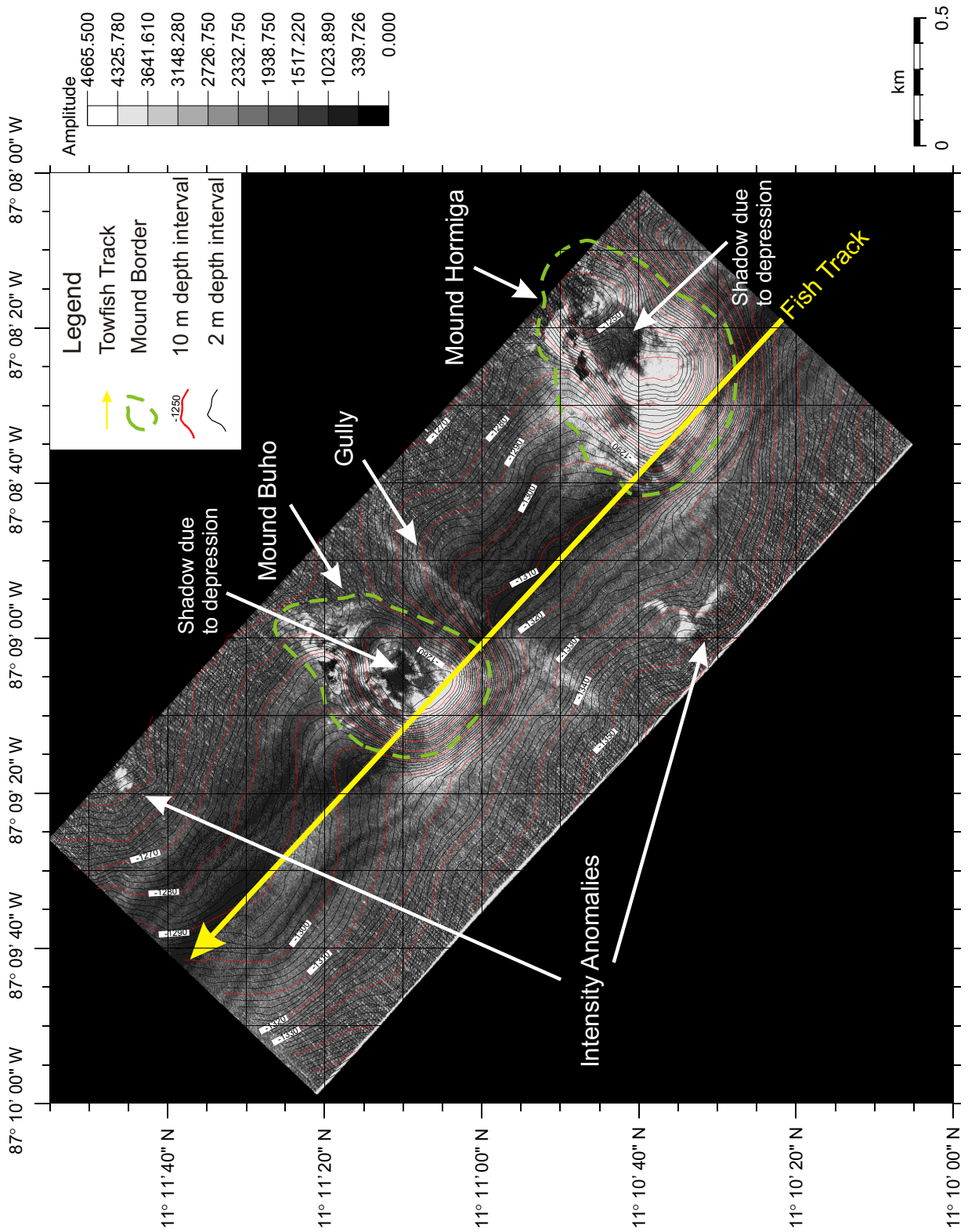


Figure 4.24: Sidescan sonar image of the test area with Mound Buho, Mound Hormiga, and two distinct intensity anomalies in the far range, processed with *PRISM*.

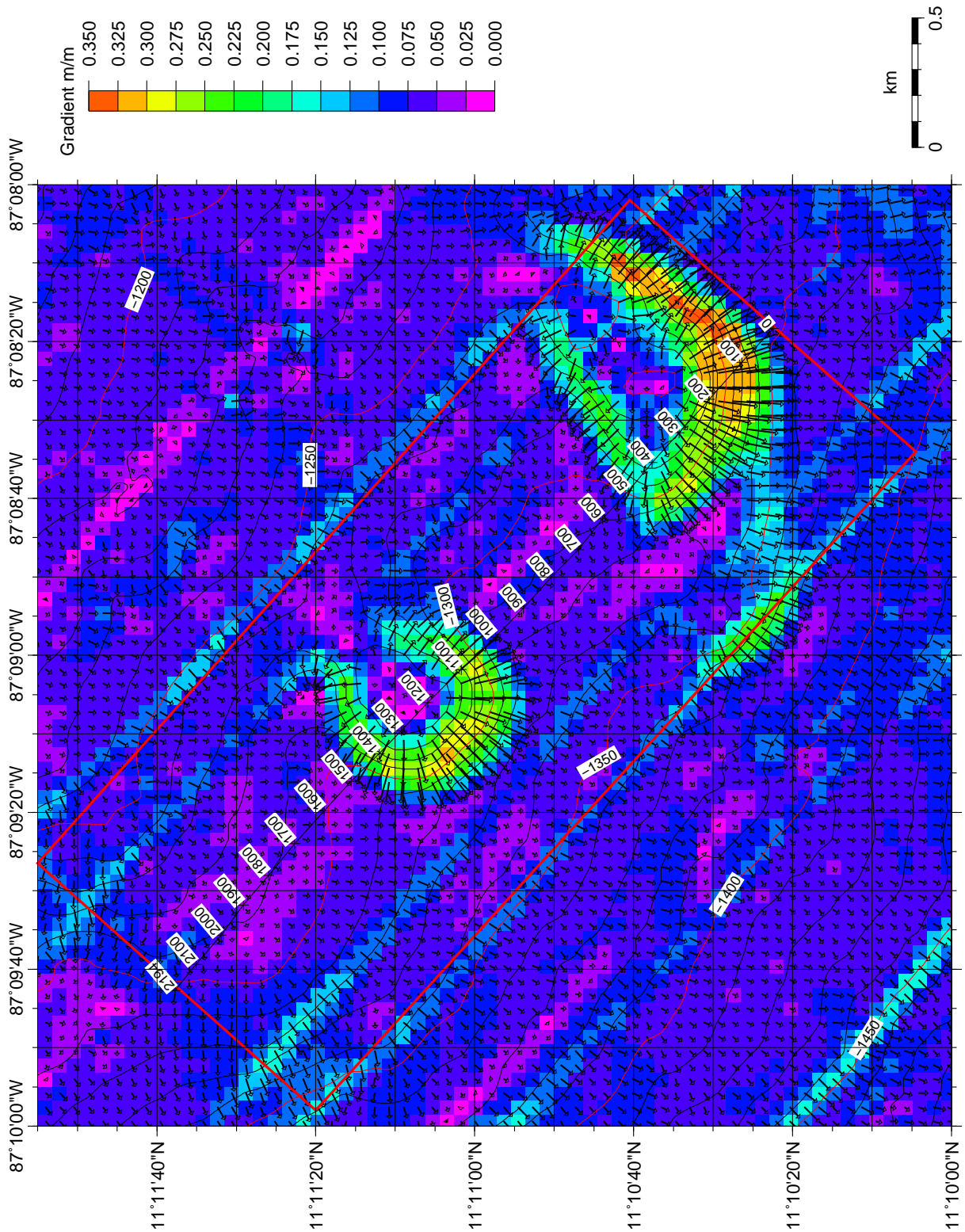


Figure 4.26: Color coded gradient map of the test area. Vectors show the direction of slope, with length of vectors indicating the steepness. Numbers along fish track (black line) are ping numbers. Red box marks test area.

4.5.1 Processing the test area

Two input parameters have a major influence on the processing of the test area data:

- The bathymetry used for sampling the depth, gradient, and azimuth at the vehicle and sample locations, and
- the shading function used to reduce the original, raw backscatter data.

A change in the input bathymetry does not only change the slope of the grid cells, but also the relative heights between transducer and the samples on the seafloor. A change of the relative height changes then also the incidence angle of the acoustic beam on a grid cell. For the interpretation of a sidescan sonar image it can therefore be quite difficult to estimate the influence of the various parameters, and to predict, where amplitude values are increased or decreased due to the morphology. Usually someone thinks that topographic influence is mainly determined by the angle of slope of a grid cell. To visualize in a first approach this influence of slope a *topographic reduction factor* is introduced. It is the sinus of the slope along the acoustic beam of a grid cell, subtracted or added to 1.0, depending on whether the grid cell is inclined towards or away from the transducer. The reduction factor can vary therefore (theoretically) between 0 and 2. When a grid cell is inclined towards the transducer, the original amplitude value is multiplied with a number smaller than 1, when it is inclined away, it is multiplied with a number larger than 1, respectively.

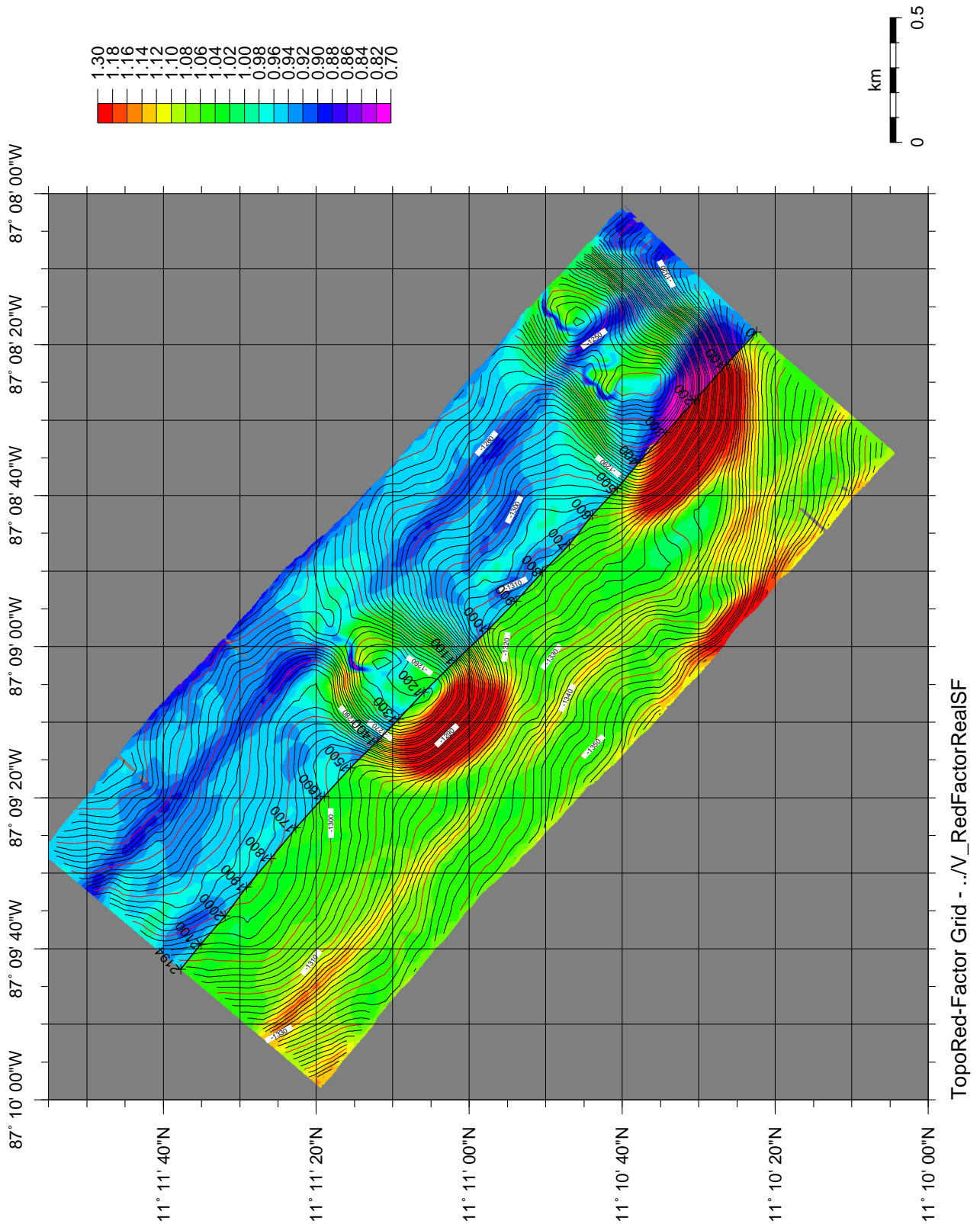
When gridding the reduction factor, the resulting image looks as one would expect: Steep areas inclined away from the transducer have factors larger than 1.0, whereas areas inclined towards the transducer have factors smaller than 1.0 (figure 4.27).

In another initial approach simply the sinus of the calculated incidence angle is used as the shading coefficient. The original amplitude values are then multiplied with the corresponding coefficients. This reduces the values in the nadir area very strongly, because the coefficients are close to zero, and leaves them unchanged in the far range where the coefficients are close to 1. But plotting the corrected amplitude values reveals that they are still too high in the nadir area compared to the far range. The shading is therefore not satisfying.

To get a quantification of the topographic influence in the test area, I used different bathymetries as input for the processing. The *synthetic* bathymetries have been generated from the accurate (real) one, and are:

- a plain and horizontal seafloor at the average water depth (-1339 metres)
- a plain but inclined seafloor, created as the 2-D trend polynomial surface
- a smoothed bathymetry, created by filtering with a boxcar filter of 0.5 km width

For each run the original amplitude values are re-calculated according to the incidence angle of the acoustic beam relative to the local normal on the seafloor. The incidence



angle in turn depends on the underlain bathymetry. The idea is that resulting amplitude grids from different runs can be subtracted from each other, and a difference in amplitude value is equivalent to the effect of topography.

For example, in a first run the horizontal bathymetry is used, and the topographic effect is fully contained in the resulting image. In a second run a smoothed or the real bathymetry is used as input, and the effect of topography is reduced or eliminated as described in section 4.2.7. The difference between the two grids shows then the influence of seafloor morphology on the backscatter signal.

For this approach the shading function shown in figure 4.19 is used, and the amplitude values are corrected according to the formula 4.25.

Finally it is important to mention, that in the vehicle navigation file the water depth information has to be resampled from the input bathymetry grid in use. The water depth is used for the calculation of the towfish depth.

4.6 Results and discussion

Each process run of the test area produces a log file containing all parameters of the calculations, as described at the end of section 4.4. These parameters can be gridded and plotted to get a map representation, and therefore a better understanding of their spatial variation. To investigate a single ping, an across-track profile of the shading coefficients applied to each sample, as well as the seafloor depth at the sample locations can be plotted. Such profiles show then the change in the applied shading coefficient due to the change in the underlain seafloor morphology.

Figure 4.29 shows a map of the raw amplitude data of all seafloor samples. The map has the same geographic reference as the processed maps and facilitates direct comparison. The very bright amplitudes in the nadir result from a steeper incidence of the sound wave on the seafloor and less transmission loss than in the far range, and indicate that no shading has been applied yet. The mound structures are hardly to detect.

Figure 4.30 and figure 4.31 show the shading coefficients when a horizontal and plain seafloor is used, and the result when these coefficients are applied to the raw data. The shading coefficients show two maxima very close and parallel to the nadir, and decrease continuously to the far range, according to the shading function (figure 4.19). The undulation of the colour intervals is due to the variation of the towfish elevation above the (horizontal) seafloor, which results in different incidence angles. The different width of some colour bands between port and starboard side results from small asymmetries of the shading function. The resulting amplitude image looks similar to the *PRISM* processed image (figure 4.24), but because no filtering has been applied the image looks noisy in the far range.

Figures 4.32 and 4.33 show in principle the same maps, but this time the surveyed, real bathymetry has been used for the processing. The shading coefficient map shows a more complicated pattern, especially at the mound locations where the morphology is more rugged, and fast changes in dip and azimuth occur. By comparing both shading coefficient maps, it is possible to infer where the amplitudes will be increased or decreased when considering the morphology. A smaller coefficient will result in higher amplitudes, and vice versa (e.g. upslope flank of Mound Hormiga). But in a first visual comparison of the resulting amplitude maps, only minor changes can be observed.

To identify regions where the amplitude values are increased or decreased, it is a good way to subtract the two grids from each other. Then the absolute and relative (i.e. expressed as percentage) changes between them can be imaged (figures 4.34 and 4.35). Both maps indicate five important results:

- Large areas where the seafloor morphology follows the general trend of inclination show only minor changes ($\leq \pm 5\%$). In general the upslope parts (where the inclination of the seafloor is towards the transducer) are decreased slightly, and the downslope parts (where the inclination of the seafloor is away from the transducer) are increased.

- The mound flanks show mainly an increase in their backscatter amplitudes, despite the fact that they have already high values. Especially the flanks downslope of the vehicle track are subject to the highest increase in backscatter in the test area. This supports the assumption that the mound structures consist of different lithologies with higher roughness than the normal hemipelagic seafloor coverage.
- The top areas of the mounds show both, decrease in amplitude values and increase. This seems to depend on small scale topography. The depression on Mound Hormiga shows a decrease in amplitude values on the side which is facing the transducer, as one would expect, and a moderate increase in its center. But in the processed amplitude image there is no difference observed.
- The amplitude values of the intensity anomaly north of Mound Buho are increased, whereas the values of the anomaly west of Mound Hormiga are slightly decreased ($\leq -5\%$).
- It is surprising that through the consideration of the topography the amplitude values are *decreased* considerably in the regions downslope of the two mounds. Here the seafloor is inclined away from the vehicle, and an increase would be expected.

A possible explanation for the last point is that following the steep mound flanks, where the incidence angle of an acoustic wave is increased due to the inclination of a grid cell away from the transducer, the seafloor turns more horizontal, and the incidence angle decreases. Additionally the larger depth intensifies this effect, as shown in figure 4.28. A smaller incidence angle results in higher shading coefficients, and hence in a stronger reduction of amplitude values.

Such effects can be investigated quite well in cross-sections of a ping, showing (real) bathymetry, and applied shading coefficients for horizontal and real seafloor (figures 4.36 and 4.37). For example a cross-section over Mound Buho (figure 4.37) shows that just upslope the nadir a small depression follows. Here the amplitude values are more or less unchanged. At the outer rim of this depression where the morphology steepens a little bit towards the transducer, the values are decreased. Following the rim, a slope away from the transducer results in an increase of the amplitudes. Then the morphology follows the general trend, leading to a decrease in the amplitude values. But it is important to note that generally the differences between the shading coefficients are very small.

A cross-section over Mound Hormiga (figure 4.36) reveals that it was crossed downslope of the summit. Therefore the first part of the seafloor upslope of the vehicle track is inclined towards the transducer, and the amplitude values are decreased ($\sim 40\text{--}110$ metres distance from nadir). The morphology then descends from this first summit to a small saddle, leading to a stronger increase in amplitude values. The ascend from the saddle to the second summit is paralleled by a decrease in the amplitudes. Over the top of the second summit the seafloor is again inclined away from the transducer despite the general trend. This results in a larger area of increased amplitude values in the far range.

As already mentioned in section 4.5.1, a change in seafloor morphology has two distinctive effects on the incidence angle of an acoustic sound wave on the seafloor. The one is the inclination of the considered grid cell, the other is a change in relative height between vehicle and seafloor grid cell. Figure 4.28 sketches the situation, when a horizontal seafloor is inclined.

It can be seen that the two effects are opposing: Increasing the relative height decreases the incidence angle, but the rotation of the surface increases it. Decreasing the relative height increases the incidence angle, but the rotation of the surface decreases it.

When, with a certain slope α at a distance d , the two opposing processes just compensate, the incidence angle would be the same as on a horizontal seafloor, and the corrected amplitude values would change then from decrease to increase or vice versa, relative to a horizontal seafloor. This is the situation downslope of the two mounds, where a strong increase on the mound flanks turns into a decrease further downslope, as mentioned above.

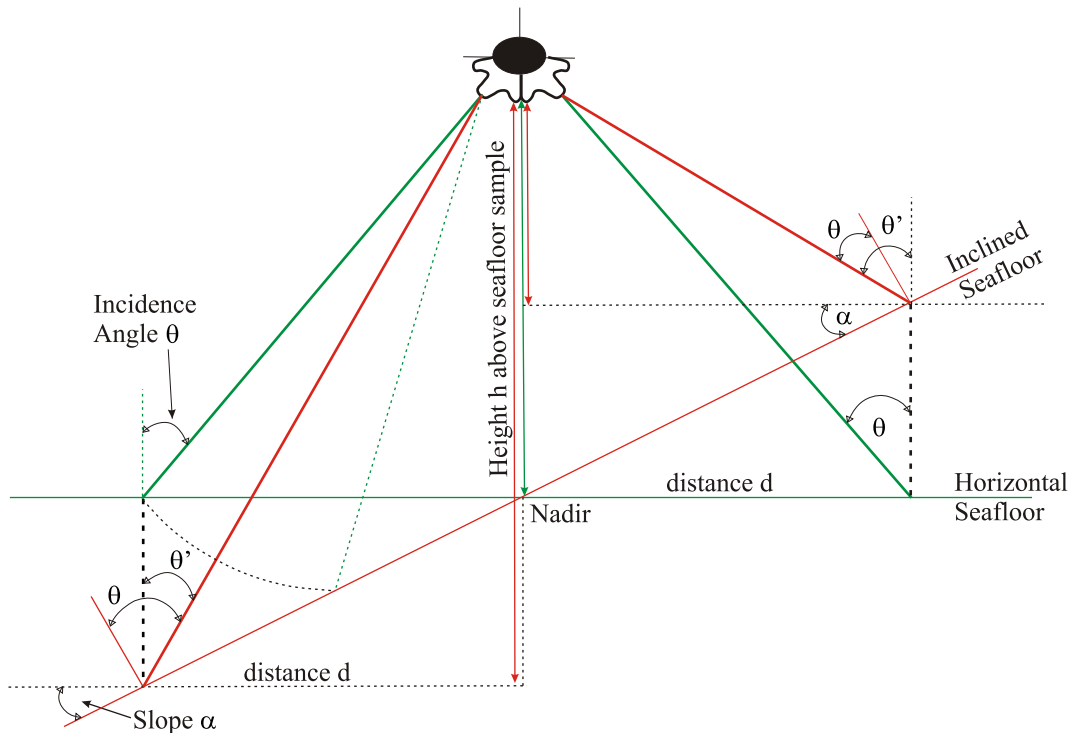


Figure 4.28: Influence of seafloor slope α and relative height between towfish and grid cell on incidence angle θ measured against local normal to seafloor. Decreasing relative height increases the incidence angle and vice versa. Inclination towards transducer decreases the incidence angle, inclination away from transducer increases it. Green: Situation for horizontal seafloor. Red: Situation for inclined seafloor.

4.6. RESULTS AND DISCUSSION

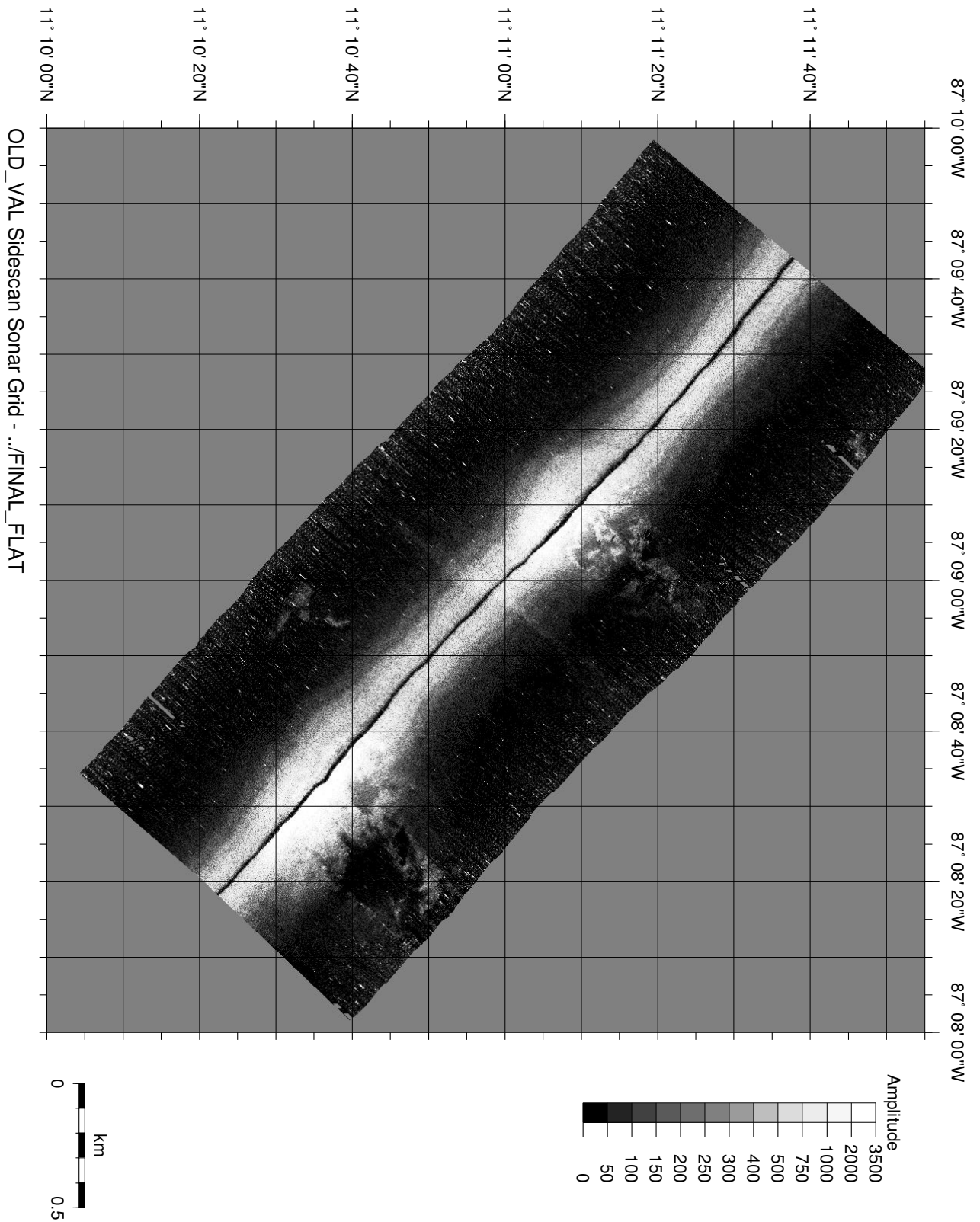


Figure 4.29: Map representation of raw sidescan sonar data without any shading or topographic correction applied. Amplitude values in nadir are much higher than in far range due to steeper incidence of sound wave and less transmission loss.

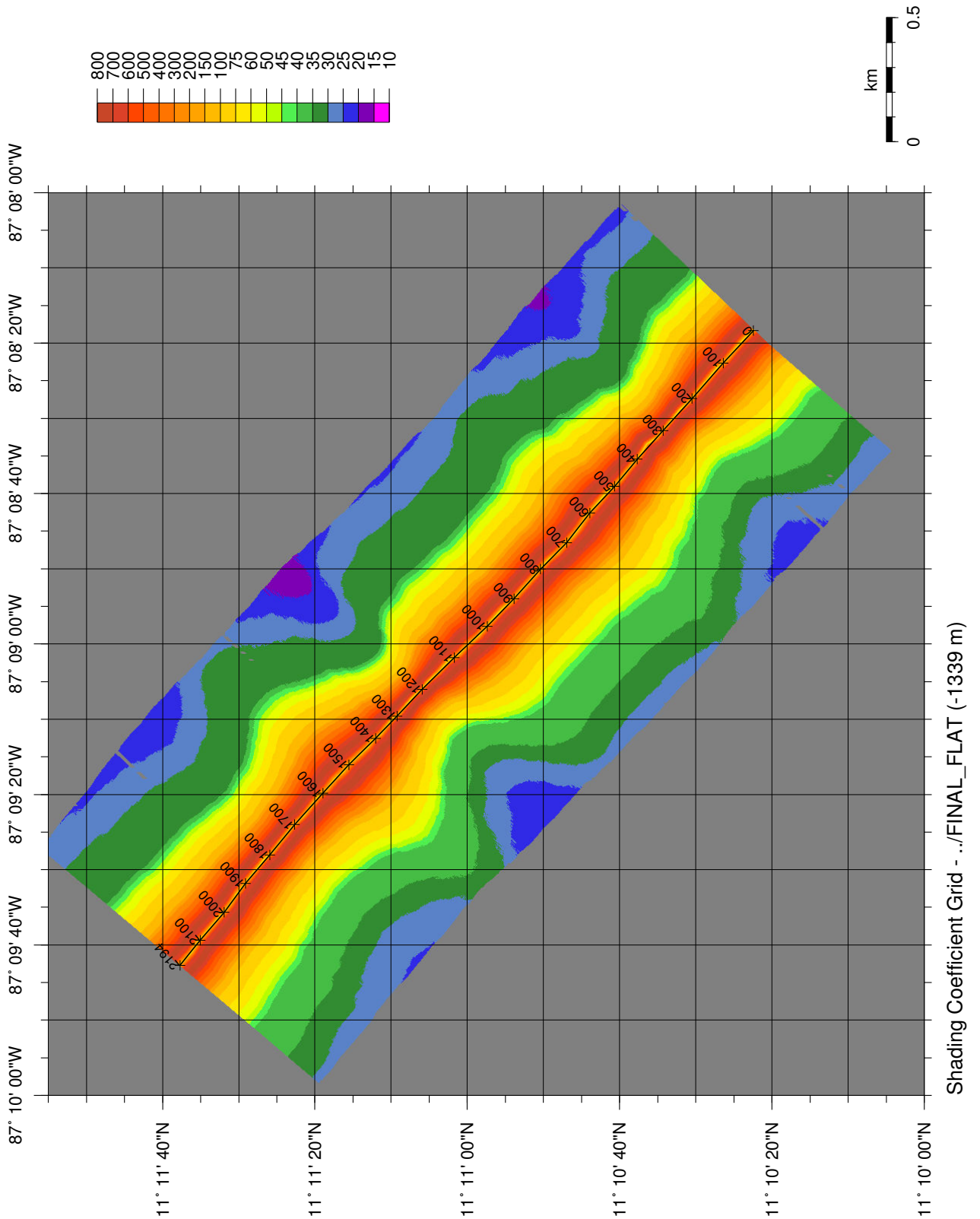


Figure 4.30: Shading coefficients for a horizontal, plain seafloor. The undulation of the values is due to the variable vehicle elevation above seafloor. With a constant elevation the shading coefficient intervals would be parallel to the vehicle track. The difference in width of the bands between port and starboard side (e.g. green bands) is due to slight asymmetries in the shading function (see figure 4.19).

4.6. RESULTS AND DISCUSSION

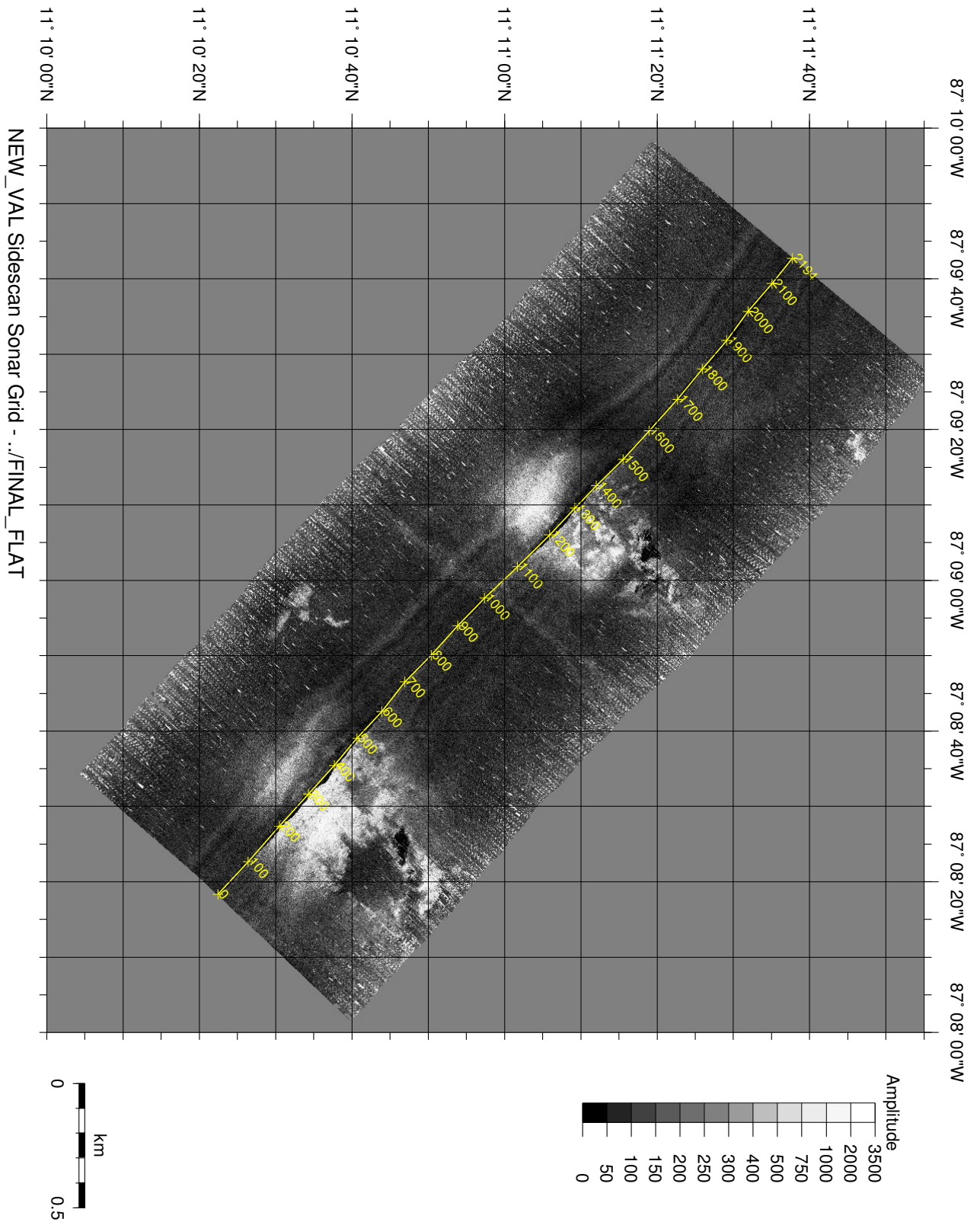


Figure 4.31: Shading coefficients from figure 4.30 applied to raw data. The backscatter values are not corrected for any topographic influence.

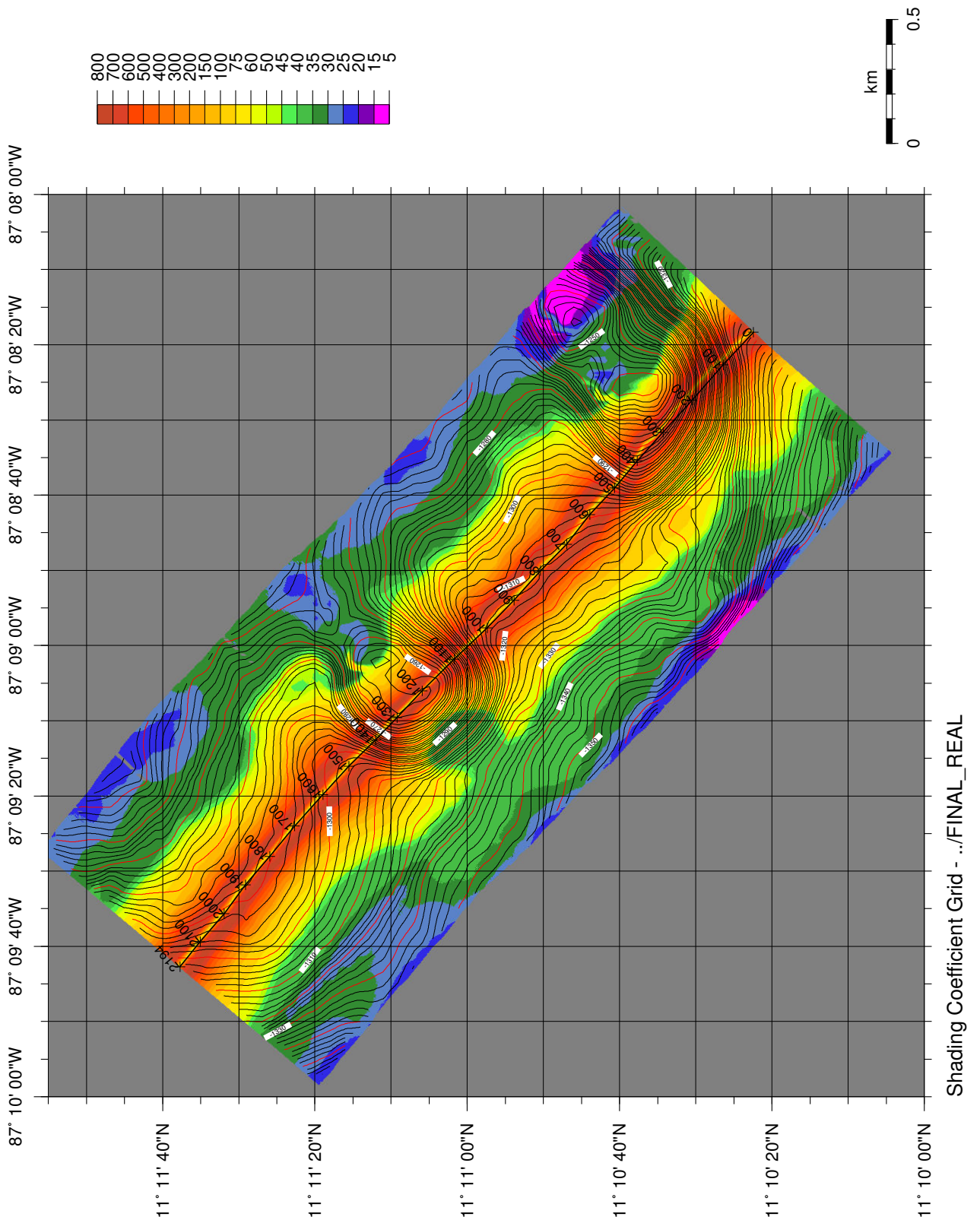


Figure 4.32: Calculated shading coefficients for the surveyed (real) *Simrad EM120* Bathymetry. Due to the morphology the pattern is not regular any more.

4.6. RESULTS AND DISCUSSION

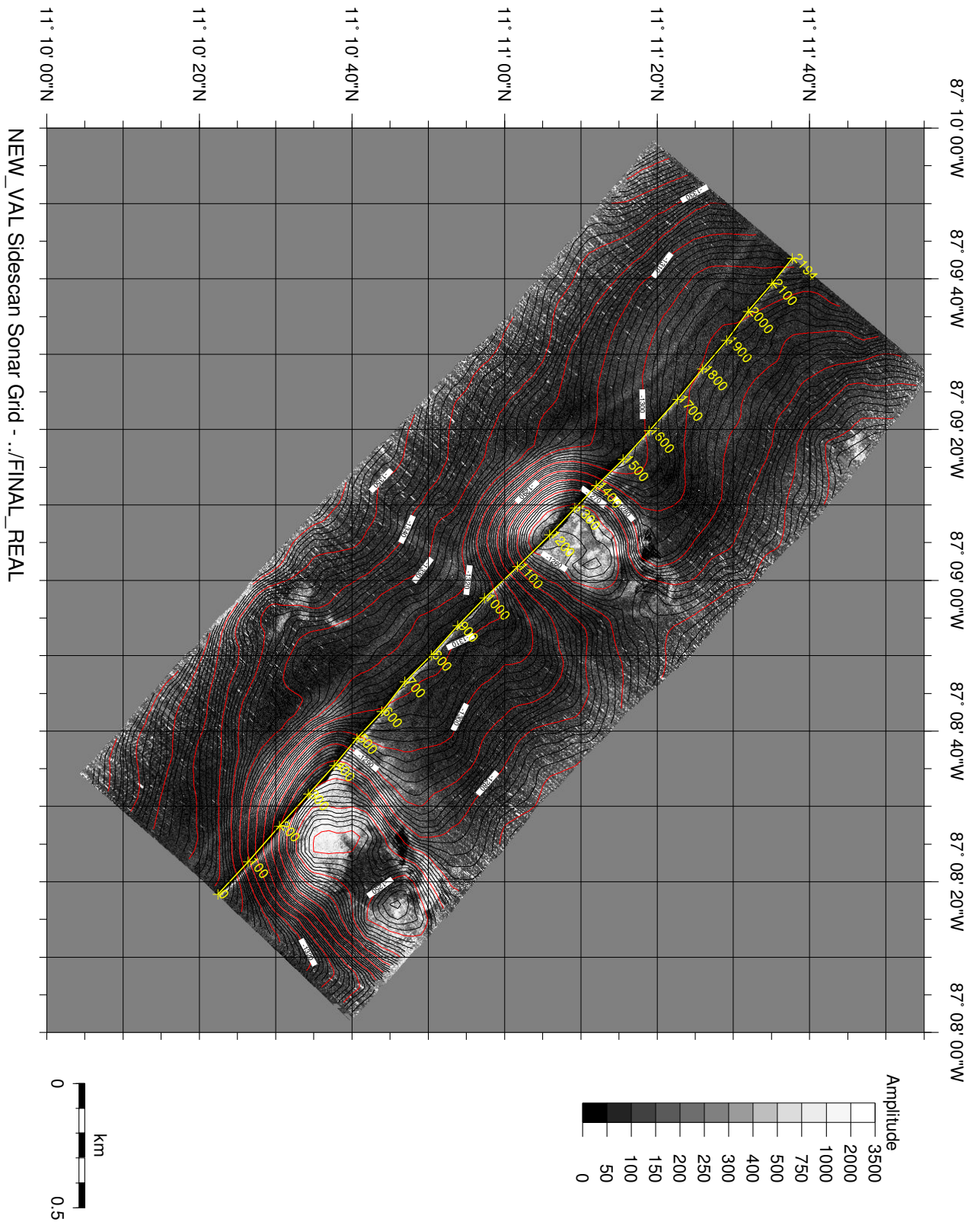


Figure 4.33: Shading coefficients from figure 4.32 applied to raw data. The backscatter values are corrected for seafloor topography. Same colour palette as in figure 4.31 is used. No significant (visual) differences to uncorrected image are observed.

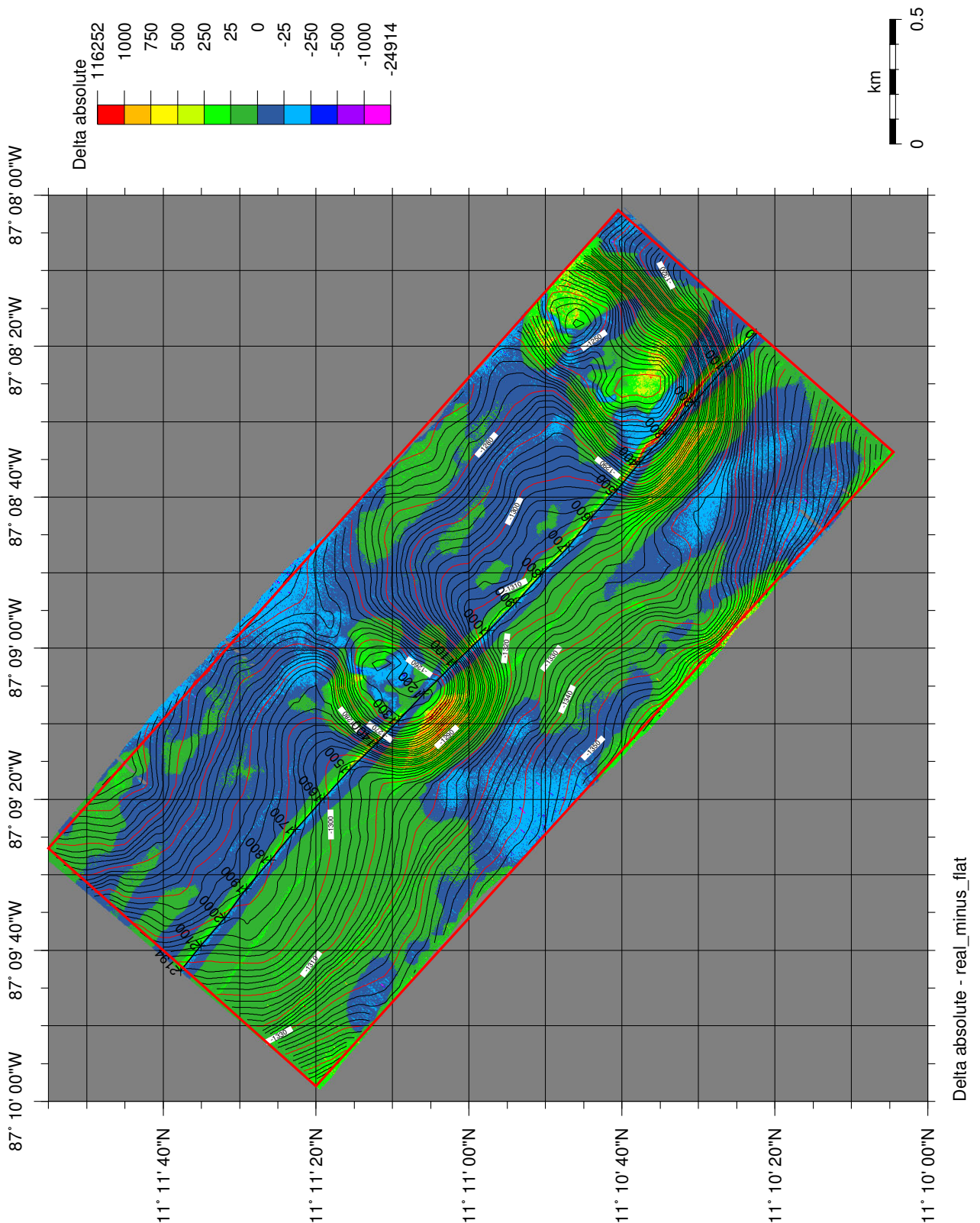


Figure 4.34: Amplitude values of process run with horizontal seafloor subtracted from amplitude values of process run with actual surveyed bathymetry. When considering morphology, major increase occurs on mound flanks and tops (light green, yellow to red colours). Decrease occurs upslope where seafloor slopes towards vehicle track (bright blue), but surprisingly also downslope of mounds. Large seafloor areas are changed only little (dark green, dark blue).

4.6. RESULTS AND DISCUSSION

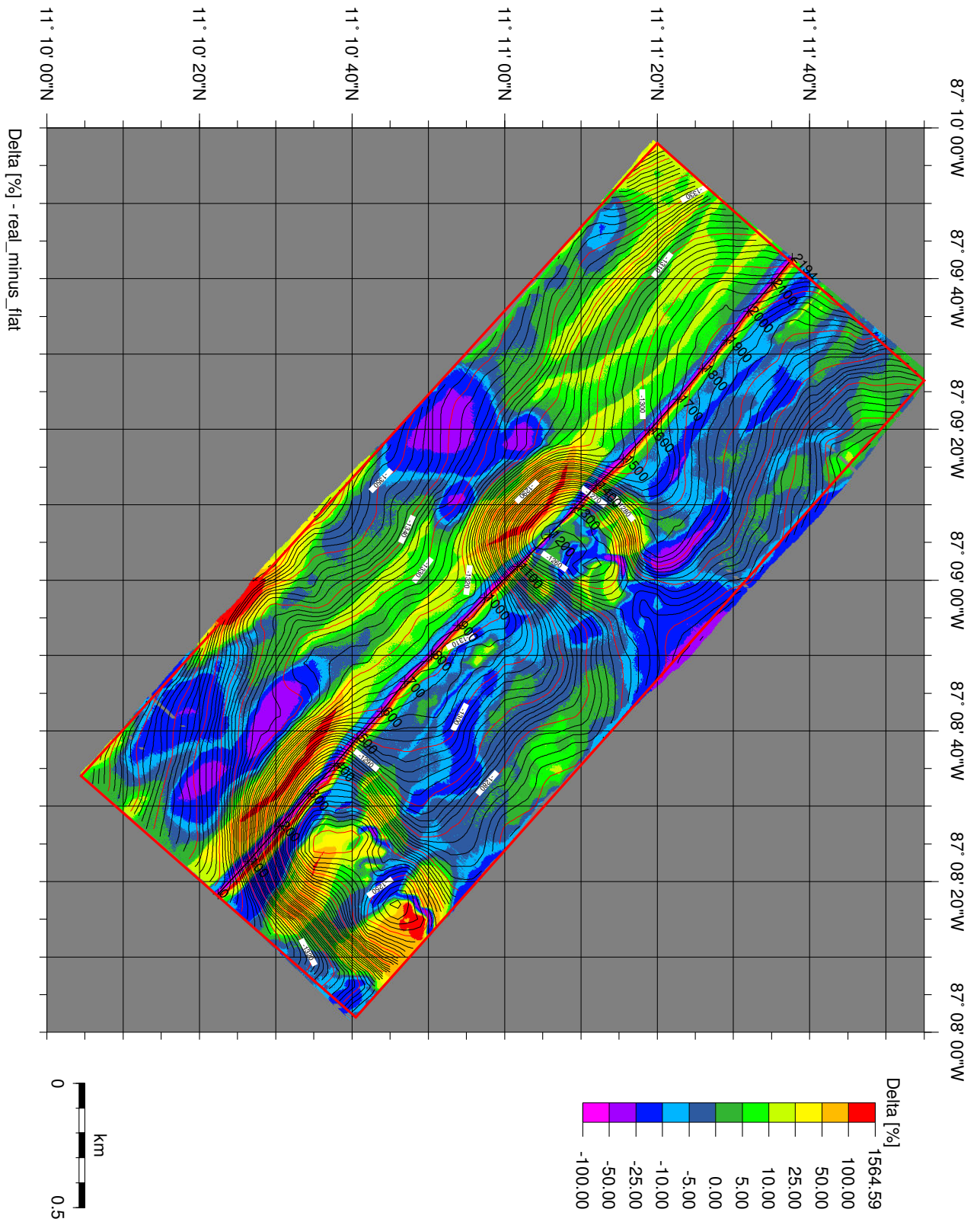


Figure 4.35: Change of amplitude values in percentage when applying the actual surveyed, real seafloor morphology instead of a horizontal seafloor. Figure supports observations from figure 4.34.

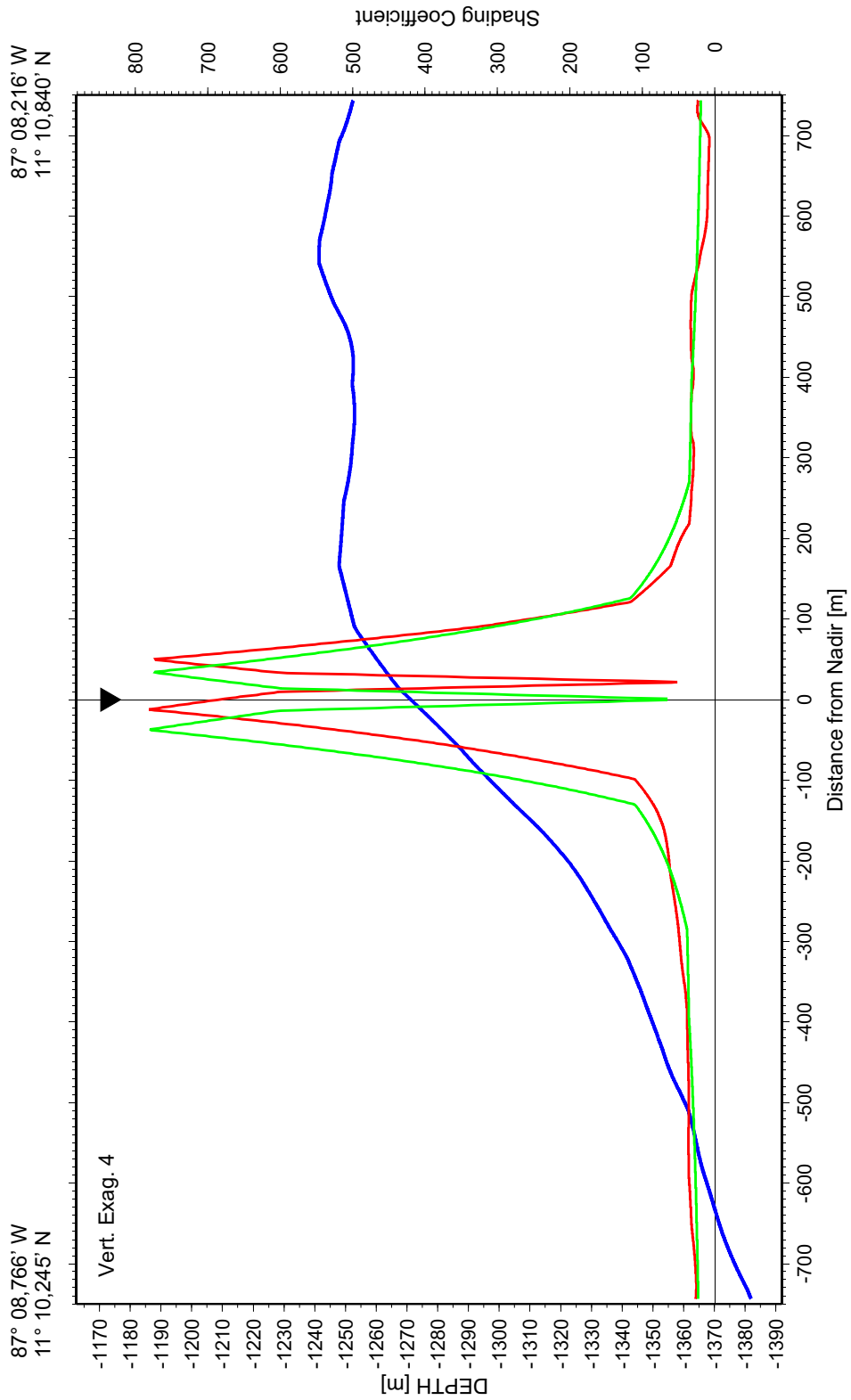


Figure 4.36: Cross-section over Mound Hormiga (ping 250) showing depth (blue) and applied shading coefficients from process runs with horizontal bathymetry (green) and real bathymetry (red). Black inverted triangle represents vehicle location.

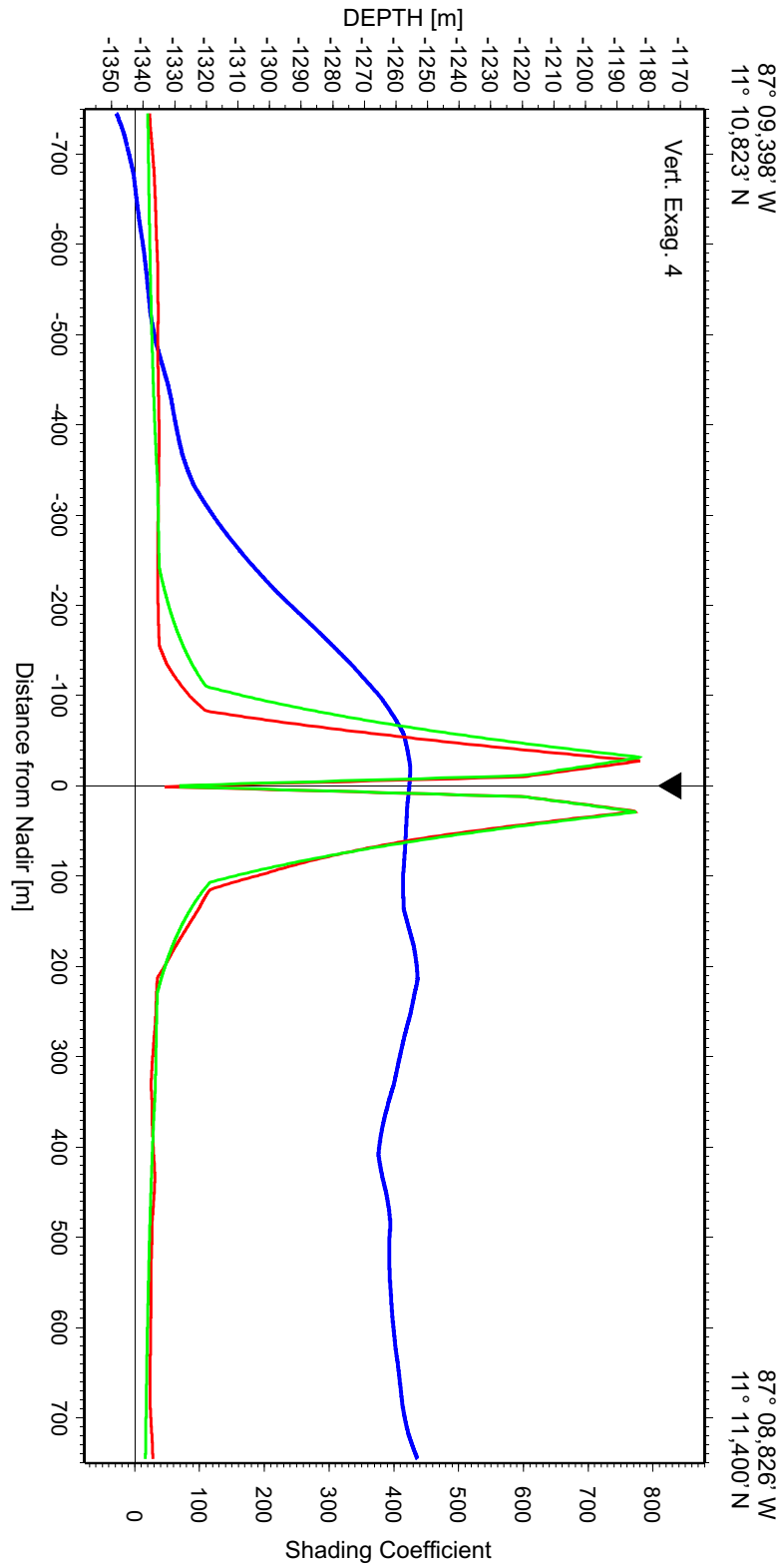


Figure 4.37: Cross-section over Mound Buho (ping 1220) showing depth (blue) and applied shading coefficients from process runs with horizontal bathymetry (green) and real bathymetry (red). Black inverted triangle represents vehicle location.

4.7 Conclusions and Outlook

From the presented analysis the following conclusions can be summarized:

- The general seafloor inclination on continental slopes does not have a significant influence on DTS-1 backscatter data.
- The influence on amplitude strength is significant where mound structures deform the seafloor, but in the processed sidescan sonar images only minor changes can be observed when compared to uncorrected images.
- The high backscatter of the mounds and intensity anomalies is not reduced when seafloor morphology is considered in the processing. Therefore mounds and intensity anomalies have a different lithology and roughness.
- Seafloor morphology has two important effects on the incidence angle of a sound wave: The slope of a seafloor grid cell, and the relative height between seafloor grid cell and sidescan vehicle. It is also important to consider the azimuth of the seafloor inclination.
- The angular variation in backscatter response of a sensor (its shading function), and its application in the processing has a major influence on the resulting images. To estimate the influence of morphology, it is important to consider the gradient of the function for a certain change in incidence angle (cf. figures 4.10, 4.13, 4.19).

As an outlook for future work in this field, I suggest:

- In the current processing the incoming time signal is directly related to points on a *horizontal* seafloor of increasing distances from the nadir. Here the *real* seafloor morphology should be considered, to allocate the backscatter signals to their real position on the seafloor (*migration* of backscatter samples). Also multiple reflections should be considered (see figure 4.38).
- The DTS-1 shading function used in this analysis should be constrained more precisely for large incidence angles. At a vehicle elevation of 100 m, beam angles between 70° and 82° correspond to nadir distances of 275 m–710 m, and cover therefore a large part of the ground range! In this angle range the used shading function is not well constrained due to noise and strong amplification of the incoming signal.
- More shading functions for different (known) seafloor types should be recorded. They may allow then a rough classification of seafloor types in other regions (figure 4.13).
- A calibration of the DTS-1 sensor should be tested, so that quantitative amplitude measurements can be acquired, and theoretical models be applied in the processing and analysis.

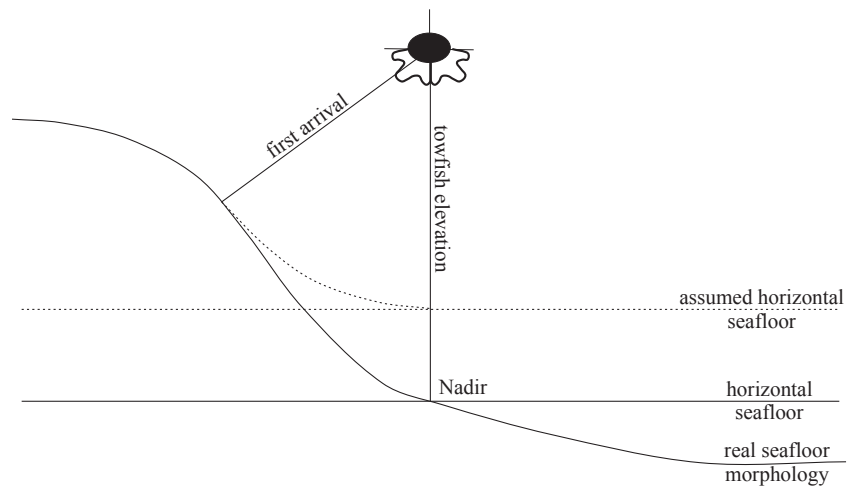


Figure 4.38: Migration of recorded sample amplitude value to its real location on seafloor. Picked first arrivals do not necessarily reflect the correct vehicle elevation above seafloor. For an accurate reduction of topographic influence on backscatter signals, such a migration would be desirable. Also multiple reflections have to be considered.

5

Canyon system on the continental slope offshore Nicaragua

Erosion of canyons in continental slopes is one of the main processes creating and modifying slope morphology [Mitchell, 2005a]. The subbottom profiler data show at many canyon side walls truncation of layers indicating such erosion. The processes eroding the sediments can be debris flows, slumps, or turbidity currents. But also enhanced currents in the canyons can lead to non-deposition of sediments. In this case the vertical relief of a canyon represents only partly the erosion of indurated sediments or bedrock [Mitchell, 2005a].

In the southeastern part of the survey area five major canyons can be distinguished, numbered from 1 to 5 (see figure 5.1). Whether these canyons originate at the shelf break or somewhere below at the continental slope is not clear, the source depths given in table 5.1 are the uppermost depths, up to which they can be traced in the data. The canyons terminate downslope in water depths between 2400 and 2600 metres, where the slope is less stable and characterized by abundant slumping structures. Only canyon 5 ends at 1650 metres, in a zone between 1800 and 1600 metres water depth, where the canyons are in general less deep incised.

	Canyon 1	Canyon 2	Canyon 3	Canyon 4	Canyon 5
source depth [m]	600	525	560	660	650
end depth [m]	2400	2600	2615	2400	1650
length [km]	24.5	25	25	27	17
largest relief [m]	115	100	110	130	140
largest width [m]	1500	2500	2000	2400	2400
thalweg gradient [°]	4.86	5.28	4.74	3.49	2.86
[cm/m]	8.5	9.25	8.3	6.1	5.0

Table 5.1: Major canyons in working area.

The long-profiles of the canyons show a linear to slightly convex-upward gradient. The non-linearity is mainly observed at the canyons number 1 and 4, where the thalweg is deflected. In the case of canyon 1, the convexity is probably due to the topographic bulge upslope of Masaya Slide. Once erosion has proceeded to a state of equilibrium, the long-profile of a canyon will become upward-concave [Mitchell, 2005b]. It can be concluded therefore that the canyon system observed is not yet in equilibrium condition but the slope is still undergoing tectonic movements. The gradients of the main canyons are around 8–9 cm/m (4–5°), decreasing slightly to the southeast to about 5–6 cm/m (~3°).

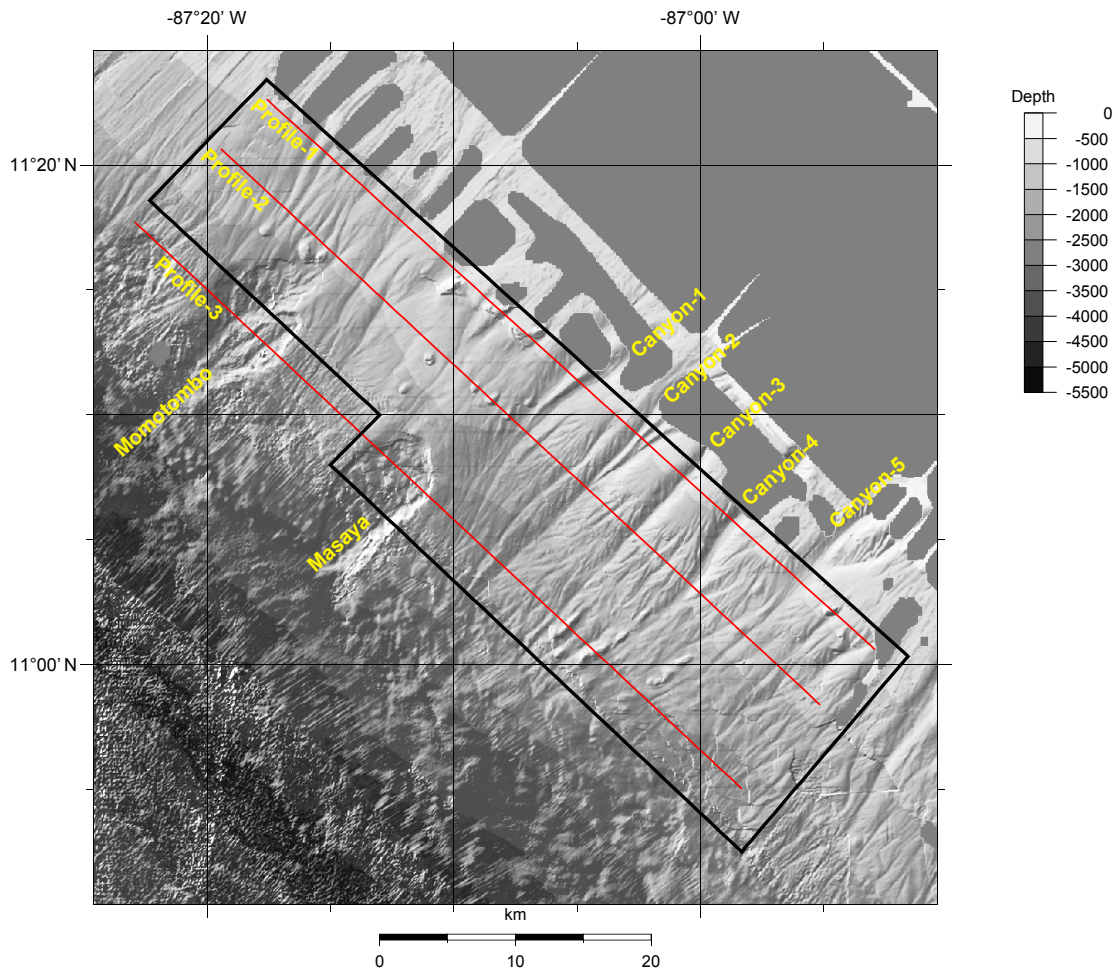


Figure 5.1: Shaded bathymetry map of survey area with location of depth profiles along slope and canyon numbering.

The canyon system is characterized by the five large canyons and tributary canyons originating at the broad ridges between them. The confluence of the tributary canyons or side channels with their principal canyons does not occur at the same elevation level, i. e. the erosion level of the side arms is above the erosion level of the main canyons. They form therefore slightly elevated hanging valleys above the main canyon floors. This implies that the canyon system is probably characterized by less-frequent large erosive events along the main canyons and a higher number of small events along the channels on the broad ridges [Mitchell, 2005a].

The slope-parallel topographic sections through the survey area (figure 5.2) show very clearly, how the broad inter-canyon divides first have smooth surfaces along the upslope border (figure 5.2, top), are then dissected by the tributary canyons (figure 5.2, middle), until they are almost completely removed, leaving back only the more resistant mound ridges (figure 5.2, bottom, e. g. between canyon 3 and 4).

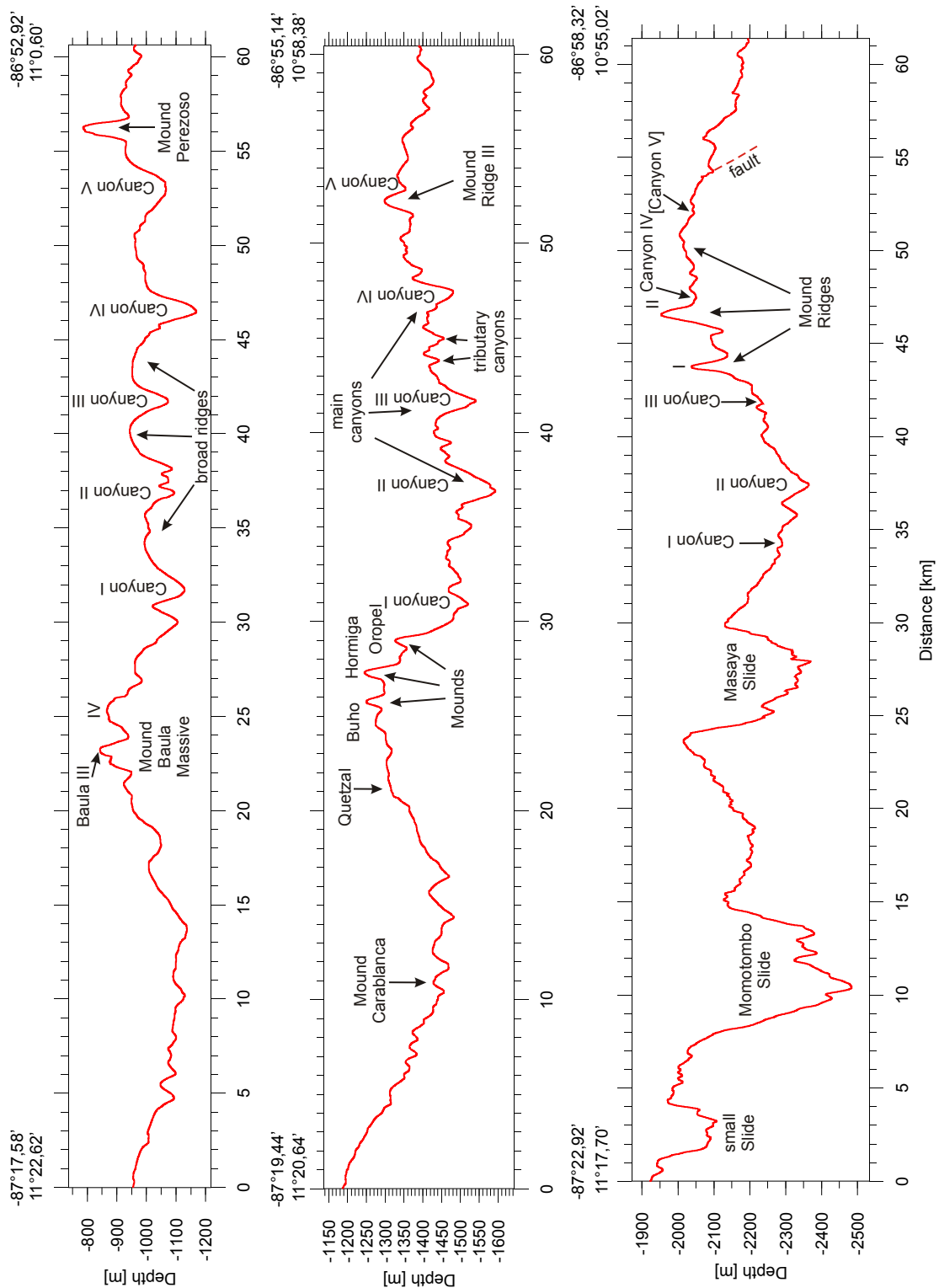


Figure 5.2: Topographic sections parallel slope across survey area offshore Nicaragua. Top: Profile along upslope border. Middle: Profile in mid region. Bottom: Profile along downslope border. See figure 5.1 for location. Note the dissection of the inter-canyon divides by tributary canyons and the erosion of the divides, leaving back the more resistant mound ridges (e. g. between canyon III and IV).

6

Momotombo Slide and Masaya Slide

Slides are common features on inclined areas of the seafloor, especially where weak geologic material is subjected to strong environmental stresses like earthquakes, large storm waves, high internal pore pressures or tectonic oversteepening [Hampton et al., 1996]. They can be recognized in acoustic reflection profiles, multibeam bathymetry maps, or sidescan sonar images, and generally show two essential features: A failure or slide surface, and a displaced mass of sediment or rock [Hampton et al., 1996]. Because a gravity-driven slide may transform (partly or wholly) into a plastic flow (e. g. debris flow) or a turbidity current, sometimes the displaced (and disintegrated) mass is difficult to recognize on the basis of morphology [Mulder and Cochonat, 1996].

The continental slope offshore Nicaragua is characterized by a gently dipping upper slope and a steep middle slope [Ranero et al., 2000a]. This break is marked by numerous low fault scarps and a zone of general slumping (figure 6.1). Beneath the slope a small, tectonically active frontal prism is attached to the margin wedge. Further to the northwest the sliding and slumping zone ends and is replaced by a canyon system which crosses the entire slope. The slide at the transition shows a narrowing and channelization of the track where the sediment mass moved along. The gliding slab probably disintegrated on its way downslope and transformed into a debris-flow and turbidity current, flowing over the frontal prism into the trench, leaving behind the erosive scar on the prism (figure 6.1).

Table 6.1 shows some morphometric numbers of Momotombo- and Masaya Slides. The overall length is measured from the headwall to the distance where the slope cover is still affected by the slide. It is for both slides not possible to identify a clear slide mass. The largest slide thickness is taken from cross-sections parallel to the slope and is the distance between the undisturbed seafloor and the slide bottom. The area and volume of the slides are calculated with a GIS. The slides are covered with a trend-surface, representing the pre-slide seafloor, and the volume is the space between the trend-surface and the slide floor. The area given is then the area of the trend-surface.

The headwall scarps of Momotombo Slide and Masaya Slide are at 1650 m and 1800 m water depth, respectively. They are slightly above the general slumping zone, and it can be assumed that both slides originated at the steeper middle slope but retrograded upslope to their present location (figure 6.1). Cross-sections perpendicular to the trench through the slides show an increase in the gradient from about 3.8° (6.7 cm/m) on the upper slope to about 7.0° (12.3 cm/m) on the middle slope for Momotombo Slide and an increase from 4.0° (7.0 cm/m) to 9.5° (16.9 cm/m) for Masaya Slide.

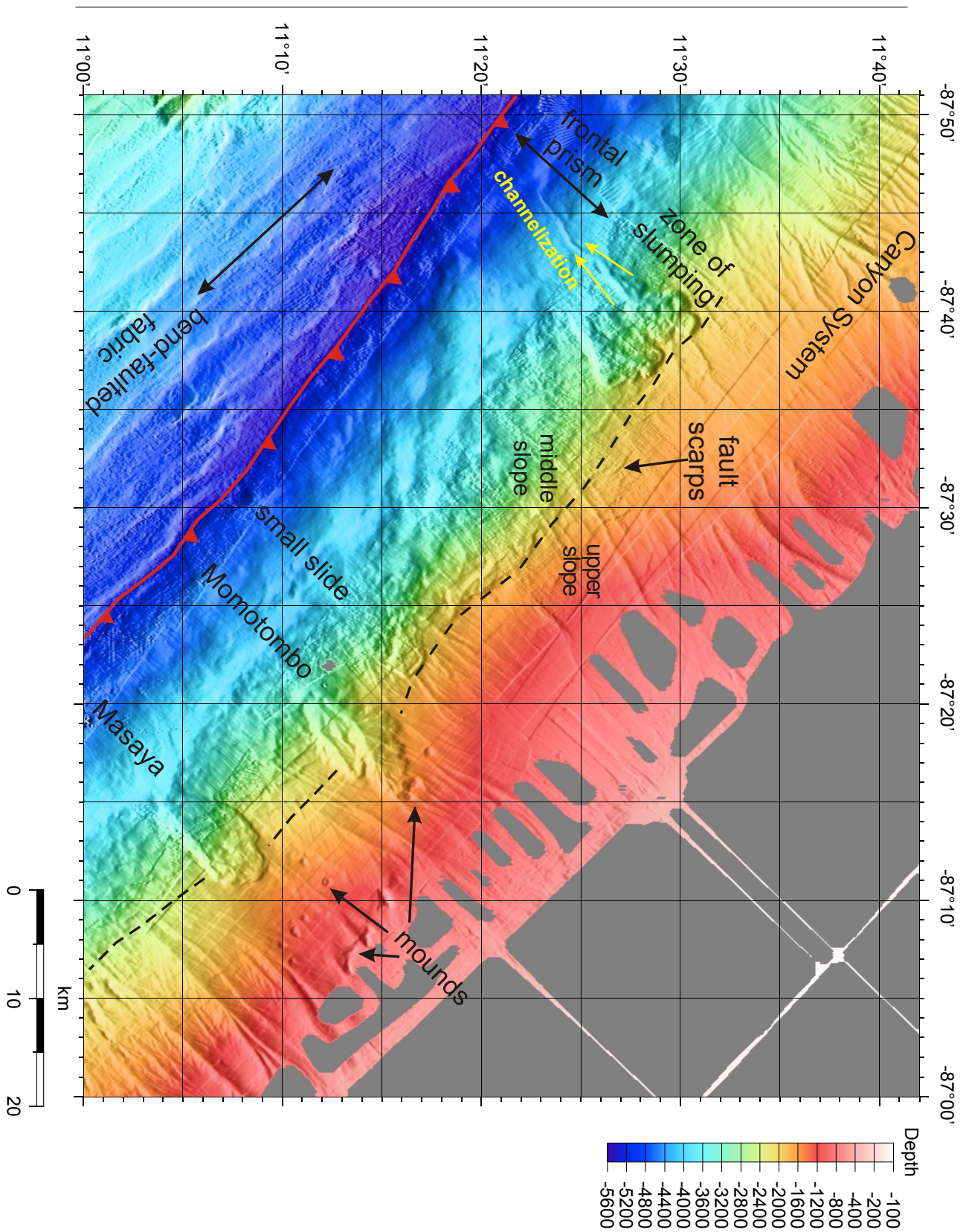


Figure 6.1: Slides and slumps on the continental slope offshore Nicaragua. The two slides described here are Momotombo Slide and Masaya Slide, respectively. Note the general zone of increased slumping from approximately 1800–2400 m water depth down to the frontal prism.

	Momotombo Slide	Masaya Slide
overall length [km]	18.5 (7.3)	12.3
largest width [km]	7.6 (2.7)	6.5
largest thickness [m]	460 (260)	370
area [km ²]	85	65
volume [km ³]	10.5	7.7
water depth headwall [m]	1650 (1880)	1800
height headwall [m]	80–110	150–180
Skempton ratio [thickness/length]	0.025 (0.037)	0.031

Table 6.1: Morphometric numbers of Momotombo Slide and Masaya Slide. Numbers in brackets are measures from smaller (successive, adjacent) part of Momotombo Slide (stage II in figure 6.2). The numbers are based on the morphology of the slides, because geologic information on slide planes and displaced masses are missing. The *Skempton ratio* is more a qualitative number, which shows that the slides have a ‘translational’ gliding mechanism (< 0.15).

Momotombo Slide Although the slide floor of Momotombo Slide is not really planar but slightly scoop-shaped, the slide was generated by a translational gliding mechanism. This suggests the very small Skempton ratio of the thickness to the length of the slide (table 6.1). The slide floor shows a developed erosion and sediment transport pattern, and some canyons from upslope are eroding the headwall scarp (figure 6.2). Therefore the event has probably a higher age compared to the Masaya Slide. The location of the slide headwall is at 1650 m water depth, which is approximately 200 m above and in 6 km lateral distance from the upper to middle slope break. One possibility is that the slide originated at the steeper middle slope and retrograded upslope, perhaps triggering an adjacent, smaller slide (stage II in figure 6.2). On the other hand it can be speculated that the mounds which are located directly at the slide headwall (Mounds Congo and Carablanca) are responsible for the triggering of the event. The resistive shear strength of the sediment could have been lowered by seepage along a fault, gas hydrate dissociation or a slight oversteepening of the slope by shallow sediment mobilization [Hampton et al., 1996]. This question can only be answered with detailed knowledge of the timing of the slide and the history of the fluid venting activity. A clear slide mass can not be observed in the Momotombo Slide area. It must be assumed that it is either eroded or the sediment mass disintegrated during the failure and transformed into a plastic flow or turbidity current and was transported into the trench. The foot of the slide is narrowing slightly which could be interpreted as a hint for a channelized flow, supporting the second hypothesis. Momotombo Slide is larger in area and volume than Masaya Slide. With a total slide scar volume of around 10 km³ it could have had the potential to generate a tsunami [von Huene et al., 2004b].

Masaya Slide Masaya Slide shows also a translational gliding mechanism. The slab-like slide mass moved downhill, disintegrated only to a smaller degree into larger blocks and is still present. Some amount of the slide mass was transported a larger distance, probably by forming plastic flows, and sedimented on the frontal prism, which is indicated by the small bulge (figure 6.2). Larger or high-density turbidity currents were probably not generated, as erosional features are missing. The movement of the slide mass was oblique in direction to the southeast and south which could be caused by the larger bulge on the upper slope. This bulge suggests that the slide was triggered by oversteepening and failure in the wake of a subducting seamount [von Huene et al., 2004b]. The missing of a clear fault pattern as described for seamount scars offshore Costa Rica [Dominguez et al., 1998; Hühnerbach et al., 2005], could be explained by several reasons: A smaller size of the subducted seamount, the greater dip of the subducting plate which attenuates morphological effects of lower-plate asperities faster, or a thicker upper plate offshore Nicaragua [von Huene et al., 2004b]. Masaya Slide shows only very little retrogression. This can be inferred from the main headwall scarp which is not just circular but shows three segments (figure 6.2).

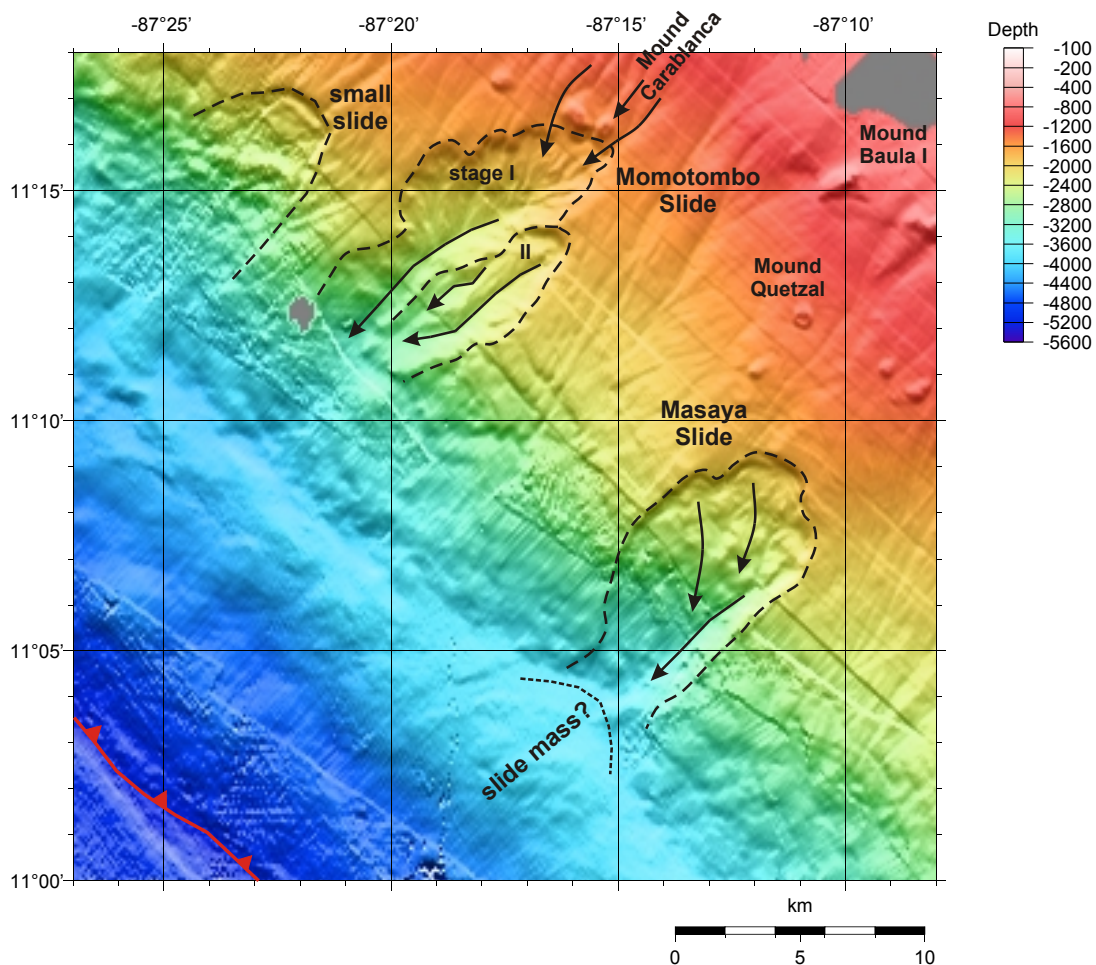


Figure 6.2: Momotombo- and Masaya-Slide in northern part of survey area. See text for discussion.

Conclusions and Outlook

Geoacoustic methods are applied in this study to reveal the nature and formation mechanisms of cold seep sites offshore Nicaragua. A high number of mound structures and backscatter anomalies is identified. They occur in different settings on the slope: Upslope slide areas, along headwalls of slides, as isolated massives, or forming ridges between deeply incised canyons. Based on their size and morphology, their backscatter facies in high-resolution sidescan sonar images, their structure in subbottom profiles, and their fluid venting activity inferred from seafloor observations, three major types are distinguished. They are end-members, and transitions between them are possible. Mound volumes with respect to mound base areas are indicative for the mound type.

The mounds do not show any indications of eruptive processes, like mud flows. They are no mud volcanoes. However there are indications of diapiric processes and sediment mobilization in the subsurface. The source depth of the mobilized sediment is unknown. But the primary process is fluid venting and associated authigenic carbonate formation. The carbonates can occur as crusts or chemoherms, and show bright backscatter in the sidescan sonar images. Erosion is a major factor for the shaping of the mound structures, especially where canyons incise into the slope. The proposed mound model assumes variations in the fluid venting activity and hence carbonate precipitation.

The influence of topography on the sidescan sonar signal is low for a wide range of the swath, and many geometric situations between transducer and seafloor. The characteristic IFM-GEOMAR DTS-1 backscatter vs. incidence angle relationship is determined, and applied to a test area. It can be concluded, that the influence is only relevant in the nadir area or the very near range, or if the seafloor gradient is that high, that the seafloor is illuminated at steep incidences. Much of the observed high backscatter is therefore due to an increased seafloor roughness.

Future research should be directed to reveal the deep structure beneath the venting sites in high resolution, and to reveal the history and timing of their formation. A promising approach is the correlation between tephra stratigraphy and high-resolution subbottom profiles.

The processing algorithm of the sidescan sonar data can be improved, when the true location of the sample values on the seafloor is considered. The characteristic 'shading function' should be constrained more precisely, and investigated for different seafloor types.

A

Sediment penetration depths of sonar systems

Signals from sidescan sonar or multibeam sonar systems can penetrate seabed sediments, and may image features which are buried beneath the surface [Mitchell, 1993]. Based on published sediment attenuation measurements from Stoll [1985], Mitchell [1999] predicts potential maximum penetration depths for different frequencies, based on a simple acoustical model [Mitchell, 1993].

$$h = \Delta BS \cdot \sin \theta / 2\alpha \quad (\text{A.1})$$

- ΔBS = acoustic contrast [dB]
- θ = incidence angle of acoustic beam on seafloor surface
- α = minimum attenuation coefficient [dB/m] at a given sonar frequency

For the IFM-GEOMAR DTS-1 Sidescan Sonar System with 75 kHz centre frequency, the minimum attenuation coefficient is approximately 5 dB/m (figure A.1). Assuming a typical acoustical contrast of 20–30 dB between fine abyssal mud overlying a rocky surface [Mitchell, 1993], 2–3 m of sediment cover would be necessary, to blank the signal from the bare rock at vertical incidence. At incidence angles of 45° the sediment cover would have to be 1.4–2.1 m, and at grazing angles of 15° 51–77 cm, respectively. It has to be mentioned that these values are maxima and most likely the system will image only shallower depths. These estimates do not account for uncertainties in the attenuation coefficient and for differences in surface roughness [Mitchell, 1999].

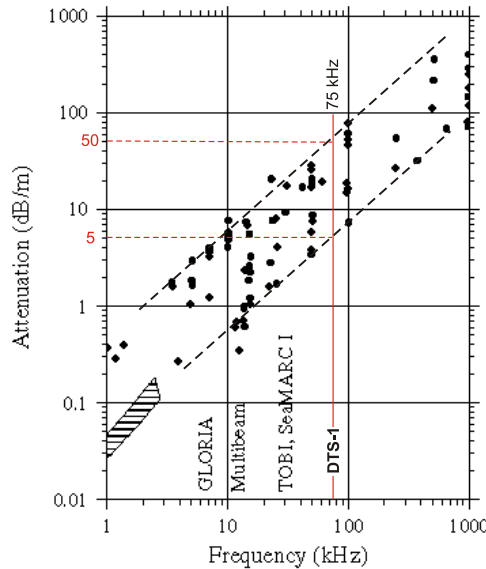


Figure A.1: Attenuation coefficients of marine sediments for different sonar systems (modified from Mitchell [1999]).

B

List of mound structures / intensity anomalies offshore Nicaragua

The following table lists in spatial order observed mound structures and backscatter anomalies offshore Nicaragua (cf. figure 3.1).

Abbreviations: *M*: Mound; *A*: Backscatter Anomaly;
H: Height[metres]; *L*: Length[metres]; *W*: Width[metres];
?: speculative, no direct observation;
+++: very strong occurrence; ++: strong occurrence; +: occurrence;
-: less occurrence; --: no occurrence;
OFOS: Ocean Floor Observation System (video sled).

Table B.1: Spatially grouped list of observed mound structures and backscatter anomalies offshore Nicaragua (cf. figure 3.1).

Name	Type	Lat	Lon	Depth	Description	H	L	W	Carb.	Fauna
<i>Slide Area</i>										
Tucan	M	11°17,46' N	87°17,48' W	-1430	circular, dome-shaped mound with irregular backscatter and central depression, in ~1400 m distance to headwall of Momotombo Slide	80	1290	1140	?	?
Congo	M	11°16,80' N	87°15,99' W	-1400	slightly elongated, dome-shaped mound along headwall of Momotombo Slide, ev. separated by fault from Md. Carablanca	100	1090	810	?	?
Carablanca	M	11°16,42' N	87°15,27' W	-1430	mound with two small summits along headwall of Momotombo Slide and characteristic circular high/low backscatter alterations, due to carbonate layers; top area shows shadowing due to microtopography; erosion of mound by bordering gully in the NW	70	1060	915	++	+
A.S1	A	11°13,75' N	87°14,82' W	-1750	rounded high backscatter patch at the flank of a canyon	20	445	275	?	?
<i>Central Area</i>										
Quetzal	M	11°12,32' N	87°10,93' W	-1310	circular, dome-shaped mound with central depression probably caused by slumping of the SW flank, on the central bulge upslope Masaya Slide; carbonate blocks along rim and flanks, slight moat on SE side	60	920	865	++	+

Table B.1, Central Area.

Name	Type	Lat	Lon	Depth	Description	H	L	W	Carb.	Fauna
Buho	M	11°11,18' N	87°09,07' W	-1260	circular to elongated, dome-shaped mound with flat top and flat upslope side on central bulge above Masaya Slide; irregular and patchy backscatter on top; thinning out of strata against NW flank of mound; no signs of strong activity along OFOS track	40	890	690	+	—
Hormiga	M	11°10,67' N	87°08,40' W	-1260	elongated, dome-shaped mound with two summits on the southern flank of the central bulge upslope Masaya Slide; irregular and patchy backscatter with shadows; widespread carbonates on top of summits, very few vent fauna; SE flank bordered by chaotic channel deposits	60	1095	850	++	—
Bocaraca	M	11°10,54' N	87°06,91' W	-1260	concentric mound on the flank of a canyon on the south border of the central bulge	50	735	590	?	?
Oropel	M	11°09,97' N	87°07,74' W	-1340	in a slope parallel line with Mds. Quetzal, Buho, Hormiga, where the central bulge descends into a canyon	50	685	435	?	?
Pargo	M	11°11,06' N	87°12,00' W	-1530	slightly elongated mound with small depression on top; ~2.5 km downslope of Md. Quetzal; shadows on top probably caused by carbonate blocks; similar to Md. Quetzal, but smaller	50	520	490	+	?

Table B.1, Central Area.

Name	Type	Lat	Lon	Depth	Description	H	L	W	Carb.	Fauna
Iguana	M/A	11°12,29' N	87°09,28' W	-1210	mound almost without topographic expression at shoulder of canyon; very bright backscatter with irregular border to surrounding normal seafloor amplitudes; landward part is covered by onlapping sediments; at southern border many carbonates and active vent fauna (incl. bacterial mats)	20	480	380	++	+++
A.C1	A	11°13,17' N	87°09,27' W	-1150	ev. exposed carbonates on a ridge between two small canyons	30	450	300	?	?
A.C2	A	11°11,78' N	87°09,30' W	-1245	small, but fresh looking anomaly	10	190	120	?	?
A.C3	A	11°10,53' N	87°08,97' W	-1340	fresh looking, irregular outline	30	380	350	?	?
A.C4	A	11°10,46' N	87°06,67' W	-1330	larger high-backscatter patch on flank and floor of a canyon, ev. related to Md. Bocaraca	60	380	275	?	?
A.C5	A	11°09,45' N	87°07,80' W	-1510	very small patch at head of small canyon	20	120	110	?	?
A.C6	A	11°09,33' N	87°07,32' W	-1515	three centers of bright backscatter over ridge between two small canyons	25	600	380	?	?
A.C7	A	11°08,55' N	87°07,51' W	-1650	one bright backscatter patch at flank of a larger canyon	30	540	220	?	?
A.C8	A	11°07,99' N	87°07,32' W	-1690	small bright spot at floor of small canyon	25	230	150	?	?
A.C9	A	11°07,44' N	87°07,89' W	-1825	very small bright spot at floor of small canyon	15	120	80	?	?
A.C10	A	11°05,60' N	87°07,76' W	-2130	speckled backscatter at floor of large canyon	25	260	250	?	?

Table B.1

Name	Type	Lat	Lon	Depth	Description	H	L	W	Carb.	Fauna
<i>Baula Massive</i>										
Baula I	M	11°15,22' N	87°09,94' W	-870	very large, elongated mound with two summits probably generated through slumping along E side; belongs to a group of mounds upslope an escarpment; top area largely covered by continuous, massive and fractured carbonates, up to several meters thick (carbonate pavement); no sediment coverage	180	2150	1630	+++	--
Baula II	M	11°14,38' N	87°08,42' W	-860	angular to rounded mound with flat top and high backscatter in top area, ev. some slumping to SW side	70	750	700	?	?
Baula III	M	11°14,27' N	87°07,90' W	-800	dome-shaped mound with irregular base and bright backscatter on SW flank; depression on top is in acoustic shadow	110	900	630	?	?
Baula IV	M	11°13,55' N	87°07,44' W	-850	small, flat mound at the escarpment with circular bands of high backscatter	70	710	500	?	?
Baula V	M	11°13,36' N	87°06,55' W	-800	SSW flank of mound exposed by escarpment	120	1260	840	?	?
A.B1	A	11°13,08' N	87°07,27' W	-960	small high-backscatter patch at base of the escarpment	25	250	150	?	?
A.B2	A	11°12,69' N	87°06,62' W	-1000	high-backscatter patch at flank of canyon	30	450	270	?	?

Table B.1

Name	Type	Lat	Lon	Depth	Description	H	L	W	Carb.	Fauna
<i>Perezoso Area</i>										
Perezoso	M	11°02,26' N	86°54,69' W	-780	large, cone-shaped mound with steep flanks and central depression on top in similar water depth as Baula Massive	130	940	780	?	?
Colibri	M	11°01,14' N	86°54,21' W	-920	small, slightly elongated and ridge-like mound with smooth surface and patchy, irregular backscatter; perhaps small slump to the S	30	620	580	?	?
<i>Mound Ridge I</i>										
R1.1	M	11°01,88' N	87°05,08' W	-2010	elongated, ridge-like mound with patchy backscatter on top and flanks	70	1480	540	?	?
R1.2	M	11°01,32' N	87°05,78' W	-2110	elongated, curved mound with patchy backscatter on top and on flank to canyon; perhaps small slump into northern canyon	70	1050	650	?	?
<i>Mound Ridge II</i>										
A.R2.1	A	11°03,13' N	87°00,32' W	-1450	circular high-backscatter patch on floor of large canyon bordering the ridge in the SE; patch is ~3.5 km upslope from where the ridge starts	80	780	540	?	?

Table B.1, Mound Ridge II.

Name	Type	Lat	Lon	Depth	Description	H	L	W	Carb.	Fauna
R2.2	M	11°02,13' N	87°02,12' W	-1670	elongated dome-shaped mound with high backscatter and small shadows in top area	60	860	410	?	?
A.R2.3	A	11°01,47' N	87°02,84' W	-1850	circular, very bright high-backscatter patch on upslope flank of mound	15	370	300	?	?
R2.4	M	11°01,20' N	87°03,06' W	-1840	elongated, dome-shaped mound with steep flanks, and high backscatter with larger shadow areas on top	90	1020	650	?	?
R2.5	M	11°00,67' N	87°03,96' W	-1930	large, more flat and sphere-shaped mound with several centres of high backscatter in top area	110	1460	1150	?	?
R2.6	M	11°00,36' N	87°04,67' W	-1990	cone-shaped mound with elongated base and perhaps some slumping on SW flank	110	1200	680	?	?
R2.7	M	11°00,58' N	87°05,56' W	-2170	rounded, hill-shaped mound between Mound Ridge I and II; not fully imaged in sidescan sonar data	80	880	710	?	?
A.R2.8	A	10°59,69' N	87°04,73' W	-2160	small unusual backscatter patch above a kind of slump headwall	30	510	280	?	?
A.R2.9	A	10°59,82' N	87°04,65' W	-2145	small unusual backscatter patch above a kind of slump headwall	10	160	140	?	?
A.R2.10	A	10°59,53' N	87°05,12' W	-2250	small unusual backscatter patch above a kind of slump headwall	40	350	300	?	?

Table B.1

Name	Type	Lat	Lon	Depth	Description	H	L	W	Carb.	Fauna
<i>Mound Ridge III</i>										
R3.1	M	11°02,18' N	86°57,44' W	-1190	small, hill-shaped mound with flat topography and patchy backscatter in top area	40	500	440	?	?
A.R3.2	A	11°01,47' N	86°57,72' W	-1280	patchy high backscatter at flank of canyon; not directly related to mound ridge	50	850	430	?	?
Morpho (R3.3)	M	11°00,18' N	87°00,68' W	-1660	elongated, dome-shaped mound with rough, small-scale morphology in top area, resulting in shadows and strong reflections; onlapping sediments in the NW, erosive contact in the SE; carbonate blocks with sediment ponds in between in top area and presence of vent fauna	70	1360	730	++	++
R3.4	M	10°59,76' N	87°01,22' W	-1750	large, rounded mound with high backscatter and shadows on top and on flanks	60	1020	920	?	?
R3.5	M	10°59,35' N	87°01,71' W	-1870	mound with circular and patchy high backscatter in top area; perhaps continuation of ridge from mound R3.4	40	530	470	?	?
A.R3.6	A	10°58,85' N	87°03,28' W	-2100	several centres of patchy and high backscatter at flank of a flat hill	70	950	700	?	?

Bibliography

- Auboin, J., von Huene, R., 1985. Summary: Leg 84, Middle America Trench transect off Guatemala and Costa Rica. In: von Huene, R., Auboin, J. (Eds.), Initial Reports DSDP. Vol. 84. Washington, pp. 939–957.
- Augustin, J. M., Le Suave, R., Lurton, X., Voisset, M., Dugelay, S., Satra, C., 1996. Contribution of the Multibeam Acoustic Imagery to the Exploration of the Sea-Bottom: Examples of SOPACMAPS 3 and ZoNeCo 1 Cruises. *Marine Geophysical Researches* 18, 459–486.
- Bahlburg, H., Breitzkreuz, C., 2004. *Grundlagen der Geologie*, 2nd Edition. Elsevier GmbH, Spektrum Akademischer Verlag.
- Barckhausen, U., Ranero, C. R., von Huene, R., Cande, S. C., Roeser, H. A., 2001. Revised tectonic boundaries in the Cocos Plate off Costa Rica: Implications for the segmentation of the convergent margin and for plate tectonic models. *Journal of Geophysical Research* 106 (B9), 19207–19220.
- Berhorst, A., 2006. Die Struktur des aktiven Kontinentalhangs vor Nicaragua und Costa Rica - marin-seismische Steil- und Weitwinkelmessungen. Dissertation, Christian-Albrechts-Universität.
- Blondel, P., 2002. Seabed Classification at Ocean Margins. In: Wefer, G., Billett, D., Hebbeln, D., Joergensen, B., Schlueter, M., van Weering, T. (Eds.), *Ocean Margin Systems*. Springer, pp. 125–141.
- Blondel, P., Murton, B. J., 1997. *Handbook of Seafloor Sonar Imagery*. Wiley-Praxis Series in Remote Sensing. John Wiley and Sons Ltd. in association with Praxis Publishing Ltd., Chichester.
- Boetius, A., Ravensschlag, K., Schubert, C. J., Rickert, D., Widdel, F., Gieskes, A., Amann, R., Joergensen, B. B., Witte, U., Pfannkuche, O., 2000. A marine microbial consortium apparently mediating anaerobic oxidation of methane. *Nature* 407, 623–626.
- Boetius, A., Suess, E., 2004. Hydrate Ridge: a natural laboratory for the study of microbial life fueled by methane from near-surface gas hydrates. *Chemical Geology* 205, 291–310.

BIBLIOGRAPHY

- Bohrmann, G., Heeschen, K., Jung, C., Weinrebe, W., Baranov, B., Cailleau, B., Heath, R., Hühnerbach, V., Hort, M., Masson, D., Trummer, I., 2002. Widespread fluid expulsion along the seafloor of the Costa Rica convergent margin. *Terra Nova* 14, 69–79.
- Bouma, A. H., Roberts, H. H., Coleman, J. M., 1990. Acoustical and Geological Characteristics of Near-Surface Sediments, Upper Continental Slope of Northern Gulf of Mexico. *Geo-Mar Lett* 10, 200–208.
- Bowles, F. A., Jack, R. N., Carmichael, I. S. E., 1973. Investigation of Deep-Sea Volcanic Ash Layers from Equatorial Pacific Cores. *Geological Society of America Bulletin* 84, 2371–2388.
- Breitzke, M., Bialas, J., 2003. A deep-towed multichannel seismic streamer for very high-resolution surveys in full ocean depth. *First Break* 21, 59–65.
- Breitzke, M., Bialas, J., Buerk, D., Fekete, N., Flueh, E. R., Klaeschen, D., Klaucke, I., Papenberg, C., Ranero, C., the SO173-1 Working Group, 2003. A high-resolution deep-towed seismic survey in the mound region along the continental slope off Nicaragua. In: AGU General Assembly.
- Brekhovskikh, L. M., Lysanov, Y. P., 2003. *Fundamentals of Ocean Acoustics*, 3rd Edition. AIP Series in Modern Acoustics and Signal Processing. AIP Press/Springer, New York.
- Brown, K. M., 1990. The Nature and Hydrogeologic Significance of Mud Diapirs and Diatremes for Accretionary Systems. *J. Geophys. Res.* 95 (B6), 8969–8982.
- Brown, K. M., Tryon, M. D., DeShon, H. R., Dorman, L. M., Schwartz, S. Y., 2005. Correlated transient fluid pulsing and seismic tremor in the Costa Rica subduction zone. *Earth and Planetary Science Letters*.
- Carr, M. J., Stoiber, R. E., 1990. Volcanism. In: Dengo, G., Case, J. (Eds.), *The Geology of North America. Vol. H, The Caribbean Region*. Geol. Soc. of Am., Boulder, Colorado, pp. 375–391.
- Carson, B., Seke, E., Paskevich, V., Holmes, M. L., 1994. Fluid expulsion sites on the Cascadia accretionary prism: Mapping diagenetic deposits with processed GLORIA imagery. *J. Geophys. Res.* 99 (B6), 11959–11969.
- DeMets, C., 2001. A new estimate for present-day Cocos-Caribbean plate motion: Implications for slip along the Central American volcanic arc. *Geophysical Research Letters* 28 (21), 4043–4046.
- Dominguez, S., Lallemand, S. E., Malavieille, J., von Huene, R., 1998. Upper plate deformation associated with seamount subduction. *Tectonophysics* 293, 207–224.
- Fekete, N., 2006. Dewatering through Mud Mounds on the continental Fore-arc of Costa Rica. Dissertation, Christian-Albrechts-Universität.

- Flueh, E., Söding, E., Suess, E. (Eds.), 2004. RV SONNE Cruise Report SO173/1, 3 & 4 - Subduction II: The Central American Continental Margin. Vol. 115 of GEOMAR Report. GEOMAR, Kiel.
- Flueh, E. R., Ranero, C., von Huene, R., 2000. The Costa Rican Pacific margin: from accretion to erosion. *Zbl. Geol. Paläont.*, 669–678.
- GEBCO, 2003. General Bathymetric Charts of the Ocean.
- Gerriets, A., von Lom-Keil, H., Spiess, V., Zwanzig, C., Bruns, R., 2003. A major upgrade of the sediment echosounder ATLAS PARASOUND and the digital acquisition software ParaDigMA for high-resolution sea floor studies. EGS - AGU - EUG Joint Assembly, Abstracts from the meeting held in Nice, France, 6 - 11 April 2003, 11720.
- Greinert, J., Bohrmann, G., Elvert, M., 2002a. Stromatolitic fabric of authigenic carbonate crusts: results of anaerobic methane oxidation at cold seeps in 4850 m water depth. *Int J Earth Sci* 91, 698–711.
- Greinert, J., Weinrebe, W., Gimpel, P., Brockhoff, J., 2002b. Detailed Bathymetric Mapping and Side Scan Surveys in the Investigation of Cold Fluid Vent Sites and associated Gas Hydrate Occurrences. *The Hydrographic Journal* 106, 15–19.
- Grevemeyer, I., Kopf, A., Fekete, N., Kaul, N., Villinger, H. W., Heesemann, M., Wallmann, K., Spieß, V., Gennerich, H.-H., Müller, M., Weinrebe, W., 2004. Fluid flow through active mud dome Mound Culebra offshore Nicoya Peninsula, Costa Rica: evidence from heat flow surveying. *Marine Geology* 207, 145–157.
- Hammerstad, E., 2000. EM Technical Note - Backscattering and Seabed Image Reflectivity. Tech. rep., Kongsberg Simrad.
- Hampton, M. A., Lee, H. J., Locat, J., 1996. Submarine Landslides. *Reviews of Geophysics* 34 (1), 33–59.
- Han, X., Suess, E., Sahling, H., Wallmann, K., 2004. Fluid venting activity on the Costa Rica Margin: New results from authigenic carbonates. *Int J Earth Sci* 93, 596–611.
- Henry, P., Lallemand, S., Nakamura, K.-I., Tsunogai, U., Mazzotti, S., Kobayashi, K., 2002. Surface expression of fluid venting at the toe of the Nankai wedge and implications for flow paths. *Marine Geology* 187, 119–143.
- Henry, P., Le Pichon, X., Lallemand, S., Foucher, J.-P., Westbrook, G., Hobart, M., 1990. Mud volcano field seaward of the Barbados accretionary complex: a deep-towed side scan sonar survey. *J. Geophys. Res.* 95, 8917–8929.
- Hensen, C., Wallmann, K., Schmidt, M., Ranero, C. R., Suess, E., 2004. Fluid expulsion related to mud volcanism at Costa Rica continental margin - a window to the subducting slab. *Geology* 32, 201–204.

BIBLIOGRAPHY

- Hühnerbach, V., Masson, D. G., Bohrmann, G., Bull, J. M., Weinrebe, W., 2005. Deformation and submarine landsliding caused by seamount subduction beneath the Costa Rica continental margin - new insights from high-resolution sidescan sonar data. In: Hodgson, D. M., Flint, S. S. (Eds.), *Submarine Slope Systems: Processes and Products*. Vol. 244. Geological Society London, Special Publications, London, pp. 195–205.
- Ivanov, M. K., Limonov, A. F., van Weering, T. C. E., 1996. Comparative characteristics of the Black Sea and Mediterranean Ridge mud volcanoes. *Marine Geology* 132, 253–271.
- IXSEA-OCEANO, 2002. POSIDONIA 6000 User Manual. OCEANO Technologies, 29200 Brest - France.
- Johnson, H. P., Helferty, M., 1990. The Geological Interpretation of Side-Scan Sonar. *Reviews of Geophysics* 28 (4), 357–380.
- Johnson, J. E., Goldfinger, C., Suess, E., 2003. Geophysical constraints on the surface distribution of authigenic carbonates across the Hydrate Ridge region, Cascadia margin. *Marine Geology* 202, 79–120.
- Jollivet, D., Faugeres, J.-C., Griboulard, R., Desbruyeres, D., Blanc, G., 1990. Composition and spatial organization of a cold seep community on the south barbados accretionary prism: Tectonic, geochemical and sedimentary context. *Progress in Oceanography* 24 (1-4), 25–45.
- Kahn, L. M., Silver, E. A., Orange, D., Kochevar, R., McAdoo, B., 1996. Surficial evidence of fluid expulsion from the Costa Rica accretionary prism. *Geophysical Research Letters* 23 (8), 887–890.
- Kimura, G., Silver, E. A., Blum, P., Blanc, G., Bolton, A., Clennell, M. B., Griffin, J. R., Housen, B., Ibaraki, M., Kanamatsu, T., Kastner, M., Lindsley-Griffin, N., Lueckge, A., McIntosh, K., Meschede, M., Morris, J., Muza, J., Myers, G., Protti, M., Saether, O., Saito, S., Scholl, D., Spence, G., Tobin, H., Vannucchi, P., White, L., 1997. *Proceedings of the Ocean Drilling Program, Init. Repts. Vol. 170*. Texas A&M University, College Station TX, Ocean Drilling Program.
- Klaucke, I., Masson, D. G., Petersen, C. J., Weinrebe, W., *subm.* Multi-frequency geoaoustic imaging of fluid escape structures offshore Costa Rica: implications for seep processes. *Geochemistry Geophysics Geosystems*.
- Klaucke, I., Sahling, H., Buerk, D., Weinrebe, W., Bohrmann, G., 2005. Mapping deep-water gas emissions with high-resolution sidescan sonar. *Eos, Trans. Am. Geophys. Un.*
- Kopf, A., Behrmann, J. H., 2000. Extrusion dynamics of mud volcanoes on the Mediterranean Ridge accretionary complex. In: Vendeville, B., Mart, Y., Vigneresse, J.-L. (Eds.), *From the Arctic to the Mediterranean: Salt, shale, and igneous diapirs in and*

- around Europe. Vol. 174. Journal of the Geological Society, Spec. Publ., London, pp. 169–204.
- Kopf, A., Klaeschen, D., Mascle, J., 2001. Extreme efficiency of mud volcanism in dewatering accretionary prisms. *Earth and Planetary Science Letters* 189, 295–313.
- Krastel, S., Spiess, V., Ivanov, M., Weinrebe, W., Bohrmann, G., Shashkin, P., Heidersdorf, F., 2003. Acoustic investigations of mud volcanoes in the Sorokin Trough, Black Sea. *Geo-Mar Lett* 23, 230–238.
- Kulm, L. D., Suess, E., Moore, J. C., Carson, B., Lewis, B. T., Ritger, S. D., Kadko, D. C., Thornburg, T. M., Embley, R. W., Rugh, W. D., Massoth, G. J., Langseth, M. G., Cochran, G. R., Scamman, R. L., 1986. Oregon Subduction Zone: Venting, Fauna, and Carbonates. *Science* 231, 561–566.
- Lance, S., Henry, P., Le Pichon, X., Lallemand, S., Chamley, H., Rostek, F., Faugeres, J.-C., Gonthier, E., Olu, K., 1998. Submersible study of mud volcanoes seaward of the Barbados accretionary wedge: sedimentology, structure and rheology. *Marine Geology* 145, 255–292.
- Langseth, M. G., Silver, E. A., 1996. The Nicoya convergent margin - a region of exceptionally low heat flow. *Geophysical Research Letters* 23 (8), 891–894.
- Le Bas, T., 2002. P.R.I.S.M. - Processing of Remotely-sensed Imagery for Seafloor Mapping. A collection of software for the processing, analysis and enhancement of side-scan sonar imagery using geometric and radiometric corrections for seafloor characterisation and mapping.
- Limonov, A. F., Ivanov, M. K., Foucher, J.-P., 1998. Deep-towed side-scan survey of the United Nations Rise, eastern Mediterranean. *Geo-Mar Lett* 18, 115–126.
- Luff, R., Greinert, J., Wallmann, K., Klauke, I., Suess, E., 2005. Simulation of long-term feedbacks from authigenic carbonate crust formation at cold vent sites. *Chemical Geology* 216, 157–174.
- Lurton, X., 2002. *An Introduction to Underwater Acoustics: Principles and Applications*. Springer-Praxis Books in Geophysical Sciences. Springer in association with Praxis Publishing, Chichester, UK.
- Maltman, A. J., Bolton, A., 2003. How sediments become mobilized. In: Van Rensbergen, P., Hillis, R., Maltman, A., Morley, C. (Eds.), *Subsurface Sediment Mobilization*. Vol. 216. Geological Society, London, Special Publications, pp. 9–20.
- Mau, S., Rehder, G., Arroyo, I. G., Gossler, J., Suess, E., submitted. Variations in CH₄ seepage from mud extrusions and landslides offshore Costa Rica affected by seismotectonics. *Geo-Mar Lett*.

BIBLIOGRAPHY

- McAdoo, B. G., Orange, D. L., Silver, E. A., McIntosh, K., Abbott, L., Galewsky, J., Kahn, L., Protti, M., 1996. Seafloor structural observations, Costa Rica accretionary prism. *Geophysical Research Letters* 23 (8), 883–886.
- McIntosh, K., Silver, E., Shipley, T. H., 1993. Evidence and mechanism for forearc extension at the accretionary Costa Rica convergent margin. *Tectonics* 12, 1380–1392.
- McIntosh, K. D., Silver, E. A., Ahmed, I., Berhorst, A., Ranero, C. R., Kelly, R. K., Flueh, E. R., submitted, 2005. The Nicaraguan Convergent Margin: Seismic Reflection Imaging of the source of a Tsunami Earthquake. US Margins Special Publication.
- Meschede, M., Frisch, W., 1998. A plate-tectonic model for the Mesozoic and Early Cenozoic history of the Caribbean plate. *Tectonophysics* 296, 269–291.
- Meschede, M., Zweigel, P., Kiefer, E., 1999. Subsidence and extension at a convergent plate margin: evidence for subduction erosion of Costa Rica. *Terra Nova* 11, 112–117.
- Milkov, A. V., 2000. Worldwide distribution of submarine mud volcanoes and associated gas hydrates. *Marine Geology* 167, 29–42.
- Mitchell, N. C., 1993. A model for attenuation of backscatter due to sediment accumulations and its application to determine sediment thickness with GLORIA sidescan sonar. *J. Geophys. Res.* 98 (B12), 22477–22493.
- Mitchell, N. C., 1999. Penetration depths of sonars and image interpretation. URL: <http://www.ocean.cf.ac.uk/people/neil/sonar/pen.html> .
- Mitchell, N. C., 2005a. Erosion of canyons in continental slopes. In: Hodgson, D. M., Flint, S. S. (Eds.), *Submarine Slope Systems: Processes and Products*. Vol. 244. Geological Society London, Special Publications, pp. 131–140.
- Mitchell, N. C., 2005b. Interpreting long-profiles of canyons in the USA Atlantic continental slope. *Marine Geology* 214, 75–99.
- Mitchell, N. C., Somers, M. L., 1989. Quantitative backscatter measurements with a long-range sidescan sonar. *IEEE J. Oceanic Engineering* 14, 368–374.
- Moerz, T., Fekete, N., Kopf, A., Brueckmann, W., Kreiter, S., Huenerbach, V., Masson, D., Hepp, D. A., Schmidt, M., Kutterolf, S., Sahling, H., Abegg, F., Spiess, V., Suess, E., Ranero, C. R., 2005. Styles and productivity of mud diapirism along the Middle American margin, part ii: Mound Culebra and Mounds 11, and 12. In: Martinelli, G., Panahi, B. (Eds.), *Mud volcanoes, geodynamics and seismicity*. NATO Sci. Ser. IV: Dordrecht (Springer), pp. 49–76.
- Mörz, T., Kopf, A., Brückmann, W., 2003. Structural Sedimentology of Mounds. In: Söding, E., Wallmann, K., Suess, E., Flueh, E. (Eds.), *RV METEOR, Cruise Report M54/2+3, Fluids and subduction Costa Rica 2002*. Vol. 111. GEOMAR, Kiel.

- Mulder, T., Cochonat, P., 1996. Classification of Offshore Mass Movements. *Journal of Sedimentary Research* 66 (1), 43–57.
- Murton, B. J., Biggs, J., 2003. Numerical modelling of mud volcanoes and their flows using constraints from the Gulf of Cadiz. *Marine Geology* 195, 223–236.
- Osborne, M. J., Swarbrick, R. E., 1997. Mechanisms for Generating Overpressure in Sedimentary Basins: A Reevaluation. *AAPG Bulletin* 81 (6), 1023–1041.
- Paull, C. K., Hecker, B., Commeau, R., Freeman-Lynde, R. P., Neumann, C., Corso, W. P., Golubic, S., Hook, J. E., Sikes, E., Curray, J., 1984. Biological communities at the florida escarpment resemble hydrothermal vent taxa. *Science* 226 (4677), 965–967.
- Planke, S., Svensen, H., Hovland, M., Banks, D. A., Jamtveit, B., 2003. Mud and fluid migration in active mud volcanoes in Azerbaijan. *Geo-Mar Lett* 23, 258–268.
- Protti, M., Guendel, F., McNally, K., 1995. Correlation between the age of the subducting Cocos plate and the geometry of the Wadati-Benioff zone under Nicaragua and Cost Rica. In: Mann, P. (Ed.), *Geologic and Tectonic Development of the Caribbean Plate Boundary in Southern Central America*. Vol. 295. Spec. Pap. Geol. Soc. Am., pp. 309–343.
- Ranero, C. R., Phipps Morgan, J., McIntosh, K., Reichert, C., 2003. Bending-related faulting and mantle serpentinitization at the Middle America trench. *Nature* 425, 367–373.
- Ranero, C. R., von Huene, R., 2000. Subduction erosion along the Middle America convergent margin. *Nature* 404, 748–752.
- Ranero, C. R., von Huene, R., Flueh, E., Duarte, M., Baca, D., McIntosh, K., 2000a. A cross section of the convergent Pacific margin of Nicaragua. *Tectonics* 19 (2), 335–357.
- Ranero, C. R., von Huene, R., Weinrebe, W., McIntosh, K., Reichert, C., 2000b. Mass Transfer and Fluid Flow Paths Related to Subduction Erosion at the Middle America Convergent Margin. *Eos, Trans. Am. Geophys. Un. - (Fall Meeting Supplement)* 81, 48.
- Rew, R., Davis, G., 1990. Netcdf: an interface for scientific data access. *Computer Graphics and Applications, IEEE* 10 (4), 76–82, Unidata Program Center, Boulder, CO.
- Ritger, S., Carson, B., Suess, E., 1987. Methane-derived authigenic carbonates formed by subduction-induced pore-water expulsion along the Oregon/Washington margin. *Geological Society of America Bulletin* 98, 147–156.
- Sahling, H., Masson, D. G., Ranero, C. R., Hühnerbach, V., Weinrebe, W., Klauke, I., Bürk, D., Brückmann, W., Suess, E., *subm.* Fluid seepage at the continental margin offshore Costa Rica and Nicaragua. *Geochemistry Geophysics Geosystems*.

BIBLIOGRAPHY

- Sahling, H., Rickert, D., Lee, R. W., Linke, P., Suess, E., 2002. Macrofaunal community structure and sulfide flux at gas hydrate deposits from the Cascadia convergent margin, NE Pacific. *Marine Ecology Progress Series* 231, 121–138.
- Screaton, E. J., Saffer, D. M., 2005. Fluid expulsion and overpressure development during initial subduction at the Costa Rica convergent margin. *Earth Planet. Sci. Lett.* 233, 361–374.
- SFB574, 2003. Volatiles and Fluids in Subduction Zones: Climate Feedback and Trigger Mechanisms for Natural Disasters. Progress Report Phase 1, Christian-Albrechts-University.
- Shipley, T. H., McIntosh, K. D., Silver, E. A., Stoffa, P. L., 1992. Three-Dimensional Seismic Imaging of the Costa Rica Accretionary Prism: Structural Diversity in a Small Volume of the Lower Slope. *J. Geophys. Res.* 97 (B4), 4439–4459.
- Shipley, T. H., Stoffa, P. L., Dean, D. F., 1990. Underthrust sediments, fluid migration paths, and mud volcanoes associated with the accretionary wedge off Costa Rica: Middle America trench. *J. Geophys. Res.* 95, 8743–8752.
- Sibuet, M., Juniper, S. K., Pautot, G., 1988. Cold-seep benthic communities in the Japan subduction zones: Geological control of community development. *Journal of Marine Research* 46 (2), 333–348.
- Silver, E., Kastner, M., Fisher, A., Morris, J., McIntosh, K., Saffer, D., 2000. Fluid flow paths in the Middle America Trench and Costa Rica margin. *Geology* 28 (8), 679–682.
- Stockwell Jr., J. W., May 1999. The CWP/SU: Seismic Unix Package. *Computers and Geosciences*.
- Stoll, R. D., 1985. Marine sediment acoustics. *J. Acoust. Soc. Am.* 77, 1789–1799.
- Suess, E., Carson, B., Ritger, S. D., Moore, J. C., Jones, M. L., Kulm, G. R., Cochrane, G. R., 1985. Biological communities at vent sites along the subduction zone off Oregon. *Biol. Soc. Wash. Bull.* 6, 475–484.
- Suess, E., Massoth, G. J., 1984. Evidence for venting of pore waters from subducted sediments of the Oregon continental margin. *Eos, Transactions, American Geophysical Union* 65:1089.
- Talukder, A. R., Bialas, J., Klaeschen, D., Buerk, D., Brueckmann, W., Reston, T., Breitzke, M., in press. High-resolution, deep tow, multichannel seismic and sidescan sonar survey of the submarine mounds and associated BSR off Nicaragua Pacific margin. *Marine Geology*.
- Talukder, A. R., Comas, M. C., Soto, J. I., 2003. Pliocene to Recent mud diapirism and related mud volcanoes in the Alboran Sea (Western Mediterranean). In: Van Rensbergen, P., Hillis, R., Maltman, A., Morley, C. (Eds.), *Subsurface Sediment Mobilization*. Vol. 216. Geological Society, London, Special Publications, pp. 443–459.

- Teichert, B. M. A., Bohrmann, G., Suess, E., 2005. Chemoherms on Hydrate Ridge - Unique microbially-mediated carbonate build-ups growing into the water column. *Palaeogeography, Palaeoclimatology, Palaeoecology* 227, 67–85.
- Urick, R. J., 1983. Principles of underwater sound, 3rd Edition. Peninsula Publishing.
- Van Rensbergen, P., Hillis, R. R., Maltman, A. J., Morley, C. K., 2003. Subsurface sediment mobilization: introduction. In: Van Rensbergen, P., Hillis, R., Maltman, A., Morley, C. (Eds.), *Subsurface Sediment Mobilization*. Vol. 216. Geological Society, London, Special Publications, pp. 1–8.
- Vogt, P. R., Gardner, J., Crane, K., 1999. The Norwegian-Barents-Svalbard (nbs) continental margin: Introducing a natural laboratory of mass wasting, hydrates, and ascent of sediment, pore water, and methane. *Geo-Mar Lett* 19, 2–21.
- von Huene, R., Ranero, C. R., Vannucchi, P., 2004a. Generic model of subduction erosion. *Geology* 32 (10), 913–916.
- von Huene, R., Ranero, C. R., Watts, P., 2004b. Tsunamigenic slope failure along the Middle America Trench in two tectonic settings. *Marine Geology* 203, 303–317.
- von Huene, R., Ranero, C. R., Weinrebe, W., Hinz, K., 2000. Quaternary convergent margin tectonics of Costa Rica, segmentation of the Cocos Plate, and Central American volcanism. *Tectonics* 19 (2), 314–334.
- Walther, C. H. E., Flueh, E. R., Ranero, C. R., von Huene, R., Strauch, W., 2000. Crustal structure across the Pacific margin of Nicaragua: evidence for ophiolitic basement and a shallow mantle sliver. *Geophys. J. Int.* 141, 759–777.
- Weinrebe, W., Klauke, I., 2005. *Surveying Deep-water Seeps at Convergent Continental Margins*. Hydro International.
- Wessel, P., Smith, W. H. F., 1991. Free software helps map and display data. *Eos Trans., AGU* 72, 441.

List of Figures

1.1	Plate tectonic situation of Central America	3
1.2	Major tectonic elements of the central american continental margin	5
1.3	Tectonic model of an erosional convergent margin	7
1.4	Segmentation of the study area offshore Nicaragua	12
1.5	Gradient map of survey area	13
1.6	Simrad EM-120 amplitude map and IFM-GEOMAR DTS-1 sidescan sonar mosaic offshore Nicaragua	14
2.1	DTS-1 towfish track offshore Nicaragua	16
2.2	IFM-GEOMAR DTS-1 sidescan sonar system	18
2.3	Layout of the deep-towed sidescan sonar/streamer system	19
2.4	Components of the deep-tow recording and control system	20
2.5	PRISM mapsheets of sidescan sonar survey offshore Nicaragua	25
2.6	PRISM processing workflow	26
2.7	ERDAS Imagine processing workflow	27
2.8	Examples of sediment echosounding data	29
3.1	Mound Structures and Backscatter Anomalies offshore Nicaragua	35
3.2	Sidescan sonar image on seafloor DEM – Momotombo Slide Area	36
3.3	Subbottom profiles in Momotombo Slide Area	38
3.4	Seafloor observations at Mound Carablanca	39
3.5	Sidescan sonar image on seafloor DEM – Central Area and Baula Massive	40
3.6	Subbottom profile across Mound Buho and Mound Hormiga	43
3.7	Seafloor observations at Mound Buho	44
3.8	Seafloor observations at Mound Hormiga	45
3.9	Seafloor observations at Mound Quetzal	47

LIST OF FIGURES

3.10	Subbottom profile across Mound Iguana	49
3.11	Seafloor observations at Mound Iguana	50
3.12	Sidescan sonar image on seafloor DEM – Mound Buho/Hormiga Area	51
3.13	Subbottom profiles of sub-seafloor structure	52
3.14	Sidescan sonar image on seafloor DEM – Baula Massive	53
3.15	Subbottom profiles across Baula Massive	55
3.16	Seafloor observations at Mound Baula I	56
3.17	Sidescan sonar image on seafloor DEM – Mounds Perezoso & Colibri	57
3.18	Sidescan sonar image on seafloor DEM – Mound Ridges	59
3.19	Subbottom profile across Mound Morpho	60
3.20	Seafloor observations at Mound Morpho	61
3.21	Seafloor pictures from mounds offshore Nicaragua	62
3.22	Sidescan image and subbottom profile of possible gas hydrate occurrences	64
3.23	Mound morphologies imaged as TIN’s	66
3.24	Calculated mound volumes per base area	68
3.25	Generic model of mound structure formation	74
4.1	Geometry of target scattering	82
4.2	Target strengths for spheres of different radii as a function of frequency	84
4.3	Insonified surface at grazing incidence	85
4.4	Multibeam acquisition beam geometry	85
4.5	Geometrical model of volume backscattering	86
4.6	Coherent reflection and scattering by a rough surface	87
4.7	Decomposition of a rough surface into spatial spectral components	88
4.8	General relation of backscattering strength vs. incidence angle	89
4.9	Diffuse scattering at a Lambert scatterer	90
4.10	Backscatter strength BS over incidence angle θ for Lambert’s law	91
4.11	Facet backscattering	92
4.12	Bragg backscattering	93
4.13	Backscatter strength on a horizontal and an inclined seafloor	94
4.14	Calculation of shading coefficients	96
4.15	Profile sections for calculation of DTS-1 shading function	96
4.16	Shading coefficients over nadir distance for test area	97

4.17 Seafloor slope causing differing port and starbord amplitude peaks	98
4.18 Along-track seafloor morphology, vehicle depth and -elevation in test area	99
4.19 Linear approximation of shading function derived in test area	100
4.20 Generation of image pixels from a sidescan sonar ping	102
4.21 Flowchart of program <i>TopoRed</i>	104
4.22 Geometry between sidescan transducer and bathymetry grid cell	105
4.23 Spatial relation between incident acoustic beam and bathymetry grid cell	107
4.24 PRISM sidescan sonar image of test area	109
4.25 Color coded shaded bathymetry map of test area	110
4.26 Color coded gradient map of test area	111
4.27 Topographic reduction factors for surveyed (real) bathymetry	113
4.28 Influence of seafloor slope and relative height on incidence angle	117
4.29 Map representation of raw sidescan sonar data	118
4.30 Shading coefficients for a horizontal, plain seafloor	119
4.31 Shading coefficients from figure 4.30 applied to raw data	120
4.32 Shading coefficients for surveyed (real) bathymetry	121
4.33 Shading coefficients from figure 4.32 applied to raw data	122
4.34 Difference in amplitude values between process runs with horizontal and real seafloor	123
4.35 Change of amplitude values in percentage between process runs with hori- zontal and real seafloor	124
4.36 Shading coefficients of ping 250 across Mound Hormiga	125
4.37 Shading coefficients of ping 1220 across Mound Buho	126
4.38 Sample migration to true location on seafloor	128
5.1 Location of depth profiles and canyons in survey area	130
5.2 Topographic sections parallel slope across survey area	131
6.1 Slides and slumps on continental slope offshore Nicaragua	134
6.2 Momotombo- and Masaya-Slide in northern part of survey area	136
A.1 Attenuation coefficients of marine sediments for different sonar systems	139

List of Tables

2.1	Iterative gridding parameters during bathymetry processing	22
3.1	Morphometric numbers and volumes of mounds offshore Nicaragua	67
5.1	Major canyons in working area.	129
6.1	Morphometric numbers of Momotombo Slide and Masaya Slide	135
B.1	Mound Structures and Backscatter Anomalies offshore Nicaragua	142

Acknowledgements

I would like to thank...

Prof. Dr. Hans-Jürgen Götze for supervising this work and his continuous support and advice.

Prof. Dr. Timothy J. Reston for acting as co-referee.

The SFB 574 at the University of Kiel and in particular the DFG for financial support of this work.

Dr. Wilhelm Weinrebe, permanent leader of the subproject A1 in the SFB 574, for introducing me to bathymetry processing, sending me to various cruises, and signing all forms of whichever nature.

Dr. Ingo Klaucke for guiding me through science and other places on this wonderful planet.

Dr. Heiko Sahling for his assistance in the analysis of the seafloor video data and the identification of the vent fauna.

Dr. Jörg Petersen and Dr. Cord Papenberg for their help with Seismic Unix and the scripts to correct the subbottom profiler data.

Dr. Jürgen Goßler for his ongoing interest in this work and the fruitful scientific, political and financial discussions.

Dr. Arnim Berhorst and Dr. Matthias Zillmer for proof-reading.

Wolfgang Plager for being the wizard of data transformation.

All colleagues of the *SFB 574* and the *Geodynamics* department for creating a friendly and nice working atmosphere.

The crew and scientists of RV Sonne Cruise 173/1 for the successful data acquisition.

Last but not least the software packages used for processing, analysis, interpretation, visualization and typesetting: PRISM, CARAIBES, ERDAS Imagine, ESRI ArcGIS, IVS3d Fledermaus, GMT, MB-System, Seismic Unix, L^AT_EX... running on Linux, Windows XP, MacOS X and Sun Workstations... and www.leo.org, the online dictionary.

My family and friends for their patience with me.

Erklärung

Hiermit erkläre ich, dass die von mir für das Promotionsverfahren vorgelegte Abhandlung ‘Geoacoustic investigations of cold vents and sedimentary processes at the active continental margin offshore Nicaragua’, abgesehen von der Beratung der Betreuer, nach Inhalt und Form meine eigene Arbeit ist. Bisher ist die Arbeit noch nicht an anderer Stelle im Rahmen eines Prüfungsverfahrens vorgelegt worden.

Dietmar Bürk.

Curriculum Vitae

Personal details:

Name: Dietmar Bürk
Date of Birth: 02. October 1966
Place of Birth: Schwenningen am Neckar
Citizenship: German

Education:

since 06/2003: PhD student in the SFB 574 at the IFM-GEOMAR
07/1994: Diplom in Geology
1990-1994: Graduate Studies in Geology/Palaeontology at the University of Freiburg
1989-1990: Studies in Geology, Computer Science, and Macroeconomics at Brock University, St.Catharines, Ontario, Canada
1987-1989: Undergraduate Studies in Geology/Palaeontology at the University of Freiburg
1986-1987: Military Service in München, Sonthofen, and Sigmaringen
1977-1986: Fürstenberg-Gymnasium, Donaueschingen
Abitur: 06/1986
1973-1977: Heinrich-Feurstein-Grundschule, Donaueschingen

Work experience:

1998-2003: Software Developer for SmallWorld GIS at isys software GmbH in Freiburg
1996-1998: GIS Programmer at Geomatics International GmbH, Lahr
1994-1995: Landesamt für Geologie, Rohstoffe und Bergbau, Freiburg